



Multi-Scale models and computational methods for aerothermodynamics

Alessandro Munafo

► To cite this version:

Alessandro Munafo. Multi-Scale models and computational methods for aerothermodynamics. Other. Ecole Centrale Paris, 2014. English. NNT: 2014ECAP0008 . tel-00997437

HAL Id: tel-00997437

<https://theses.hal.science/tel-00997437>

Submitted on 28 May 2014

HAL is a multi-disciplinary open access archive for the deposit and dissemination of scientific research documents, whether they are published or not. The documents may come from teaching and research institutions in France or abroad, or from public or private research centers.

L'archive ouverte pluridisciplinaire **HAL**, est destinée au dépôt et à la diffusion de documents scientifiques de niveau recherche, publiés ou non, émanant des établissements d'enseignement et de recherche français ou étrangers, des laboratoires publics ou privés.

THÈSE

présentée par

Alessandro Munafò

pour l'obtention du

GRADE de DOCTEUR

Formation doctorale : Énergétique

Laboratoire d'accueil : Laboratoire d'Énergétique Moléculaire et Macroscopique, Combustion (EM2C) du CNRS et de l'ECP

Multi-Scale Models and Computational Methods for Aerothermodynamics

Soutenue le 21 Janvier 2014

Rapporteurs :

M.	Bruno	D.	Chercheur CNR, IMIP
M.	Giovangigli	V.	Dir. de Recherche CRNS, CMAP

Jury :

Mme	Bourdon	A.	Dir. de Recherche CNRS, EM2C UPR 288
Mme	Gamba	I. M.	Professeur, ICES UT Austin
M.	Jaffe	R. L.	Chercheur, NASA ARC
M.	Magin	T. E.	Associate Professor, VKI
M.	Massot	M.	Professeur CNRS, EM2C UPR 288
M.	Panesi	M.	Assistant Professor, UIUC

Acknowledgements

After the end of my PhD at the von Karman Institute for Fluid Dynamics and Ecole Centrale Paris, I would like to thank the following people.

First of all, I would like to thank my PhD supervisors, Prof. Thierry Magin and Dr. Anne Bourdon, for offering me the possibility to do a PhD on aerothermodynamics and for trusting in my capabilities. Your supervision was always very clear, constant and helpful. You gave me a lot of good advices and, more importantly, you were never too busy when it was time to discuss with me about research related topics. In the long term, this is one of the factors that can make the difference between a successful and an unsuccesfull research program.

I would like to thank Prof. Vincent Giovangigli and Dr. Domenico Bruno for accepting to review my thesis, and Prof. Marco Panesi, Prof. Marc Massot, Prof. Irene Gamba and Dr. Richard Jaffe, for accepting to be jury members at my PhD defense.

Thanks to Dr. Rich Jaffe for providing the NASA Ames quantum chemistry database used in the present thesis, and for introducing me to the fantastic world of *ab-initio* calculations.

Thanks to Prof. Marco Panesi for the continuous support, ideas and the useful discussions we had on state-to-state modeling for non-equilibrium flows. You really helped me a lot, especially during the first part of my PhD while I was “digesting” the NASA Ames database. I owe you part of the results of my thesis.

Thanks to Prof. Irene Gamba and Dr. Jeff Haack for offering me the possibility to work with them on deterministic Boltzmann solvers. I think that the success of our joint collaboration clearly indicates that bigger advancements in research could be achieved if communities that usually work on their own (in our case engineers and mathematicians) would exchange ideas more often.

Thanks to Dr. Mike Kapper and Dr. Jean-Luc Cambier for providing the two-dimensional code used in the present thesis and for the useful discussions we had on Riemann solvers and high-order methods for non-equilibrium flows.

Thanks to Prof. Olivier Chazot. You have been a very good supervisor during my Short Training Program and Diploma Course at VKI.

Thanks to Prof. Hermann Deconinck. You have been a very good teacher and introduced me to computational methods during the Diploma Course. If I have chosen to continue and work on computational methods during my PhD, it is also because of you.

Thanks to Dr. Domenico “Mimmo” Giordano. I really enjoyed the conversations we had on quantum chemistry, kinetic theory, statistical mechanics and linear irreversible thermodynamics.

Thanks to Dr. Kelly Stephani and (again) Prof. Marco Panesi for hosting me at their place in Austin. I will never forget that month I spent together with you two during my first visit at UT Austin.

Thanks to all my VKI and ECP friends for all the wonderful moments we spent together at work and out of work. In particular, I would like to thank my PhD colleagues and collaborators Erik, JB, Bernd, Alessandro Turchi, Khalil, Andrea, Damien, Aurélien, Boris, Domingo, Jesus, Tamas, Fabio, François, Benoit, Aurélie, Bruno and Georgios, and my Diploma Course “italian connection” fellows Dino, Antonino, Manfredi, Francesco Baldani, Francesco Giannattasio and Alessandro Sanna.

Last, but not least, I want to thank my parents, Diego and Giuliana, and my sister, Sara, for their continuous support and love. When the night was there, they always stood by me.

The research presented in this thesis has been financially supported by the European Research Council Starting Grant #259354.

Abstract

This thesis aimed at developing multi-scale models and computational methods for aerothermodynamics applications.

The research on multi-scale models has focused on internal energy excitation and dissociation of molecular gases in atmospheric entry flows. The scope was two-fold: to gain insight into the dynamics of internal energy excitation and dissociation in the hydrodynamic regime and to develop reduced models for Computational Fluid Dynamics applications. The reduced models have been constructed by coarsening the resolution of a detailed rovibrational collisional model developed based on *ab-initio* data for the $\text{N}_2(^1\Sigma_g^+)$ - $\text{N}(^4\text{S}_u)$ system provided by the Computational Quantum Chemistry Group at NASA Ames Research Center. Different mechanism reduction techniques have been proposed. Their application led to the formulation of conventional macroscopic multi-temperature models and vibrational collisional models, and innovative energy bin models. The accuracy of the reduced models has been assessed by means of a systematic comparison with the predictions of the detailed rovibrational collisional model. Applications considered are inviscid flows behind normal shock waves, within converging-diverging nozzles and around axisymmetric bodies, and viscous flows along the stagnation-line of blunt bodies. The detailed rovibrational collisional model and the reduced models have been coupled to two flow solvers developed from scratch in FORTRAN 90 programming language (SHOCKING_F90 and SOLVER_FVMCC_F90). The results obtained have shown that the innovative energy bin models are able to reproduce the flow dynamics predicted by the detailed rovibrational collisional model with a noticeable benefit in terms of computing time. The energy bin models are also more accurate than the conventional multi-temperature and vibrational collisional models.

The research on computational methods has focused on rarefied flows. The scope was to formulate a deterministic numerical method for solving the Boltzmann equation in the case of multi-component gases with internal energy by accounting for both elastic and inelastic collisions. The numerical method, based on the weighted convolution structure of the Fourier transformed Boltzmann equation, is an extension of an existing spectral-Lagrangian method, valid for a mono-component gas without internal energy. During the development of the method, particular attention has been devoted to ensure the conservation of

mass, momentum and energy while evaluating the collision operators. Conservation is enforced through the solution of constrained optimization problems, formulated in a consistent manner with the collisional invariants.

The extended spectral-Lagrangian method has been implemented in a parallel computational tool (BEST; Boltzmann Equation Spectral Solver) written in C programming language.

Applications considered are the time-evolution of an isochoric gaseous system initially set in a non-equilibrium state and the steady flow across a normal shock wave. The accuracy of the proposed numerical method has been assessed by comparing the moments extracted from the velocity distribution function with Direct Simulation Monte Carlo (DSMC) method predictions. In all the cases, an excellent agreement has been found. The computational results obtained for both space homogeneous and space inhomogeneous problems have also shown that the enforcement of conservation is mandatory for obtaining accurate numerical solutions.

Résumé

Cette thèse porte sur le développement de modèles multi-échelles et de méthodes de calcul pour les applications aérothermodynamiques.

Le travail de recherche sur les modèles multi-échelles met l'accent sur l'excitation énergétique et la dissociation dans des gaz moléculaires pour des écoulements de rentrée atmosphérique. L'objectif est double : mieux comprendre la dynamique des processus d'excitation énergétique et de dissociation dans le régime hydrodynamique et développer des modèles réduits pour des applications de calcul en dynamique des fluides (CFD). Les modèles réduits ont été construits en diminuant la résolution d'un modèle détaillé de collisions rovibrationnelles élaboré au départ d'une base de données *ab-initio* pour le système N₂(¹Σ_g⁺)-N(⁴S_u) par le groupe de chimie quantique du centre de recherche de NASA Ames. Différentes techniques de réduction de ce mécanisme ont été proposées. Leur application a conduit à la formulation de modèles macroscopiques classiques multi-températures et de type collisions vibrationnelles, et de modèles innovants de paniers d'énergie. La précision des modèles réduits a été évaluée au moyen d'une comparaison systématique des résultats avec les prédictions obtenues à l'aide du modèle détaillé des collisions rovibrationnelles. Les applications envisagées sont les écoulements non-visqueux derrière des ondes de choc normales, dans des tuyères convergentes-divergentes et autour de corps de révolution, ainsi que les écoulements visqueux le long de la ligne d'arrêt de corps émuossés. Le modèle détaillé de collisions rovibrationnelles et les modèles réduits ont été couplés à deux solveurs d'écoulement développés en langage de programmation FORTRAN 90 (SHOCKING_F90 et SOLVER_FVMCC_F90). Les résultats obtenus ont montré que les modèles de paniers d'énergie permettent de reproduire avec précision la dynamique d'écoulement prédites par le modèle détaillé de collisions rovibrationnelles tout en exhibant un avantage notable en termes de temps de calcul. Les modèles de paniers d'énergie sont aussi plus précis que les modèles classiques multi-température et de collision vibrationnelle. Le travail de recherche sur les méthodes de calcul a porté sur les écoulements raréfiés. L'objectif était de formuler une méthode numérique de type déterministe pour résoudre l'équation de Boltzmann dans le cas de gaz à plusieurs composants y compris l'énergie interne en considérant à la fois pour les collisions élastiques et inélastiques. La méthode numérique, basée sur la structure de convolution pondérée de la transformée de Fourier de l'équation de Boltz-

mann, est une extension d'une méthode spectrale existante de type Lagrange, valable pour un gaz à un composant sans énergie interne. Lors de l'élaboration de la méthode, une attention particulière a été consacrée à la conservation de la masse, de la quantité de mouvement et de l'énergie lors de l'évaluation des opérateurs de collision. La propriété de conservation est assurée en résolvant un problème d'optimisation sous contraintes, formulées d'une manière compatible avec les invariants de collision.

La méthode spectrale-Lagrangienne étendue utilise un outil de calcul parallèle (BEST ; Boltzmann Equation Spectral Solver) écrit en langage de programmation C.

Les applications considérées sont l'évolution temporelle d'un système gazeux isochore initialement figé dans un état de déséquilibre et l'écoulement constant à travers une onde de choc normale. La précision de la méthode numérique proposée a été évaluée en comparant les moments extraits de la fonction de distribution de vitesse avec les prédictions de la méthode de simulation directe Monte Carlo (DSMC). Dans tous les applications étudiées, un excellent accord a été trouvé. Les résultats des calculs obtenus pour les problèmes spatiaux hétérogènes et homogènes ont également démontré l'importance d'imposer la propriété de conservation pour l'obtention de solutions numériques précises.

List of Publications

The results obtained in this thesis have been published in 4 archival papers:

1. A. Munafò, M. Panesi, R. L. Jaffe, G. Colonna, A. Bordon, T. E. Magin (2012). QCT-based vibrational collisional models applied to nonequilibrium nozzle flows, *Eur. Phys. J. D* 66, 188.
2. A. Munafò, M. Panesi, T. E. Magin (2014). Boltzmann rovibrational collisional coarse-grained model for internal energy excitation and dissociation in hypersonic flows. *Phys. Rev. E* 89(2), 023001.
3. A. Munafò, J. R. Haack, I. M. Gamba, T. E. Magin (2014). A spectral-Lagrangian Boltzmann solver for a multi-energy level gas. *J. Comput. Phys.* 264, 152–176.
4. A. Bourdon, J. Annaloro, A. Bultel, M. Capitelli, G. Colonna, A. Guy, T. E. Magin, A. Munafò, M.-Y. Perrin (2014). Reduction of state-to-state to macroscopic models for hypersonics. *OPPJ*, in press.

2 conference proceedings with peer-review:

1. M. Panesi, T. E. Magin, A. Munafò, A. Bourdon, R. L. Jaffe, D. W. Schwenke. (2010). Rovibrational internal energy excitation and dissociation of nitrogen in hypersonic flows. *Proc. of the 2010 CTR Summer Program, Center for Turbulence Research, Stanford University, Stanford, CA.*
2. A. Munafò, J. R. Haack, I. M. Gamba, T. E. Magin (2012). Investigation of nonequilibrium internal energy excitation in shock waves by means of a spectral-Lagrangian Boltzmann solver. *Proc. of the 28th International Symposium on Rarefied Gasdynamics, Zaragoza, Spain.*

and 6 conference proceedings without peer-review:

1. A. Munafò, M. Panesi, R. L. Jaffe, A. Lani, T. E. Magin (2010). Vibrational state to state kinetics in expanding and compressing nitrogen flows. AIAA Paper 2010-4335. 10th AIAA/ASME Joint Thermophysics and Heat Transfer Conference, Chicago, IL.
2. A. Munafò, M. Panesi, R. L. Jaffe, G. Colonna, T. E. Magin (2011). Application of vibrational state-to-state collisional models for atmospheric entry flows. *Proc. of the 7th ESA Symposium on Aerothermodynamics*

LIST OF PUBLICATIONS

- for Space Vehicles*, Brugge, Belgium.
- 3. E. Torres, A. Munafò, T. E. Magin (2011). Internal energy excitation and dissociation in nitrogen flows using DSMC. *Proc. of the 7th Symposium on Aerothermodynamics for Space Vehicles*, Brugge, Belgium.
 - 4. A. Munafò, M. Panesi, R. L. Jaffe, A. Bourdon, T. Magin. (2011). Mechanism reduction for rovibrational energy excitation and dissociation of molecular nitrogen in hypersonic flows. AIAA Paper 2011-3623. 11th AIAA/ASME Joint Thermophysics and Heat Transfer Conference, Honolulu, HW.
 - 5. A. Munafò and M. G. Kapper and J.-L. Cambier and T. E. Magin (2012). Investigation of nonequilibrium effects in axisymmetric nozzle and blunt body nitrogen flows by means of a reduced rovibrational collisional model. AIAA Paper 2012-0647. 50h AIAA Aerospace Sciences Meeting including the New Horizons Forum and Aerospace Exposition, Nashville, TN.
 - 6. A. Munafò, E. Torres, J. R. Haack, I. M. Gamba, T. E. Magin (2013). Investigation of nonequilibrium effects across shock waves by means of a spectral-Lagrangian Boltzmann solver. AIAA Paper 2013-0305. 51th AIAA Aerospace Sciences Meeting, Dallas, TX.

Contents

Abstract	v
Résumé	vii
List of Publications	ix
Nomenclature	xxix
Introduction	1
I Physico-Chemical Models for Non-Equilibrium Flows	15
1 Kinetic Approach	17
1.1 Assumptions	17
1.2 The Boltzmann Equation	19
1.3 Equilibrium Solution	25
1.4 Non-Equilibrium Solution	28
1.5 Maxwell Transfer Equations	29
1.6 The Conservation Equations of Gasdynamics	31
1.7 Summary	31
2 Hydrodynamic Approach	33
2.1 State-to-State Chapman-Enskog Method	33
2.2 Zeroth-Order Solution	37
2.3 Zeroth-Order Hydrodynamic Equations and First-Order Solution	38
2.4 First-Order Hydrodynamic Equations	40
2.5 Summary	47
3 Development of Quantum Based Chemical Models	49
3.1 The NASA Ames Database	49
3.2 Multi-Temperature Model	58
3.3 Vibrational Collisional Model	63
3.4 Energy Bin Model	65
3.5 Unified Notation	72

3.6 Intermediate Conclusions	75
II Integration of Coarse-Grained Models in Hydrodynamic Flows	77
4 ODE Solver for Flows Behind Normal Shock Waves	79
4.1 Governing Equations and Numerical Method	79
4.2 Application of the RVC Model	80
4.3 Application of the Reduced Models (MT, VC, BRVC and URVC)	90
4.4 Intermediate conclusions	96
5 CFD Solvers for Aerothermodynamic Flows	99
5.1 Governing Equations in Conservation Law Form	99
5.2 Numerical Methods	103
5.3 Quasi-One-Dimensional Nozzle Flows	111
5.4 Stagnation-Line Flows	126
5.5 Inviscid Axisymmetric Flows	135
5.6 Intermediate Conclusions	142
III Development of a Deterministic Kinetic Flow Solver	145
6 Extension of a Conservative Spectral-Lagrangian Method to Multi-Component Gases and Inelastic Collisions	147
6.1 The Weak Form of The Partial Collision Operators	147
6.2 The Fourier Transform of the Partial Collision Operators	149
6.3 Numerical Method	151
6.4 Intermediate Conclusions	159
7 Applications of the BEST code	161
7.1 Gas without Internal Energy: Flow across a Normal Shock Wave in Ar	161
7.2 Multi-Component Gas without Internal Energy	171
7.3 Gas with Internal Energy	178
7.4 Intermediate Conclusions	187
Conclusions	189
Perspectives	193
A Fitting Expressions for MT Models	195
B ODE sets in Canonical Form	197
B.1 RVC, VC, BRVC and URVC models	197
B.2 MT models	198

C Eigensystems	201
C.1 Two-Dimensional Flows	201
C.2 One-Dimensional Flows	206
C.3 Stagnation-line Flows	207
D Positive-Negative Split Jacobians	209
D.1 One-Dimensional Flows	209
D.2 Stagnation-Line Flows	209
E Source Term Jacobians	211
E.1 Kinetic Process Source Term	211
E.2 Convective Source Term	214
F Diffusive Jacobians for Stagnation-Line Flows	215
F.1 Diffusive Flux	217
F.2 Diffusive Source Term	218
G Fourier Transform of the Partial Collision Operators	219
G.1 Partial Elastic Collision Operator	219
G.2 Partial Inelastic Collision Operator	220
H Isotropic Convolution Weights	223
H.1 Elastic Collisions	223
H.2 Inelastic Collisions	225
I Discrete Fourier Transforms and Weighted Convolutions	227
I.1 Fourier and inverse Fourier Transform	227
I.2 Weighted Convolution	229
J Solution of the Constrained Optimization Problems	231
J.1 Elastic Collisions	231
J.2 Inelastic Collisions	232
K Discrete Macroscopic Moments	235
References	251

List of Tables

4.1	Free-stream conditions for normal shock wave studies.	81
4.2	RVC model. Position, N mole fraction and temperatures for the locations at which the population distributions are extracted.	85
4.3	Number of energy bins used for the BRVC and URVC models.	93
5.1	RVC model. Position, N_2 mole fraction and temperatures for the locations at which the population distributions are extracted.	112
5.2	RVC, BRVC(50), VC and MTP model comparison. Outlet values for the N_2 mole fraction, translational temperature and velocity (EAST facility nozzle).	115
5.3	BRVC(50), VC and MTP model comparison. Outlet values for the N_2 mole fraction, translational temperature and velocity (F4 and Scirocco nozzles).	120
5.4	BRVC(50) model. Position, N_2 mole fraction and temperatures for the locations at which the energy bin population distributions are extracted (Scirocco nozzle).	122
5.5	BRVC model. Outlet values of the N_2 mole fraction and related relative error for different number of energy bins (the relative error on the N_2 mole fraction is estimated by taking the VC model solution as the exact solution).	125
5.6	BRVC(20) model. Wall pressure, N mole fraction, heat flux and internal temperature for different values of the free-stream pressure.	127
5.7	BRVC(20) and MTP model. Wall heat flux and N mole fraction values.	133
5.8	BRVC model. Wall heat flux and N mole fraction for different numbers of energy bins.	135
7.1	Flow across a normal shock wave in Ar. Post-shock conditions and VHS model parameters.	162
7.2	Flow across a normal shock wave in Ar. Simulation parameters.	163
7.3	Masses and diameters of Ne and Ar.	171
7.4	Isochoric equilibrium relaxation of a Ne-Ar gas. Number of velocity nodes and related L_1 and L_2 norms of the error on the gas temperature ($N_t = 300$).	173

7.5	Flow across a normal shock wave in a Ne-Ar gas. Simulation parameters.	175
7.6	Isochoric equilibrium relaxation of a multi-energy level gas. Level degeneracies and energies.	179
7.7	Isochoric equilibrium relaxation of a multi-energy level gas. Final values of temperature and level densities (comparison between simulation and equilibrium calculations).	180
7.8	Flow across a normal shock wave in a multi-energy level gas. Level degeneracies and energies.	181
7.9	Flow across a normal shock wave in a multi-energy level gas. Simulation parameters.	181
A.1	Relaxation time fitting parameters.	195
A.2	Chemistry coupling factor fitting parameters.	196

List of Figures

1	Relevant physico-chemical phenomena occurring during a planetary descent of a space vehicle (credits NASA Ames Research Center).	1
2	Flow regime classification according to the Knudsen number.	2
3.1	Rotational structure of the vibrational levels of $\text{N}_2(^1\Sigma_g^+)$ (one level over four is plotted; crosses bound levels, stars predissociated levels).	51
3.2	Vibrational and rotational energy spacings of $\text{N}_2(^1\Sigma_g^+)$	52
3.3	Internal energy and specific heat of $\text{N}_2(^1\Sigma_g^+)$ (unbroken lines NASA ARC, dashed lines RR-HO).	52
3.4	Analytical fit of the N_3 PES with the $\text{N}-\text{N}-\text{N}$ angle constrained to 115° . Blue regions have low energy and orange/red regions have high energy. The potential energy minima corresponding to $\text{Na} + \text{N}_b\text{N}_c$ and $\text{N}_a\text{N}_b + \text{N}_c$ are shown. These arrangements are connected by a reaction path for the exchange reaction which has a barrier and shallow minimum labeled $\text{N}_a\text{N}_b\text{N}_c$ (credits NASA Ames Research Center).	54
3.5	Extracted relaxation times (unbroken line $\tau_{\text{N}-\text{N}_2}^{\text{tra-int}} p_N$, dashed line $\tau_{\text{N}-\text{N}_2}^{\text{tra-vib}} p_N$, dotted-dashed line $\tau_{\text{N}-\text{N}_2}^{\text{tra-rot}} p_N$).	60
3.6	Chemistry coupling factors (unbroken line $C_{\text{N}_2}^{\text{dis-int}}$, dashed line $C_{\text{N}_2}^{\text{dis-vib}}$, dotted-dashed line $C_{\text{N}_2}^{\text{dis-rot}}$).	60
3.7	Comparison between the NASA ARC and U Bari databases for the vibrational dissociation and inelastic collisional excitation rate coefficients (lines NASA ARC, lines with symbols U Bari; numbers indicate the vibrational levels involved in the transitions).	65
4.1	RVC model. Temperature evolution behind the shock wave for different values of the free-stream pressure (unbroken lines T , dashed lines T_{int} , dotted-dashed lines T_{vib} , dotted lines T_{rot}).	81
4.2	RVC model. N mole fraction evolution behind the shock wave for different values of the free-stream pressure ($u_\infty = 10 \text{ km/s}$; unbroken lines $p_\infty = 0.33 \text{ torr}$, dashed lines $p_\infty = 0.1 \text{ torr}$, dotted-dashed lines $p_\infty = 0.05 \text{ torr}$).	82

4.3 RVC model. Translational temperature and N mole fraction evolution behind the shock wave for different values of the free-stream velocity ($p_\infty = 0.1$ torr; unbroken lines $u_\infty = 11$ km/s, dashed lines $u_\infty = 10$ km/s, dotted-dashed lines $u_\infty = 9$ km/s, lines with circles $u_\infty = 8$ km/s, lines with squares $u_\infty = 7$ km/s, lines with triangles $u_\infty = 6$ km/s).	83
4.4 RVC model. Temperature and N mole fraction evolution behind the shock wave with/without exchange processes ($p_\infty = 0.1$ torr and $u_\infty = 10$ km/s; in (a) unbroken line T with exchange, dashed line T_{int} with exchange, dotted-dashed line T without exchange, dotted line T_{int} without exchange; in (b) unbroken line with exchange, dashed line without exchange).	84
4.5 RVC model. Temperature and N mole fraction evolution behind the shock wave with/without predissociation ($p_\infty = 0.1$ torr and $u_\infty = 10$ km/s; in (a) unbroken line T with predissociation, dashed line T_{int} with predissociation, dotted-dashed line T without predissociation, dotted line T_{int} without predissociation; in (b) unbroken line with predissociation, dashed line without predissociation).	84
4.6 RVC model. Comparative evolution of the N mole fraction and rovibrational energy level distribution behind the shock wave ($p_\infty = 0.1$ torr and $u_\infty = 10$ km/s; the symbols in (a) highlight the locations at which the population distributions, plotted in (b), are extracted).	86
4.7 RVC model. Evolution behind the shock wave of the population of the rovibrational energy levels lying close to the ground-state ($p_\infty = 0.1$ torr and $u_\infty = 10$ km/s; the locations at which the distributions are plotted are the same as those of fig. 4.6).	86
4.8 RVC model. Rotational energy level distribution for the ground and the first three excited vibrational states at $x = 3.6 \times 10^{-3}$ m ($p_\infty = 0.1$ torr and $u_\infty = 10$ km/s; in (a) the unbroken lines represent the Boltzmann distributions at the rotational temperatures T_{rot}^v).	87
4.9 RVC model. Translational and rotational temperature evolution behind the shock wave ($p_\infty = 0.1$ torr and $u_\infty = 10$ km/s; unbroken line T , dashed line T_{rot} , line with circles T_{rot}^0 , line with squares T_{rot}^1 , line with triangles T_{rot}^2 , line with diamonds T_{rot}^3).	88

4.10 RVC model. Evolution of the vibrational and rotational specific population distributions behind the shock wave ($p_\infty = 0.1$ torr and $u_\infty = 10$ km/s; in (a) line with circles $x = 2.5 \times 10^{-5}$ m, line with squares $x = 2.5 \times 10^{-4}$ m, line with triangles $x = 2.3 \times 10^{-3}$ m, line with diamonds $x = 3.2 \times 10^{-3}$ m, dotted line $x = 3.4 \times 10^{-3}$ m, dotted-dashed line $x = 3.6 \times 10^{-3}$ m, dashed line $x = 3.9 \times 10^{-3}$ m, unbroken line $x = 5.1 \times 10^{-3}$ m; in (b) circles $x = 2.5 \times 10^{-5}$ m, squares $x = 2.5 \times 10^{-4}$ m, triangles $x = 2.3 \times 10^{-3}$ m, diamonds $x = 3.2 \times 10^{-3}$ m, unbroken line $x = 3.9 \times 10^{-3}$ m, dashed line $x = 5.1 \times 10^{-3}$ m).	89
4.11 RVC and MT model comparison. Temperature and N mole fraction evolution behind the shock wave ($p_\infty = 0.1$ torr and $u_\infty = 10$ km/s; in (a) unbroken line T RVC, dashed line T_{int} RVC, dotted-dashed line T_{vib} RVC, dotted line T_{rot} RVC, line with circles T MT, line with squares T_{int} MT, line with triangles T_{vib} MT, line with diamonds T_{rot} MT; in (b) unbroken line RVC, dashed line MT).	90
4.12 RVC and MT model comparison. Mass production and energy transfer term evolution behind the shock wave ($p_\infty = 0.1$ torr and $u_\infty = 10$ km/s; in (a) unbroken line RVC, dashed line MT; in (b) unbroken line $\Omega_{N_2}^{\text{dis-vib}}$ RVC, dashed line $\Omega_{N_2}^{\text{dis-rot}}$ RVC, dotted-dashed line $\Omega_{N_2}^{\text{tra-vib}}$ RVC, dotted line $\Omega_{N_2}^{\text{dis-rot}}$ RVC, line with circles $\Omega_{N_2}^{\text{dis-vib}}$ MT, line with squares $\Omega_{N_2}^{\text{dis-rot}}$ MT, line with diamonds $\Omega_{N_2}^{\text{tra-vib}}$ MT, line with triangles $\Omega_{N_2}^{\text{dis-rot}}$ MT).	91
4.13 RVC and MT model comparison. Temperature evolution behind the shock wave switching off dissociation ($p_\infty = 0.1$ torr and $u_\infty = 10$ km/s; unbroken line T RVC, dashed line T_{vib} RVC, dotted-dashed line T_{rot} RVC, line with circles T MT, line with squares T_{vib} MT, line with triangles T_{rot} MT).	91
4.14 RVC model. Time evolution of the macroscopic dissociation rate coefficient (unbroken line $T = 10\,000$ K, dashed line $T = 15\,000$ K, dotted-dashed line $T = 20\,000$ K, line with circles $T = 30\,000$ K, line with squares $T = 40\,000$ K).	92
4.15 RVC, BRVC(50), VC, MT and MTP model comparison. Translational temperature and N mole fraction evolution behind the shock wave ($p_\infty = 0.1$ torr and $u_\infty = 10$ km/s; unbroken lines RVC, dashed lines BRVC(50), dotted-dashed lines VC, lines with circles MT, lines with squares MTP).	94
4.16 RVC and BRVC(50) model comparison. Mass production and energy transfer term evolution behind the shock wave ($p_\infty = 0.1$ torr and $u_\infty = 10$ km/s; in (a) unbroken line RVC, dashed line BRVC(50); in (b) unbroken line $\Omega_{N_2}^{\text{tra-int}}$ RVC, dashed line $\Omega_{N_2}^{\text{dis-int}}$ RVC, line with circles $\Omega_{N_2}^{\text{tra-int}}$ BRVC(50), line with squares $\Omega_{N_2}^{\text{dis-int}}$ BRVC(50)).	94

4.17 BRVC model. Bin number convergence study on the temperatures and the N mole fraction for the flow behind a normal shock wave ($p_\infty = 0.1$ torr and $u_\infty = 10$ km/s; unbroken lines BRVC(2), dashed lines BRVC(5), dotted-dashed lines BRVC(10), dotted lines BVRC(20), lines with circles BRVC(50), lines with squares BRVC(100)).	95
4.18 BRVC and URVC models. Internal temperature evolution behind the shock wave for different numbers of energy bins ($p_\infty = 0.1$ torr and $u_\infty = 10$ km/s; unbroken line BRVC(5), dashed line BRVC(50), dotted-dashed line URVC(5), dotted line URVC(50)).	96
5.1 Node and cell ordering convention in the 2D structured grid code in use.	108
5.2 Normalized area distribution of the EAST facility nozzle (inlet $x = -0.025$ m, throat $x = 0$ m, outlet $x = 0.083$ m).	111
5.3 RVC Model. N ₂ mole fraction and temperature evolution along the axis of the EAST facility nozzle (in (b) unbroken line T , dashed line T_{int} , dotted line T_{vib} , dotted-dashed line T_{rot}).	112
5.4 RVC model. Comparative evolution of the N ₂ mole fraction and the rovibrational energy level distribution along the axis of the EAST facility nozzle (the symbols in (a) highlight the locations at which the population distributions, plotted in (b), are extracted).	113
5.5 RVC model. Evolution along the axis of the EAST facility nozzle of the population of the rovibrational energy levels lying close to the ground-state (the locations at which the distributions are plotted are the same as those of fig. 5.4).	113
5.6 RVC model. Rotational energy level distribution for the ground and the first five excited vibrational states at the location $x = 5 \times 10^{-2}$ m along the axis of the EAST facility nozzle (the unbroken lines in (a) represent the Boltzmann distributions at the rotational temperatures T_{rot}^v).	114
5.7 RVC model. Evolution of the vibrational and rotational specific population distributions along the axis of the EAST facility nozzle (in (a) unbroken line $x = -2.5 \times 10^{-2}$ m, dashed line $x = 1.1 \times 10^{-4}$ m, dotted-dashed line $x = 1 \times 10^{-2}$ m, dotted line $x = 2 \times 10^{-2}$ m, line with circles $x = 3 \times 10^{-2}$ m, line with squares $x = 4 \times 10^{-2}$ m, line with triangles $x = 5 \times 10^{-2}$ m; in (b) circles $x = -2.5 \times 10^{-2}$ m, crosses $x = 1.1 \times 10^{-4}$ m, squares $x = 1 \times 10^{-2}$ m, plus $x = 2 \times 10^{-2}$ m, triangles $x = 3 \times 10^{-2}$ m, stars $x = 4 \times 10^{-2}$ m, diamonds $x = 5 \times 10^{-2}$ m).	115

5.8 RVC, BRVC(50), VC and MTP model comparison. N ₂ mole fraction evolution along the axis of the EAST facility nozzle (unbroken line RVC, dashed line BRVC(50), dotted-dashed line VC, dotted line MTP).	116
5.9 RVC, BRVC(50), VC and MTP model comparison. N ₂ mass production term evolution along the axis of the EAST facility nozzle (unbroken line RVC, dashed line BRVC(50), dotted-dashed line VC, dotted line MTP).	117
5.10 RVC, BRVC(50), VC and MTP model comparison. Energy transfer term evolution along the axis of the EAST facility nozzle (in (a) unbroken line $\Omega_{N_2}^{dis-int}$ RVC, dashed line $\Omega_{N_2}^{dis-vib}$ RVC, dotted-dashed line $\Omega_{N_2}^{dis-int}$ BRVC(50), dotted-line line $\Omega_{N_2}^{dis-vib}$ VC, line with circles $\Omega_{N_2}^{dis-vib}$ MTP; in (b) unbroken line $\Omega_{N_2}^{tra-int}$ RVC, dashed line $\Omega_{N_2}^{tra-vib}$ RVC; dotted-dashed line $\Omega_{N_2}^{tra-int}$ BRVC(50), dotted-line line $\Omega_{N_2}^{tra-vib}$ VC, line with circles $\Omega_{N_2}^{tra-vib}$ MTP). . .	117
5.11 RVC and VC model comparison. Vibrational specific population distributions along the axis of the EAST facility nozzle (lines with circles RVC, lines with squares VC; the reported values for the N ₂ mole fraction, translational and vibrational temperatures refer to the RVC model solution).	118
5.12 Normalized area distributions of the F4 and Scirocco nozzles (in (a) inlet $x = -0.5$ m, throat $x = 0$ m, outlet $x = 3$ m; in (b) inlet $x = -0.28$ m, throat $x = 0$ m, outlet $x = 5$ m).	119
5.13 BRVC(50), VC and MTP model comparison. N ₂ mole fraction, velocity and temperature evolution along the axis of the F4 and Scirocco nozzles (in (a)-(d) unbroken lines BRVC(50), dashed lines VC, dotted-dashed lines MTP; in (e)-(f) lines with circles T BRVC(50), lines with squares T VC, lines with triangles T MTP, unbroken lines T_{int} BRVC(50), dashed lines T_{vib} VC, dotted-dashed lines T_{vib} MTP).	121
5.14 BRVC(50) model. Comparative evolution of the N ₂ mole fraction and the energy bin population distribution along the axis of the Scirocco nozzle (the symbols in (a) highlight the locations where the population distributions, plotted in (b), are extracted; in (b) line with circles $x = -3 \times 10^{-1}$ m, line with squares $x = -4.03 \times 10^{-3}$ m, line with triangles $x = 3.46 \times 10^{-2}$ m, line with diamonds $x = 8.46 \times 10^{-2}$ m, line with stars $x = 1.35 \times 10^{-1}$ m, unbroken line $x = 2.85 \times 10^{-1}$ m, dashed line $x = 3.5 \times 10^{-1}$ m, dotted-dashed line $x = 5.29 \times 10^{-1}$ m, dotted line $x = 6.94 \times 10^{-1}$ m).	123

5.15 BRVC(50) model. Energy bin population distributions at the locations $x = 2.85 \times 10^{-1}$ m and $x = 6.94 \times 10^{-1}$ m along the axis of the Scirocco nozzle (the dashed and the dotted-dashed lines indicate the Boltzmann distributions at the translational and internal temperature, respectively).	123
5.16 BRVC model. Influence of the number of energy bins on the N ₂ mole fraction evolution along the axis of the F4 and Scirocco nozzles (unbroken lines BRVC(2), dotted-broken lines BRVC(10), dashed lines BRVC(50), dotted lines BRVC(500), lines with circles VC, lines with squares MTP).	124
5.17 BRVC model. Energy bin population distribution at the location $x = 2.85 \times 10^{-1}$ m along the axis of the Scirocco nozzle for different numbers of energy bins (unbroken line BRVC(5), dashed line BRVC(10), dotted line BRVC(20), dotted-dashed line BVVC(50), circles BRVC(100), triangles BRVC(500); the reported values for the N ₂ mole fraction, translational and internal temperatures refer to the BRVC(50) model solution).	125
5.18 BRVC(20) model. Temperature and N mole fraction evolution along the stagnation-line for different values of the free-stream pressure (unbroken lines $p_\infty = 0.05$ torr, dashed lines $p_\infty = 0.1$ torr, dotted-dashed lines $p_\infty = 0.33$ torr).	126
5.19 BRVC(20) model. Heat flux evolution along the stagnation-line for different values of the free-stream pressure (unbroken line $p_\infty = 0.05$ torr, dashed line $p_\infty = 0.1$ torr, dotted-dashed line $p_\infty = 0.33$ torr).	127
5.20 BRVC(20) model. Translational and internal temperature profiles within the boundary layer for different values of the free-stream pressure (unbroken lines T , dashed lines T_{int}).	128
5.21 BRVC(20) model. Comparative evolution of the N mole fraction and the energy bin population distribution across the shock wave. The circles in fig. 5.21(a) indicate the locations at which the population distributions, plotted in fig. 5.21(b), are extracted (in fig. 5.21(b) line with circles $r = 0.425$ m, line with squares $r = 0.4245$ m, line with diamonds $r = 0.4242$ m, line with triangles $r = 0.424$ m, unbroken line $r = 0.4237$ m , dashed line $r = 0.4235$ m , dotted-dashed line $r = 0.423$ m, dotted line $r = 0.4225$ m).	129
5.22 BRVC(20) model. Comparative evolution of the N mole fraction and the energy bin population distribution in the post-shock equilibrium area. The circles in (a) indicate the locations at which the population distributions, plotted in (b), are extracted (in (b) line with circles $r = 0.421$ m, unbroken line $r = 0.416$ m , dashed line $r = 0.413$ m , dotted-dashed line $r = 0.411$ m, dotted line $r = 0.406$ m).	130

5.23 BRVC(20) model. Comparative evolution of the N mole fraction and the energy bin population distribution in the boundary layer. The circles in (a) indicate the locations at which the population distributions, plotted in (b), are extracted (in (b) line with circles $r = 0.404$ m, line with squares $r = 0.402$ m, unbroken line $r = 0.401$ m, dashed line $r = 0.4005$ m, dotted-dashed line $r = 0.4002$ m , dotted line $r = 0.4$ m)	130
5.24 BRVC(20) model. Energy bin population distributions at the locations $r = 0.4$ m (wall) and $r = 0.402$ m in the boundary layer (the dashed and the dotted-dashed lines indicate the Boltzmann distributions at the translational and internal temperature, respectively).	131
5.25 BRVC(20) and MTP model comparison. Temperature and N mole fraction evolution along the stagnation-line for different values of the free-stream pressure ((a)-(b) $p_\infty = 0.05$ torr, (c)-(d) $p_\infty = 0.1$ torr, (e)-(f) $p_\infty = 0.33$ torr; in (a), (c) and (e) unbroken lines T BRVC(20), dashed lines T_{int} BRVC(20), dotted-dashed lines T MTP, dotted lines T_{vib} MTP; in (b), (d) and (f) unbroken lines BRVC(20), dashed lines MTP).	132
5.26 BRVC(20) and MTP model comparison. Heat flux evolution along the stagnation-line for different values of the free-stream pressure (unbroken line BRVC(20) $p_\infty = 0.05$ torr, dashed line BRVC(20) $p_\infty = 0.1$ torr, dotted-dashed line BRVC(20) $p_\infty = 0.33$ torr, line with circles MTP $p_\infty = 0.05$ torr, line with squares MTP $p_\infty = 0.1$ torr, line with diamonds MTP $p_\infty = 0.33$ torr).	133
5.27 BRVC model. Translational temperature and N mole fraction evolution along the stagnation-line for different numbers of energy bins ((a)-(b) $p_\infty = 0.05$ torr , (c)-(d) $p_\infty = 0.1$ torr, (e)-(f) $p_\infty = 0.33$ torr; unbroken lines BRVC(10), dotted lines BRVC(20), dashed lines BRVC(100)).	134
5.28 VC model. Mesh used for the EAST facility nozzle (4 blocks, 200×50 cells; one node over two is plotted along both the axial and radial directions).	136
5.29 VC model. Density and velocity distributions within the EAST facility nozzle.	137
5.30 VC model. Temperature and mole fraction evolution along the axis of the EAST facility nozzle (in (a) unbroken line T , dashed line T_{vib} ; in (b) unbroken line N, dashed line N ₂).	138
5.31 VC model. Evolution of the vibrational population distribution along the axis of the EAST facility nozzle (unbroken line $x = -2.5 \times 10^{-2}$ m, dashed line $x = -6 \times 10^{-3}$ m, dotted-dashed line $x = 0$ m, line with circles $x = 2.4 \times 10^{-2}$ m, line with squares $x = 5.4 \times 10^{-2}$ m, line with triangles $x = 8.3 \times 10^{-2}$ m).	138

5.32 VC model. Comparison between the computed and experimental normalized vibrational population distributions for the EAST facility nozzle (unbroken lines calculations, circles experiments).	139
5.33 VC model. Mesh used for the flow over a sphere (12 blocks, 90×360 cells; one node over three is plotted along both the axial and radial directions).	140
5.34 VC model. Temperature and N mole fraction distributions around the sphere.	141
5.35 VC model. Temperature and N mole fraction evolution along the stagnation-line (in (a) unbroken line T , dashed line T_{vib} ; in (b) unbroken line N, dashed line N_2).	141
5.36 VC model. Evolution of the $N_2(v)$ mole fractions and the vibrational population distribution along the stagnation-line (in (a) unbroken line $N_2(0)$, dashed line $N_2(1)$, dotted-dashed line $N_2(2)$, dotted line $N_2(3)$, line with circles $N_2(4)$, line with squares $N_2(5)$, line with triangles $N_2(6)$, crosses $N_2(7)$, plus $N_2(8)$, stars $N_2(9)$; in (b) unbroken line $x = -0.55$ m, dashed line $x = -0.53$ m, dotted-dashed line $x = -0.525$ m, dotted line $x = -0.52$ m, line with circles $x = -0.515$ m, line with squares $x = -0.5$ m).	142
7.1 Flow across a normal shock wave in Ar. Density evolution for different values of the free-stream Mach number (lines BEST, symbols DSMC(Torres)).	163
7.2 Flow across a normal shock wave in Ar. Temperature evolution for different values of the free-stream Mach number (unbroken lines T BEST, dashed lines T_x BEST, dotted-dashed lines T_y BEST, symbols DSMC(Torres)).	164
7.3 Flow across a normal shock wave in Ar. Heat flux evolution for different values of the free-stream Mach number (lines BEST, symbols DSMC(Torres)).	165
7.4 Flow across a normal shock wave in Ar. Normal viscous stress evolution for different values of the free-stream Mach number (lines BEST, symbols DSMC(Torres)).	165

7.5 Flow across a normal shock wave in Ar. Comparative evolution of the density and the c_x axis component of the velocity distribution function ($M_\infty = 6.5$; the symbols in (a) and (c) highlight the locations at which the velocity distribution function, plotted in (b) and (d), is extracted; in (b) unbroken line $x = -2 \times 10^{-2}$ m, dashed line $x = -4 \times 10^{-3}$ m, dotted-dashed line $x = -2 \times 10^{-3}$ m, line with circles $x = -1 \times 10^{-3}$ m, line with squares $x = 0$ m, line with triangles $x = 1 \times 10^{-3}$ m; in (d) unbroken line $x = 1.6 \times 10^{-3}$ m, dashed line $x = 2 \times 10^{-3}$ m, dotted-dashed line $x = 3 \times 10^{-3}$ m, line with circles $x = 4 \times 10^{-3}$ m, line with squares $x = 6 \times 10^{-3}$ m, line with triangles $x = 2 \times 10^{-2}$ m).	166
7.6 Flow across a normal shock wave in Ar. Evolution of the projection on the (c_x, c_y) plane of the velocity distribution function ($M_\infty = 6.5$).	167
7.7 Flow across a normal shock wave in Ar. Comparison between the computed and experimental density profiles for different values of the free-stream Mach number (unbroken lines BEST, symbols experiments).	168
7.8 Flow across a normal shock wave in Ar. Comparison between the computed and experimental density profiles for different cross-section models ($M_\infty = 3.38$; unbroken line VHS, dashed line LJ, dotted-dashed line PL, symbols experiments).	169
7.9 Flow across a normal shock wave in Ar. Comparison of the density profiles obtained by solving the Boltzmann and the Navier-Stokes equations for different values of the free-stream Mach number (unbroken lines BEST, dashed lines NS).	170
7.10 Isochoric equilibrium relaxation of a Ne-Ar gas. Time-evolution of the species and gas density and temperature (unbroken line gas BEST, dashed line Ne BEST, dotted-dashed line Ar BEST, symbols DSMC(Torres)).	172
7.11 Isochoric equilibrium relaxation of a Ne-Ar gas. Time-evolution of the c_x axis component of the species velocity distribution functions (unbroken lines $t = 5 \times 10^{-9}$ s, dashed lines $t = 1.4 \times 10^{-8}$ s, dotted-dashed lines $t = 2.4 \times 10^{-8}$ s, lines with circles $t = 5.0 \times 10^{-8}$ s, lines with squares $t = 1.5 \times 10^{-7}$ s).	173
7.12 Isochoric equilibrium relaxation of a Ne-Ar gas. L_1 and L_2 norms of the error on the gas temperature with and without conservation constraint (unbroken line E_1 with conservation, dashed line E_2 with conservation, dotted-dashed line E_1 without conservation, dotted line E_2 without conservation; circles are added to highlight the number of velocity nodes used).	174

- 7.13 Isochoric equilibrium relaxation of a Ne-Ar gas. Time-evolution of the gas temperature with and without conservation constraint ($N_c = 16$; unbroken line with conservation, dashed line without conservation). 174
- 7.14 Flow across a normal shock wave in a Ne-Ar gas. Evolution of the species hydrodynamic velocity and parallel temperature ($M_\infty = 2$; unbroken lines Ne BEST, dashed line Ar BEST, symbols DSMC(Torres)). 176
- 7.15 Flow across a normal shock wave in a Ne-Ar gas. Evolution of the gas density, temperature and related parallel and transverse components($M_\infty = 2$; lines BEST, symbols DMSC(Torres); in (b) unbroken line T , dashed line T_x , dotted-dashed line T_y). 176
- 7.16 Flow across a normal shock wave in a Ne-Ar gas. Comparative evolution of the density and the c_x axis component of the velocity distribution functions of Ne and Ar ($M_\infty = 2$; the symbols in (a) and (c) highlight the locations at which the species velocity distribution functions, plotted in (b) and (d), are extracted; in (b) and (d) unbroken lines $x = -1 \times 10^{-2}$ m, dashed lines $x = -1.1 \times 10^{-3}$ m, dotted-dashed lines $x = -1 \times 10^{-4}$ m, lines with circles $x = 9 \times 10^{-4}$ m, lines with squares $x = 1.9 \times 10^{-3}$ m, lines with triangles $x = 1 \times 10^{-2}$ m). 177
- 7.17 Isochoric equilibrium relaxation of a multi-energy level gas. Time-evolution of the level densities and temperatures (lines BEST, symbols DSMC(Torres); in (a) unbroken line ρ_1 , short dashed line ρ_2 , long dashed line ρ_3 , dotted-dashed dashed line ρ_4 , dotted line ρ_5 ; in (b) unbroken line T , dashed line T_{int}). 180
- 7.18 Flow across a normal shock wave in a multi-energy level gas. Evolution of the level mass fractions, diffusion velocities, velocities and temperatures ($M_\infty = 3$; unbroken lines level 1 BEST, dashed lines level 2 BEST, symbols DSMC(Torres)). 182
- 7.19 Flow across a normal shock wave in a multi-energy level gas. Evolution of the gas density, pressure, velocity, translational temperature and related parallel and transverse components, internal temperature, normal viscous stress and heat flux ($M_\infty = 3$; lines BEST, symbols DSMC(Torres); in (d) unbroken line T , dashed line T_x , dotted-dashed line T_y , dotted line T_{int}). 183

7.20 Flow across a normal shock wave in a multi-energy level gas. Comparative evolution of the level densities and the related c_x axis component of the velocity distribution functions ($M_\infty = 3$; the symbols in (a) and (c) highlight the locations at which the level velocity distribution functions, plotted in (b) and (d), are extracted; in (b) and (d) unbroken lines $x = -2 \times 10^{-2}$ m, dashed lines $x = -2.5 \times 10^{-3}$ m, dotted-dashed lines $x = -1 \times 10^{-3}$ m, dotted lines $x = -1 \times 10^{-4}$ m, lines with circles $x = 3 \times 10^{-4}$ m, lines with squares $x = 9 \times 10^{-4}$ m, lines with triangles $x =$ 1.9×10^{-3} m, lines with diamonds $x = 2 \times 10^{-2}$ m).	184
7.21 Flow across a normal shock wave in a multi-energy level gas. Evolution of the projection on the (c_x, c_y) plane of the velocity distribution function of level 1 ($M_\infty = 3$).	185
7.22 Flow across a normal shock wave in a multi-energy level gas. Evolution of the projection on the (c_x, c_y) plane of the velocity distribution function of level 2 ($M_\infty = 3$).	186

Nomenclature

Latin Characters:

a	Degeneracy	\mathcal{E}	Generalized internal energy state set
A	Cross-sectional nozzle area or 2D cell surface	f	Velocity distribution function
\mathbf{A}	Flux Jacobian matrix	\mathbf{F}	Flux vector
b	Upwind wave speed	\mathcal{F}	Flux tensor
\mathcal{B}	Energy bin level set	g	Relative velocity magnitude
\mathbf{B}	Auxiliary vector	G	Center of mass velocity magnitude
c	Frozen Speed of sound or molecular velocity	\mathbf{g}	Relative velocity vector
c_v	Constant volume specific heat	\mathbf{G}	Flux vector or center of mass velocity vector
c_p	Constant pressure specific heat	h	Specific enthalpy of velocity node index
C_v	Constant volume volumetric specific heat	H	Specific total enthalpy
C_p	Constant pressure volumetric specific heat	h_p	Planck's constant
C	Chemistry coupling factor or peculiar velocity magnitude	i	Level or cell index
\mathcal{C}	Collision set	\mathcal{I}	Internal energy level set
\mathbf{c}	Molecular velocity vector	\mathbf{I}	Identity matrix
\mathbf{C}	Peculiar velocity vector	\mathbf{I}	Second-order identity tensor
d	Molecular diameter	j	Level or cell index
D	Diffusion coefficient	J	Rotational quantum number
\mathcal{D}	Binary diffusion coefficient	\mathcal{J}	Rotational energy level set
e	Specific energy	k	Rate coefficient or level index
E	Specific total energy or level energy	\mathcal{K}	Energy bin set
		k_b	Boltzmann's constant

l	Level index or cell side length	s	Species index
L	Left eigenvector matrix	S	Source term vector
m	Mass	t	time
\mathcal{M}	Molar mass	T	Temperature
M	Block matrix	\mathcal{T}	Discrete time domain
n	Number density or time-level index	u	Velocity component
\mathbf{n}	Unit normal vector component	U	Conservative variable vector
\mathcal{N}_c	Number of chemical components	v	Velocity component or vibrational quantum number
\mathcal{N}_e	Number of chemical elements	V	Velocity magnitude
\mathcal{N}_s	Number of species	\mathcal{V}	Vibrational energy level set or discrete velocity domain
N_A	Avogadro's number	w	Integration weight or vibrational quantum number
n	Unit normal vector	W	Transition probability
p	Pressure or species index	W	Characteristic variable vector
p	Primitive variable	x	Spatial coordinate
P	Primitive variable vector	x	Position vector
q	Heat-flux vector component or species index	X	Mole fraction
q	Heat-flux vector	\mathcal{X}	Discrete position domain
Q	Collision operator	y	Spatial coordinate or mass fraction
r	Species index or radial coordinate	z	Spatial coordinate or species index
r	Ratio of consecutive differences	Z	Partition function
R	Right eigenvector matrix	∞	Free-stream quantity
̃R	Right-hand-side residual		

Greek Characters:

α	Component index	θ	Thermal diffusion coefficient
β	Statistical weight	μ	Reduced mass
γ	Frozen specific heat ratio	ν	Correspondence index
δ	Kronecker's delta	ρ	Density
η	Shear viscosity	σ	Cross-section
λ	Thermal conductivity or eigenvalue	τ	Stress tensor component or relaxation-time
Λ	Eigenvalue matrix		

τ	Stress tensor	ω	Mass production term
ϕ	Slope limiter function	ω	Scattering direction unit
φ	Test function		vector
χ	Thermal diffusion ratio	Ω	Energy transfer term
ψ	Collisional invariant		
Ψ	Integration matrix		

Abbreviations:

B	Bound
BDF	Backward Differentiation Formula
BE	Backward-Euler
BEST	Boltzmann Equation Spectral Solver
BGK	Bhatnagar-Gross-Krook
BP	Bound and Predissociated
BRVC	Boltzmann Rovibrational Collisional
c	Convective or collision
C	Center
CFL	Courant-Friedrichs-Lowy
CE	Chapman-Enskog
d	diffusion or diffusive
dis	dissociation
DSMC	Direct Simulation Monte Carlo
e	element
el	elastic
eq	equilibrium
exc	exchange
EAST	Electric Arc Shock Tube
FE	Forward-Euler
FFT	Fast Fourier Transform
FFTW	Fastest Fourier Transform in the West
FHO	Force Harmonic Oscillator
FV	Finite Volume
GSL	GNU Scientific Library
HS	hard-sphere
HO	Harmonic Oscillator
in	inelastic
int	internal
i-pre	inverse-predissociation
IVP	Initial Value Problem
k	kinetic (process)
kin	kinetic (energy)
L	Left
LJ	Lennard-Jones

LTE	Local Thermodynamic Equilibrium
MP	Monotonicity-Preserving
MT	Multi-temperature
MTP	Multi-temperature Park
MUSCL	Monotone Upstream Centered Schemes for Conservation Laws
NS	Nuclear spin or Navier-Stokes
ODE	Ordinary Differential Equation
NASA ARC	NASA Ames Research Center
pre	predissociation
ps	post-shock
P	Predissociated
PES	Potential Energy Surface
QCT	Quasi-Classical Trajectory
QSS	Quasi-Steady State
rot	rotational
re	reactive
rec	recombination
ref	reference
R	Right
RR	Rigid-Rotor
RK	Runge-Kutta
RVC	Rovibrational Collisional
s	source
sc	self-consistent
STS CE	State-to-State Chapman-Enskog
tra	translational
URVC	Uniform Rovibrational Collisional
vib	vibrational
VC	Vibrational Collisional
VHS	variable-hard-sphere
WKB	Wentzel-Kramers-Brillouin

Introduction

Motivation

Hypersonic aerothermodynamics finds its chief application in the description of the flow surrounding a space vehicle during a planetary descent (Anderson 1989; Park 1990; Gnoffo 1999). The computation of such a flow is extremely challenging and, due to the multi-discipline and multi-physics nature of the problem, it requires the integration of different subjects such as chemical kinetics, quantum and statistical mechanics, electromagnetic theory, material science, computational methods and high-performance computing techniques. An accurate modeling of aerothermodynamic flows must account for all the relevant physico-chemical phenomena occurring both in gas and solid phases and is important for the design of heat-shields of space vehicles and for a correct interpretation of experimental measurements in high-enthalpy wind tunnels. The achievement of this task is complicated due to the existence of a very broad spectrum of the physical time-scales involved. Figure 1 provides a graphical sketch of the relevant physico-chemical phenomena occurring in the surrounding of a re-entry vehicle during the peak-heating condition.

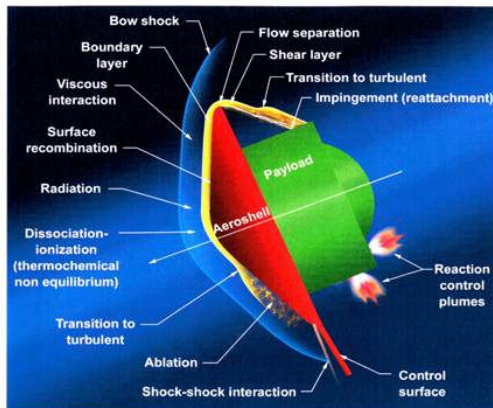


Figure 1: Relevant physico-chemical phenomena occurring during a planetary descent of a space vehicle (credits NASA Ames Research Center).

The modeling of aerothermodynamic flows must account for non-equilibrium effects. Non-equilibrium is a consequence of the finite rate nature of the processes occurring within the flow. The mathematical model to be adopted for describing the gas motion depends on the Knudsen number Kn , defined as the ratio between the molecular mean-free-path (average distance traveled by molecules between successive collisions) and a characteristic dimension of the problem under investigation, such as the space-vehicle nose radius (Ferziger and Kaper 1972; Bird 1994). The Knudsen number is a measure of the degree of rarefaction of a flow and, depending on its value, different flow regimes can be distinguished (see fig. 2).

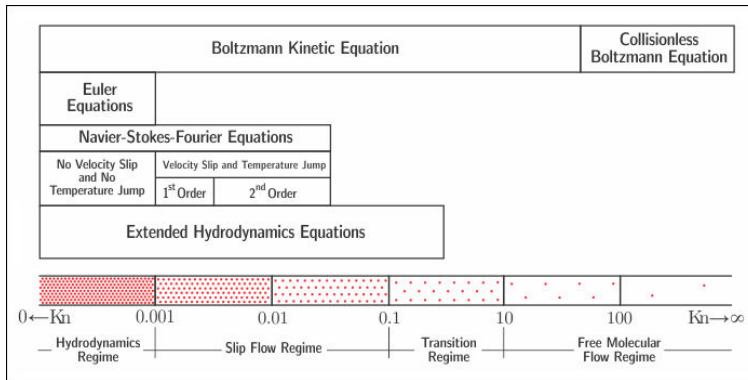


Figure 2: Flow regime classification according to the Knudsen number.

During a planetary entry, all the flow regimes shown in fig. 2 are encountered and, for each one, the relevant physico-chemical phenomena to be taken into account differ.

In the early phase of the descent, the vehicle enters the upper layers of the planetary atmosphere. Due to the extremely low value of the gas density, the incoming gas particles directly collide with the vehicle surface, where they can be both reflected or absorbed, without colliding with each other. Flows in this regime are referred to as free-molecular flows (Bird 1994; Gnoffo 1999). After passing this zone, the atmosphere becomes denser. Collisions among the gas particles can no longer be neglected. The flux of impinging particles experiences collisions with those being re-emitted at the vehicle surface. This collisional transfer of information creates a compression zone in front of the vehicle, where the density, pressure and temperature increase smoothly. The dimensional extent of this region is comparable with the characteristic dimensions of the vehicle. Flows in this regime are referred to as transition flows. In these conditions, the collisions between the gas particles are not energetic enough to cause substantial excitation of atom/molecule internal degrees of freedom (such as rotation and vibration of molecules, and electronic states of atoms and molecules) or breaking of chemical bonds. This is usually accompa-

nied by low energy transfer rates to the vehicle surface.¹ A correct description of free-molecular and transitional flows is important for an accurate determination of the aerodynamic coefficients and for a correct planning of the planetary entry path. In the free-molecular and transition regimes, appreciable changes of flow properties (such as velocity and temperature) occur over the same time-scales needed for the translational degree of freedom to attain local equilibrium (Maxwell-Boltzmann velocity distribution function; Bird 1994). In this situation, one must go beyond a hydrodynamic model based on the Navier-Stokes equations. If the gas is sufficiently dilute (which is the case for aerothermodynamic flows), a kinetic description based on the Boltzmann equation of the Kinetic Theory of Gases can be adopted (Ferziger and Kaper 1972). The Boltzmann equation is an integro-differential equation describing the evolution in the phase-space of the one-particle velocity distribution function. Once the velocity distribution function known, flow properties can be computed by means of suitable moments. The Boltzmann equation is composed of two parts: the streaming operator and the collision operator. The streaming operator is a linear differential operator that accounts for the effects of the molecular motion between collisions (it can be also interpreted as a material derivative in the phase-space; Giovangigli 1999). The collision operator is a non-linear integral operator that accounts for the effects of collisions among the gas particles. In the case of free-molecular flows, where the collisions in gas-phase can be neglected, the collision-less Boltzmann equation can be adopted.

Proceeding further with the descent, the atmospheric density increases and the Knudsen number assumes values of the order of 0.1 or smaller. In view of the higher collisional rate among the gas particles, the width of the compression region in front of the vehicle progressively reduces its thickness. However, rarefied gas effects still play an important role and cannot be neglected. Examples are the velocity slip and the temperature jump at the vehicle surface. This flow regime is referred to as slip-flow regime (Bird 1994). In this situation, a hydrodynamic description based on the Navier-Stokes equations is not sufficiently accurate and gives a poor description of the flow. A possible alternative to the use of the Boltzmann equation (always valid from the free-molecular to the hydrodynamic regime) is represented by extended hydrodynamic models such as Moment Methods (Struchtrup 2005) or the Navier-Stokes equations with slip boundary conditions (Gnoffo 1999).

In the last phase of descent, due to a further increase of the atmospheric density, gas-phase collisions become more frequent and energetic. The compression region in front of the vehicle becomes a shock wave whose thickness (of the order of some mean-free-paths) becomes negligible compared to the vehicle characteristic dimensions. Flows in this regime are referred to as continuum or hydrodynamic flows (Gnoffo 1999). In the zone immediately behind the shock wave, collisions between the gas particles lead to the excitation of the

¹This is not the case for ballute entry and descent (Gnoffo 1999).

internal degrees of freedom of atoms and molecules. When collisions are energetic enough, dissociation reactions can occur. The atoms produced as a result of the dissociation can recombine in the boundary layer with a consequent release of their energy of formation. This causes a substantial increase of the wall heat flux (compared to the rarefied flow regime), which becomes, for this phase of the planetary entry, the main design parameter. The wall heat flux must be accurately predicted in order to prevent mission failure. If the re-entry speed is high enough (*e.g.* 10 km/s for a Lunar return), ionization may also occur. The gas contained in the region between the shock wave and the vehicle surface (usually referred to as shock-layer; Gnoffo 1999) becomes a partially ionized plasma where radiative transitions take place (Mihalas and Mihalas 1999; Zel'dovich and Raizer 2002). The surface heat flux is now made of two contributions, convective and radiative, with the latter becoming more and more important when increasing the entry speed. Heats-shields of modern reentry vehicles are usually equipped with ablative materials, with the purpose of reducing heat transfer rates. The gas and solid phase ablation products can interact with the flow in the boundary layer and the radiation field. Possible consequences of these interactions are transition to turbulence and radiation enhancement associated to particle spallation.

In the hydrodynamic regime, rarefied gas effects are limited to regions of steep gradients where the local Knudsen number is high (such as the interior part of the shock wave and the base flow). Outside of these zones, the Navier-Stokes equations hold. In order to provide an accurate description of the flow, the transport fluxes and the production terms due to collisional processes in the Navier-Stokes equations should be consistently related to the non-equilibrium state of the gas. This can be achieved by applying the Chapman-Enskog method to the Boltzmann equation (Ferziger and Kaper 1972; Giovangigli 1999; Nagnibeda and Kustova 2009). The application of the Chapman-Enskog method enables to obtain explicit relations for the transport fluxes and the production terms in the Navier-Stokes equations. When charged particles are produced, electromagnetic fields may arise, and the mutual influence between the flow and the electromagnetic fields should be taken into account by coupling the Navier-Stokes and the Maxwell equations (Giordano 2002). In practice, this is never done and a simplified approach is adopted. This consists in coupling the Navier-Stokes equations with the Radiative Transfer Equation (Vincenti and Kruger 1965; Mihalas and Mihalas 1999; Zel'dovich and Raizer 2002). The Radiative Transfer Equation describes the evolution of the radiation field intensity due to radiation emission, absorption and scattering. In the case of the occurrence of ablation phenomena, the flow and radiation field governing equations should be coupled with a mathematical model for the portion of the vehicle surface undergoing ablation.

The different flow regimes shown in fig. 2 and described in detail for the case of a planetary descent, are also encountered in high-enthalpy wind tunnel flows. In this case, a proper accounting of the physico-chemical phenomena is im-

portant for a correct interpretation of experimental measurements and their extrapolation to in-flight conditions.

Goals of the Thesis

The previous introductory discussion has summarized the main features of aerothermodynamic flows and has also shown how complex these flows are in terms of modeling and computation. Despite the research efforts performed in the past years and the increasing computational power and resources, the computation of aerothermodynamic flows still poses problems. This is mainly due to the lack of accurate physical models (within a wide range of conditions) for collisional and radiative processes and transport phenomena in gas phase, and to the lack of unified deterministic computational methods usable from the rarefied to the hydrodynamic regime. This has motivated the research activity of the present thesis which has been focused on the following two topics:

- Multi-scale models,
- Computational methods.

Multi-Scale Modeling for Aerothermodynamic Flows The first part of the thesis has been dedicated to the integration of quantum chemistry databases in CFD codes. The research has focused on internal energy excitation and dissociation of molecular nitrogen in atmospheric entry flows. Ionization and radiation phenomena have not been considered. The final goal was two-fold: to gain insight on the dynamics of internal energy excitation and dissociation in the hydrodynamic regime and to develop reduced models for CFD applications allowing for a more accurate description than the conventional multi-temperature models (Park 1990). The research has been carried out in collaboration with the Computational Quantum Chemistry Group at NASA Ames Research Center.

Computational Methods for Rarefied Flows The second part the thesis has focused on rarefied flows and aimed at the development of a fully deterministic numerical method for the solution of the Boltzmann equation by extending an existing spectral-Langrangian method (valid for a mono-component gas without internal energy) to multi-components gases and inelastic collisions. The final scope was the development of a parallel computational tool for the calculation of rarefied gas flows and its verification and validation by means of comparison with the Direct Simulation Monte Carlo (DSMC) method (Bird 1994) and experimental results, respectively. The research has been carried out in collaboration with the University of Texas at Austin.

Literature Review

In this section, a review of the work done in the past and of the state of the art is given for the topics on which the thesis has been focused.

Multi-Scale Modeling for Aerothermodynamic Flows

The modeling of aerothermodynamic flows started receiving attention in the 1950-1960's, when the space exploration programs of USA and USSR were being set (Anderson 1989). An accurate modeling of aerothermodynamic flows must properly account for non-equilibrium effects. As stated in the introductory discussion, these are due to the finite rate nature of collisional processes. The physical models developed during the years may be divided in two main categories: multi-temperature models and collisional models.

Multi-Temperature Models Multi-temperature models have been proposed starting from the work of Appleton and Bray (1964) as a simplified approach to overcome all the difficulties related to the modeling of non-equilibrium. In these models, mainly developed by Park (1989; 1990; 1993; 1994), the internal energy levels of the gas particles are supposed to be populated according to Boltzmann distributions at their own temperatures (*e.g.* rotation, vibrational and electronic temperatures). The conservation equations for the species mass, the total momentum and the total energy are supplemented with additional conservation equations for the components of internal energy in thermal non-equilibrium with translation (Gnoffo et al. 1989; Park 1990; Candler and MacCormack 1991; Gnoffo 1999). These additional equations have the same hyperbolic-parabolic structure of the conventional conservation equations of gas-dynamics (Hirsch 1990) and are supplied with energy transfer source terms. These are associated to the production/destruction of internal energy due to collisional processes.

In multi-temperature models, research has been mainly focused on vibrational non-equilibrium and its effect on chemical reactions (Park 1990). The presence of vibration-translation (VT) and vibration-vibration (VV) energy transfer processes is usually described through Landau-Teller (1936) relaxation models (Park 1990; Candler and MacCormack 1991). The relaxation times are taken from both theoretical and/or experimental measurements, such as those of Millikan and White (1963). The formulation of these energy-transfer terms accounts only for mono-quantum transitions (Park 1990; Capitelli et al. 2000). This assumption does not hold, as an example, in the flow immediately behind a normal shock wave (Park 1990). In this situation, due to high-temperature conditions, collisions can be energetic enough to induce multi-quantum jumps (Capitelli et al. 2000). The effect of dissociation reactions on the vibrational energy is accounted for through the chemistry-vibration (CV) source term. The latter accounts for the fact that molecules undergoing dissociation

tion/recombination cause a loss/gain of a finite amount of vibrational energy within the gas (Park 1990). The effects of vibrational non-equilibrium is also accounted for in the reaction rate coefficients (Park 1990; Park 1993; Park et al. 1994). Different models have been proposed in this field. The first attempt was the model proposed by Hammerling et al. (1959). In the successive years, many other models have been proposed. A review of many of them has been given by Losev (1996). Losev classified the different models into three categories: a) models based on intuitive premise, b) empirical/semi-empirical models and c) theoretical models. The underlying idea of almost all the models is that molecules tend to dissociate/recombine preferentially in high-lying vibrational states (Capitelli et al. 2000). An example of model belonging to the first category is that proposed by Park (1990) for computing non-equilibrium reaction rate coefficients (probably the most popular model of this kind). In Park's model, the rate coefficient for dissociation is computed at a temperature given by the geometric average of the translational and the vibrational temperatures ($T-T_{\text{vib}}$ model). Empirical/semi-empirical models have been proposed by Treanor and Marrone (1962; 1963), Knab et al. (1992), Jaffe (1986), and Landrum and Candler (1992). Among the aforementioned models, those proposed by Treanor-Marrone and Knab provide a formulation for the CV energy transfer term. The latter is developed consistently with the assumed functional form of the non-equilibrium dissociation rate coefficients. Alternative and widely used semi-empirical models for the CV energy transfer term are those proposed by Park (1988; 1989) and Candler and MacCormack (1991). In the model of Park (1988; 1989), it is assumed that the average vibrational energy lost by molecules in dissociation reactions is a fraction of their dissociation energy. This conclusion was drawn based on heat-bath calculations performed by Sharma et al. (1992) where the SSH theory (Schwartz, Slawsky, and Herzfeld 1952) was used. In the model proposed by Candler and MacCormack (1991), it is assumed that the vibrational energy lost/gained due to molecular dissociation/recombination is equal to the gas bulk vibrational energy (non-preferential dissociation model). Examples of theoretical models are those proposed by Hansen (1991), the family of Kuznetsov models (1996; 2002a; 2002b) and the impulsive collision model of Macheret (1993; 1994). More details on these models can be found in the aforementioned papers.

The investigation of rotational non-equilibrium has received less attention than vibrational non-equilibrium. This is clearly shown by the current use in CFD codes of Parkers' model (1959) for the rotational-translational (RT) energy transfer mechanism. Rotational non-equilibrium effects, despite the evidence of their existence for flows behind shock waves (Robben and Talbot 1966a; Park 1990) and in low density wind tunnels (Robben and Talbot 1966b), are mostly neglected when computing aerothermodynamic flows (in the hydrodynamic regime). This is usually justified by referring to experimental data on rotational relaxation times. These data show that, with the exception of light molecules such as H₂, HD and D₂, the RT relaxation times are orders of mag-

nitude smaller than the VT relaxation times (Chernyi et al. 2002b). The aforementioned experimental measurements refer, however, to ordinary temperatures. In a recent work, Panesi et al. (2013) have shown that the relaxation times for the RT and VT mechanisms in N₂-N collisions become comparable at high temperatures.

Multi-temperature models are routinely used in modern CFD codes (Gnoffo et al. 1989; Candler and MacCormack 1991; Lani 2009). This is due to their ease of implementation and computational efficiency. However, their use is often stretched out of the range for which they had been originally conceived. Multi-temperature models are only valid in the case of small departure from the local equilibrium. Their formulation is usually accompanied with tuning parameters (like in the model of Knab et al. 1992) of questionable and unclear physical meaning. A detailed investigation on the limits of multi-temperature models has been recently given by Park (2010).

Collisional Models Collisional or state-to-state models (Capitelli et al. 2000; Chernyi et al. 2002b; Laux 2006; Bultel et al. 2006) have been proposed in order to overcome the deficiencies of multi-temperature models. The hypothesis of a Boltzmann distribution for the internal degrees of freedom is released. Each internal energy level is treated as a separate pseudo-species. This approach provides a more accurate description than multi-temperature models as the effects of possible non-Boltzmann distributions are automatically accounted for. The higher accuracy and wider application range come at the price of more expensive calculations, due to the drastic increase of the number of species to be taken into account. Moreover, in order to obtain numerical values of cross-sections and rate coefficients for each elementary process, complex and lengthy *ab-initio* quantum-chemistry calculations are usually required. These are based on a two-step process: a) Generation of the Potential Energy Surface (PES) from first principles b) Cross-section evaluation based on trajectory calculations. The second step consists in a repeated study of the collision dynamics for different values of the collision parameters such as relative kinetic energy, relative orientation angles and initial quantum states. The cross-section for a given process is then computed as the ratio between the number of its occurrences and the total number of collisional events (Park 1990). Rate coefficients are obtained by averaging the cross-sections over a Maxwell-Boltzmann velocity distribution function. In view of the great number (infinite in theory) of possible combinations for the collision parameters, their numerical values are selected by means of sampling techniques. This induces stochastic noise in the generated cross-sections. For processes such as heavy-particle impact internal energy excitation and dissociation, the collision dynamics can be studied within the framework of classical mechanics. This is accomplished by solving Hamilton's equations, where the interaction potential in the Hamiltonian is given by the PES (Park 1990). The whole procedure is referred to as Quasi-Classical Trajectory (QCT) method (Park 1990).

Approximate methods for computing elementary process rate coefficients have been proposed (Chernyi et al. 2002a) in order to avoid lengthly *ab-initio* calculations. One of the most popular is the Forced Harmonic Oscillator (FHO) model. The FHO model is based on the application of the Kerner-Treanor method (1958; 1965) to the semi-classical approximation of the Schrödinger equation for a non-rotating molecule. The FHO model has been used by Adamovich (1995a; 1998) for computing VT and VV rate coefficients for N₂-N₂, N₂-O₂ and O₂-O₂ interactions.

The development of collisional models has been mainly focused on non-equilibrium vibrational kinetics (Capitelli 1986; Capitelli et al. 2000). Vibrational collisional models have been developed based on both QCT calculations (Esposito et al. 1999; 2000; 2006) and approximate models (such as the previously mentioned FHO model). Applications have considered the study of the vibrational level dynamics in flows behind shock waves (Cambier and Moreau 1993; Adamovich et al. 1995b; Treanor et al. 1996; Aliat et al. 2003, Panesi et al. 2009; 2011), within converging-diverging nozzles (Colonna et al. 1999; Colonna and Capitelli 2001; Babu and Subramaniam 1995), in the stagnation region of blunt bodies (Armenise et al. 1994; Candler et al. 1997) and in atmospheric pressure air plasmas (Gessman et al. 1997; Pierrot et al. 1999; Laux 2006). The results shown in the aforementioned papers indicate that collisional processes such as dissociation/recombination induce heavy distortions in the vibrational level population distributions, thereby demonstrating the inaccuracy of a multi-temperature description.

The development of rovibrational collisional models has started receiving attention only recently. The main reason for this delay is the number of rovibrational energy levels and related transitions which one must take into account (*e.g.* for a diatomic molecule such as N₂, the number of rovibrational energy levels of its electronic ground-state is of the order of 10 000). Examples of rovibrational collisional models are the NASA Ames database for the N₂ molecule (Jaffe et al. 2008; Chaban et al. 2008; Schwenke 2008; Jaffe et al. 2009) used in the present thesis and those developed by Esposito et al. (1999), and Kim et al. (2009) for the H₂ molecule.

The use of collisional models in multi-dimensional CFD computations has become feasible only recently, thanks to the advances in the computational resources (Kapper and Cambier 2011a; Kapper and Cambier 2011b; Panesi and Lani 2013).

Computational Methods for Rarefied Flows

Computational methods for (rarefied) aerothermodynamic flows started to be developed at the same time as physical models for collisional processes. During the years, computational methods of different natures have been proposed. These can be grouped in two main categories: stochastic methods and deterministic methods.

Stochastic Methods At the time when researchers started to seek for efficient numerical methods for rarefied flow problems (around the 1960's), the computational power available was very limited. Obtaining numerical solutions to the full Boltzmann equation was out of discussion. This led to the development of the Direct Simulation Monte Carlo (DSMC) method (Bird 1994). The DSMC method, mainly developed by Bird (1967; 1970) in the initial phase, is a particle-based technique and aims at obtaining stochastic solutions of the Boltzmann equation. In the DSMC method, the gas is represented by a set of gas particles. Each of the gas particle represents a collection of a great number of molecules (the order can vary between 10^{10} and 10^{20} , depending on the problem being investigated). The numerical solution is built by alternating the transport and collision steps. In the first, particles are let to freely move in space. In the second, particles are let to collide between each other. Collision pairs are selected through the use of random numbers. Macroscopic quantities are found by sampling over time the particle microscopic properties within each computational cell. The combination of the transport and collision steps in the DSMC method aims at replicating (stochastically) the molecular behavior of dilute gases, where, in absence of external fields, molecules moving along straight-line trajectories are suddenly scattered into new directions due to collisions. This makes the DSMC method consistent with the theory underlying the Boltzmann equation.

The original DSMC method of Bird was initially developed for a mono-component gas without internal energy and applied to solve one-dimensional problems (Bird 1970). Later, its capabilities were extended to deal with multi-component gases with internal energy (Boyd 1990; Boyd 1991; Koura 1992; Koura 1994; Bruno et al. 2002) and chemical reactions (Boyd 1992; Hash and Hassan 1993; Bird 1994). Applications to multi-dimensional rarefied flows have become feasible and are routinely performed at the present time, thanks to the achievements in computational resources (Ivanov and Gimelshein 1998; Ivanov et al. 2006; Boyd 2008).

The DSMC method has proven to be robust and accurate (Ivanov et al. 2006). However, it shares the drawbacks of stochastic methods, the main one being the statistical noise of the numerical results. This issue can deteriorate the solution accuracy and is particularly felt for low speed and unsteady problems (Bird 1994). Moreover, for flows in the transitional and in the hydrodynamic regime, the use of the DSMC method can becomes expensive, due to the need of an extremely high number of particles.

Deterministic Methods Parallel to the development of the DSMC method, research efforts have been also spent in the development of deterministic methods for the numerical solution of the Boltzmann equation in the rarefied regime. The solution of the Boltzmann equation by means of numerical techniques represents a computational challenge. This is due to the integro-differential nature of the equation. Another source of difficulty is the high-dimensionality

of the problem, since numerical solutions must be sought in the phase-space. The main advantage of a deterministic method over a stochastic one (such as DSMC) is that numerical solutions are not affected by noise. Deterministic methods can also be applied to flow problems in the hydrodynamic and transition regime, where the use of the DSMC method can become expensive (Kolobov et al. 2007).

In all the methods that have been proposed, the phase-space is discretized by keeping separate the discretization of the position and velocity spaces. The position space and the related discretization of the streaming operator are realized by means of Finite Difference, Finite Volume and Discontinuous-Galerkin methods (Hirsch 1990; Leveque 2008; Cockburn et al. 2011). The discretization of the velocity space and the related algorithm for the evaluation of the collision operator is what distinguishes, up to a certain extent, one method from the others. Once a decision made concerning the discretization of the streaming and collision operators, numerical solutions are found by means of a time-marching approach. In many cases (though not always), the solution update is performed through operator-splitting methods (Oran and Boris 2000), due to their ease of implementation and low storage requirements compared to implicit methods.

The first deterministic methods for rarefied gas flows were proposed at the same time when the DSMC method was being developed. These methods were based on model Boltzmann equations (Cercignani 2000). In the latter, the Boltzmann collision operator is replaced with simpler phenomenological expressions (or model collision operators; Cercignani 2000). One of the most popular (if not the most popular) among this class of models is the Bhatnagar, Gross and Krook (BGK) model (1954), where the collision operator is replaced with a Jeans-like relaxation term. Examples of other phenomenological models are the Ellipsoidal-Statistical model developed independently by Cercignani (1967) and Holway (1966), the generalized Krook model proposed by Shakhov (1968) and the polynomial and trimodal gain function models of Seagal and Ferziger (1970). When using the aforementioned models, the discretization of the velocity space is realized by selecting a set of points contained within a cube of finite extent in the velocity space. Phenomenological models are still used in multi-dimensional Boltzmann solvers (Zang and Huang 1995; Mieussens 2000), as they are computationally cheaper than the DSMC method. The particularly simple structure of the model collision operators (such as BGK) makes possible the use of implicit methods (Mieussens 2000; Mieussens and Struchtrup 2004). This is of particular importance if one is interested only in steady-state solutions, as the time-steps that can be used are usually several orders of magnitude bigger than the maximum allowable time-steps for explicit methods. These advantages come at the price of higher memory requirements and coding efforts. The accuracy of phenomenological models deteriorates in flows where the velocity distribution function experiences a significant departure from the local equilibrium (Mieussens and Struchtrup 2004), such as across strong shock

waves. This motivated the research toward methods enabling the numerical evaluation of the Boltzmann collision operator.

The first deterministic method for the full Boltzmann equation was the Discrete-Velocity-Method (DVM) proposed by Broadwell (1964). The base idea consists in representing the state of the gas, in the velocity space, by a finite set of velocities. In this way, the solution of the Boltzmann equation becomes equivalent to the solution of a coupled set of differential equations (this is also valid when the DVM is applied to model Boltzmann equations described before). The work of Broadwell served as basis for the development of successive variants of his DVM. Examples are the method of Varghese and coworkers (1994; 2011; 2012) and the Discrete-Ordinate-Method (DOM) of Tcheremissine (1998; 2001). Both methods were originally developed for a mono-component gas without internal energy and have been successfully extended to treat multi-component gases with internal energy (Tcheremissine 2006; Clarke et al. 2012; Josyula et al. 2011). In the method of Varghese, the internal energy is treated classically, while in the DOM of Tcheremissine a semi-classical approach is employed. The DOM has been also applied to compute multi-dimensional rarefied flows (Chen et al. 2007; Kolobov et al. 2007). In the aforementioned DVMs, the collision operator is evaluated numerically with the aid of stochastic techniques for multi-dimensional integrals. Hence, these methods are not fully deterministic in a strict sense. Other examples of DVMs can be found in the book of Aristov (2001).

The numerical methods described before have been mainly developed by engineers within the aerospace community. The applied mathematics community has also given its contribution. In this case, research efforts have been focused more on the properties of the numerical schemes such as conservation, positivity, order of accuracy and error estimates. The physical model usually consists of a mono-component gas without internal energy. In order to make the analysis more tractable and amenable to formal manipulations, the hard-sphere or Maxwell cross-section models are usually employed (Cercignani 2000). The available scientific literature in this field is, as it is for DVMs, quite vast. Among all the proposed methods, it is worth to cite the family of numerical kernel methods developed by Sone, Ohwada and Aoki (1989; 1993; 2001), the spectral methods proposed by Bobylev, Ryasanow and Gamba (1975; 1988; 1999; 2009; 2010; 2012a; 2012b) and those developed by Pareschi, Russo and Filbet (2000; 2003; 2011).

Since the present thesis focuses on spectral methods for rarefied flows, it is worth to give a deeper and historical review of them. Deterministic spectral methods for the Boltzmann equation grew from the work of Bobylev (1975; 1988). In his work, Bobylev showed that the Fourier transformed Boltzmann equation takes a closed form in the case of Maxwell molecules and integrable angular cross-section. Numerical approximations using this type of approach were first proposed by Pareschi and Perthame (1996). Using this representation, Bobylev and Rjasanow developed methods using the Fourier transform

in the case of Maxwell molecules (1997) and hard-spheres (1999) to derive a weighted convolution structure for the collision operator which was approximated by a numerical quadrature. Later, Pareschi and Russo (2000) applied this Fourier transformed framework to develop methods for Maxwell molecules, hard-spheres and variable hard-spheres cases using a collocation method, which uses orthogonal polynomials to reduce the weighted convolution integral to a convolution sum of the collocation coefficients. In the case of hard-spheres in three dimensions, it was shown that the computation of the collision operator can be reduced to $O(N^3 \log N)$ operations, where N is the number of grid points in one dimension of the velocity space. However, the above techniques could not be easily extended to arbitrary cross-section models (Bobylev and Ryasanow 1999; Filbet and Russo 2003) and did not allow for the exact conservation of mass, momentum and energy during collisions (Filbet and Russo 2003). In order to meet the conservation requirement, Gamba and Tharkabhushanam (2009; 2010) have proposed a spectral-Lagrangian method which exploits, in analogy with those mentioned before, the weighted convolution structure of the Fourier transform Boltzmann equation. The conservation of mass, momentum and energy during collisions is achieved through the solution of a constrained optimization problem. Convergence studies for this method and numerical examples have been shown by Gamba and Tharkabhushanam (2009; 2010) and analysis has been performed by Alonso et al. (2013) in order to show that the conservation constraints do not affect the spectral accuracy of the method. In the work by Haack and Gamba (2012a) the spectral-Lagrangian method has been further generalized to the more realistic case of angularly dependent cross-sections. None of the above spectral methods has been so far extended to the case of multi-component gases with discrete internal energy levels. This extension is needed if one wishes to study internal energy excitation and relaxation behind a shock wave or the flow across a hypersonic boundary layer. In this situation, conservation becomes a more pressing concern, especially when taking into account inelastic collisions leading to a net energy transfer between the translational and the internal degrees of freedom of the gas.

For flows in the transition regime, a possible alternative to deterministic Boltzmann solvers is represented by Moment Methods (Struchtrup 2005). Examples are the regularized 13-moment (R13) method developed by Struchtrup and Torrilhon (2003; 2004), which is based on the 13 moment method of Grad (1949), or the Gaussian moment closure method developed by Levermore and Morokoff (1998). In Moment Methods, the set of moment equations can be usually cast into systems of hyperbolic conservation laws for which robust and efficient numerical methods have been developed (Leveque 2002). This fact explains also why moment methods are computationally cheaper than deterministic Boltzmann solvers. The current formulation of most Moment Methods (such as the Gaussian moment closure of Levermore) refer to the case of a mono-component gas without internal energy. Extensions to multi-component gases, though possible (Martins et al. 2011; Kapper et al. 2011), are not trivial. Moreover, for

some flow conditions, the system of moment equations may lose hyperbolicity (Struchtrup and Torrilhon 2003; Kapper et al. 2011), thus making the development of numerical schemes and the related implementation more difficult.

Manuscript Structure

The manuscript is structured as follows. Part I deals with the physico-chemical modeling of non-equilibrium flows. Chapter 1 describes the kinetic approach which is based on Boltzmann equation of the Kinetic Theory of Gases. In ch. 2 it is shown how to obtain a hydrodynamic description based on the application of the Chapman-Enskog method to the Boltzmann equation. The general notation introduced in chs. 1-2 refers to multi-component gases with discrete internal energy levels and is used consistently throughout the whole manuscript. Chapter 3 describes the NASA quantum chemistry database for internal energy excitation and dissociation and the reduced models that have been developed based on that.

Part II deals with the integration of the developed reduced models in hydrodynamic flow solvers. In ch. 4, an Ordinary-Differential-Equation solver developed by the author is used for the investigation of inviscid flows behind normal shock waves. Chapter 5 deals with the application of CFD solvers developed by the author for computing inviscid flows within converging-diverging nozzles, viscous stagnation-line flows and inviscid axisymmetric flows.

Part III deals with the development of computational methods for rarefied flows. Chapter 6 describes the proposed extension of an existing spectral-Lagrangian method for the Boltzmann equation to multi-component gases and inelastic collisions. Applications of the numerical method (implemented in a parallel computational tool developed by the author) are shown in ch. 7, where results are compared with those obtained by means of the DSMC method and experimental measurements.

Conclusions and perspectives are given at the end of the manuscript. In order to make the manuscript easier to read, the details of some mathematical developments have been placed in apps. A-K.

Part I

Physico-Chemical Models for Non-Equilibrium Flows

Chapter 1

Kinetic Approach

This chapter describes the kinetic approach for multi-component dilute gases based on the Boltzmann equation. The Boltzmann equation is the fundamental equation of the Kinetic Theory of Gases and aims at providing a statistical description of dilute gaseous systems. This is motivated by the fact that, in many situations, one is more interested in molecular-averaged quantities than a detailed representation of the state of the gas at the molecular level.

The present chapter is structured as follows. Section 1.1 introduces the model assumptions and the definition of the one-particle velocity distribution function. The Boltzmann equation is introduced and described in detail in sec. 1.2. The equilibrium solution of the Boltzmann equation (Maxwell-Boltzmann velocity distribution function) and the related gas thermodynamic properties are discussed in sec. 1.3. Section 1.4 introduces molecular-averaged quantities of interest outside of equilibrium conditions. Section 1.5 describes the procedure for obtaining the Maxwell transfer equations. These equations are then used in sec. 1.6 for obtaining the conservation equations of gasdynamics.

1.1 Assumptions

The gas is made of atoms and molecules. The presence of charged particles (such as ions and electrons) is not accounted for. Based on a quasi-classical approach, it is assumed that the chemical components may have only certain discrete internal energy levels. For atoms, the internal energy levels correspond to the electronic levels. In the case of molecules, they also account for the presence of rovibrational levels, due to the relative motion of the particle nuclei. The chemical components are stored in the set \mathcal{S} . The subsets \mathcal{S}_a and \mathcal{S}_m store the atomic and molecular components, respectively (where $\mathcal{S} = \mathcal{S}_a \cup \mathcal{S}_m$). The chemical elements are stored in the set \mathcal{S}_e . The number of atoms of the chemical element l contained within the chemical component s is given by the entry ν_s^l of the stoichiometric matrix $\boldsymbol{\nu}$. The internal energy level i of a chemical component s is indicated with the notation s_i . Its degeneracy and internal

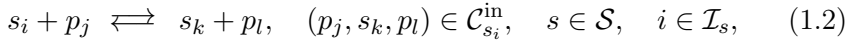
energy (including the formation energy) are indicated with the symbols a_{s_i} and E_{s_i} , respectively. The internal energy levels of a chemical component s are sorted by increasing energy and stored in the set \mathcal{I}_s . The symbols m_s and m_e^l are used for the masses of the chemical component s and the chemical element l , respectively. The related molar masses are $\mathcal{M}_s = N_A m_s$ and $\mathcal{M}_e^l = N_A m_e^l$, respectively (where N_A is Avogadro's number).

The following assumptions are introduced for the physical model:

1. The gas is dilute and composed of point particles.
2. There are no external forces.
3. The Boltzmann-Grad limit holds.
4. Ionization phenomena are neglected.
5. The interactions between particles are only collisional and comprise:
 - Elastic collisions:



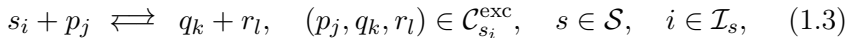
- Non reactive inelastic collisions:



where the inelastic collision set $\mathcal{C}_{s_i}^{\text{in}}$ for s_i is defined as $\mathcal{C}_{s_i}^{\text{in}} = \{(p_j, s_k, p_l) \mid p \in \mathcal{S}, \quad i \neq k \vee j \neq l, \quad k \in \mathcal{I}_s, \quad j, l \in \mathcal{I}_p\}$. Examples of non reactive inelastic collisions are:



- Exchange chemical reactions:

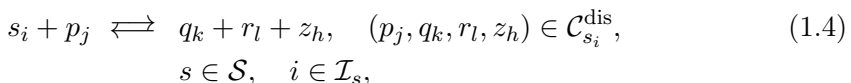


where the exchange reaction set $\mathcal{C}_{s_i}^{\text{exc}}$ for s_i is defined as $\mathcal{C}_{s_i}^{\text{exc}} = \{(p_j, q_k, r_l) \mid s \neq q \wedge p \neq r, \quad p, q, r \in \mathcal{S}, \quad j \in \mathcal{I}_p, \quad k \in \mathcal{I}_q, \quad l \in \mathcal{I}_r\}$.

Examples of exchange chemical reactions are:



- Three-body dissociation/recombination reactions:



where $\mathcal{C}_{s_i}^{\text{dis}}$ is the set of three-body dissociation/recombination reactions where s_i is the first reactant. A rigorous definition of the set $\mathcal{C}_{s_i}^{\text{dis}}$ would be rather complicated and, since it is not used in what follows, it is not

provided. Notice that for eq. (1.4) to be a dissociation/recombination reaction, at least one of the chemical components among s and p must be a molecule. Examples of three-body dissociation recombination reactions are:



Based on the previous assumptions, it is possible to introduce a one-particle velocity distribution function $f_{s_i} = f_{s_i}(\mathbf{x}, \mathbf{c}_{s_i}, t)$. The velocity distribution function plays the role of a phase-space density and can be given the following interpretation:

$f_{s_i}(\mathbf{x}, \mathbf{c}_{s_i}, t) d\mathbf{x} d\mathbf{c}_{s_i}$ = expectation value of the number of particles of the chemical component s occupying the internal energy level i contained within the volume $d\mathbf{x} d\mathbf{c}_{s_i}$ around the point $(\mathbf{x}, \mathbf{c}_{s_i})$ of the phase-space at time t .

1.2 The Boltzmann Equation

The evolution in the phase-space of the velocity distribution function is described by the Boltzmann equation (Ferziger and Kaper 1972; Giovangigli 1999; Nagnibeda and Kustova 2009):

$$\mathfrak{D}_{s_i} f_{s_i} = Q_{s_i}^{\text{el}} + Q_{s_i}^{\text{in}} + Q_{s_i}^{\text{re}}, \quad s \in \mathcal{S}, \quad i \in \mathcal{I}_s, \quad (1.5)$$

where the streaming operator $\mathfrak{D}_{s_i}()$ is defined as $\mathfrak{D}_{s_i}() = \partial() / \partial t + \mathbf{c}_{s_i} \cdot \nabla_{\mathbf{x}}()$ in absence of external forces. The streaming operator represents a material derivative in the phase-space and describes the effects of particle motion in absence of collisions. The right-hand-side of the Boltzmann equation is given by the sum of the elastic, inelastic and reactive collision operators ($Q_{s_i}^{\text{el}}$, $Q_{s_i}^{\text{in}}$ and $Q_{s_i}^{\text{re}}$, respectively) that account for the effects of the collisional processes listed in sec. 1.1.

1.2.1 The Elastic Collision Operator

The elastic collision operator $Q_{s_i}^{\text{el}} = Q_{s_i}^{\text{el}}(\mathbf{x}, \mathbf{c}_{s_i}, t)$ accounts for the effects of elastic collisions (1.1) and reads:

$$Q_{s_i}^{\text{el}} = \sum_{\substack{p \in \mathcal{S} \\ j \in \mathcal{I}_p}} Q_{s_i p_j}, \quad s \in \mathcal{S}, \quad i \in \mathcal{I}_s, \quad (1.6)$$

where the partial elastic collision operator $Q_{s_i p_j} = Q_{s_i p_j}(\mathbf{x}, \mathbf{c}_{s_i}, t)$ is:

$$Q_{s_i p_j} = \iint_{\mathcal{S}^2 \times \mathbb{R}^3} \left(f'_{s_i} f'_{p_j} - f_{s_i} f_{p_j} \right) \sigma_{s_i p_j} g d\omega' d\mathbf{c}_{p_j}, \quad (1.7)$$

$$s, p \in \mathcal{S}, \quad i \in \mathcal{I}_s, \quad j \in \mathcal{I}_p,$$

where \mathbf{c}_{p_j} is the velocity of p_j , $g = |\mathbf{c}_{s_i} - \mathbf{c}_{p_j}|$ is the relative velocity magnitude between the colliding particles, $\omega' = |\mathbf{c}'_{s_i} - \mathbf{c}'_{p_j}| / |\mathbf{c}_{s_i} - \mathbf{c}_{p_j}|$ is the unit vector along the scattering direction and $\sigma_{s_i p_j}$ is the differential cross-section for elastic scattering. In eq. (1.7), and in what follows, primed variables refer to post-collisional values. These are related to pre-collisional values through conservation of mass, momentum and energy. The differential cross-section $\sigma_{s_i p_j} = \sigma_{s_i p_j}(g, \omega')$ is related to that for the inverse process $\sigma_{s_j p_i}(g', \omega)$ through the following micro-reversibility relation that can be obtained from Fermi's golden rule (Dellacherie 2003; Nagnibeda and Kustova 2009):

$$\sigma_{s_i p_j}(g, \omega') g d\omega' d\mathbf{c}_{s_i} d\mathbf{c}_{p_j} = \sigma_{s_j p_i}(g', \omega) g' d\omega d\mathbf{c}'_{s_i} d\mathbf{c}'_{p_j}, \quad (1.8)$$

$$s, p \in \mathcal{S}, \quad i \in \mathcal{I}_s, \quad j \in \mathcal{I}_p.$$

A relation (not involving differentials) between the direct and inverse process cross-sections can be obtained as follows. The velocity differential products $d\mathbf{c}_{s_i} d\mathbf{c}_{p_j}$ and $d\mathbf{c}'_{s_i} d\mathbf{c}'_{p_j}$ can be written as $d\mathbf{G} g^2 dg d\omega$ and $d\mathbf{G} g'^2 dg' d\omega'$, respectively (where \mathbf{G} is the center of mass velocity; Ferziger and Kaper 1972; Mitchner and Kruger 1973). The substitution of the previous relations and the use of $g = g'$ (valid for an elastic collision) in eq. (1.8), leads to:

$$\sigma_{s_i p_j}(g, \omega') = \sigma_{s_i p_j}(g', \omega), \quad s, p \in \mathcal{S}, \quad i \in \mathcal{I}_s, \quad j \in \mathcal{I}_p. \quad (1.9)$$

1.2.2 The Inelastic Collision Operator

The inelastic collision operator $Q_{s_i}^{\text{in}} = Q_{s_i}^{\text{in}}(\mathbf{x}, \mathbf{c}_{s_i}, t)$ accounts for the effects of non reactive inelastic collisions (1.2) and reads:

$$Q_{s_i}^{\text{in}} = \sum_{\substack{(p_j, s_k, p_l) \\ \in \mathcal{C}_{s_i}^{\text{in}}}} Q_{s_i p_j}^{s_k p_l}, \quad s \in \mathcal{S}, \quad i \in \mathcal{I}_s, \quad (1.10)$$

where the partial inelastic collision operator $Q_{s_i p_j}^{s_k p_l} = Q_{s_i p_j}^{s_k p_l}(\mathbf{x}, \mathbf{c}_{s_i}, t)$ is:

$$Q_{s_i p_j}^{s_k p_l} = \iint_{\mathcal{S}^2 \times \mathbb{R}^3} \left[\left(\frac{\beta_{s_k} \beta_{p_l}}{\beta_{s_i} \beta_{p_j}} \right) f'_{s_k} f'_{p_l} - f_{s_i} f_{p_j} \right] \sigma_{s_i p_j}^{s_k p_l} g d\omega' d\mathbf{c}_{p_j}, \quad (1.11)$$

$$(p_j, s_k, p_l) \in \mathcal{C}_{s_i}^{\text{in}}, \quad s \in \mathcal{S}, \quad i \in \mathcal{I}_s.$$

Quantity β_{s_i} is defined as $\beta_{s_i} = h_p^3 / (a_{s_i} m_s^3)$, where h_p is Planck's constant. The differential cross-section $\sigma_{s_i p_j}^{s_k p_l} = \sigma_{s_i p_j}^{s_k p_l}(g, \omega')$ is related to that for the inverse

process $\sigma_{s_k p_l}^{s_i p_j}(g', \omega)$ through following micro-reversibility relation that can be obtained (as for the elastic case in sec. 1.2.1) from Fermi's golden rule:

$$\beta_{s_k} \beta_{p_l} \sigma_{s_i p_j}^{s_k p_l}(g, \omega') g d\omega' d\mathbf{c}_{s_i} d\mathbf{c}_{p_j} = \beta_{s_i} \beta_{p_j} \sigma_{s_k p_l}^{s_i p_j}(g', \omega) g' d\omega d\mathbf{c}'_{s_k} d\mathbf{c}'_{p_l}, \quad (1.12)$$

$$(p_j, s_k, p_l) \in \mathcal{C}_{s_i}^{\text{in}}, \quad s \in \mathcal{S}, \quad i \in \mathcal{I}_s.$$

Equation (1.12) can be manipulated to obtain a relation (not involving differentials) between the direct and inverse process cross-sections. It can be shown that, also for the case of a non reactive inelastic collision, the velocity differential products $d\mathbf{c}_{s_i} d\mathbf{c}_{p_j}$ and $d\mathbf{c}'_{s_k} d\mathbf{c}'_{p_l}$ in eq. (1.12) can be written as $d\mathbf{G} g^2 dg d\omega$ and $d\mathbf{G} g'^2 dg' d\omega'$, respectively (Mitchner and Kruger 1973). The substitution of the previous relations and the use of $g dg = g' dg'$ (valid for a generic binary collision) in eq. (1.12), leads to:

$$\sigma_{s_k p_l}^{s_i p_j}(g', \omega) = \sigma_{s_i p_j}^{s_k p_l}(g, \omega') \left(\frac{\beta_{s_k} \beta_{p_l}}{\beta_{s_i} \beta_{p_j}} \right) \left/ \left(1 - \frac{2\Delta E_{s_i p_j}^{s_k p_l}}{g^2 \mu_{sp}} \right) \right., \quad (1.13)$$

$$(p_j, s_k, p_l) \in \mathcal{C}_{s_i}^{\text{in}}, \quad s \in \mathcal{S}, \quad i \in \mathcal{I}_s,$$

where the reduced mass of the chemical components s and p is $\mu_{sp} = m_s m_p / (m_s + m_p)$ and the global internal energy jump $\Delta E_{s_i p_j}^{s_k p_l}$ is defined as $\Delta E_{s_i p_j}^{s_k p_l} = (E_{s_k} + E_{p_l}) - (E_{s_i} + E_{p_j})$. In obtaining eq. (1.13), the relation $g'^2 = g^2 (1 - 2\Delta E_{s_i p_j}^{s_k p_l} / g^2 \mu_{sp})$, which can be obtained from the collision dynamics, has been exploited (Mitchner and Kruger 1973).

1.2.3 The Reactive Collision Operator

The reactive collision operator accounts for the effects of exchange reactions (1.3) and three body dissociation/recombination reactions (1.4) and reads:

$$Q_{s_i}^{\text{re}} = Q_{s_i}^{\text{exc}} + Q_{s_i}^{\text{dis}}, \quad s \in \mathcal{S}, \quad i \in \mathcal{I}_s, \quad (1.14)$$

where the exchange collision operator $Q_{s_i}^{\text{exc}} = Q_{s_i}^{\text{exc}}(\mathbf{x}, \mathbf{c}_{s_i}, t)$ accounts for the effects of exchange reactions, the dissociation collision operator $Q_{s_i}^{\text{dis}} = Q_{s_i}^{\text{dis}}(\mathbf{x}, \mathbf{c}_{s_i}, t)$ accounts for the effects of three body dissociation/recombination reactions. The exchange collision operator is:

$$Q_{s_i}^{\text{exc}} = \sum_{\substack{(p_j, q_k, r_l) \\ \in \mathcal{C}_{s_i}^{\text{exc}}}} Q_{s_i p_j}^{q_k r_l}, \quad s \in \mathcal{S}, \quad i \in \mathcal{I}_s, \quad (1.15)$$

where the partial exchange collision operator $Q_{s_i p_j}^{q_k r_l} = Q_{s_i p_j}^{q_k r_l}(\mathbf{x}, \mathbf{c}_{s_i}, t)$ is:

$$Q_{s_i p_j}^{q_k r_l} = \iint_{\mathcal{S}^2 \times \mathfrak{R}^3} \left[\left(\frac{\beta_{q_k} \beta_{r_l}}{\beta_{s_i} \beta_{p_j}} \right) f'_{q_k} f'_{r_l} - f_{s_i} f_{p_j} \right] \sigma_{s_i p_j}^{q_k r_l} g d\omega' d\mathbf{c}_{p_j}, \quad (1.16)$$

$$(p_j, q_k, r_l) \in \mathcal{C}_{s_i}^{\text{exc}}, \quad s \in \mathcal{S}, \quad i \in \mathcal{I}_s.$$

The differential cross section $\sigma_{s_i p_j}^{q_k r_l} = \sigma_{s_i p_j}^{q_k r_l}(g, \omega')$ is related to that for the inverse process $\sigma_{q_k r_l}^{s_i p_j} = \sigma_{q_k r_l}^{s_i p_j}(g', \omega)$ through the following micro-reversibility relation that can be obtained (as for the elastic and inelastic cases in secs. 1.2.1-1.2.2) from Fermi's golden rule:

$$\beta_{q_k} \beta_{r_l} \sigma_{s_i p_j}^{q_k r_l}(g, \omega') g d\omega' d\mathbf{c}_{s_i} d\mathbf{c}_{p_j} = \beta_{s_i} \beta_{p_j} \sigma_{q_k r_l}^{s_i p_j}(g', \omega) g' d\omega d\mathbf{c}'_{q_k} d\mathbf{c}'_{r_l}, \quad (1.17)$$

$$(p_j, q_k, r_l) \in \mathcal{C}_{s_i}^{\text{exc}}, \quad s \in \mathcal{S}, \quad i \in \mathcal{I}_s.$$

The application of the same procedure used in sec. 1.2.2, allows for writing a relation (not involving differentials) between the direct and inverse process cross-sections:

$$\sigma_{q_k p_l}^{s_i p_j}(g', \omega) = \sigma_{s_i p_j}^{q_k r_l}(g, \omega') \left(\frac{\beta_{q_k} \beta_{r_l}}{\beta_{s_i} \beta_{p_j}} \right) \left/ \left(\frac{\mu_{sp}}{\mu_{qr}} - \frac{2\Delta E_{s_i p_j}^{q_k r_l}}{g^2 \mu_{qr}} \right) \right., \quad (1.18)$$

$$(p_j, q_k, r_l) \in \mathcal{C}_{s_i}^{\text{exc}}, \quad s \in \mathcal{S}, \quad i \in \mathcal{I}_s.$$

The dissociation collision operators is:

$$Q_{s_i}^{\text{dis}} = \sum_{\substack{(p_j, q_k, r_l \\ z_h) \in \mathcal{C}_{s_i}^{\text{dis}}}} Q_{s_i p_j}^{q_k r_k z_h}, \quad s \in \mathcal{S}, \quad i \in \mathcal{I}_s, \quad (1.19)$$

where $Q_{s_i p_j}^{q_k r_k z_h} = Q_{s_i p_j}^{q_k r_k z_h}(\mathbf{x}, \mathbf{c}_{s_i}, t)$ is the partial dissociation collision operator. The general expression for the partial dissociation collision operator is rather complicated and can be found in the book of Giovangigli (1999). Some examples are given here for dissociation/recombination reactions involving only diatomic molecules (Ludwig and Heil 1960; Kuščer 1991; Alexeev et al. 1994).

For a dissociation/recombination reaction $s_i + p_j = q_k + r_l + p_h$ (where the chemical component s is a diatomic molecule, q and r are its constitutive atoms, and $s \neq p$), the partial dissociation collision operator for s_i is:

$$Q_{s_i p_j}^{q_k r_l p_h} = \iint_{\mathbb{R}^3 \times \mathbb{R}^3 \times \mathbb{R}^3} \left[\left(\frac{\beta_{q_k} \beta_{r_l} \beta_{p_h}}{\beta_{s_i} \beta_{p_j}} \right) f'_{q_r} f'_{r_l} f'_{p_h} - f_{s_i} f_{p_j} \right] W_{s_i p_j}^{q_k r_l p_h} d\mathbf{c}_{p_j} d\mathbf{c}'_{q_k} \times$$

$$d\mathbf{c}'_{r_l} d\mathbf{c}'_{p_h}, \quad (p_j, q_k, r_l, p_h) \in \mathcal{C}_{s_i}^{\text{dis}}, \quad s \in \mathcal{S}, \quad i \in \mathcal{I}_s. \quad (1.20)$$

Quantity $W_{s_i p_j}^{q_k r_l p_h}$ is the dissociation probability (Giovangigli 1999) and is related to the dissociation cross-section by the relation $g \sigma_{s_i p_j}^{q_k r_l p_h}(g, \omega') d\omega' = W_{s_i p_j}^{q_k r_l p_h} d\mathbf{c}'_{q_k} d\mathbf{c}'_{r_l} d\mathbf{c}'_{p_h}$. The dissociation probability $W_{s_i p_j}^{q_k r_l p_h}$ is related to the recombination probability $W_{q_k r_l p_h}^{s_i p_j}$ through the following micro-reversibility relation (Giovangigli 1999):

$$W_{s_i p_j}^{q_k r_l p_h} \beta_{q_k} \beta_{r_l} \beta_{p_h} = W_{q_k r_l p_h}^{s_i p_j} \beta_{s_i} \beta_{p_j}, \quad (1.21)$$

$$(p_j, q_k, r_l, p_h) \in \mathcal{C}_{s_i}^{\text{dis}}, \quad s \in \mathcal{S}, \quad i \in \mathcal{I}_s.$$

For the situation $s = p$, eq. (1.20) can be used except when $i = j = h$. In this case, eq. (1.20) must be replaced with (Giovangigli 1999):

$$\begin{aligned} Q_{s_i s_i}^{q_k r_l s_i} = & 2 \iint \iint \left[\left(\frac{\beta_{q_k} \beta_{r_l}}{\beta_{s_i}} \right) f'_{q_r} f'_{r_l} f_{s_i}^{**} - f_{s_i} f_{s_i}^* \right] W_{s_i s_i}^{q_k r_l s_i} d\mathbf{c}_{s_i}^* d\mathbf{c}'_{q_k} d\mathbf{c}'_{r_l} d\mathbf{c}_{s_i}^{**} - \\ & \iint \iint \left[\left(\frac{\beta_{q_k} \beta_{r_l}}{\beta_{s_i}} \right) f'_{q_r} f'_{r_l} f_{s_i} - f_{s_i}^* f_{s_i}^{**} \right] W_{s_i s_i}^{q_k r_l s_i} d\mathbf{c}_{s_i}^* d\mathbf{c}_{s_i}^{**} d\mathbf{c}'_{q_k} d\mathbf{c}'_{r_l}, \\ (s_i, q_k, r_l, s_i) \in \mathcal{C}_{s_i}^{\text{dis}}, \quad s \in \mathcal{S}, \quad i \in \mathcal{I}_s, \end{aligned} \quad (1.22)$$

where the superscripts * and ** are used to distinguish between the different velocity classes of s_i . The first term on the right-hand-side of eq. (1.22) accounts for the dissociation of molecules belonging to the velocity class \mathbf{c}_{s_i} . The second term accounts for the fact that molecules belonging to the same velocity class may be created as a result of the collision.

1.2.4 Collisional Invariants

During an elastic collision, the number of particles in each internal energy level, the total momentum and the total energy are conserved. This leads to the introduction of the elastic collisional invariants (Giovangigli 1999):

$$\begin{pmatrix} \psi_{s_i}^{\text{el } p_j} \\ \psi_{s_i}^{\text{el } \mathcal{N}_s+1} \\ \psi_{s_i}^{\text{el } \mathcal{N}_s+2} \\ \psi_{s_i}^{\text{el } \mathcal{N}_s+3} \\ \psi_{s_i}^{\text{el } \mathcal{N}_s+4} \end{pmatrix} = \begin{pmatrix} m_s \delta_{sp} \delta_{ij} \\ m_s \mathbf{c}_{s_i} \\ \frac{1}{2} m_s c_{s_i}^2 + E_{s_i} \end{pmatrix}, \quad s, p \in \mathcal{S}, \quad i \in \mathcal{I}_s, \quad j \in \mathcal{I}_p, \quad (1.23)$$

where the number of species is defined as $\mathcal{N}_s = \sum_{s \in \mathcal{S}} \#(\mathcal{I}_s)$. The symbol δ stands for Kronecker's delta. Quantity $c_{s_i}^2 = \mathbf{c}_{s_i} \cdot \mathbf{c}_{s_i}$ is the magnitude-squared of the vector \mathbf{c}_{s_i} . After introducing the set of indices for the elastic collisional invariants, $\mathcal{I}^{\text{el}} = \{s_i, \mathcal{N}_s + 1, \dots, \mathcal{N}_s + 4 \mid s \in \mathcal{S}, i \in \mathcal{I}_s\}$, it is possible to write the relation $\psi_{s_i}^{\text{el } \nu} + \psi_{p_j}^{\text{el } \nu} = \psi_{s_i}^{\text{el } \nu'} + \psi_{p_j}^{\text{el } \nu'}$ in order to express the conservation of the number of particles in each internal energy level, total momentum and total energy for the elastic collision $s_i + p_j = s_i + p_j$. The kernel of the elastic collision operator $Q_{s_i}^{\text{el}}$ is spanned by the elastic collisional invariants (Giovangigli 1999):

$$\sum_{\substack{s \in \mathcal{S} \\ i \in \mathcal{I}_s}} \int_{\mathbb{R}^3} \psi_{s_i}^{\text{el } \nu} Q_{s_i}^{\text{el}} d\mathbf{c}_{s_i} = 0, \quad \nu \in \mathcal{I}^{\text{el}}. \quad (1.24)$$

For a non reactive inelastic collision, due to the transitions among the internal energy levels, the number of particles in each internal energy level is no longer

conserved. In this situation, the number particles for each chemical component is conserved, together with the total momentum and total energy. This leads to the introduction of the inelastic collisional invariants (Giovangigli 1999):

$$\begin{pmatrix} \psi_{s_i}^{\text{in } p} \\ \psi_{s_i}^{\text{in } \mathcal{N}_c+1} \\ \psi_{s_i}^{\text{in } \mathcal{N}_c+2} \\ \psi_{s_i}^{\text{in } \mathcal{N}_c+3} \\ \psi_{s_i}^{\text{in } \mathcal{N}_c+4} \end{pmatrix} = \begin{pmatrix} m_s \delta_{sp} \\ m_s \mathbf{c}_{s_i} \\ \frac{1}{2} m_s c_{s_i}^2 + E_{s_i} \end{pmatrix}, \quad s, p \in \mathcal{S}, \quad i \in \mathcal{I}_s, \quad (1.25)$$

where the number of chemical components is defined as $\mathcal{N}_c = \#(\mathcal{S})$. A set of indices can be also introduced for the inelastic collisional invariants, $\mathcal{I}^{\text{in}} = \{s, \mathcal{N}_c + 1, \dots, \mathcal{N}_c + 4 \mid s \in \mathcal{S}\}$. Based on that and on eq. (1.25), it is possible to write the relation $\psi_{s_i}^{\text{in } \nu} + \psi_{p_j}^{\text{in } \nu} = \psi_{s_k}^{\text{in } \nu'} + \psi_{p_l}^{\text{in } \nu'}$ in order to express the conservation of the number of particles for each chemical component, total momentum and total energy for the non reactive inelastic collision $s_i + p_j = s_k + p_l$. The kernel of the inelastic collision operator $Q_{s_i}^{\text{in}}$ is spanned by the inelastic collisional invariants (Giovangigli 1999):

$$\sum_{\substack{s \in \mathcal{S} \\ i \in \mathcal{I}_s}} \int_{\mathbb{R}^3} \psi_{s_i}^{\text{in } \nu} Q_{s_i}^{\text{in}} d\mathbf{c}_{s_i} = 0, \quad \nu \in \mathcal{I}^{\text{in}}. \quad (1.26)$$

When the collision is reactive, the number of particles for each chemical element is conserved, together with the total momentum and the total energy. This leads to the introduction of the reactive collisional invariants (Giovangigli 1999):

$$\begin{pmatrix} \psi_{s_i}^{\text{re } l} \\ \psi_{s_i}^{\text{re } \mathcal{N}_e+1} \\ \psi_{s_i}^{\text{re } \mathcal{N}_e+2} \\ \psi_{s_i}^{\text{re } \mathcal{N}_e+3} \\ \psi_{s_i}^{\text{re } \mathcal{N}_e+4} \end{pmatrix} = \begin{pmatrix} \nu_s^l m_e^l \\ m_s \mathbf{c}_{s_i} \\ \frac{1}{2} m_s c_{s_i}^2 + E_{s_i} \end{pmatrix}, \quad l \in \mathcal{S}_e, \quad s \in \mathcal{S}, \quad i \in \mathcal{I}_s, \quad (1.27)$$

where the number of chemical elements is defined as $\mathcal{N}_e = \#(\mathcal{S}^e)$. A set of indices can be also introduced for the reactive collisional invariants, $\mathcal{I}^{\text{re}} = \{l, \mathcal{N}_e + 1, \dots, \mathcal{N}_e + 4 \mid l \in \mathcal{S}_e\}$. Based on that and on eq. (1.27), it is possible to write the relations $\psi_{s_i}^{\text{re } \nu} + \psi_{p_j}^{\text{re } \nu} = \psi_{p_k}^{\text{re } \nu'} + \psi_{r_l}^{\text{re } \nu'}$ and $\psi_{s_i}^{\text{re } \nu} + \psi_{p_j}^{\text{re } \nu} = \psi_{q_k}^{\text{re } \nu'} + \psi_{r_l}^{\text{re } \nu'} + \psi_{z_h}^{\text{re } \nu'}$ in order to express the conservation of the number of particles for each chemical element, total momentum and total energy for the exchange reaction $s_i + p_j = q_k + r_l$ and the three-body dissociation/recombination reaction $s_i + p_j = q_k + r_l + z_h$, respectively. The kernel of the reactive collision operator $Q_{s_i}^{\text{re}}$ is spanned by the reactive collisional invariants (Giovangigli 1999):

$$\sum_{\substack{s \in \mathcal{S} \\ i \in \mathcal{I}_s}} \int_{\mathbb{R}^3} \psi_{s_i}^{\text{re } \nu} Q_{s_i}^{\text{re}} d\mathbf{c}_{s_i} = 0, \quad \nu \in \mathcal{I}^{\text{re}}. \quad (1.28)$$

1.2.5 Conserved Macroscopic Properties

The collisional invariants introduced in sec. 1.2.4, allow for the introduction of the following macroscopic properties as average molecular quantities:

$$\rho_{s_i} = \sum_{\substack{p \in \mathcal{S} \\ j \in \mathcal{I}_p}} \int_{\mathbb{R}^3} \psi_{p_j}^{\text{el } s_i} f_{p_j} d\mathbf{c}_{p_j}, \quad s \in \mathcal{S}, \quad i \in \mathcal{I}_s, \quad (1.29)$$

$$\rho_s = \sum_{\substack{p \in \mathcal{S} \\ j \in \mathcal{I}_p}} \int_{\mathbb{R}^3} \psi_{p_j}^{\text{in } s} f_{p_j} d\mathbf{c}_{p_j}, \quad s \in \mathcal{S}, \quad (1.30)$$

$$\rho_e^l = \sum_{\substack{s \in \mathcal{S} \\ i \in \mathcal{I}_s}} \int_{\mathbb{R}^3} \psi_{s_i}^{\text{re } l} f_{s_i} d\mathbf{c}_{s_i}, \quad l \in \mathcal{S}_e, \quad (1.31)$$

$$\rho \mathbf{v} = \sum_{\substack{s \in \mathcal{S} \\ i \in \mathcal{I}_s}} \int_{\mathbb{R}^3} \begin{pmatrix} \psi_{s_i}^{\text{re } \mathcal{N}_e+1} \\ \psi_{s_i}^{\text{re } \mathcal{N}_e+2} \\ \psi_{s_i}^{\text{re } \mathcal{N}_e+3} \end{pmatrix} f_{s_i} d\mathbf{c}_{s_i}, \quad (1.32)$$

$$\rho E = \sum_{\substack{s \in \mathcal{S} \\ i \in \mathcal{I}_s}} \int_{\mathbb{R}^3} \psi_{s_i}^{\text{re } \mathcal{N}_e+4} f_{s_i} d\mathbf{c}_{s_i}, \quad (1.33)$$

where the densities of the energy level s_i , the chemical component s and the chemical element l are $\rho_{s_i} = m_s n_{s_i}$, $\rho_s = m_s n_s$ and $\rho_e^l = m_e^l n_e^l$, respectively (where n_{s_i} , n_s and n_e^l are the related number densities). The gas density is $\rho = \sum_{l \in \mathcal{S}_e} \rho_e^l$, or alternatively, $\rho = \sum_{s \in \mathcal{S}} \rho_s$ with $\rho_s = \sum_{i \in \mathcal{I}_s} \rho_{s_i}$. Quantity \mathbf{v} is the (hydrodynamic) velocity vector, whose Cartesian components along the x , y and z axes are indicated with u , v and w , respectively. Quantity ρE is the gas total energy density and is the sum of the translational, internal and kinetic energy density contributions, $\rho E = \rho e^{\text{tra}} + \rho e^{\text{int}} + \rho e^{\text{kin}}$. The gas kinetic energy density is $\rho e^{\text{kin}} = (1/2)\rho \mathbf{v} \cdot \mathbf{v}$. The sum of the gas translational and internal energy densities gives the gas thermal energy density, $\rho e = \rho e^{\text{tra}} + \rho e^{\text{int}}$. The macroscopic properties defined in eqs. (1.29)-(1.33) are the quantities that are conserved in a flow in view of the properties satisfied by the elastic, inelastic and reactive collision operators as stated in eqs. (1.24), (1.26) and (1.28).

1.3 Equilibrium Solution

1.3.1 The Maxwell-Boltzmann Distribution Function

Under equilibrium conditions, the use of Boltzmann's H-theorem allows to show that the solution of the Boltzmann equation is given by the Maxwell-Boltzmann velocity distribution function (Ferziger and Kaper 1972; Giovangigli 1999):

$$f_{s_i}^{\text{eq}} = \frac{1}{\beta_{s_i}} \frac{n_s^{\text{eq}}}{Z_s^{\text{tra}}(T^{\text{eq}}) Z_s^{\text{int}}(T^{\text{eq}})} \exp \left(-\frac{m_s |\mathbf{c}_{s_i} - \mathbf{v}|^2}{2k_b T^{\text{eq}}} - \frac{E_{s_i}}{k_b T^{\text{eq}}} \right), \quad (1.34)$$

$$s \in \mathcal{S}, \quad i \in \mathcal{I}_s,$$

where the superscript eq stands for equilibrium and k_b is Boltzmann's constant. Quantity T^{eq} is the gas (equilibrium) temperature and quantity n_s^{eq} is the (equilibrium) number density of the chemical component s , which is equal to $\sum_{i \in \mathcal{I}_s} n_{s_i}^{eq}$. The (equilibrium) translational and internal partition function of the chemical component s are:

$$Z_s^{\text{tra}}(T^{eq}) = \left(\frac{2\pi m_s k_b T^{eq}}{h_p^2} \right)^{3/2}, \quad Z_s^{\text{int}}(T^{eq}) = \sum_{i \in \mathcal{I}_s} a_{s_i} \exp \left(-\frac{E_{s_i}}{k_b T^{eq}} \right), \quad s \in \mathcal{S}. \quad (1.35)$$

The integration of eq. (1.34) over the velocity space leads to the Boltzmann distribution law:

$$\frac{n_{s_i}^{eq}}{n_s^{eq}} = \frac{a_{s_i}}{Z_s^{\text{int}}(T^{eq})} \exp \left(-\frac{E_{s_i}}{k_b T^{eq}} \right), \quad s \in \mathcal{S}, \quad i \in \mathcal{I}_s. \quad (1.36)$$

Equation (1.36) allows for computing the internal energy level population of each chemical component in equilibrium conditions. The chemical component (equilibrium) number densities are related to the (equilibrium) pressure and temperature through Dalton's law of partial pressures, $p^{eq} = \sum_{s \in \mathcal{S}} n_s^{eq} k_b T^{eq}$, and their values can be determined (for given pressure, temperature and elemental fractions) by solving a system of non linear algebraic equations. This system is obtained by writing down the expressions for the equilibrium constants of a set of linearly independent chemical reactions and the equations expressing the conservation of the mass of each chemical element (the details of the procedure can be found in the books of Anderson 1989 and Vincenti and Kruger 1965).

In alternative to the use of number densities (as done in eq. (1.36)), the gas chemical composition can be specified in terms of mole and mass fractions (indicated with the symbols X and y , respectively):

$$X_{s_i}^{eq} = \frac{n_{s_i}^{eq}}{n^{eq}}, \quad y_{s_i}^{eq} = \frac{\rho_{s_i}^{eq}}{\rho^{eq}}, \quad s \in \mathcal{S}, \quad i \in \mathcal{I}_s, \quad (1.37)$$

where the gas (equilibrium) number density and density are $n^{eq} = \sum_{s \in \mathcal{S}} n_s^{eq}$ and $\rho^{eq} = \sum_{s \in \mathcal{S}} \rho_s^{eq}$, respectively. By definition, mole and mass fractions satisfy the following constraints:

$$\sum_{\substack{s \in \mathcal{S} \\ i \in \mathcal{I}_s}} X_{s_i}^{eq} = 1, \quad \sum_{\substack{s \in \mathcal{S} \\ i \in \mathcal{I}_s}} y_{s_i}^{eq} = 1, \quad (1.38)$$

and are related by the following relation:

$$X_{s_i}^{eq} = y_{s_i}^{eq} \frac{\mathcal{M}_{s_i}^{eq}}{\mathcal{M}^{eq}}, \quad s \in \mathcal{S}, \quad i \in \mathcal{I}_s, \quad (1.39)$$

where the (equilibrium) gas molar mass is $\mathcal{M}^{eq} = \sum_{s \in \mathcal{S}} X_s^{eq} \mathcal{M}_s$. It is important to mention that the definitions for mole and mass fractions given in eq. (1.37) can be also used outside of equilibrium conditions.

1.3.2 Thermodynamic Properties

When the velocity distribution function is Maxwell-Boltzmann, the gas translational and internal energy densities assume the following expressions:

$$\rho e^{\text{tra eq}} = \sum_{s \in \mathcal{S}} n_s^{\text{eq}} k_b T^{\text{eq}} 2 \frac{\partial \ln Z_s^{\text{tra}}(T^{\text{eq}})}{\partial T^{\text{eq}}}, \quad (1.40)$$

$$\rho e^{\text{int eq}} = \sum_{s \in \mathcal{S}} n_s^{\text{eq}} k_b T^{\text{eq}} 2 \frac{\partial \ln Z_s^{\text{int}}(T^{\text{eq}})}{\partial T^{\text{eq}}}. \quad (1.41)$$

The gas (equilibrium) enthalpy density is obtained by adding the pressure to the (equilibrium) thermal energy density, $\rho h^{\text{eq}} = \rho e^{\text{eq}} + p^{\text{eq}}$ (where $\rho e^{\text{eq}} = \rho e^{\text{tra eq}} + \rho e^{\text{int eq}}$).

The gas translational and internal energy densities provided in eqs. (1.40)-(1.41) can be also written as $\rho e^{\text{tra eq}} = \sum_{s \in \mathcal{I}_s} \rho_s^{\text{eq}} e_s^{\text{tra eq}}(T^{\text{eq}})$ and $\rho e^{\text{int eq}} = \sum_{s \in \mathcal{I}_s} \rho_s^{\text{eq}} e_s^{\text{int eq}}(T^{\text{eq}})$, respectively, where the specific translational and internal energies of the chemical component s are:

$$e_s^{\text{tra eq}}(T^{\text{eq}}) = \frac{k_b T^{\text{eq}} 2}{m_s} \frac{\partial \ln Z_s^{\text{tra}}(T^{\text{eq}})}{\partial T^{\text{eq}}}, \quad (1.42)$$

$$e_s^{\text{int eq}}(T^{\text{eq}}) = \frac{k_b T^{\text{eq}} 2}{m_s} \frac{\partial \ln Z_s^{\text{int}}(T^{\text{eq}})}{\partial T^{\text{eq}}}, \quad (1.43)$$

The sum of eqs. (1.42)-(1.43) gives the (equilibrium) specific thermal energy of the chemical components s :

$$e_s^{\text{eq}}(T^{\text{eq}}) = e_s^{\text{tra eq}}(T^{\text{eq}}) + e_s^{\text{int eq}}(T^{\text{eq}}), \quad s \in \mathcal{S}, \quad (1.44)$$

and its specific enthalpy is obtained as $h_s^{\text{eq}}(T^{\text{eq}}) = e_s^{\text{eq}}(T^{\text{eq}}) + k_b T^{\text{eq}} / m_s$. Based on the previous definitions, the gas (equilibrium) enthalpy density can be also written as $\rho h^{\text{eq}} = \sum_{s \in \mathcal{S}} \rho_s^{\text{eq}} h_s^{\text{eq}}(T^{\text{eq}})$.

The constant volume and pressure (equilibrium) specific heats of the chemical component s can be computed by differentiating (with respect to the equilibrium temperature) the expressions for its specific energy and enthalpy, respectively:

$$c_{v,s}^{\text{eq}}(T^{\text{eq}}) = \frac{de_s^{\text{eq}}(T^{\text{eq}})}{dT^{\text{eq}}}, \quad c_{p,s}^{\text{eq}}(T^{\text{eq}}) = c_{v,s}^{\text{eq}}(T^{\text{eq}}) + \frac{k_b}{m_s}, \quad (1.45)$$

$$c_{v,s}^{\text{tra eq}}(T^{\text{eq}}) = \frac{de_s^{\text{tra eq}}(T^{\text{eq}})}{dT^{\text{eq}}}, \quad c_{p,s}^{\text{tra eq}}(T^{\text{eq}}) = c_{v,s}^{\text{tra eq}}(T^{\text{eq}}) + \frac{k_b}{m_s}, \quad (1.46)$$

$$c_{v,s}^{\text{int eq}}(T^{\text{eq}}) = \frac{de_s^{\text{int eq}}(T^{\text{eq}})}{dT^{\text{eq}}}, \quad c_{p,s}^{\text{int eq}}(T^{\text{eq}}) = c_{v,s}^{\text{int eq}}(T^{\text{eq}}), \quad (1.47)$$

where the translational and internal components satisfy the obvious relations $c_{v,s}^{\text{eq}}(T^{\text{eq}}) = c_{v,s}^{\text{tra eq}}(T^{\text{eq}}) + c_{v,s}^{\text{int eq}}(T^{\text{eq}})$ and $c_{p,s}^{\text{eq}}(T^{\text{eq}}) = c_{p,s}^{\text{tra eq}}(T^{\text{eq}}) + c_{p,s}^{\text{int eq}}(T^{\text{eq}})$.

1.4 Non-Equilibrium Solution

Outside of equilibrium conditions, the solution of the Boltzmann equation (1.5) is no longer given by the Maxwell-Boltzmann velocity distribution function. The thermodynamic properties introduced in equilibrium conditions in sec. 1.3.2 can be generalized, as it is shown in ch. 2. Moreover, additional macroscopic moments can be introduced. These moments (which can be also computed in equilibrium conditions) are:

- Diffusion velocities:

$$\mathbf{v}_{s_i}^d = \frac{m_s}{\rho_{s_i}} \int_{\mathbb{R}^3} \mathbf{C}_{s_i} f_{s_i} d\mathbf{c}_{s_i}, \quad s \in \mathcal{S}, \quad i \in \mathcal{I}_s, \quad (1.48)$$

where the peculiar velocity is $\mathbf{C}_{s_i} = \mathbf{c}_{s_i} - \mathbf{v}$.

- Translational temperature components:

$$T_{s_i \alpha} = \frac{m_s}{n_{s_i} k_b} \int_{\mathbb{R}^3} C_{s_i \alpha}^2 f_{s_i} d\mathbf{c}_{s_i}, \quad \alpha \in \{x, y, z\}, \quad s \in \mathcal{S}, \quad i \in \mathcal{I}_s, \quad (1.49)$$

- Translational temperatures:

$$T_{s_i} = \frac{T_{s_i x} + T_{s_i y} + T_{s_i z}}{3}, \quad s \in \mathcal{S}, \quad i \in \mathcal{I}_s, \quad (1.50)$$

- Translational temperature components (gas):

$$T_\alpha = \frac{1}{n} \sum_{\substack{s \in \mathcal{S} \\ i \in \mathcal{I}_s}} n_{s_i} T_{s_i \alpha}, \quad \alpha \in \{x, y, z\}, \quad (1.51)$$

- Translational temperature (gas):

$$T = \frac{T_x + T_y + T_z}{3}, \quad (1.52)$$

- Viscous stress tensor:

$$\underline{\tau} = - \sum_{\substack{s \in \mathcal{S} \\ i \in \mathcal{I}_s}} \int_{\mathbb{R}^3} m_s \mathbf{C}_{s_i} \otimes \mathbf{C}_{s_i} f_{s_i} d\mathbf{c}_{s_i} + p \underline{\mathbf{I}}, \quad (1.53)$$

where the symbols \otimes and $\underline{\mathbf{I}}$ stand for the tensor product and the second-order identity tensor, respectively. The gas pressure is always computed based on Dalton's law of partial pressures, $p = \sum_{s \in \mathcal{S}} n_s k_b T$.

- Heat flux vector:

$$\mathbf{q} = \sum_{\substack{s \in \mathcal{S} \\ i \in \mathcal{I}_s}} \int_{\mathbb{R}^3} \left(\frac{1}{2} m_s C_{s_i}^2 + E_{s_i} \right) \mathbf{C}_{s_i} f_{s_i} d\mathbf{c}_{s_i}. \quad (1.54)$$

Notice that when the velocity distribution function is Maxwell-Boltzmann, the equilibrium properties defined in sec. 1.3 are retrieved by means of eqs. (1.48)-(1.54). In this situation, the diffusion velocities, the stress tensor and heat flux vector are identically zero.

1.5 Maxwell Transfer Equations

The Boltzmann equation (1.5) can be used for obtaining equations describing the evolution of average molecular quantities (Maxwell transfer equations). The procedure consists in taking moments of the Boltzmann equation and goes as follows. Given a molecular quantity $\varphi_{s_i} = \varphi_{s_i}(\mathbf{c}_{s_i})$, one can define the gas molecular average quantity $\bar{\varphi} = \bar{\varphi}(\mathbf{x}, t)$ as:

$$\bar{\varphi} = \sum_{\substack{s \in \mathcal{S} \\ i \in \mathcal{I}_s}} \int_{\mathbb{R}^3} f_{s_i} \varphi_{s_i} d\mathbf{c}_{s_i}, \quad s \in \mathcal{S}, \quad i \in \mathcal{I}_s. \quad (1.55)$$

The equation describing the evolution of the property $\bar{\varphi}$ can be obtained by multiplying both sides the Boltzmann equation (1.5) by φ_{s_i} , integrating over the velocity space, and then summing over all the energy levels of each chemical component:

$$\sum_{\substack{s \in \mathcal{S} \\ i \in \mathcal{I}_s}} \int_{\mathbb{R}^3} \mathfrak{D}_{s_i} f_{s_i} \varphi_{s_i} d\mathbf{c}_{s_i} = \sum_{\substack{s \in \mathcal{S} \\ i \in \mathcal{I}_s}} \int_{\mathbb{R}^3} \left(Q_{s_i}^{\text{el}} + Q_{s_i}^{\text{in}} + Q_{s_i}^{\text{re}} \right) \varphi_{s_i} d\mathbf{c}_{s_i}. \quad (1.56)$$

The integral on the left-hand-side of eq. (1.56) can be manipulated to give:

$$\frac{\partial \bar{\varphi}}{\partial t} + \nabla_{\mathbf{x}} \cdot \bar{\varphi} \mathbf{v} + \nabla_{\mathbf{x}} \cdot \sum_{\substack{s \in \mathcal{S} \\ i \in \mathcal{I}_s}} \int_{\mathbb{R}^3} \mathbf{C}_{s_i} f_{s_i} \varphi_{s_i} d\mathbf{c}_{s_i} = \sum_{\substack{s \in \mathcal{S} \\ i \in \mathcal{I}_s}} \int_{\mathbb{R}^3} \left(Q_{s_i}^{\text{el}} + Q_{s_i}^{\text{in}} + Q_{s_i}^{\text{re}} \right) \varphi_{s_i} d\mathbf{c}_{s_i}. \quad (1.57)$$

The left-hand-side of eq. (1.57) is made of three terms. The first represents the changes of $\bar{\varphi}$ due to local effects. The second (convective flux) is due to the advection of $\bar{\varphi}$ with the mean flow at the velocity \mathbf{v} . The third (transport or diffusive flux) represents the transport of the molecular quantity φ_{s_i} with respect to the mean flow. The right-hand-side of eq. (1.57) is the volumetric production rate of $\bar{\varphi}$ due to collisions.

The use of the elastic collisional invariants (1.23) as molecular quantity φ_{s_i} in eq. (1.57), leads to the mass conservation equation for all internal energy levels of each chemical component, and the conservation equations for global momentum and energy:

$$\frac{\partial \rho_{s_i}}{\partial t} + \nabla_{\mathbf{x}} \cdot \left(\rho_{s_i} \mathbf{v} + \rho_{s_i} \mathbf{v}_{s_i}^d \right) = \omega_{s_i}, \quad s \in \mathcal{S}, \quad i \in \mathcal{I}_s, \quad (1.58)$$

$$\frac{\partial \rho \mathbf{v}}{\partial t} + \nabla_{\mathbf{x}} \cdot (\rho \mathbf{v} \otimes \mathbf{v} + p \mathbf{I} - \underline{\tau}) = \mathbf{0}_3, \quad (1.59)$$

$$\frac{\partial \rho E}{\partial t} + \nabla_{\mathbf{x}} \cdot (\rho \mathbf{v} H - \underline{\tau} \mathbf{v} + \mathbf{q}) = 0, \quad (1.60)$$

where the gas total enthalpy density is $\rho H = \rho E + p$. Due to conservation of global momentum and energy, the right-hand-side of eqs. (1.59)-(1.60) is zero

(this can also be shown mathematically by using the collisional invariants). On the other hand, the mass production terms ω_{s_i} are not zero, in the most general situation, and read:

$$\omega_{s_i} = m_s \int_{\mathbb{R}^3} (Q_{s_i}^{\text{in}} + Q_{s_i}^{\text{re}}) d\mathbf{c}_{s_i}, \quad s \in \mathcal{S}, \quad i \in \mathcal{I}_s. \quad (1.61)$$

Only the inelastic and reactive collisions contribute to the mass production terms ω_{s_i} . This directly follows from the properties satisfied by the elastic collisional invariants as stated in eq. (1.24). The mass production terms and the diffusion fluxes sum up to zero:

$$\sum_{\substack{s \in \mathcal{S} \\ i \in \mathcal{I}_s}} \omega_{s_i} = 0, \quad \sum_{\substack{s \in \mathcal{S} \\ i \in \mathcal{I}_s}} \rho_{s_i} \mathbf{v}_{s_i}^d = \mathbf{0}_3. \quad (1.62)$$

The first equality in eq. (1.62) follows from the properties of the inelastic and reactive collisional invariants (eqs. (1.26) and (1.28), respectively). The second equality comes directly from the definition of the diffusion velocities given in eq. (1.48). Both results given in eq. (1.62) are a consequence of the law of mass conservation.

The hydrodynamic equations (1.58)-(1.60) represent the conservation equation of gasdynamics. Notice that a mass conservation equation is written for all the internal energy levels of each chemical component of the gas. In this way, the internal energy levels are treated as if they were separate pseudo-species. This approach is referred to as state-to-state approach (Capitelli et al. 2000; Naguibeda and Kustova 2009). For this reason, in what follows the word species is used when referring to the internal energy levels of a given chemical component. When the molecular quantity φ_{s_i} in eq. (1.57) is set equal to the first \mathcal{N}_e components of the reactive collisional invariants (1.27), one obtains the element mass conservation (or continuity) equations:

$$\frac{\partial \rho_e^l}{\partial t} + \nabla_{\mathbf{x}} \cdot (\rho_e^l \mathbf{v} + \rho_e^l \mathbf{v}_e^{dl}) = 0, \quad l \in \mathcal{S}_e, \quad (1.63)$$

where the diffusion velocity of the chemical element l is:

$$\mathbf{v}_e^{dl} = \frac{m_e^l}{\rho_e^l} \sum_{\substack{s \in \mathcal{S} \\ i \in \mathcal{I}_s}} \int_{\mathbb{R}^3} \nu_s^l \mathbf{C}_{s_i} f_{s_i} d\mathbf{c}_{s_i}, \quad l \in \mathcal{S}_e. \quad (1.64)$$

The right-hand-side of eq. (1.27) is zero in view of the properties satisfied by the reactive collisional invariants as stated in eq. (1.28). The sum of eq. (1.63) over all the chemical elements gives the global mass (or continuity) conservation equation:

$$\frac{\partial \rho}{\partial t} + \nabla_{\mathbf{x}} \cdot \rho \mathbf{v} = 0. \quad (1.65)$$

Equation (1.65) can be also obtained by summing eq. (1.58) over all the species, and then using eq. (1.62) in the results obtained.

1.6 The Conservation Equations of Gasdynamics

The conservation equations (1.58)-(1.60) translate into a mathematical form the laws of mass, momentum and energy conservation applied to a fluid flow. They are always valid, as they have been obtained by taking moments of the Boltzmann equation (1.5) without making further assumptions than those stated in sec. 1.1. Since the study of non-equilibrium flows requires, in the most general situation, to trace of all the gas species (*i.e.* to use a state-to-state approach), a hydrodynamic description can be achieved by considering the species, the global momentum and global energy conservation equations:

$$\frac{\partial \rho_{s_i}}{\partial t} + \nabla_{\mathbf{x}} \cdot (\rho_{s_i} \mathbf{v} + \rho_{s_i} \mathbf{v}_{s_i}^d) = \omega_{s_i}, \quad s \in \mathcal{S}, \quad i \in \mathcal{I}_s, \quad (1.66)$$

$$\frac{\partial \rho \mathbf{v}}{\partial t} + \nabla_{\mathbf{x}} \cdot (\rho \mathbf{v} \otimes \mathbf{v} + p \mathbf{I} - \underline{\tau}) = \mathbf{0}_3, \quad (1.67)$$

$$\frac{\partial \rho E}{\partial t} + \nabla_{\mathbf{x}} \cdot (\rho \mathbf{v} H - \underline{\tau} \mathbf{v} + \mathbf{q}) = 0. \quad (1.68)$$

Equations (1.66)-(1.68) can be cast in the so called conservation law form:

$$\frac{\partial \mathbf{U}}{\partial t} + \nabla_{\mathbf{x}} \cdot \underline{\mathcal{F}} - \nabla_{\mathbf{x}} \cdot \underline{\mathcal{F}}^d = \mathbf{S}, \quad (1.69)$$

where \mathbf{U} and \mathbf{S} are the conservative variable and source term vectors, respectively, and $\underline{\mathcal{F}}$ and $\underline{\mathcal{F}}^d$ are the inviscid and diffusive flux tensors, respectively. The expressions of the vectors and tensors in eq. (1.69) are:

$$\mathbf{U} = [\rho_{s_i} \quad \rho \mathbf{v} \quad \rho E]^T, \quad (1.70)$$

$$\mathbf{S} = [\omega_{s_i} \quad \mathbf{0}_3 \quad 0]^T, \quad (1.71)$$

$$\underline{\mathcal{F}} = [\rho_{s_i} \mathbf{v} \quad \rho \mathbf{v} \otimes \mathbf{v} + p \mathbf{I} \quad \rho \mathbf{v} H]^T, \quad (1.72)$$

$$\underline{\mathcal{F}}^d = [-\rho_{s_i} \mathbf{v}_{s_i}^d \quad \underline{\tau} \quad \underline{\tau} \mathbf{v} - \mathbf{q}]^T, \quad (1.73)$$

$$s \in \mathcal{S}, \quad i \in \mathcal{I}_s,$$

where the symbol T stands for the transpose operator. Equations (1.66)-(1.68) are balance equations in open form (Giordano 2002) as they lack of constitutive relations. The latter express the transport fluxes and the mass production terms as a function of flow properties and the related gradients (Ferziger and Kaper 1972; Giovangigli 1999; Nagnibeda and Kustova 2009). In ch. 2 it is shown how these constitutive relations can be obtained based on asymptotic solutions of the Boltzmann equation. The application of this procedure enables to obtain a (closed form) hydrodynamic description and determines, at the same time, its range of applicability.

1.7 Summary

This chapter has provided a detailed description of the Boltzmann equation for multi-component dilute gases with discrete internal energy levels. A general no-

tation has been introduced in order to account for the existence of three kinds of collisional processes: elastic, inelastic and reactive. For each one, the expressions of the related collision operators and collisional invariants have been given. The set of collisional invariants have been used to define macroscopic conserved quantities and derive the conservation equations of gasdynamics (in open form) based on the Maxwell transfer equations. The closed form of the hydrodynamic equations is obtained in ch. 2, where it is shown how the application of the Chapman-Enskog method (within a context of a state-to-state approach) enables to explicitly relate the transport fluxes and the mass production terms to flow quantities and related gradients. The theoretical contents of this chapter are also used in ch. 6 for the development of a deterministic spectral-Lagrangian numerical method for solving the Boltzmann equation for multi-component gases with discrete internal energy levels.

Chapter 2

Hydrodynamic Approach

This chapter describes how to obtain a hydrodynamic model for multi-component dilute gases with internal energy based on the application of the Chapman-Enskog method to the Boltzmann equation.

The present chapter is structured as follows. Section 2.1 presents the Chapman-Enskog method for the Boltzmann equation within the context of a state-to-state approach. The zeroth-order solution for the velocity distribution function is computed in sec. 2.2. This result is then used in sec. 2.3 for obtaining the Euler equations and the first-order solution. Finally, the Navier-Stokes equations are obtained in sec. 2.4. In the same section 2.4, explicit constitutive relations for the transport fluxes and the mass production terms are established to complete the open form hydrodynamic equations given at the end of ch. 1.

2.1 State-to-State Chapman-Enskog Method

The Chapman-Enskog (CE) method aims at obtaining asymptotic solutions of the Boltzmann equation (1.5). Based on a dimensional analysis, the Boltzmann equation (1.5) can be rescaled to emphasize the different time-scales of the collisional processes:

$$\mathfrak{D}_{s_i} f_{s_i} = \frac{1}{\varepsilon} Q_{s_i}^{\text{el}} + \varepsilon^a (Q_{s_i}^{\text{in}} + Q_{s_i}^{\text{re}}), \quad s \in \mathcal{S}, \quad i \in \mathcal{I}_s. \quad (2.1)$$

The perturbation parameter ε plays the role of a Knudsen number and is assumed to be small enough such that a hydrodynamic description of the system is possible, $\varepsilon \ll 1$ (*i.e.* the gas is collision dominated). The value of the parameter a depends on the regime under consideration (Giovangigli 1999). The case $a = -1$ corresponds to the kinetic equilibrium regime (Ern and Giovangigli 1998). In this situation, inelastic and reactive collisions are as fast as elastic collisions. The cases $a = 0$ and $a = 1$ correspond to the strong reaction regime and Maxwellian reaction regime, respectively. In the applications on which this thesis focuses (aerothermodynamic flows), elastic collisions occur over time-scales which are much shorter than those of inelastic and reactive collisions.

This justifies the assumption of a Maxwellian regime ($a = 1$). In view of this, eq. (2.1) becomes:

$$\mathfrak{D}_{s_i} f_{s_i} = \frac{1}{\varepsilon} Q_{s_i}^{\text{el}} + \varepsilon (Q_{s_i}^{\text{in}} + Q_{s_i}^{\text{re}}), \quad s \in \mathcal{S}, \quad i \in \mathcal{I}_s. \quad (2.2)$$

The term $1/\varepsilon$ in eq. (2.2) emphasizes the dominant effect of elastic collisions in driving the velocity distribution function towards the local equilibrium.

Asymptotic solutions of the Boltzmann equation (2.2) are sought by writing the velocity distribution function as a truncated series of the perturbation parameter ε (Giovangigli 1999):

$$f_{s_i} = f_{s_i}^0 (1 + \varepsilon \phi_{s_i}^1 + \varepsilon^2 \phi_{s_i}^2) + \mathcal{O}(\varepsilon^2), \quad s \in \mathcal{S}, \quad i \in \mathcal{I}_s, \quad (2.3)$$

where quantities $\phi_{s_i}^1$ and $\phi_{s_i}^2$ are, respectively, the first and second-order perturbation to the zeroth-order distribution function $f_{s_i}^0$. According to the CE method, the gas is described at successive orders of the ε parameter as equivalent to as many time-scales.

The CE method is well established for multi-component gases without internal energy, where only elastic collisions occur (Chapman and Cowling 1970; Ferziger and Kaper 1972). When the effects of the internal structure, inelastic and reactive collisions are added, the application of the CE method becomes more challenging. This is due to the wide spectrum of time-scales involved in the problem. Many research efforts have been spent in this field. The first work was that of Wang-Chang and Uhlenbeck (1951), valid for a mono-component gas with discrete internal energy levels. The theory developed by Wang-Chang and Uhlenbeck is rigorous for the case when the time-scales of elastic and inelastic collisions are comparable, while it is only approximate for the more realistic condition in which elastic collisions are faster than the inelastic ones. The work of Wang-Chang and Uhlenbeck was later generalized by Mason and Monchick (1962; 1963) who extended the theory to multi-component gases with discrete internal energy levels. Deviations from thermo-chemical non-equilibrium in molecular flows have been studied later, for instance by Pascal and Brun (1993) and Kustova and Nagnibeda (1998). In strong non-equilibrium flows, the characteristic times for gasdynamics and relaxation processes become comparable, and therefore, the equations for flow quantities (such as temperature and velocity) should be coupled to the equations for physico-chemical kinetics (Nagnibeda and Kustova 2009). A difficulty is to derive a proper scaling for the Boltzmann equation, that accounts for the different relaxation times. An elegant approach based on a dimensional analysis has been proposed by Petit and Darrozes (1975) for the translational relaxation processes between the electrons and heavy particles in a plasma. The resulting scaling affects not only the different terms of the streaming and collision operators of the kinetic equations, but also the collision operators themselves and the collisional invariants (Graille et al. 2009). Degond and Lucquin-Desreux (1996) have expanded the collision

operators in terms of the perturbation parameter driving non-equilibrium phenomena, such as the square root of the electron heavy-particle mass ratio for plasmas in translational non-equilibrium. When the Knudsen number is small enough, a multi-scale CE expansion method allows to derive conservation equations for continuum flows. A similar multi-scale approach with expansion of the collision operators in the perturbation parameter has also been applied to study ionization phenomena (Graille et al. 2008).

Magin et al. (2012) have proposed a multi-scale CE method for the treatment of internal energy relaxation in a mono-component gas with discrete internal energy levels. The coexistence of fast and slow collisions in the system results in thermal non-equilibrium between the translational and internal energy modes. The scaling is derived based on a dimensional analysis, and collisions are divided in two categories, based on the magnitude of the net internal energy jump (see eq. (1.13)). For fast collisions, this quantity is assumed to be lower than an energy threshold equal to a fraction of a characteristic thermal energy for the gas that is controlled by a small parameter. The study of the dynamics of a fast binary collision, yields the dependence of the particle velocities on the perturbation parameter. A lemma allows to split the internal energy of all the levels into perturbed elastic and inelastic contributions for the fast collisions. A CE expansion allows for a description of the system based on a continuum approach. The introduction of perturbed energy levels is crucial to separate the energy collision invariant into fast collisional invariants. As opposed to conventional perturbations methods (Kustova and Nagnibeda 1998), the fast collision operator is expanded in the small parameter used to define the threshold for the net energy for fast collisions. The gas particle population is shown to thermalize to a quasi-equilibrium state described by a Maxwell-Boltzmann distribution function in thermal non-equilibrium with the translational temperature and the internal temperature. The role of the fast collisions is the thermalization of the translational and internal energy modes. Euler equations for the conservation of the mass, momentum, translational energy, and internal energy are also derived. The observed role of the slow collisions is to contribute to the thermal relaxation of the translational and internal energy modes.

Another issue which arises when applying the CE method to gases with internal degrees of freedom is the existence or not of bulk viscosity. In the work of Wang-Chang and Uhlenbeck (1951) it was shown that the bulk viscosity appeared in the constitutive relations when elastic and inelastic collisions occur over the same time-scales, while this was not the case when elastic collisions are faster than the inelastic ones. There has been a lot of debate in the Kinetic Theory community on this topic (see, for instance, the papers cited above). The recent works by Bruno, Esposito and Giovangigli (2012; 2013) have investigated in detail the relation between bulk viscosity and internal energy relaxation.

The conceptual problems encountered in the aforementioned references for the CE method are due to the difficulty of casting the multi-scale energy level and reaction dynamics in a multi-temperature model or in a detailed kinetics

model where a state-to-state approach is used only for some internal energy modes (such as molecular vibration; Kustova and Nagnibeda 1998).

In the present thesis, an alternative approach is proposed. The CE method for the Boltzmann equation is extended to gases with internal energy and inelastic and reactive collisions with the purpose of obtaining a hydrodynamic description which is purely state-to-state (*i.e.* State-to-State Chapman-Enskog; STS CE). In this way, there is no need for splitting the inelastic and reactive collision operators in their fast and slow components. The application of the STS CE method enables to obtain a closed form set of hydrodynamic equations, where each internal energy level is treated as a separate pseudo-species. This set of hydrodynamic equations can be then used for developing macroscopic models, as shown in ch. 3.

The application of the STS CE method starts by injecting the truncated series $f_{s_i} = f_{s_i}^0(1 + \varepsilon\phi_{s_i}^1 + \varepsilon^2\phi_{s_i}^2)$ in eq. (2.2):

$$\begin{aligned} & \mathfrak{D}_{s_i}f_{s_i}^0 + \varepsilon \mathfrak{D}_{s_i}\phi_{s_i}^1 f_{s_i}^0 + \varepsilon^2 \mathfrak{D}_{s_i}\phi_{s_i}^2 f_{s_i}^0 + \mathcal{O}(\varepsilon^2) = \frac{1}{\varepsilon} \sum_{\substack{p \in \mathcal{S} \\ j \in \mathcal{I}_p}} Q_{s_ip_j}(f_{s_i}^0, f_{p_j}^0) + \\ & \sum_{\substack{p \in \mathcal{S} \\ j \in \mathcal{I}_p}} \left[Q_{s_ip_j}(f_{s_i}^0, \phi_{p_j}^1 f_{p_j}^0) + Q_{s_ip_j}(\phi_{s_i}^1 f_{s_i}^0, f_{p_j}^0) \right] + \\ & \varepsilon \sum_{\substack{p \in \mathcal{S} \\ j \in \mathcal{I}_p}} \left[Q_{s_ip_j}(f_{s_i}^0, \phi_{p_j}^2 f_{p_j}^0) + Q_{s_ip_j}(\phi_{s_i}^2 f_{s_i}^0, f_{p_j}^0) + Q_{s_ip_j}(\phi_{s_i}^1 f_{s_i}^0, \phi_{p_j}^1 f_{p_j}^0) \right] + \\ & \varepsilon(Q_{s_i}^{\text{in}0} + Q_{s_i}^{\text{re}0}) + \mathcal{O}(\varepsilon^2), \quad s \in \mathcal{S}, \quad i \in \mathcal{I}_s, \end{aligned} \quad (2.4)$$

where the notation $Q_{s_i}^{\text{in}0}$ and $Q_{s_i}^{\text{re}0}$ indicates that the inelastic and reactive collision operators must be evaluated by using the zeroth-order velocity distribution function. Solutions to eq. (2.4) are sought by assuming that the latter is satisfied at the different orders of ε :

$$\varepsilon^{-1} \quad 0 = \sum_{\substack{p \in \mathcal{S} \\ j \in \mathcal{I}_p}} Q_{s_ip_j}(f_{s_i}^0, f_{p_j}^0), \quad (2.5)$$

$$\varepsilon^0 \quad \mathfrak{D}_{s_i}f_{s_i}^0 = \sum_{\substack{p \in \mathcal{S} \\ j \in \mathcal{I}_p}} \left[Q_{s_ip_j}(f_{s_i}^0, \phi_{p_j}^1 f_{p_j}^0) + Q_{s_ip_j}(\phi_{s_i}^1 f_{s_i}^0, f_{p_j}^0) \right], \quad (2.6)$$

$$\begin{aligned} \varepsilon^1 \quad & \mathfrak{D}_{s_i}\phi_{s_i}^1 f_{s_i}^0 = \sum_{\substack{p \in \mathcal{S} \\ j \in \mathcal{I}_p}} \left[Q_{s_ip_j}(f_{s_i}^0, \phi_{p_j}^2 f_{p_j}^0) + Q_{s_ip_j}(\phi_{s_i}^2 f_{s_i}^0, f_{p_j}^0) \right] + \\ & \sum_{\substack{p \in \mathcal{S} \\ j \in \mathcal{I}_p}} Q_{s_ip_j}(\phi_{s_i}^1 f_{s_i}^0, \phi_{p_j}^1 f_{p_j}^0) + (Q_{s_i}^{\text{in}0} + Q_{s_i}^{\text{re}0}), \end{aligned} \quad (2.7)$$

$$\begin{aligned} \varepsilon^2 \quad & \dots = \dots, \\ & s \in \mathcal{S}, \quad i \in \mathcal{I}_s. \end{aligned}$$

The uniqueness of the solution of eq. (2.4) (provided it exists) is enforced by imposing that the conserved macroscopic quantities defined in eqs. (1.29)-(1.33) can be computed based on the zeroth-order distribution function only:

$$\rho_{s_i} = \int_{\mathbb{R}^3} m_s f_{s_i}^0 d\mathbf{c}_{s_i}, \quad s \in \mathcal{S}, \quad i \in \mathcal{I}_s, \quad (2.8)$$

$$\rho \mathbf{v} = \sum_{\substack{s \in \mathcal{S} \\ i \in \mathcal{I}_s}} \int_{\mathbb{R}^3} m_s \mathbf{c}_{s_i} f_{s_i}^0 d\mathbf{c}_{s_i}, \quad (2.9)$$

$$\rho E = \sum_{\substack{s \in \mathcal{S} \\ i \in \mathcal{I}_s}} \int_{\mathbb{R}^3} \left(\frac{1}{2} m_s c_{s_i}^2 + E_{s_i} \right) f_{s_i}^0 d\mathbf{c}_{s_i}. \quad (2.10)$$

For the sake of convenience, the linearized collision operator \mathcal{F}_{s_i} is introduced:

$$\begin{aligned} \mathcal{F}_{s_i}(\phi) &= - \sum_{\substack{p \in \mathcal{S} \\ j \in \mathcal{I}_p}} \left[Q_{s_i p_j} (f_{s_i}^0, \phi_{p_j} f_{p_j}^0) + Q_{s_i p_j} (\phi_{s_i} f_{s_i}^0, f_{p_j}^0) \right] \\ &= - \sum_{\substack{p \in \mathcal{S} \\ j \in \mathcal{I}_p}} \iint_{\mathcal{S}^2 \times \mathbb{R}^3} f_{s_i}^0 \left(\phi'_{s_i} + \phi'_{p_j} - \phi_{s_i} - \phi_{p_j} \right) \sigma_{s_i p_j} g d\omega' d\mathbf{c}_{p_j}, \quad (2.11) \\ &\quad s \in \mathcal{S}, \quad i \in \mathcal{I}_s. \end{aligned}$$

The collisional invariants associated to the linearized collision operator are the elastic collisional invariants (1.23) (Giovangigli 1999). Hence:

$$\mathcal{F}_{s_i}(\psi_{s_i}^{\text{el}\nu}) = 0, \quad \nu \in \mathcal{I}^{\text{el}}, \quad s \in \mathcal{S}, \quad i \in \mathcal{I}_s. \quad (2.12)$$

The linearized collision operator satisfies the further property:

$$\sum_{\substack{s \in \mathcal{S} \\ i \in \mathcal{I}_s}} \int_{\mathbb{R}^3} \psi_{s_i}^{\text{el}\nu} f_{s_i} \mathcal{F}_{s_i}(\phi) d\mathbf{c}_{s_i} = 0, \quad \nu \in \mathcal{I}^{\text{el}}. \quad (2.13)$$

2.2 Zeroth-Order Solution

The zeroth-order velocity distribution function is obtained by solving eq. (2.5), which corresponds to the order ε^{-1} in the STS CE method:

$$\sum_{\substack{p \in \mathcal{S} \\ j \in \mathcal{I}_p}} Q_{s_i p_j} (f_{s_i}^0, f_{p_j}^0) = 0, \quad s \in \mathcal{S}, \quad i \in \mathcal{I}_s. \quad (2.14)$$

The zeroth-order velocity distribution function is found as follows. Multiplying eq. (2.14) by $\ln f_{s_i}^0$, integrating over the velocity space, and summing the result obtained over all the species gives:

$$\sum_{\substack{s \in \mathcal{S} \\ i \in \mathcal{I}_s}} \sum_{\substack{p \in \mathcal{S} \\ j \in \mathcal{I}_p}} \iint_{\mathcal{S}^2 \times \mathbb{R}^3} (f_{s_i}^{0'} f_{p_j}^{0'} - f_{s_i}^0 f_{p_j}^0) \ln \left(\frac{f_{s_i}^{0'} f_{p_j}^{0'}}{f_{s_i}^0 f_{p_j}^0} \right) \sigma_{s_i p_j} g d\omega' d\mathbf{c}_{p_j} d\mathbf{c}_{s_i}. \quad (2.15)$$

The comparison of eq. (2.15) with eq. (1.24) shows that quantity $\ln f_{s_i}^0$ is a collisional invariant. Hence, it can be written as a linear combination of the elastic collisional invariants:

$$\ln f_{s_i}^0 = m_s \alpha_{s_i}^1 + m_s \mathbf{c}_{s_i} \cdot \boldsymbol{\alpha}_{s_i}^2 + \left(\frac{1}{2} m_s C_{s_i}^2 + E_{s_i} \right) \alpha_{s_i}^3 \quad s \in \mathcal{S}, \quad i \in \mathcal{I}_s. \quad (2.16)$$

The values of the constants $\alpha_{s_i}^1$, $\boldsymbol{\alpha}_{s_i}^2$ and $\alpha_{s_i}^3$ can be found by imposing the constraints (2.8)-(2.10). After some algebra, one obtains:

$$\alpha_{s_i}^1 = \frac{1}{m_s} \left[\ln \left(\frac{n_{s_i}}{\beta_{s_i} Z_s^{\text{tra}}(T)} \right) - \frac{1}{k_b T} \left(\frac{1}{2} m_s \mathbf{v} \cdot \mathbf{v} - E_{s_i} \right) \right], \quad (2.17)$$

$$\begin{aligned} \boldsymbol{\alpha}_{s_i}^2 &= \frac{1}{k_b T} \mathbf{v}, \quad \alpha_{s_i}^3 = -\frac{1}{k_b T}, \\ s \in \mathcal{S}, \quad i \in \mathcal{I}_s. \end{aligned} \quad (2.18)$$

The substitution of eqs. (2.17)-(2.18) in eq. (2.16) gives:

$$f_{s_i}^0 = \frac{1}{\beta_{s_i}} \frac{n_{s_i}}{Z_s^{\text{tra}}(T)} \exp \left(-\frac{m_s C_{s_i}^2}{2 k_b T} \right), \quad s \in \mathcal{S}, \quad i \in \mathcal{I}_s. \quad (2.19)$$

Equation (2.19) shows that the zeroth-order solution is a Maxwell-Boltzmann velocity distribution function (only for the translation) at the local translational temperature T . Notice that, in the present situation, the number density n_{s_i} is no longer given by the Boltzmann distribution law (1.36). Instead, it must be found as a solution of the hydrodynamic equations that are being derived. In view of the result stated in eq. (2.19), the gas thermodynamic properties can be computed based on the equilibrium relations given in sec. 1.3.2, with exception of those related to the internal degrees of freedom. For instance, to compute the gas internal energy density, eq. (1.41) can no longer be used. Instead, the general definition $\rho e^{\text{int}} = \sum_{s \in \mathcal{S}} \sum_{i \in \mathcal{I}_s} n_{s_i} E_{s_i}$ must be adopted.

2.3 Zeroth-Order Hydrodynamic Equations and First-Order Solution

The first-order perturbation function $\phi_{s_i}^1$ is the solution of eq. (2.6) which corresponds to the order ϵ^0 in the STS CE method. By exploiting the relation $f_{s_i}^{0'} f_{p_j}^{0'} = f_{s_i}^0 f_{p_j}^0$, which is satisfied by the zeroth-order solution (2.15), it is possible to rewrite eq. (2.6) as:

$$-f_{s_i}^0 \mathcal{F}_{s_i}(\phi^1) = \mathfrak{D}_s f_{s_i}^0, \quad s \in \mathcal{S}, \quad i \in \mathcal{I}_s, \quad (2.20)$$

where the linearized collision operator defined in eq. (2.11) has been introduced. Equation (2.20) is a linear, inhomogeneous Fredholm integral equation of second

kind (Ferziger and Kaper 1972). From the theory of Fredholm integral equations, it is known that the inhomogeneous equation (2.20) is solvable if quantity $\mathcal{D}_s f_{s_i}^0$ is orthogonal to the solution of the related homogeneous equation, $\mathcal{F}_{s_i}(\phi^1) = 0$. As shown in eq. (2.13), the homogeneous equation $\mathcal{F}_{s_i}(\phi^1) = 0$ is satisfied if ϕ^1 is equal to any of the elastic collisional invariants. Hence, the solvability condition for eq. (2.20) becomes:

$$\sum_{\substack{s \in \mathcal{S} \\ i \in \mathcal{I}_s}} \int_{\mathbb{R}^3} \psi_{s_i}^{\text{el} \nu} \mathcal{D}_s f_{s_i}^0 = 0, \quad \nu \in \mathcal{I}^{\text{el}}. \quad (2.21)$$

The substitution of the expression for $f_{s_i}^0$ (eq. (2.19)) in eq. (2.21) yields the zeroth-order hydrodynamic equations:

$$\frac{\partial \rho_{s_i}}{\partial t} + \nabla_{\mathbf{x}} \cdot (\rho_{s_i} \mathbf{v}) = 0, \quad s \in \mathcal{S}, \quad i \in \mathcal{I}_s, \quad (2.22)$$

$$\frac{\partial \rho \mathbf{v}}{\partial t} + \nabla_{\mathbf{x}} \cdot (\rho \mathbf{v} \otimes \mathbf{v} + p \mathbf{I}) = \mathbf{0}_3, \quad (2.23)$$

$$\frac{\partial \rho E}{\partial t} + \nabla_{\mathbf{x}} \cdot (\rho \mathbf{v} H) = 0. \quad (2.24)$$

Equations (2.22)-(2.24) are the Euler equations.

In order to solve for $\phi_{s_i}^1$, it is more convenient to rewrite eq. (2.20) as:

$$\mathcal{F}_{s_i}(\phi^1) = -\frac{1}{f_{s_i}^0} \mathcal{D}_s f_{s_i}^0, \quad s \in \mathcal{S}, \quad i \in \mathcal{I}_s, \quad (2.25)$$

and to re-express the uniqueness constraints (2.8)-(2.10) as:

$$\sum_{\substack{s \in \mathcal{S} \\ i \in \mathcal{I}_s}} \int_{\mathbb{R}^3} \psi_s^{\text{el} \nu} f_{s_i}^0 \phi_{s_i}^r d\mathbf{c}_{s_i} = 0, \quad r \in \{1, 2\}, \quad \nu \in \mathcal{I}^{\text{el}}. \quad (2.26)$$

By making use of the expression for $f_{s_i}^0$ and the zeroth-order hydrodynamic equations (2.22)-(2.24), it is possible to re-express quantity $-1/f_{s_i}^0 \mathcal{D}_s f_{s_i}^0$ in eq. (2.25) as (Ferziger and Kaper 1972):

$$-\frac{1}{f_{s_i}^0} \mathcal{D}_s f_{s_i}^0 = -\underline{\Psi}_{s_i}^\eta : \nabla_{\mathbf{x}} \mathbf{v} - p \sum_{\substack{p \in \mathcal{S} \\ j \in \mathcal{I}_p}} \underline{\Psi}_{s_i}^{D_{pj}} \cdot \mathbf{d}_{pj} - \underline{\Psi}_{s_i}^{\lambda'} \cdot \nabla_{\mathbf{x}} \left(\frac{1}{k_b T} \right), \quad (2.27)$$

$$s \in \mathcal{S}, \quad i \in \mathcal{I}_s,$$

where the diffusion driving forces have been introduced and defined as $p \mathbf{d}_{s_i} = \nabla_{\mathbf{x}} p_{s_i}$. Quantities $\underline{\Psi}_{s_i}^\eta$, $\underline{\Psi}_{s_i}^{D_{pj}}$ and $\underline{\Psi}_{s_i}^{\lambda'}$ are defined as:

$$\underline{\Psi}_{s_i}^\eta = \frac{m_s}{k_b T} \left(\mathbf{C}_{s_i} \otimes \mathbf{C}_{s_i} - \frac{1}{3} C_{s_i}^2 \mathbf{I} \right), \quad s \in \mathcal{S}, \quad i \in \mathcal{I}_s, \quad (2.28)$$

$$\underline{\Psi}_{s_i}^{D_{pj}} = \frac{1}{p_{s_i}} \left(\delta_{sp} \delta_{ij} - \frac{\rho_{s_i}}{\rho} \right) \mathbf{C}_{s_i}, \quad s, p \in \mathcal{S}, \quad i \in \mathcal{I}_s, \quad j \in \mathcal{I}_p, \quad (2.29)$$

$$\underline{\Psi}_{s_i}^{\lambda'} = \left(\frac{5}{2} k_b T - \frac{1}{2} m_s C_{s_i}^2 \right) \mathbf{C}_{s_i}, \quad s \in \mathcal{S}, \quad i \in \mathcal{I}_s. \quad (2.30)$$

Using eqs. (2.27)-(2.30), eq. (2.25) becomes:

$$\mathcal{F}_{s_i}(\phi^1) = -\underline{\Psi}_{s_i}^\eta : \nabla_{\mathbf{x}} \mathbf{v} - p \sum_{\substack{p \in \mathcal{S} \\ j \in \mathcal{I}_p}} \phi_{s_i}^{D_{pj}} \cdot \mathbf{d}_{pj} - \underline{\Psi}_{s_i}^{\lambda'} \cdot \nabla_{\mathbf{x}} \left(\frac{1}{k_b T} \right), \quad (2.31)$$

$$s \in \mathcal{S}, \quad i \in \mathcal{I}_s.$$

By linearity and isotropy of the linearized collision operator \mathcal{F}_{s_i} (Ferziger and Kaper 1972), the first-order perturbation function $\phi_{s_i}^1$ is expressed in terms of the velocity vector gradient, diffusion driving forces, and temperature gradient as:

$$\phi_{s_i}^1 = -\underline{\phi}_{s_i}^\eta : \nabla_{\mathbf{x}} \mathbf{v} - p \sum_{\substack{p \in \mathcal{S} \\ j \in \mathcal{I}_p}} \phi_{s_i}^{D_{pj}} \cdot \mathbf{d}_{pj} - \underline{\phi}_{s_i}^{\lambda'} \cdot \nabla_{\mathbf{x}} \left(\frac{1}{k_b T} \right), \quad (2.32)$$

$$s \in \mathcal{S}, \quad i \in \mathcal{I}_s.$$

where the tensorial functions $\underline{\phi}_{s_i}^\eta$ and the vectorial functions $\phi_{s_i}^{D_{pj}}$ and $\underline{\phi}_{s_i}^{\lambda'}$ are unknown and need to be determined. The substitution of eq. (2.32) in eq. (2.31) yields the following linear, inhomogeneous integral equations which are satisfied by the functions $\underline{\phi}_{s_i}^\eta$, $\phi_{s_i}^{D_{pj}}$ and $\underline{\phi}_{s_i}^{\lambda'}$:

$$\mathcal{F}_{s_i}(\underline{\phi}^\eta) = \underline{\Psi}_{s_i}^\eta, \quad s \in \mathcal{S}, \quad i \in \mathcal{I}_s, \quad (2.33)$$

$$\mathcal{F}_{s_i}(\phi^{D_{pj}}) = \underline{\Psi}_{s_i}^{D_{pj}}, \quad s, p \in \mathcal{S}, \quad i \in \mathcal{I}_s, \quad j \in \mathcal{I}_p, \quad (2.34)$$

$$\mathcal{F}_{s_i}(\underline{\phi}^{\lambda'}) = \underline{\Psi}_{s_i}^{\lambda'}, \quad s \in \mathcal{S}, \quad i \in \mathcal{I}_s, \quad (2.35)$$

where the compact notation $\underline{\phi}^\eta = (\underline{\phi}_{s_i}^\eta)_{s \in \mathcal{S}, i \in \mathcal{I}_s}$, $\phi^{D_{pj}} = (\phi_{s_i}^{D_{pj}})_{s \in \mathcal{S}, i \in \mathcal{I}_s}$ and $\underline{\phi}^{\lambda'} = (\underline{\phi}_{s_i}^{\lambda'})_{s \in \mathcal{S}, i \in \mathcal{I}_s}$ has been introduced. The solution of eqs. (2.33)-(2.35) must be found by imposing the scalar constraints obtained by replacing $\phi_{s_i}^1$ in eq. (2.26) with the functions $\underline{\phi}^\eta$, $\phi^{D_{pj}}$ and $\underline{\phi}^{\lambda'}$, respectively (Ferziger and Kaper 1972).

2.4 First-Order Hydrodynamic Equations

The second-order perturbation function $\phi_{s_i}^2$ is the solution of eq. (2.7), which corresponds to the order ϵ^1 in the STS CE method:

$$-f_{s_i}^0 \mathcal{F}_{s_i}(\phi^2) = \mathfrak{D}_{s_i} \phi_{s_i}^1 f_{s_i}^0 - \sum_{\substack{p \in \mathcal{S} \\ j \in \mathcal{I}_p}} Q_{s_i p_j} (\phi_{s_i}^1 f_{s_i}^0, \phi_{p_j}^1 f_{p_j}^0) - (Q_{s_i}^{\text{in}0} + Q_{s_i}^{\text{re}0}),$$

$$s \in \mathcal{S}, \quad i \in \mathcal{I}_s. \quad (2.36)$$

The solvability condition for eq. (2.36) is obtained, as in sec. 2.3, by imposing the orthogonality of its right-hand-side with the elastic collision invariants (which satisfy the homogeneous equation $\mathcal{F}_{s_i}(\phi^2) = 0$):

$$\sum_{\substack{s \in \mathcal{S} \\ i \in \mathcal{I}_s}} \int_{\mathbb{R}^3} \psi_s^{\text{el}\nu} [\mathfrak{D}_{s_i} \phi_{s_i}^1 f_{s_i}^0 - (Q_{s_i}^{\text{in}0} + Q_{s_i}^{\text{re}0})] d\mathbf{c}_{s_i} = 0, \quad \nu \in \mathcal{I}^{\text{el}}. \quad (2.37)$$

Notice that the contribution of the elastic collision operators disappears in view of eq. (1.24). Combining eq. (2.37) with eq. (2.21), one obtains the first-order hydrodynamic equations:

$$\frac{\partial \rho_{s_i}}{\partial t} + \nabla_{\mathbf{x}} \cdot (\rho_{s_i} \mathbf{v} + \rho_{s_i} \mathbf{v}_{s_i}^d) = \omega_{s_i}, \quad s \in \mathcal{S}, \quad i \in \mathcal{I}_s, \quad (2.38)$$

$$\frac{\partial \rho \mathbf{v}}{\partial t} + \nabla_{\mathbf{x}} \cdot (\rho \mathbf{v} \otimes \mathbf{v} + p \mathbf{I} - \underline{\tau}) = \mathbf{0}_3, \quad (2.39)$$

$$\frac{\partial \rho E}{\partial t} + \nabla_{\mathbf{x}} \cdot (\rho \mathbf{v} H - \underline{\tau} \mathbf{v} + \mathbf{q}) = 0. \quad (2.40)$$

The transport fluxes and the mass production terms are:

$$\mathbf{v}_{s_i}^d = \frac{m_s}{\rho_{s_i}} \int_{\mathbb{R}^3} \mathbf{C}_{s_i} \phi_{s_i}^1 f_{s_i}^0 d\mathbf{c}_{s_i}, \quad s \in \mathcal{S}, \quad i \in \mathcal{I}_s, \quad (2.41)$$

$$\underline{\tau} = - \sum_{\substack{s \in \mathcal{S} \\ i \in \mathcal{I}_s}} \int_{\mathbb{R}^3} m_s \mathbf{C}_{s_i} \otimes \mathbf{C}_{s_i} \phi_{s_i}^1 f_{s_i}^0 d\mathbf{c}_{s_i} + p \mathbf{I} \quad (2.42)$$

$$\mathbf{q} = \sum_{\substack{s \in \mathcal{S} \\ i \in \mathcal{I}_s}} \int_{\mathbb{R}^3} \left(\frac{1}{2} m_s C_{s_i}^2 + E_{s_i} \right) \mathbf{C}_{s_i} \phi_{s_i}^1 f_{s_i}^0 d\mathbf{c}_{s_i}, \quad (2.43)$$

$$\omega_{s_i} = m_s \int_{\mathbb{R}^3} (Q_{s_i}^{\text{in}0} + Q_{s_i}^{\text{re}0}) d\mathbf{c}_{s_i}, \quad s \in \mathcal{S}, \quad i \in \mathcal{I}_s. \quad (2.44)$$

Equations (2.38)-(2.40) are the Navier-Stokes equations. Notice that, due to the assumed Maxwellian reaction regime, no influence of the first-order perturbation function $\phi_{s_i}^1$ appears in the mass production terms as opposed to the work of Giovangigli (1999), and Nagnibeda and Kustova (2009). In secs. 2.4.1-2.4.2, the expressions obtained for $f_{s_i}^0$ and $\phi_{s_i}^1$ are exploited to obtain constitutive relations which relate the transport fluxes to macroscopic gradients. In sec. 2.4.3, the mass production terms are particularized for the case of internal energy excitation and dissociation processes (studied in detail starting from ch. 3).

2.4.1 Transport Fluxes

The constitutive relations for the transport fluxes are obtained by substituting the expressions for $f_{s_i}^0$ and $\phi_{s_i}^1$ (given in eqs. (2.19) and (2.32), respectively) in eqs. (2.41)-(2.43). For the sake of convenience, a bracket operator is introduced:

$$[\![\xi, \zeta]\!] = \sum_{\substack{s \in \mathcal{S} \\ i \in \mathcal{I}_s}} \int_{\mathbb{R}^3} f_{s_i}^0 \xi_{s_i} \mathcal{F}_{s_i}(\zeta) d\mathbf{c}_{s_i}. \quad (2.45)$$

The bracket operator $[\![\xi, \zeta]\!]$ is symmetric, $[\![\xi, \zeta]\!] = [\![\zeta, \xi]\!]$, and positive semi-definite, $[\![\xi, \xi]\!] \geq 0$ (Ferziger and Kaper 1972). After some algebra, the diffusion

velocities, viscous stress tensor and heat flux vector are found to be:

$$\mathbf{v}_{s_i}^d = - \sum_{\substack{p \in \mathcal{S} \\ j \in \mathcal{I}_p}} D_{s_i p_j} \mathbf{d}_{p_j} - \theta_{s_i} \nabla_{\mathbf{x}} \ln T, \quad s \in \mathcal{S}, \quad i \in \mathcal{I}_s, \quad (2.46)$$

$$\underline{\tau} = \eta \left[\nabla_{\mathbf{x}} \mathbf{v} + (\nabla_{\mathbf{x}} \mathbf{v})^T - \frac{2}{3} \nabla_{\mathbf{x}} \mathbf{v} \mathbf{I} \right], \quad (2.47)$$

$$\mathbf{q} = \sum_{\substack{p \in \mathcal{S} \\ j \in \mathcal{I}_p}} \rho_{p_j} h_{p_j} \mathbf{v}_{p_j}^d - \lambda' \nabla_{\mathbf{x}} T - p \sum_{\substack{p \in \mathcal{S} \\ j \in \mathcal{I}_p}} \theta_{p_j} \mathbf{d}_{p_j}, \quad (2.48)$$

where the enthalpy of p_j reads $h_{p_j} = (5/2)(k_b T/m_p) + E_{p_j}$. Quantities $D_{s_i p_j}$ and θ_{s_i} are the diffusion coefficients and thermal diffusion coefficients, respectively, and quantities η and λ' are the shear (or dynamic) viscosity and the partial thermal conductivity, respectively. The aforementioned quantities can be expressed in a compact notation, by making use of the bracket operator defined in eq. (2.45):

$$D_{s_i p_j} = \frac{p k_b T}{3} [\![\phi^{D_{s_i}}, \phi^{D_{p_j}}]\!], \quad s, p \in \mathcal{S}, \quad i \in \mathcal{I}_s, \quad j \in \mathcal{I}_p, \quad (2.49)$$

$$\theta_{s_i} = -\frac{1}{3} [\![\phi^{D_{s_i}}, \phi^{\lambda'}]\!], \quad s \in \mathcal{S}, \quad i \in \mathcal{I}_s, \quad (2.50)$$

$$\eta = \frac{k_b T}{10} [\![\phi^\eta, \phi^\eta]\!], \quad (2.51)$$

$$\lambda' = \frac{1}{3 k_b T^2} [\![\phi^{\lambda'}, \phi^{\lambda'}]\!]. \quad (2.52)$$

The first term in the diffusion velocities (2.46) yields diffusion effects due to partial pressure gradients. The second term represents the diffusion arising from a temperature gradient (Soret effect). The constitutive relation for the stress tensor (2.47) is referred to as Newton's law for the stress tensor. Notice that there is no bulk (or volume) viscosity. This can be explained by the fact that, in the STS CE method, the gas is viewed as a collection of structureless particles having different values of formation energy (*i.e.* E_{s_i}). In the expression of the heat flux (2.48), the first term is the transfer of energy by diffusion of enthalpy. The second term represents Fourier's law and the third term corresponds to the Dufour effect, that is, heat diffusion due to partial pressure gradients. The partial thermal conductivity λ' is not accessible to direct experimental measurements since, in a multi-component gas, a temperature gradient induces thermal diffusion and partial pressure gradients. So, even in the case of a stationary process (*i.e.* the diffusion velocities all vanish if the gas is at rest), the driving forces \mathbf{d}_{s_i} will be different from zero, and the heat flow due to a temperature gradient will be always accompanied by a heat flow due to partial pressure gradients. In view of this, the following alternative definitions

for the diffusion velocities and heat flux vector are introduced:

$$\mathbf{v}_{si}^d = - \sum_{\substack{p \in \mathcal{S} \\ j \in \mathcal{I}_p}} D_{s_ip_j} (\mathbf{d}_{p_j} + \chi_{p_j} \nabla_{\mathbf{x}} \ln T), \quad s \in \mathcal{S}, \quad i \in \mathcal{I}_s, \quad (2.53)$$

$$\mathbf{q} = \sum_{\substack{p \in \mathcal{S} \\ j \in \mathcal{I}_p}} \rho_{p_j} h_{p_j} \mathbf{v}_{p_j}^d - \lambda \nabla_{\mathbf{x}} T + p \sum_{\substack{p \in \mathcal{S} \\ j \in \mathcal{I}_p}} \chi_{p_j} \mathbf{v}_{p_j}^d, \quad (2.54)$$

where the thermal diffusion ratios χ_{p_j} are defined from the relations:

$$\sum_{\substack{p \in \mathcal{S} \\ j \in \mathcal{I}_p}} \chi_{p_j} = 0, \quad \sum_{\substack{p \in \mathcal{S} \\ j \in \mathcal{I}_p}} D_{s_ip_j} \chi_{p_j} = \theta_{s_i}, \quad s \in \mathcal{S}, \quad i \in \mathcal{I}_s. \quad (2.55)$$

The thermal conductivity in eq. (2.54) is defined as $\lambda = \lambda' - n k_b \sum_{p \in \mathcal{S}, j \in \mathcal{I}_p} \chi_{p_j} \theta_{p_j}$. In order to be able to compute the transport fluxes, the bracketed expressions for the transport properties in eqs. (2.49)-(2.52) must be evaluated. The procedure is outlined in sec. 2.4.2.

2.4.2 Linear Transport Systems

The bracketed expressions in eqs. (2.49)-(2.52) are evaluated by solving the integral equations (2.33)-(2.35) based on a Galerkin method which uses Laguerre-Sonine polynomials as basis functions (Magin and Degrez 2004). This leads to linear transport systems which, upon solution, provide the shear viscosity, thermal conductivity, thermal diffusion ratios and diffusion velocities. The transport systems are assembled by assuming that the elastic cross-sections $\sigma_{s_ip_j}$ do not depend on the internal quantum states (*i.e.* $\sigma_{s_ip_j} = \sigma_{sp}$).

Shear Viscosity The shear viscosity is solution of the following transport system in the first-order Laguerre-Sonine approximation:

$$\sum_{p \in \mathcal{S}} G_{sp}^\eta \alpha_p^\eta = X_s, \quad s \in \mathcal{S}, \quad \eta = \sum_{p \in \mathcal{S}} \alpha_p^\eta X_p, \quad (2.56)$$

where G_{sp}^η are the entries of the multi-component viscosity transport (symmetric) matrix:

$$G_{sp}^\eta = X_s X_p \frac{16}{5} \sqrt{\frac{2m_s m_p}{k_b T (m_s + m_p)^3}} \left(\bar{Q}_{sp}^{(2,2)} - \frac{5}{3} \bar{Q}_{sp}^{(1,1)} \right), \quad (2.57)$$

$$p \neq s, \quad s, p \in \mathcal{S},$$

$$G_{ss}^\eta = \sum_{\substack{p \neq s \\ p \in \mathcal{S}}} X_s X_p \frac{16}{5} \sqrt{\frac{2m_s m_p}{k_b T (m_s + m_p)^3}} \left(\bar{Q}_{sp}^{(2,2)} \frac{m_p}{m_s} + \frac{5}{3} \bar{Q}_{sp}^{(1,1)} \right) + \frac{X_s^2}{\eta_s}, \quad (2.58)$$

$$s \in \mathcal{S},$$

$$\eta_s = \frac{5}{16} \frac{\sqrt{\pi k_b T m_s}}{\bar{Q}_{ss}^{(2,2)}}, \quad s \in \mathcal{S}, \quad (2.59)$$

where, obviously, $X_s = \sum_{i \in \mathcal{I}_s} X_{s_i}$. Quantities $\overline{Q}_{sp}^{(i,j)}$ are reduced collision integrals. Their definitions can be found in the books of Ferziger and Kaper (1972), and Giovangigli (1999). The reduced collision integrals can be computed based on the assumed interaction potential among the colliding gas particles.

Thermal Conductivity and Thermal Diffusion Ratios The thermal conductivity is solution of the following transport system in the second-order Laguerre-Sonine approximation:

$$\sum_{p \in \mathcal{S}} G_{sp}^\lambda \alpha_p^\lambda = X_s, \quad s \in \mathcal{S}, \quad \lambda = \sum_{p \in \mathcal{S}} \alpha_p^\lambda X_p, \quad (2.60)$$

where G_{sp}^λ are the entries of the multi-component thermal conductivity transport (symmetric) matrix:

$$G_{sp}^\lambda = \frac{1}{25k_b} \frac{X_s X_p}{n \mathcal{D}_{sp}} \frac{m_s m_p}{(m_s + m_p)^2} (16A_{sp}^* + 12B_{sp}^* - 55), \quad p \neq s, \quad s, p \in \mathcal{S}, \quad (2.61)$$

$$G_{ss}^\lambda = \frac{1}{25k_b} \sum_{\substack{p \neq s \\ p \in \mathcal{S}}} \frac{X_s X_p}{n \mathcal{D}_{sp}} \frac{(30m_s^2 + 25m_p^2 - 12m_p^2 B_{sp}^* + 16m_s m_p A_{sp}^*)}{(m_s + m_p)^2} + \frac{4}{15k_b} \frac{X_s^2 m_s}{\eta_s}, \quad s \in \mathcal{S}, \quad (2.62)$$

$$A_{sp}^* = \frac{\overline{Q}_{sp}^{(2,2)}}{\overline{Q}_{sp}^{(1,1)}}, \quad B_{sp}^* = \frac{5\overline{Q}_{sp}^{(1,2)} - 4\overline{Q}_{sp}^{(1,3)}}{\overline{Q}_{sp}^{(1,1)}}, \quad s, p \in \mathcal{S}, \quad (2.63)$$

where the binary diffusion coefficient \mathcal{D}_{sp} is defined as:

$$\mathcal{D}_{sp} = \frac{1}{n} \sqrt{\frac{2\pi k_b T (m_s + m_p)}{m_s m_p}} \frac{3}{16 \overline{Q}_{sp}^{(1,1)}}, \quad s, p \in \mathcal{S}. \quad (2.64)$$

The thermal diffusion ratios ($\chi_s = \sum_{i \in \mathcal{I}_s} \chi_{s_i}$) are:

$$\chi_s = \frac{5}{2} \sum_{p \in \mathcal{S}} \Lambda_{sp} \alpha_p^\lambda, \quad s \in \mathcal{S}, \quad (2.65)$$

where Λ_{sp} are the entries of the thermal diffusion (symmetric) matrix:

$$\Lambda_{sp} = \frac{1}{25k_b} \frac{X_s X_p}{n \mathcal{D}_{sp}} \frac{m_s}{(m_s + m_p)} (12C_{sp}^* - 10), \quad p \neq s, \quad s, p \in \mathcal{S}, \quad (2.66)$$

$$\Lambda_{ss} = -\frac{1}{25k_b} \sum_{\substack{p \neq s \\ p \in \mathcal{S}}} \frac{X_s X_p}{n \mathcal{D}_{sp}} \frac{m_p}{(m_s + m_p)} (12C_{sp}^* - 10), \quad s \in \mathcal{S}, \quad (2.67)$$

$$C_{sp}^* = \frac{\overline{Q}_{sp}^{(1,2)}}{\overline{Q}_{sp}^{(1,1)}}, \quad s, p \in \mathcal{S}. \quad (2.68)$$

Diffusion Velocities The diffusion velocities are solution of the Stefan-Maxwell equations with the mass conservation constraint (1.62). Under the assumption $\mathbf{v}_{s_i}^d = \mathbf{v}_s^d$, the Stefan-Maxwell equations are:

$$\sum_{p \in \mathcal{S}} G_{sp}^d \mathbf{v}_p^d = -\left(\hat{\mathbf{d}}_s + \chi_s \nabla_{\mathbf{x}} \ln T\right), \quad s \in \mathcal{S}, \quad (2.69)$$

$$\sum_{p \in \mathcal{S}} \rho_p \mathbf{v}_p^d = \mathbf{0}_3. \quad (2.70)$$

The linear independent diffusion driving forces are defined as $\hat{\mathbf{d}}_s = \mathbf{d}_s - (\rho_s/\rho) \sum_{p \in \mathcal{S}} \mathbf{d}_p$ (where $\mathbf{d}_p = \sum_{i \in \mathcal{I}_p} \mathbf{d}_{p_i}$). In the first-order Laguerre-Sonine approximation, the entries G_{sp}^d of the Stefan-Maxwell (symmetric) matrix are:

$$G_{sp}^d = -\frac{X_s X_p}{\mathcal{D}_{sp}}, \quad p \neq s, \quad s, p \in \mathcal{S}, \quad (2.71)$$

$$G_{ss}^d = \sum_{\substack{p \neq s \\ p \in \mathcal{S}}} \frac{X_s X_p}{\mathcal{D}_{sp}}, \quad s \in \mathcal{S}. \quad (2.72)$$

The Stefan-Maxwell matrix is singular. As suggested by Magin and Degrez (2004), the Stefan-Maxwell matrix can be regularized by incorporating the mass conservation constraint (1.62) in the definition of its entries:

$$\tilde{G}_{sp}^d = G_{sp}^d + \tilde{a} \rho_s \rho_p, \quad s, p \in \mathcal{S}, \quad (2.73)$$

where \tilde{a} is a dimensional factor, for instance equal to $1/[\rho^2 \max_{s,p \in \mathcal{S}} (\mathcal{D}_{sp})]$. The diffusion velocities are then found by solving the non-singular system:

$$\sum_{p \in \mathcal{S}} \tilde{G}_{sp}^d \mathbf{v}_p^d = -\left(\hat{\mathbf{d}}_s + \chi_s \nabla_{\mathbf{x}} \ln T\right), \quad s \in \mathcal{S}. \quad (2.74)$$

2.4.3 Mass Production Terms for Internal Energy Excitation and Dissociation

In this section explicit relations are obtained for the mass production terms in the case of the collisional processes considered in ch. 3: a) internal energy excitation/de-excitation, $s_i + p = s_j + p$ (with $i \neq j$), and b) three-body dissociation/recombination, $s_i + p = p + p + p$, where s is a diatomic molecule made of two p atoms (*i.e.* $s = p \cup p$) which remain always in the ground-state. The application of eq. (2.44) and the use of the contents of secs. 1.2.2-1.2.3, allows to write, after some algebra, the mass production term ω_{s_i} as:

$$\omega_{s_i} = -(\omega_{s_i}^{\text{dis}} + \omega_{s_i}^{\text{in}}), \quad s \in \mathcal{S}, \quad i \in \mathcal{I}_s, \quad (2.75)$$

where the partial contributions due to dissociation and inelastic collisional excitation are:

$$\omega_{s_i}^{\text{dis}} = m_s n_p [n_{s_i} k_{s_i}^{\text{dis}}(T) - n_p^2 k_{s_i}^{\text{rec}}(T)], \quad (2.76)$$

$$\begin{aligned} \omega_{s_i}^{\text{in}} &= m_s n_p \sum_{\substack{j > i \\ j \in \mathcal{I}_s}} [n_{s_i} k_{s_i \rightarrow s_j}^{\text{in}}(T) - n_{s_j} k_{s_j \rightarrow s_i}^{\text{in}}(T)] - \\ &\quad m_s n_p \sum_{\substack{j < i \\ j \in \mathcal{I}_s}} [n_{s_j} k_{s_j \rightarrow s_i}^{\text{in}}(T) - n_{s_i} k_{s_i \rightarrow s_j}^{\text{in}}(T)], \end{aligned} \quad (2.77)$$

$$s \in \mathcal{S}, \quad i \in \mathcal{I}_s.$$

The dissociation and excitation rate coefficients ($k_{s_i}^{\text{dis}}(T)$ and $k_{s_i \rightarrow s_j}^{\text{in}}(T)$, with $i < j$, respectively) are defined as:

$$\begin{aligned} k_{s_i}^{\text{dis}}(T) &= \frac{1}{\beta_s \beta_p Z_s^{\text{tra}}(T) Z_p^{\text{tra}}(T)} \times \\ &\quad \iiint_{\mathcal{S}^2 \times \mathbb{R}^3 \times \mathbb{R}^3} \exp [-(m_s C_{s_i}^2 + m_p C_p^2)/(2k_b T)] \sigma_{s_i p}^{ppp} g d\omega' d\mathbf{C}_p d\mathbf{C}_{s_i}, \end{aligned} \quad (2.78)$$

$$s \in \mathcal{S}, \quad i \in \mathcal{I}_s,$$

$$\begin{aligned} k_{s_i \rightarrow s_j}^{\text{in}}(T) &= \frac{1}{\beta_s \beta_p Z_s^{\text{tra}}(T) Z_p^{\text{tra}}(T)} \times \\ &\quad \iiint_{\mathcal{S}^2 \times \mathbb{R}^3 \times \mathbb{R}^3} \exp [-(m_s C_{s_i}^2 + m_p C_p^2)/(2k_b T)] \sigma_{s_i p}^{s_j p} g d\omega' d\mathbf{C}_p d\mathbf{C}_{s_i}, \end{aligned} \quad (2.79)$$

$$s \in \mathcal{S}, \quad i < j, \quad i, j \in \mathcal{I}_s,$$

where the relation $d\mathbf{c}_{s_i} = d\mathbf{C}_{s_i}$ has been used. The recombination and de-excitation rate coefficients ($k_{s_i}^{\text{rec}}(T)$ and $k_{s_j \rightarrow s_i}^{\text{in}}(T)$, with $i < j$, respectively) are related to the dissociation and excitation rate coefficients through:

$$\frac{k_{s_i}^{\text{rec}}(T)}{k_{s_i}^{\text{dis}}(T)} = \frac{a_{s_i} Z_s^{\text{tra}}(T)}{[a_p Z_p^{\text{tra}}(T)]^2} \exp \left(\frac{2E_p - E_{s_i}}{k_b T} \right), \quad s \in \mathcal{S}, \quad i \in \mathcal{I}_s, \quad (2.80)$$

$$\frac{k_{s_j \rightarrow s_i}^{\text{in}}(T)}{k_{s_i \rightarrow s_j}^{\text{in}}(T)} = \frac{a_{s_i}}{a_{s_j}} \exp \left(\frac{E_{s_j} - E_{s_i}}{k_b T} \right), \quad s \in \mathcal{S}, \quad i < j, \quad i, j \in \mathcal{I}_s, \quad (2.81)$$

where quantity E_p is the formation energy of the p atom. Equations (2.80)-(2.81) (usually referred to as detailed balance relations) are obtained from the algebraic manipulation leading to eqs. (2.75)-(2.79) and are direct consequence of the micro-reversibility relations (1.12) and (1.21).

2.4.4 Conservation Law Form of the Navier-Stokes Equations

For the sake of later use, it is convenient to close this chapter by stating the conservation law form of the Navier-Stokes equations (2.38)-(2.40) together

with the constitutive relations obtained from the application of the STS CE method. The Navier-Stokes equations in conservation law form read:

$$\frac{\partial \mathbf{U}}{\partial t} + \nabla_{\mathbf{x}} \cdot \underline{\mathcal{F}} - \nabla_{\mathbf{x}} \cdot \underline{\mathcal{F}}^d = \mathbf{S}, \quad (2.82)$$

where the conservative variable and source term vectors, and the inviscid and diffusive flux tensors are:

$$\mathbf{U} = [\rho_{s_i} \quad \rho \mathbf{v} \quad \rho E]^T, \quad (2.83)$$

$$\mathbf{S} = [\omega_{s_i} \quad \mathbf{0}_3 \quad 0]^T, \quad (2.84)$$

$$\underline{\mathcal{F}} = [\rho_{s_i} \mathbf{v} \quad \rho \mathbf{v} \otimes \mathbf{v} + p \mathbf{I} \quad \rho \mathbf{v} H]^T, \quad (2.85)$$

$$\underline{\mathcal{F}}^d = [-\rho_{s_i} \mathbf{v}_s^d \quad \underline{\tau} \quad \underline{\tau} \mathbf{v} - \mathbf{q}]^T, \quad (2.86)$$

$$s \in \mathcal{S}, \quad i \in \mathcal{I}_s.$$

The constitutive relations for the stress tensor and heat flux vector are:

$$\underline{\tau} = \eta \left[\nabla_{\mathbf{x}} \mathbf{v} + (\nabla_{\mathbf{x}} \mathbf{v})^T - \frac{2}{3} \nabla_{\mathbf{x}} \mathbf{v} \mathbf{I} \right], \quad (2.87)$$

$$\mathbf{q} = \sum_{s \in \mathcal{S}} \mathbf{v}_s^d \sum_{i \in \mathcal{I}_s} \rho_{s_i} h_{s_i} - \lambda \nabla_{\mathbf{x}} T + p \sum_{s \in \mathcal{S}} \chi_s \mathbf{v}_s^d. \quad (2.88)$$

2.5 Summary

In this chapter a hydrodynamic description for multi-component gases with discrete internal energy levels has been obtained based on the Chapman-Enskog method for the Boltzmann equation. In order to avoid problems related to hierarchy of time-scales for inelastic and reactive processes, which must be accounted for when deriving macroscopic models such as multi-temperature, an alternative state-to-state approach has been proposed (State-to-State Chapman-Enskog method; STS CE). The final goal of the STS CE method was to obtain a set of hydrodynamic equations where each internal energy level is considered as a separate pseudo-species. Once this done, reduced models can be developed based on the state-to-state hydrodynamic equations, as shown in ch. 3. The proposed approach has the advantage of avoiding the splitting of the inelastic and reactive collision operators in fast and slow components. The STS CE method relies on the assumption that elastic collisions occur over much shorter time-scales, compared to inelastic and reactive ones (a realistic assumption for aerothermodynamic flows), and that inelastic and reactive encounters can be treated within the context of a Maxwellian reaction regime. Based on these assumptions, the Boltzmann equation has been properly rescaled (with the aid of a dimensional analysis) to look for a truncated series solution. Asymptotic zeroth and first-order solutions have been then obtained by injecting the truncated series solution in the rescaled Boltzmann equation and by applying

a procedure similar to the conventional CE method. The zeroth-order solution consisted in a Maxwell-Boltzmann velocity distribution function (only for translation) at the translational temperature. The zeroth-order solution was then used for obtaining the first-order perturbation which, in turn, enabled to obtain the Navier-Stokes equations with explicit constitutive relations for the transport fluxes and the mass production terms.

The Navier-Stokes equations obtained in this chapter are applicable to multi-component gases with discrete internal energy levels, where elastic, inelastic and reactive collisions occur. In ch. 3, the focus is restricted on a narrower set of processes (internal energy excitation and dissociation), and the governing equations obtained here are used for developing reduced models for aerothermodynamics.

Chapter 3

Development of Quantum Based Chemical Models

This chapter describes a quantum chemistry database of the Computational Quantum Chemistry Group at NASA Ames Research Center (NASA ARC) and the reduced (or coarse-grained) models developed in this thesis.

The present chapter is structured as follows. The thermodynamic and kinetic data of the NASA ARC database are described in sec. 3.1. These are used to build a rovibrational collisional model. Then, reduced models are proposed by increasing complexity. Section 3.2 describes a multi-temperature model which has been developed based on heat-bath calculations (Panesi et al. 2013). After that, a conventional vibrational collisional model is formulated in sec. 3.3 based on the assumption of rotational equilibrium (Bourdon et al. 2008; Magin et al. 2009, Munafò et al. 2010; 2012). In sec. 3.4, the Energy Bin model is presented. This is developed based on an innovative approach which consists in lumping the energy levels in energy bins, where a distribution of the energy levels is assumed. Two variants of the Energy Bin model have been proposed, corresponding to a uniform (Panesi et al. 2010; Magin et al. 2012) and a Boltzmann (Munafò et al. 2011; 2014) distribution. The chapter is concluded with sec. 3.5, where a unified notation for the coarse-grained models is presented.

3.1 The NASA Ames Database

The NASA ARC database (Jaffe et al. 2008; Chaban et al. 2008; Schwenke 2008; Jaffe et al. 2009) provides a set of consistent thermodynamic and state-to-state kinetics data for the rovibrational excitation, dissociation and predissociation of the N₂ molecule colliding with an N atom. Both chemical components are in their electronic ground-state (*i.e.* N₂(¹Σ_g⁺) - N(⁴S_u) system). The database provides also kinetic data for a small portion of all the possible rovibrational transitions for the N₂(¹Σ_g⁺)-N₂(¹Σ_g⁺) system (Panesi et al. 2013). These have not been taken into account in the present thesis.

3.1.1 Thermodynamics

The chemical component set introduced in ch. 1 is $\mathcal{S} = \{\text{N}, \text{N}_2\}$. Since both N and N₂ are in their electronic ground-state, no electronic energy is considered (unlike in existing electronic specific collisional models; Panesi et al. 2011; Annaloro and Bultel 2013). Hence, only the rovibrational energy level set of N₂ (\mathcal{I}_{N_2}) is needed, and quantity E_{N} coincides with the formation energy of N. The number of rovibrational energy levels N₂(v, J) of the electronic ground-state of N₂ is 9390, where the indices v and J stand for the vibrational and rotational quantum numbers, respectively. The energy of a given (v, J) level can be written as the sum of the vibrational and rotational contributions:

$$E_{vJ} = \tilde{E}_v + \Delta\tilde{E}_v(J), \quad v \in \mathcal{V}_{\text{N}_2}, \quad J \in \mathcal{J}_v, \quad (3.1)$$

where $\mathcal{V}_{\text{N}_2} = \{0, \dots, v_{\max}\}$ is the set storing the vibrational quantum numbers and $\mathcal{J}_v = \{0, \dots, J_{\max}(v)\}$ is the set storing the rotational quantum numbers for a given vibrational quantum state. The vibrational energy \tilde{E}_v is defined as the energy of the rotationless level ($J = 0$) having vibrational quantum number v . The rotational energy is defined based on the vibrational energy as $\Delta\tilde{E}_v(J) = E_{vJ} - \tilde{E}_v$. The energy splitting adopted in eq. (3.1) is arbitrary defined and other choices are possible (Jaffe 1987). The degeneracy a_{vJ} of the rovibrational energy levels is:

$$a_{vJ} = (2J + 1) a_{vJ}^{\text{NS}}, \quad a_{vJ}^{\text{NS}} = \begin{cases} 6 & \text{even } J \\ 3 & \text{odd } J \end{cases}, \quad v \in \mathcal{V}_{\text{N}_2}, \quad J \in \mathcal{J}_v. \quad (3.2)$$

Quantity a_{vJ}^{NS} is the nuclear spin degeneracy of N₂. Its dependence on the rotational quantum number J is due to the fact that the total wave function of N₂ must be symmetric with respect to exchanging the nuclei (Bose-Einstein statistics; Jaffe et al. 2008; Chaban et al. 2008; Schwenke 2008; Jaffe et al. 2009). The number of vibrational energy levels is 61 ($v_{\max} = 60$) and for the vibrational ground-state ($v = 0$) the maximum rotational quantum number is 279. Most of the rovibrational levels (7421) are bound (B). This means that their energy is lower than the dissociation energy relative to the ($v = 0, J = 0$) level, equal to 9.75 eV. The remaining levels are predissociated (P), or quasi-bound. Thus, their energy is higher than the dissociation energy relative to the level ($v = 0, J = 0$), but lower than the J dependent centrifugal barrier (Jaffe 1987). All the rotationless levels ($J = 0$) are bound. The numerical values of the rovibrational energy levels have been obtained by applying the Wentzel-Kramers-Brillouin (WKB) approximation (Schwenke 1988) using the potential for N₂(¹ Σ_g^+) developed by Le Roy et al. (2006).

In some situations (see sec. 3.4), it is more convenient to represent the rovibrational energy levels by adopting the storage scheme of the set \mathcal{I}_{N_2} (*i.e.* by sorting them by increasing energy) and denoting them by means of a global index i . The correspondence between the i and (v, J) notations can be expressed

as:

$$i = i(v, J), \quad v \in \mathcal{V}_{N_2}, \quad J \in \mathcal{J}_v, \quad (3.3)$$

and conversely by the relations:

$$v = v(i), \quad J = J(i), \quad i \in \mathcal{I}_{N_2}. \quad (3.4)$$

When the i notation is used, the degeneracy of the rovibrational energy level i is written as $a_i = (2J(i) + 1) a_i^{\text{NS}}$.

For the sake of later convenience, it is useful to introduce the subsets $\mathcal{I}_{N_2}^B$ and $\mathcal{I}_{N_2}^P$ storing, respectively, the bound and the predissociated rovibrational energy levels of N_2 , and the subsets \mathcal{J}_v^B and \mathcal{J}_v^P storing, respectively, the bound and predissociated rotational levels of the vibrational level v . These satisfy the relations $\mathcal{I}_{N_2}^B \cup \mathcal{I}_{N_2}^P = \mathcal{I}_{N_2}$, $\mathcal{I}_{N_2}^B \cap \mathcal{I}_{N_2}^P = \emptyset$, $\mathcal{J}_v^B \cup \mathcal{J}_v^P = \mathcal{J}_v$ and $\mathcal{J}_v^B \cap \mathcal{J}_v^P = \emptyset$. Before concluding this section, it is instructive to investigate the thermodynamic data of the NASA ARC database in more detail. Figure 3.1 shows how the rotational levels are distributed across the vibrational ladder. The number of rotational levels per each vibrational state decreases when increasing the vibrational quantum number.

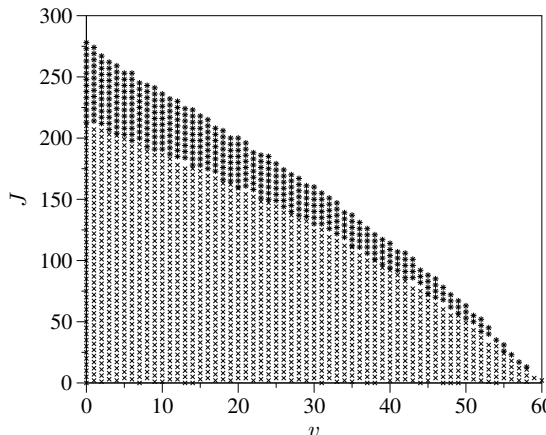


Figure 3.1: Rotational structure of the vibrational levels of $N_2(^1\Sigma_g^+)$ (one level over four is plotted; crosses bound levels, stars predissociated levels).

Figure 3.2 shows the vibrational and rotational spacings, defined as $(\tilde{E}_{v+1} - \tilde{E}_v)/k_B$ and $(\Delta\tilde{E}_v(J+1) - \Delta\tilde{E}_v(J))/k_B$, respectively. The decrease of the vibrational spacing (fig. 3.2(a)) when increasing the vibrational quantum number is a clear indication of anharmonicity effects starting from the first excited vibrational level. At low energies, the rotational spacing for the vibrational ground-state (fig. 3.2(b)) behaves linearly as in the Rigid-Rotor (RR) model (Pauling and Wilson Jr. 1985). Non-linearities appear for high-lying rotational levels when approaching the J dependent centrifugal barrier.

Figure 3.3 shows the equilibrium internal energy and constant volume specific heat of $\text{N}_2(^1\Sigma_g^+)$, obtained based on eqs. (1.43) and (1.47), respectively:

$$e_{\text{N}_2}^{\text{int}}(T^{\text{eq}}) = \frac{k_b T^{\text{eq}}}{m_{\text{N}_2}} \frac{\partial \ln Z_{\text{N}_2}^{\text{int}}(T^{\text{eq}})}{\partial T^{\text{eq}}}, \quad c_v^{\text{int}}_{\text{N}_2}(T^{\text{eq}}) = \frac{de_{\text{N}_2}^{\text{int}}(T^{\text{eq}})}{dT^{\text{eq}}}, \quad (3.5)$$

where the internal partition function is computed based on eq. (1.35), $Z_{\text{N}_2}^{\text{int}}(T^{\text{eq}}) = \sum_{i \in \mathcal{I}_{\text{N}_2}} a_i \exp(-E_i/k_b T^{\text{eq}})$.

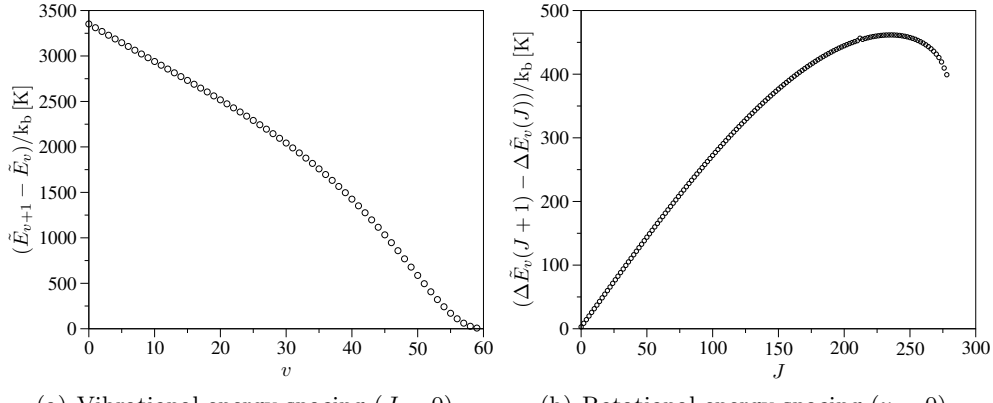


Figure 3.2: Vibrational and rotational energy spacings of $\text{N}_2(^1\Sigma_g^+)$.

In fig. 3.3 the internal energy and specific heat values obtained based on the Rigid-Rotor and Harmonic-Oscillator (RR-HO) models are also shown (Pauling and Wilson Jr. 1985). The comparison confirms that the RR-HO approximation works well at low temperatures, while it becomes inaccurate at high temperatures (in particular for the specific heat).

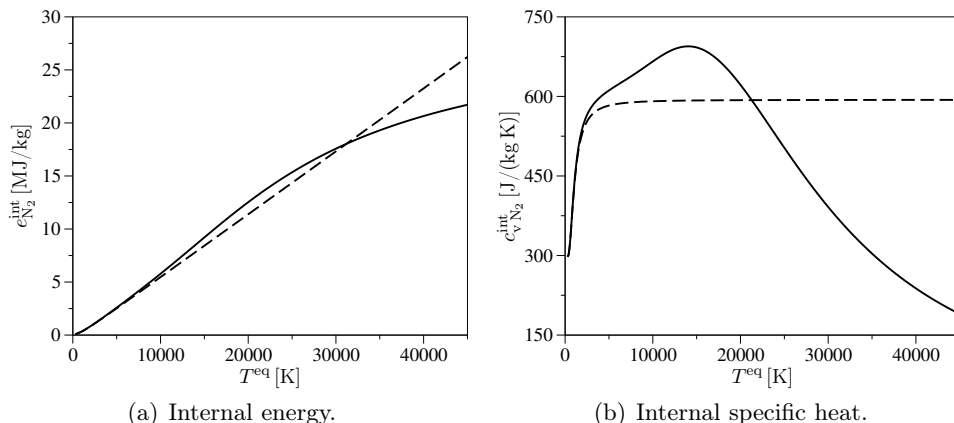
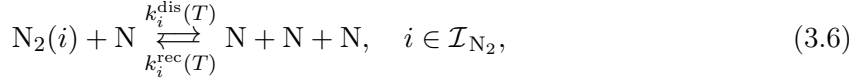


Figure 3.3: Internal energy and specific heat of $\text{N}_2(^1\Sigma_g^+)$ (unbroken lines NASA ARC, dashed lines RR-HO).

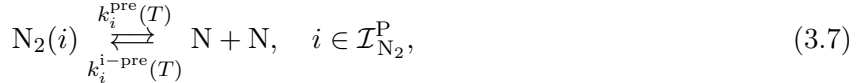
3.1.2 Rate Coefficients

The NASA ARC database for the $\text{N}_2(^1\Sigma_g^+)$ - $\text{N}(^4\text{S}_u)$ system provides more than 20×10^6 rate coefficients for the following processes:

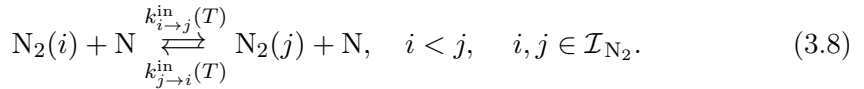
- Collisional dissociation of bound and predissociated levels:



- Predissociation, or tunneling, of predissociated levels:



- Inelastic collisional excitation among all levels:



The excitation rate coefficient $k_{i \rightarrow j}^{\text{in}}(T)$ (with $i < j$) accounts for the contribution of both inelastic (non-reactive) and exchange processes:

$$k_{i \rightarrow j}^{\text{in}}(T) = k_{i \rightarrow j}^{\text{in-in}}(T) + k_{i \rightarrow j}^{\text{in-exc}}(T), \quad i < j, \quad i, j \in \mathcal{I}_{\text{N}_2}. \quad (3.9)$$

The first term $k_{i \rightarrow j}^{\text{in-in}}(T)$ represents the contribution of the inelastic process, where the kinetic energy is transferred into internal energy during the collision. The second term $k_{i \rightarrow j}^{\text{in-exc}}(T)$ represents the contribution of the exchange process. In this situation, the transfer between kinetic and internal energies occurs via substitution of one bounded atom of the molecule with the colliding partner. The importance of the exchange process has been assessed and studied by Panesi et al. (2013) based on heat-bath calculations.

The rate coefficients for the exothermic processes ($k_i^{\text{rec}}(T)$, $k_i^{i-\text{pre}}(T)$ and $k_{j \rightarrow i}^{\text{in}}(T)$, with $i < j$, respectively) are computed based on micro-reversibility:

$$\frac{k_i^{\text{rec}}(T)}{k_i^{\text{dis}}(T)} = \frac{a_i Z_{\text{N}_2}^{\text{tra}}(T)}{[a_N Z_{\text{N}}^{\text{tra}}(T)]^2} \exp\left(\frac{2E_{\text{N}} - E_i}{k_b T}\right), \quad i \in \mathcal{I}_{\text{N}_2}, \quad (3.10)$$

$$\frac{k_i^{i-\text{pre}}(T)}{k_i^{\text{pre}}(T)} = \frac{a_i Z_{\text{N}_2}^{\text{tra}}(T)}{[a_N Z_{\text{N}}^{\text{tra}}(T)]^2} \exp\left(\frac{2E_{\text{N}} - E_i}{k_b T}\right), \quad i \in \mathcal{I}_{\text{N}_2}^P, \quad (3.11)$$

$$\frac{k_{j \rightarrow i}^{\text{in}}(T)}{k_{i \rightarrow j}^{\text{in}}(T)} = \frac{a_i}{a_j} \exp\left(\frac{E_j - E_i}{k_b T}\right), \quad i < j, \quad i, j \in \mathcal{I}_{\text{N}_2}. \quad (3.12)$$

The degeneracy of N is $a_N = 12$ (nuclear and electronic spin contributions). The translational partition functions of N and N_2 are obtained based on eq. (1.35):

$$Z_{\text{N}}^{\text{tra}}(T) = \left(\frac{2\pi m_{\text{N}} k_b T}{h_p^2}\right)^{3/2}, \quad Z_{\text{N}_2}^{\text{tra}}(T) = \left(\frac{2\pi m_{\text{N}_2} k_b T}{h_p^2}\right)^{3/2}. \quad (3.13)$$

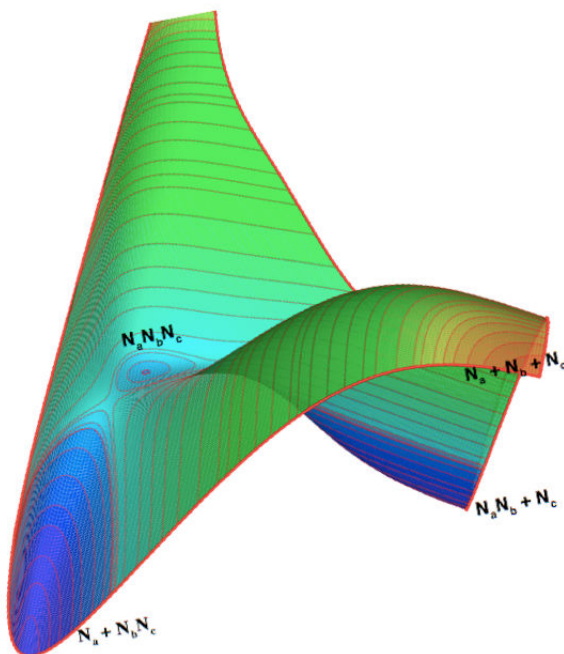


Figure 3.4: Analytical fit of the N_3 PES with the $\text{N} - \text{N} - \text{N}$ angle constrained to 115° . Blue regions have low energy and orange/red regions have high energy. The potential energy minima corresponding to $\text{N}_a + \text{N}_b\text{N}_c$ and $\text{N}_a\text{N}_b + \text{N}_c$ are shown. These arrangements are connected by a reaction path for the exchange reaction which has a barrier and shallow minimum labeled $\text{N}_a\text{N}_b\text{N}_c$ (credits NASA Ames Research Center).

Numerical values for the rate coefficients have been obtained by integrating over a Maxwell-Boltzmann distribution function (for the translational energy) the cross-sections computed by applying the following two-step procedure:

- Generation of the N_3 Potential Energy Surface (PES) based on first principle quantum-chemistry calculations (Jaffe et al. 2008; Schwenke 2008). The N_3 PES provides a representation of the potential energy of three nitrogen atoms in any arbitrary arrangement and geometry. For example, if the N atoms are labeled N_a , N_b and N_c (as in fig. 3.4), the PES describes the N_aN_b , N_aN_c and N_bN_c dinitrogen molecules, separated atoms ($\text{N}_a + \text{N}_b + \text{N}_c$) and a possible triatomic complex ($\text{N}_a\text{N}_b\text{N}_c$ and its permutations). If one considers the collision between $\text{N}_a\text{N}_b(v, J)$ and N_c , the possible outcomes are $\text{N}_a\text{N}_b(v', J') + \text{N}_c$, $\text{N}_a\text{N}_c(v', J') + \text{N}_b$, $\text{N}_b\text{N}_c(v', J') + \text{N}_a$ and $\text{N}_a + \text{N}_b + \text{N}_c$. The first is a non reactive inelastic collision and the last is a dissociation reaction. The other two outcomes represent an exchange reaction (see eq. (3.9)), where the atoms comprising the final molecule are different from the initial molecule.
- Application of the Quasi-Classical Trajectory (QCT) method (Park 1990) in order to compute cross-sections.

Rate coefficients are available at nine values of the gas translational temperature: 7500, 10 000, 12 500, 15 000, 20 000, 25 000, 30 000, 40 000 and 50 000 K. The total number of possible combinations for the collisional excitation process (3.7) is around 44×10^6 . However, due to the stochastic nature of the QCT method, only 19×10^6 excitation rate coefficients are available. An accurate investigation of the kinetic data revealed that most of the missing rate coefficients refer both to processes that have a small transition probability (*i.e.* $j >> i$ in eq. (3.7)) or to processes that are quantum-mechanically forbidden (*i.e.* inelastic collisions for which the rotation quantum number variation $|J(j) - J(i)|$ is odd). Hence, the missing kinetic data refer to processes that have a small (or no) effect on the energy level dynamics. It is worth to mention that in the database both endothermic and exothermic rate coefficients are found. The number of exothermic rate coefficients (13.5×10^6) is higher than the number of endothermic rate coefficients (7.1×10^6). For a small number of processes (1.5×10^6), both rate coefficients are available. In order to use only endothermic rate coefficients in the calculations, exothermic rate coefficients are inverted by means of micro-reversibility. For those processes for which both types of rate coefficients are available, exothermic rate coefficients are preferentially used (Panesi et al. 2013) and the corresponding endothermic rate coefficients are found via micro-reversibility.

3.1.3 Rovibrational Collisional Model

In this section the thermodynamic and kinetic data of the NASA ARC database (described in secs. 3.1.1-3.1.2) are used to develop a rovibrational collisional (RVC) model for the $\text{N}_2(^1\Sigma_g^+)$ - $\text{N}(^4\text{S}_u)$ system. The set of master of equations is written for a homogeneous and isochoric system. This is done because the proposed reduced models (presented in secs. 3.2-3.4) are based on a kinetic mechanism reduction which is not dependent on the presence of convective and/or diffusive fluxes. The RVC model is presented for both the i and (v, J) notations.

i Notation

Master Equations The master equations for the RVC model are obtained from the Navier-Stokes equations (2.82) by neglecting the convective and diffusive flux terms, and by setting the flow velocity to zero. The final set of equations comprises the continuity equations for N and the rovibrational energy levels of N_2 , and the global energy conservation equation:

$$\frac{\partial}{\partial t} \begin{pmatrix} \rho_N \\ \rho_i \\ \rho_e \end{pmatrix} = \begin{pmatrix} \omega_N \\ \omega_i \\ 0 \end{pmatrix}, \quad i \in \mathcal{I}_{\text{N}_2}. \quad (3.14)$$

Mass Production Terms The mass production terms for N and the rovibrational energy levels of N₂ are:

$$\omega_N = \sum_{i \in \mathcal{I}_{N_2}} \omega_i^{\text{dis}} + \sum_{i \in \mathcal{I}_{N_2}^P} \omega_i^{\text{pre}}, \quad (3.15)$$

$$\omega_i = - \begin{cases} (\omega_i^{\text{dis}} + \omega_i^{\text{in}}), & i \in \mathcal{I}_{N_2}^B, \\ (\omega_i^{\text{dis}} + \omega_i^{\text{pre}} + \omega_i^{\text{in}}), & i \in \mathcal{I}_{N_2}^P, \end{cases} \quad (3.16)$$

where the partial production terms due to dissociation, predissociation and inelastic collisional excitation are:

$$\omega_i^{\text{dis}} = m_{N_2} n_N \left[n_i k_i^{\text{dis}}(T) - n_N^2 k_i^{\text{rec}}(T) \right], \quad i \in \mathcal{I}_{N_2}, \quad (3.17)$$

$$\omega_i^{\text{pre}} = m_{N_2} \left[n_i k_i^{\text{pre}}(T) - n_N^2 k_i^{\text{i-pre}}(T) \right], \quad i \in \mathcal{I}_{N_2}^P, \quad (3.18)$$

$$\begin{aligned} \omega_i^{\text{in}} = m_{N_2} n_N \sum_{\substack{j > i \\ j \in \mathcal{I}_{N_2}}} & [n_i k_{i \rightarrow j}^{\text{in}}(T) - n_j k_{j \rightarrow i}^{\text{in}}(T)] - \\ m_{N_2} n_N \sum_{\substack{j < i \\ j \in \mathcal{I}_{N_2}}} & [n_j k_{j \rightarrow i}^{\text{in}}(T) - n_i k_{i \rightarrow j}^{\text{in}}(T)], \quad i \in \mathcal{I}_{N_2}. \end{aligned} \quad (3.19)$$

The rate coefficients in eqs. (3.17)-(3.19) are computed as explained in sec. 3.1.2.

Thermodynamic Properties The gas number density is obtained by summing the contributions of N and N₂, and its pressure follows from the application of Dalton's law of partial pressures:

$$n = n_N + n_{N_2}, \quad p = n_N k_b T + n_{N_2} k_b T, \quad (3.20)$$

where the N₂ number density is computed as $n_{N_2} = \sum_{i \in \mathcal{I}_{N_2}} n_i$. The gas thermal energy density is obtained by summing the translational and formation energy of N, and the translational and internal energy of the rovibrational energy levels of N₂:

$$\rho e = \frac{3}{2} n k_b T + n_N E_N + \sum_{i \in \mathcal{I}_{N_2}} n_i E_i. \quad (3.21)$$

(v, J) Notation

Master Equations The master equations for the (v, J) notation can be obtained based on that for the i notation (3.14) through the use of the correspondence relations given in eq. (3.4):

$$\frac{\partial}{\partial t} \begin{pmatrix} \rho_N \\ \rho_{vJ} \\ \rho e \end{pmatrix} = \begin{pmatrix} \omega_N \\ \omega_{vJ} \\ 0 \end{pmatrix}, \quad v \in \mathcal{V}_{N_2}, \quad J \in \mathcal{J}_v. \quad (3.22)$$

Mass Production Terms The mass production terms for N and the rovibrational energy levels of N₂ are:

$$\omega_N = \sum_{\substack{v \in \mathcal{V}_{N_2} \\ J \in \mathcal{J}_v}} \omega_{vJ}^{\text{dis}} + \sum_{\substack{v \in \mathcal{V}_{N_2} \\ J \in \mathcal{J}_v^P}} \omega_{vJ}^{\text{pre}}, \quad (3.23)$$

$$\omega_{vJ} = - \begin{cases} (\omega_{vJ}^{\text{dis}} + \omega_{vJ}^{\text{in}}), & v \in \mathcal{V}_{N_2}, \quad J \in \mathcal{J}_v^B, \\ (\omega_{vJ}^{\text{dis}} + \omega_{vJ}^{\text{pre}} + \omega_{vJ}^{\text{in}}), & v \in \mathcal{V}_{N_2}, \quad J \in \mathcal{J}_v^P, \end{cases} \quad (3.24)$$

where the partial production terms for the (v, J) level due to dissociation, predissociation and inelastic collisional excitation are:

$$\omega_{vJ}^{\text{dis}} = m_{N_2} n_N \left[n_{vJ} k_{vJ}^{\text{dis}}(T) - n_N^2 k_{vJ}^{\text{rec}}(T) \right], \quad v \in \mathcal{V}_{N_2}, \quad J \in \mathcal{J}_v, \quad (3.25)$$

$$\omega_{vJ}^{\text{pre}} = m_{N_2} \left[n_{vJ} k_{vJ}^{\text{pre}}(T) - n_N^2 k_{vJ}^{\text{i-pre}}(T) \right], \quad v \in \mathcal{V}_{N_2}, \quad J \in \mathcal{J}_v^P, \quad (3.26)$$

$$\begin{aligned} \omega_{vJ}^{\text{in}} = m_{N_2} n_N & \sum_{\substack{w > v \\ w \in \mathcal{V}_{N_2}}} \sum_{Y \in \mathcal{J}_w} [n_{vJ} k_{vJ \rightarrow wY}^{\text{in}}(T) - n_{wY} k_{wY \rightarrow vJ}^{\text{in}}(T)] + \\ & m_{N_2} n_N \sum_{\substack{Y > J \\ Y \in \mathcal{J}_v}} [n_{vJ} k_{vJ \rightarrow vY}^{\text{in}}(T) - n_{vY} k_{vY \rightarrow vJ}^{\text{in}}(T)] - \\ & m_{N_2} n_N \sum_{\substack{w < v \\ w \in \mathcal{V}_{N_2}}} \sum_{Y \in \mathcal{J}_w} [n_{wY} k_{wY \rightarrow vJ}^{\text{in}}(T) - n_{vJ} k_{vJ \rightarrow wY}^{\text{in}}(T)] - \\ & m_{N_2} n_N \sum_{\substack{Y < J \\ Y \in \mathcal{J}_v}} [n_{vY} k_{vY \rightarrow vJ}^{\text{in}}(T) - n_{vJ} k_{vJ \rightarrow vY}^{\text{in}}(T)], \end{aligned} \quad (3.27)$$

$$v \in \mathcal{V}_{N_2}, \quad J \in \mathcal{J}_v.$$

The rate coefficients in eqs. (3.25)-(3.27) are computed as explained in sec. 3.1.2 (after applying the conversion relations given in eq. (3.4)).

Thermodynamic Properties The gas number density and pressure are computed based on eq. (3.20), where the number density of N₂ is now written as:

$$n_{N_2} = \sum_{\substack{v \in \mathcal{V}_{N_2} \\ J \in \mathcal{J}_v}} n_{vJ}. \quad (3.28)$$

When using the (v, J) notation, the gas thermal energy density assumes the following expression:

$$\rho e = \frac{3}{2} n k_b T + n_N E_N + \sum_{\substack{v \in \mathcal{V}_{N_2} \\ J \in \mathcal{J}_v}} n_{vJ} \left[\tilde{E}_v + \Delta \tilde{E}_v(J) \right]. \quad (3.29)$$

The first and second terms in the sum in eq. (3.29) represent, respectively, the gas vibrational and rotational energy densities according to the energy level splitting given in eq. (3.1).

3.2 Multi-Temperature Model

The most intuitive way for developing a multi-temperature (MT) model for the $\text{N}_2(^1\Sigma_g^+) - \text{N}(^4S_u)$ system would be to assume a Boltzmann distribution (at its own temperature) for the internal energy modes of N_2 and take the zero and first-order moments of the production terms (3.15)-(3.16) and (3.23)-(3.24). This would reduce the set of master equations (3.14) and (3.22) to the continuity equations for N and N_2 , the global energy conservation equation, and additional energy conservation equations for the internal energy modes of N_2 . The macroscopic dissociation rate coefficient would be a function of multiple temperatures. Instead of using this approach, Panesi et al. (2013) have developed a MT model for the $\text{N}_2(^1\Sigma_g^+)-\text{N}(^4S_u)$ system model based on a different procedure. They repeated isochoric and isothermal heat-bath calculations for different values of the translational temperatures. The calculations were performed in a dissociating environment (no recombination) and by neglecting the effects of predissociation. The macroscopic dissociation rate coefficient is defined as:

$$\tilde{k}_{\text{N}_2}^{\text{dis}}(T) = \frac{1}{n_{\text{N}_2}} \sum_{i \in \mathcal{I}_{\text{N}_2}} n_i k_i^{\text{dis}}(T). \quad (3.30)$$

Since the definition of a rate coefficient requires the existence of a Quasi-Steady State (QSS) population (Park 1990), its numerical value has been taken as that given by eq. (3.30) in QSS conditions. The energy transfer terms have been computed by taking the first-order moments of the production terms:

$$\Omega_{\text{N}_2}^{\text{tra-int}} = - \sum_{i \in \mathcal{I}_{\text{N}_2}} E_i \omega_i^{\text{in}}, \quad \Omega_{\text{N}_2}^{\text{dis-int}} = - \sum_{i \in \mathcal{I}_{\text{N}_2}} E_i \omega_i^{\text{dis}}, \quad (3.31)$$

$$\Omega_{\text{N}_2}^{\text{tra-vib}} = - \sum_{\substack{v \in \mathcal{V}_{\text{N}_2} \\ J \in \mathcal{J}_v}} \tilde{E}_v \omega_{vJ}^{\text{in}}, \quad \Omega_{\text{N}_2}^{\text{dis-vib}} = - \sum_{\substack{v \in \mathcal{V}_{\text{N}_2} \\ J \in \mathcal{J}_v}} \tilde{E}_v \omega_{vJ}^{\text{dis}}, \quad (3.32)$$

$$\Omega_{\text{N}_2}^{\text{tra-rot}} = - \sum_{\substack{v \in \mathcal{V}_{\text{N}_2} \\ J \in \mathcal{J}_v}} \Delta \tilde{E}_v(J) \omega_{vJ}^{\text{in}}, \quad \Omega_{\text{N}_2}^{\text{dis-rot}} = - \sum_{\substack{v \in \mathcal{V}_{\text{N}_2} \\ J \in \mathcal{J}_v}} \Delta \tilde{E}_v(J) \omega_{vJ}^{\text{dis}}. \quad (3.33)$$

In order to cast the energy transfer terms defined in eqs. (3.31)-(3.33) into a form suitable for a multi-temperature description, Panesi et al. (2013) introduced the following implicit definitions for the internal, vibrational and rotational temperatures:

- Internal temperature (T_{int}):

$$\sum_{i \in \mathcal{I}_{\text{N}_2}} n_i E_i - n_{\text{N}_2} E_{\text{N}_2}^{\text{int}}(T_{\text{int}}) = 0, \quad (3.34)$$

where the internal energy (per molecule) $E_{\text{N}_2}^{\text{int}}(T_{\text{int}})$ can be obtained by multiplying by m_{N_2} the specific internal energy given in eq. (3.5) and by replacing T with T_{int} , $E_{\text{N}_2}^{\text{int}}(T_{\text{int}}) = m_{\text{N}_2} e_{\text{N}_2}^{\text{int}}(T_{\text{int}})$.

- Vibrational and rotational temperatures (T_{vib} and T_{rot}):

$$\sum_{v \in \mathcal{V}_{N_2}} \tilde{n}_v \tilde{E}_v - n_{N_2} E_{N_2}^{\text{vib}}(T_{\text{vib}}, T_{\text{rot}}) = 0, \quad (3.35)$$

$$\sum_{\substack{v \in \mathcal{V}_{N_2} \\ J \in \mathcal{J}_v}} n_{vJ} \Delta \tilde{E}_v(J) - n_{N_2} E_{N_2}^{\text{rot}}(T_{\text{vib}}, T_{\text{rot}}) = 0. \quad (3.36)$$

The vibrational and rotational energies (per molecule; $E_{N_2}^{\text{vib}}(T_{\text{vib}}, T_{\text{rot}})$ and $E_{N_2}^{\text{rot}}(T_{\text{vib}}, T_{\text{rot}})$, respectively) are defined as:

$$E_{N_2}^{\text{vib}}(T_{\text{vib}}, T_{\text{rot}}) = k_b T_{\text{vib}}^2 \frac{\partial \ln Z_{N_2}^{\text{int}}(T_{\text{vib}}, T_{\text{rot}})}{\partial T_{\text{vib}}}, \quad (3.37)$$

$$E_{N_2}^{\text{rot}}(T_{\text{vib}}, T_{\text{rot}}) = k_b T_{\text{rot}}^2 \frac{\partial \ln Z_{N_2}^{\text{int}}(T_{\text{vib}}, T_{\text{rot}})}{\partial T_{\text{rot}}}, \quad (3.38)$$

where the two-temperature internal partition function is:

$$Z_{N_2}^{\text{int}}(T_{\text{vib}}, T_{\text{rot}}) = \sum_{\substack{v \in \mathcal{V}_{N_2} \\ J \in \mathcal{J}_v}} a_{vJ} \exp \left[-\frac{\tilde{E}_v}{k_b T_{\text{vib}}} - \frac{\Delta \tilde{E}_v(J)}{k_b T_{\text{rot}}} \right]. \quad (3.39)$$

The division of eqs. (3.37)-(3.38) by m_{N_2} gives the specific vibrational and rotational energies of N_2 ($E_{N_2}^{\text{vib}}(T_{\text{vib}}, T_{\text{rot}}) = m_{N_2} e_{N_2}^{\text{vib}}(T_{\text{vib}}, T_{\text{rot}})$ and $E_{N_2}^{\text{rot}}(T_{\text{vib}}, T_{\text{rot}}) = m_{N_2} e_{N_2}^{\text{rot}}(T_{\text{vib}}, T_{\text{rot}})$, respectively).

The multi-temperature formulations of the energy transfer terms due to inelastic collisions ($\Omega_{N_2}^{\text{tra-int}}$, $\Omega_{N_2}^{\text{tra-vib}}$ and $\Omega_{N_2}^{\text{tra-rot}}$) have been developed by assuming a Landau-Teller relaxation model:

$$\Omega_{N_2}^{\text{tra-int}} = n_{N_2} \frac{E_{N_2}^{\text{int}}(T) - E_{N_2}^{\text{int}}(T_{\text{int}})}{\tau_{N-N_2}^{\text{tra-int}}(T, p_N)}, \quad (3.40)$$

$$\Omega_{N_2}^{\text{tra-vib}} = n_{N_2} \frac{E_{N_2}^{\text{vib}}(T, T) - E_{N_2}^{\text{vib}}(T_{\text{vib}}, T_{\text{rot}})}{\tau_{N-N_2}^{\text{tra-vib}}(T, p_N)}, \quad (3.41)$$

$$\Omega_{N_2}^{\text{tra-rot}} = n_{N_2} \frac{E_{N_2}^{\text{rot}}(T, T) - E_{N_2}^{\text{rot}}(T_{\text{vib}}, T_{\text{rot}})}{\tau_{N-N_2}^{\text{tra-rot}}(T, p_N)}. \quad (3.42)$$

The relaxation times $\tau_{N-N_2}^{\text{tra-int}}$, $\tau_{N-N_2}^{\text{tra-vib}}$ and $\tau_{N-N_2}^{\text{tra-rot}}$ in eqs. (3.40)-(3.42) are all functions of the translational temperature T and of the N partial pressure, $p_N = n_N k_b T$. The procedure for their evaluation can be found in the work of Panesi et al. (2013). The product of the three relaxation times with the N partial pressure is shown in fig. 3.5. The results show that the rotational and vibrational relaxation times become comparable at high temperatures.

The energy transfer terms coupling the dissociation and the various components of the internal energy ($\Omega_{N_2}^{\text{dis-int}}$, $\Omega_{N_2}^{\text{dis-vib}}$ and $\Omega_{N_2}^{\text{dis-rot}}$) have been developed by

assuming that the average energy lost due to dissociation is a temperature dependent fraction of the dissociation energy:¹

$$\Omega_{N_2}^{\text{dis-int}} = -2m_N n_{N_2} n_N C_{N_2}^{\text{dis-int}}(T) 2E_N \tilde{k}_{N_2}^{\text{dis}}(T), \quad (3.43)$$

$$\Omega_{N_2}^{\text{dis-vib}} = -2m_N n_{N_2} n_N C_{N_2}^{\text{dis-vib}}(T) 2E_N \tilde{k}_{N_2}^{\text{dis}}(T), \quad (3.44)$$

$$\Omega_{N_2}^{\text{dis-rot}} = -2m_N n_{N_2} n_N C_{N_2}^{\text{dis-rot}}(T) 2E_N \tilde{k}_{N_2}^{\text{dis}}(T). \quad (3.45)$$

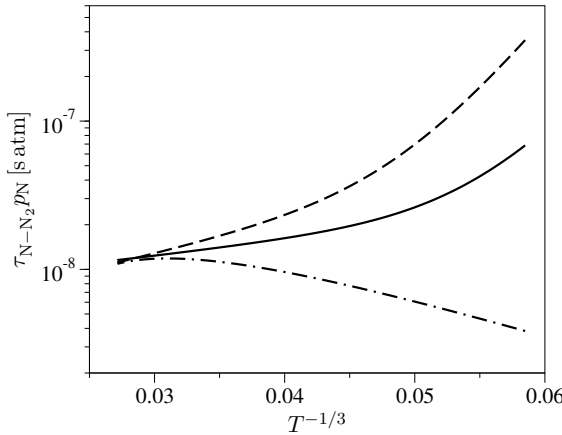


Figure 3.5: Extracted relaxation times (unbroken line $\tau_{N-N_2}^{\text{tra-int}} p_N$, dashed line $\tau_{N-N_2}^{\text{tra-vib}} p_N$, dotted-dashed line $\tau_{N-N_2}^{\text{tra-rot}} p_N$).

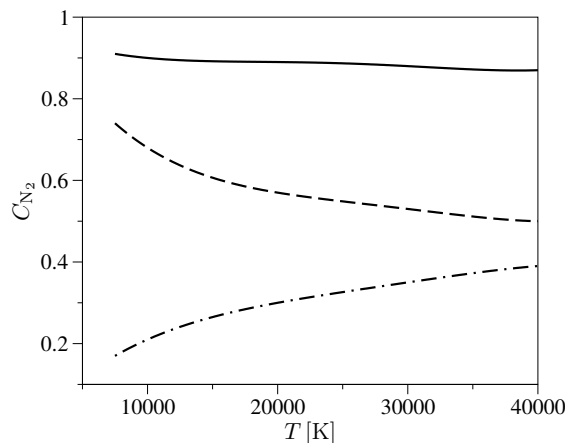


Figure 3.6: Chemistry coupling factors (unbroken line $C_{N_2}^{\text{dis-int}}$, dashed line $C_{N_2}^{\text{dis-vib}}$, dotted-dashed line $C_{N_2}^{\text{dis-rot}}$).

The chemistry coupling factors $C_{N_2}^{\text{dis-int}}$, $C_{N_2}^{\text{dis-vib}}$ and $C_{N_2}^{\text{dis-rot}}$ are only function of the translational temperature T . These quantities are shown in fig. 3.6. The

¹This model is similar to the one proposed by Park (1990) where the average vibrational energy lost by a molecule due to dissociation is 30% of its dissociation energy.

average value of the vibrational energy lost due to dissociation decreases when increasing the translational temperature. An opposite behavior is observed for the rotational energy.

The fitting expressions for the macroscopic dissociation rate coefficient, relaxation times and chemistry coupling factors are provided in app. A.

The internal temperatures and the energy transfer terms defined in eqs. (3.34)-(3.36) and (3.40)-(3.45), respectively, allow for introducing two variants of the MT model for the $\text{N}_2(^1\Sigma_g^+)$ - $\text{N}(^4\text{S}_u)$ system: T - T_{int} model and T - T_{vib} - T_{rot} model.

3.2.1 $T - T_{\text{int}}$ Model

Master Equations The master equations for the T - T_{int} model comprise the continuity equations for N and N_2 , the global energy conservation equation and the internal energy conservation equation:

$$\frac{\partial}{\partial t} \begin{pmatrix} \rho_N \\ \rho_{N_2} \\ \rho_e \\ \rho_{N_2} e_{N_2}^{\text{int}} \end{pmatrix} = \begin{pmatrix} \omega_N \\ \omega_{N_2} \\ 0 \\ \Omega_{N_2}^{\text{tra-int}} + \Omega_{N_2}^{\text{dis-int}} \end{pmatrix}. \quad (3.46)$$

Mass Production and Energy Transfer Terms The mass production terms for N and N_2 are:

$$\omega_N = 2m_N n_N \left[n_{N_2} \tilde{k}_{N_2}^{\text{dis}}(T) - n_N^2 \tilde{k}_{N_2}^{\text{rec}}(T) \right], \quad \omega_{N_2} = -\omega_N, \quad (3.47)$$

where the macroscopic recombination rate coefficient $\tilde{k}_{N_2}^{\text{rec}}(T)$ is computed based on micro-reversibility:

$$\frac{\tilde{k}_{N_2}^{\text{rec}}(T)}{\tilde{k}_{N_2}^{\text{dis}}(T)} = \frac{Z_{N_2}^{\text{tra}}(T) Z_{N_2}^{\text{int}}(T)}{[a_N Z_N^{\text{tra}}(T)]^2} \exp\left(\frac{2E_N}{k_b T}\right). \quad (3.48)$$

The energy transfer terms $\Omega_{N_2}^{\text{tra-int}}$ and $\Omega_{N_2}^{\text{dis-int}}$ are computed based on eqs. (3.40) and (3.43), respectively.

Thermodynamic Properties The gas number density and pressure are computed based on eq. (3.20). In the case of the T - T_{int} model, the expression for the gas thermal energy density simplifies to:

$$\rho e = \frac{3}{2} n k_b T + n_N E_N + n_{N_2} E_{N_2}^{\text{int}}(T_{\text{int}}). \quad (3.49)$$

The internal energies per unit mass and molecule ($e_{N_2}^{\text{int}}(T_{\text{int}})$ and $E_{N_2}^{\text{int}}(T_{\text{int}})$, respectively) are obtained based on eq. (3.34).

3.2.2 $T - T_{\text{vib}} - T_{\text{rot}}$ Model

Master Equations The master equations for the $T-T_{\text{vib}}-T_{\text{rot}}$ model comprise the continuity equations for N and N_2 , the global energy conservation equation and the vibrational and rotational energy conservation equations:

$$\frac{\partial}{\partial t} \begin{pmatrix} \rho_N \\ \rho_{\text{N}_2} \\ \rho e \\ \rho_{\text{N}_2} e_{\text{N}_2}^{\text{rot}} \\ \rho_{\text{N}_2} e_{\text{N}_2}^{\text{vib}} \end{pmatrix} = \begin{pmatrix} \omega_N \\ \omega_{\text{N}_2} \\ 0 \\ \Omega_{\text{N}_2}^{\text{tra-vib}} + \Omega_{\text{N}_2}^{\text{dis-vib}} \\ \Omega_{\text{N}_2}^{\text{tra-rot}} + \Omega_{\text{N}_2}^{\text{dis-rot}} \end{pmatrix}. \quad (3.50)$$

Mass Production and Energy Transfer Terms The mass production terms are computed as done for the $T-T_{\text{int}}$ model through eqs. (3.47)-(3.48). The energy transfer terms $\Omega_{\text{N}_2}^{\text{tra-vib}}$, $\Omega_{\text{N}_2}^{\text{tra-rot}}$, $\Omega_{\text{N}_2}^{\text{dis-vib}}$ and $\Omega_{\text{N}_2}^{\text{dis-rot}}$ are computed based on eqs. (3.41)-(3.42) and (3.44)-(3.45), respectively.

Thermodynamic Properties The gas number density and pressure are computed based on eq. (3.20). In the case of the $T-T_{\text{vib}}-T_{\text{rot}}$ model, the expression for the gas thermal energy density is:

$$\rho e = \frac{3}{2} n k_b T + n_N E_N + n_{\text{N}_2} \left[E_{\text{N}_2}^{\text{vib}}(T_{\text{vib}}, T_{\text{rot}}) + E_{\text{N}_2}^{\text{rot}}(T_{\text{vib}}, T_{\text{rot}}) \right]. \quad (3.51)$$

The vibrational and rotational energies per unit mass and molecule ($e_{\text{N}_2}^{\text{vib}}(T_{\text{vib}}, T_{\text{rot}})$, $e_{\text{N}_2}^{\text{rot}}(T_{\text{vib}}, T_{\text{rot}})$ and $E_{\text{N}_2}^{\text{vib}}(T_{\text{vib}}, T_{\text{rot}})$, $E_{\text{N}_2}^{\text{rot}}(T_{\text{vib}}, T_{\text{rot}})$, respectively) are computed by means of eqs. (3.37)-(3.38).

The MT models presented before are purely macroscopic models. In the present thesis, alternative reduced models have been developed. These consist in Vibrational Collisional and an Energy Bin models (described in secs. 3.3-3.4). These reduced models are more accurate than the MT models (as shown in ch. 4) and are built by coarsening the resolution of the energy level dynamics (from which the name coarse-grain models). This approach has the benefit of reducing the number of governing equations to be solved, and is motivated by the fact that, in CFD applications, one is mainly interested in capturing the correct dynamics of flow quantities, than resolving the finest details of the internal energy level dynamics. As for the MT models, predissociation has been neglected due its negligible effects on flow quantities (as shown in ch. 4).

3.3 Vibrational Collisional Model

The Vibrational Collisional (VC) model (Bourdon et al. 2008; Magin et al. 2009, Munafò et al. 2010; 2012) has represented the first attempt towards the development of a coarse-grained model for the $\text{N}_2(^1\Sigma_g^+)$ - $\text{N}(^4\text{S}_u)$ system. The rotational structure associated to each vibrational quantum state (see fig. 3.1) provides indeed a natural way to coarsen the resolution of the energy level dynamics. In the VC model, this is accomplished by assuming thermal equilibrium between the translational and the rotational degrees of freedom. Thus, the rotational levels within each vibrational level follow a Boltzmann distribution at the local translational temperature T :

$$\frac{n_{vJ}}{\tilde{n}_v} = \frac{a_{vJ}}{\tilde{Z}_v(T)} \exp \left[-\frac{\Delta \tilde{E}_v(J)}{k_b T} \right], \quad v \in \mathcal{V}_{\text{N}_2}, \quad J \in \mathcal{J}_v, \quad (3.52)$$

where the number density and the rotational partition function of the vibrational level v are:

$$\tilde{n}_v = \sum_{J \in \mathcal{J}_v} n_{vJ}, \quad \tilde{Z}_v(T) = \sum_{J \in \mathcal{J}_v} a_{vJ} \exp \left[-\frac{\Delta \tilde{E}_v(J)}{k_b T} \right], \quad v \in \mathcal{V}_{\text{N}_2}. \quad (3.53)$$

During the years, different VC models have been proposed. Specific examples are the VC model developed by Esposito (1999; 2006), and the one recently developed by Guy et al. (2013) based on the FHO theory. An exhaustive review of the VC models developed during the 1980-1990's can be found in the book of Capitelli et al. (2000)

Master Equations The master equations for the VC model can be obtained from those for the RVC model (3.22) by summing the equations for the (v, J) levels over the rotational levels of each vibrational state (stored in the sets \mathcal{J}_v) and by using eq. (3.52):

$$\frac{\partial}{\partial t} \begin{pmatrix} \rho_N \\ \tilde{\rho}_v \\ \rho_e \end{pmatrix} = \begin{pmatrix} \omega_N \\ \tilde{\omega}_v \\ 0 \end{pmatrix}, \quad v \in \mathcal{V}_{\text{N}_2}. \quad (3.54)$$

The mass production term and the density of the vibrational level v are defined as $\tilde{\omega}_v = \sum_{J \in \mathcal{J}_v} \omega_{vJ}$ and $\tilde{\rho}_v = m_{\text{N}_2} \tilde{n}_v$, respectively.

Mass Production Terms After some algebra, the mass production terms for N and the vibrational levels of N_2 in eq. (3.54) can be written as:

$$\omega_N = \sum_{v \in \mathcal{V}_{\text{N}_2}} \tilde{\omega}_v^{\text{dis}}, \quad \tilde{\omega}_v = - \left(\tilde{\omega}_v^{\text{dis}} + \tilde{\omega}_v^{\text{in}} \right), \quad v \in \mathcal{V}_{\text{N}_2}, \quad (3.55)$$

where the partial production terms due to vibrational dissociation and inelastic collisional excitation have the following expressions:

$$\tilde{\omega}_v^{\text{dis}} = m_{\text{N}_2} n_{\text{N}} \left[\tilde{n}_v \tilde{k}_v^{\text{dis}}(T) - n_{\text{N}}^2 \tilde{k}_v^{\text{rec}}(T) \right], \quad (3.56)$$

$$\begin{aligned} \tilde{\omega}_v^{\text{in}} = m_{\text{N}_2} n_{\text{N}} & \sum_{\substack{w > v \\ w \in \mathcal{V}_{\text{N}_2}}} \left[\tilde{n}_v \tilde{k}_{v \rightarrow w}^{\text{in}}(T) - \tilde{n}_w \tilde{k}_{w \rightarrow v}^{\text{in}}(T) \right] - \\ & m_{\text{N}_2} n_{\text{N}} \sum_{\substack{w < v \\ w \in \mathcal{V}_{\text{N}_2}}} \left[\tilde{n}_w \tilde{k}_{w \rightarrow v}^{\text{in}}(T) - \tilde{n}_v \tilde{k}_{v \rightarrow w}^{\text{in}}(T) \right], \\ v \in \mathcal{V}_{\text{N}_2}. \end{aligned} \quad (3.57)$$

The rotationally-averaged (endothermic) rate coefficients for vibrational dissociation and inelastic collisional excitation ($\tilde{k}_v^{\text{dis}}(T)$ and $\tilde{k}_{v \rightarrow w}^{\text{in}}(T)$, with $v < w$, respectively) are:

$$\tilde{k}_v^{\text{dis}}(T) = \frac{1}{\tilde{Z}_v(T)} \sum_{J \in \mathcal{J}_v} a_{vJ} k_{vJ}^{\text{dis}}(T) \exp \left[-\frac{\Delta \tilde{E}_v(J)}{k_{\text{b}} T} \right], \quad (3.58)$$

$$\begin{aligned} \tilde{k}_{v \rightarrow w}^{\text{in}}(T) = \frac{1}{\tilde{Z}_v(T)} & \sum_{J \in \mathcal{J}_v} \sum_{Y \in \mathcal{J}_w} a_{vJ} k_{vJ \rightarrow wY}^{\text{in}}(T) \exp \left[-\frac{\Delta \tilde{E}_v(J)}{k_{\text{b}} T} \right], \\ v < w, \quad v, w \in \mathcal{V}_{\text{N}_2}. \end{aligned} \quad (3.59)$$

From the algebraic manipulation needed to obtain to the VC model, it can be shown that the (exothermic) rate coefficients for recombination and inelastic collisional de-excitation ($\tilde{k}_v^{\text{rec}}(T)$ and $\tilde{k}_{w \rightarrow v}^{\text{in}}(T)$, with $v < w$, respectively) can be computed by applying micro-reversibility among the vibrational levels:

$$\frac{\tilde{k}_v^{\text{rec}}(T)}{\tilde{k}_v^{\text{dis}}(T)} = \frac{Z_{\text{N}_2}^{\text{tra}}(T) \tilde{Z}_v(T)}{\left[a_{\text{N}} Z_{\text{N}}^{\text{tra}}(T) \right]^2} \exp \left(\frac{2E_{\text{N}} - \tilde{E}_v}{k_{\text{b}} T} \right), \quad (3.60)$$

$$\begin{aligned} \frac{\tilde{k}_{w \rightarrow v}^{\text{in}}(T)}{\tilde{k}_{v \rightarrow w}^{\text{in}}(T)} &= \frac{\tilde{Z}_v(T)}{\tilde{Z}_w(T)} \exp \left(\frac{\tilde{E}_w - \tilde{E}_v}{k_{\text{b}} T} \right), \\ v < w, \quad v, w \in \mathcal{V}_{\text{N}_2}. \end{aligned} \quad (3.61)$$

The dissociation and excitation VC rate coefficients have been compared with available literature data. Figure 3.7 shows a comparison with the VC model of Esposito (1999; 2006) developed at the University of Bari (U Bari). In the VC model of Esposito, rate coefficients are available within the temperature range 20-10 000 K and have been computed by using a different set of energy levels and PES compared to those of the NASA ARC database (for more details see the aforementioned papers of Esposito). Both databases are in fair agreement as far as excitation is concerned. Some differences arise for dissociation when moving towards high-lying levels. It is worth to mention that fig. 3.7 compares rate coefficients for the same vibrational levels that do not correspond to the same energy in the NASA ARC and U Bari databases.

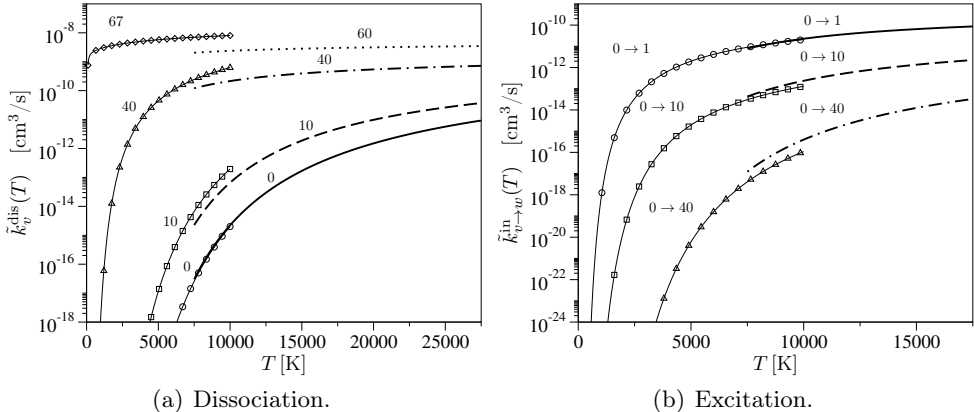


Figure 3.7: Comparison between the NASA ARC and U Bari databases for the vibrational dissociation and inelastic collisional excitation rate coefficients (lines NASA ARC, lines with symbols U Bari; numbers indicate the vibrational levels involved in the transitions).

Thermodynamics The gas number density and pressure are computed based on eq. (3.20), where the number density of N_2 is $n_{\text{N}_2} = \sum_{v \in \mathcal{V}_{\text{N}_2}} \tilde{n}_v$. The gas thermal energy density can be obtained by substituting the assumed Boltzmann distribution (3.52) for the rotational levels in eq. (3.29):

$$\rho e = \frac{3}{2} n k_b T + n_N E_N + \sum_{v \in \mathcal{V}_{\text{N}_2}} \tilde{n}_v \left[\tilde{E}_v + k_b T^2 \frac{\partial \ln \tilde{Z}_v(T)}{\partial T} \right]. \quad (3.62)$$

The temperature dependent term in the sum in eq. (3.62) represents the rotational contribution to the gas internal energy density.

The formulation of the VC model is completed with the introduction of a vibrational temperature T_{vib} . This is extracted from the level population as post-processing and defined through the following implicit relation:

$$\frac{\sum_{v \in \mathcal{V}_{\text{N}_2}} \tilde{n}_v \tilde{E}_v}{n_{\text{N}_2}} = \frac{\sum_{v \in \mathcal{V}_{\text{N}_2}} \tilde{E}_v \tilde{Z}_v(T) \exp(-\tilde{E}_v/k_b T_{\text{vib}})}{\sum_{v \in \mathcal{V}_{\text{N}_2}} \tilde{Z}_v(T) \exp(-\tilde{E}_v/k_b T_{\text{vib}})}. \quad (3.63)$$

3.4 Energy Bin Model

The Energy Bin model is the second coarse-grained model for the $\text{N}_2(^1\Sigma_g^+)$ – $\text{N}(^4\text{S}_u)$ system that has been developed in the present thesis (Magin et al. 2010; Panesi et al. 2010; Magin et al. 2012, Munafò et al. 2011; 2014). This model is built by sorting the energy levels of N_2 by increasing energy and by lumping them in energy bins. The coarsening of the energy level dynamics is realized by assuming a distribution of the energy levels with the energy bins. Two variants of the Energy Bin model have been developed: Uniform Rovibrational Collisional and Boltzmann Rovibrational Collisional models.

The procedure used for the generation of the energy bins is common to both variants and goes as follows. The rovibrational energy levels of N_2 are sorted by increasing energy (*i.e.* by adopting the storage scheme of the set \mathcal{I}_{N_2} introduced in sec. 3.1.1). The whole internal energy ladder of N_2 is first divided in two parts: one for the bound levels and the other for the predissociated levels. Secondly, both regions are evenly sub-divided with spacing:

$$\delta E_{N_2}^B = 2E_N/\mathcal{N}_{N_2}^B, \quad \delta E_{N_2}^P = (E_\star - 2E_N)/\mathcal{N}_{N_2}^P, \quad (3.64)$$

where the number of energy bins for the bound and predissociated regions ($\mathcal{N}_{N_2}^B$ and $\mathcal{N}_{N_2}^P$, respectively) are free parameters and satisfy the relation $\mathcal{N}_{N_2} = \mathcal{N}_{N_2}^B + \mathcal{N}_{N_2}^P$ (where \mathcal{N}_{N_2} is the total number of energy bins). Quantity E_\star in eq. (3.64) represents the energy of the last energy level of N_2 . The next step consists in the construction of a map between energy bins and energy levels in order to associate the energy level i with the energy bin k it belongs to:

$$\text{lev_to_bin}(i) = \begin{cases} \lfloor E_i / \delta E_{N_2}^B \rfloor + 1, & i \in \mathcal{I}_{N_2}^B, \\ \lfloor (E_i - 2E_N) / \delta E_{N_2}^P \rfloor + \mathcal{N}_{N_2}^B + 1, & i \in \mathcal{I}_{N_2}^P, \end{cases} \quad (3.65)$$

where the symbol $\lfloor \cdot \rfloor$ stands for the floor function. For sake of convenience it is useful to introduce the sets $\mathcal{K}_{N_2}^B$, $\mathcal{K}_{N_2}^P$ and \mathcal{K}_{N_2} , storing the indices, respectively, of the energy bins associated to the bound, predissociated and both the bound and predissociated levels (satisfying the relations $\mathcal{K}_{N_2}^B \cup \mathcal{K}_{N_2}^P = \mathcal{K}_{N_2}$ and $\mathcal{K}_{N_2}^B \cap \mathcal{K}_{N_2}^P = \emptyset$) and the set $\mathcal{B}_{N_2}^k$ storing the energy levels belonging to the energy bin k :

$$\mathcal{B}_{N_2}^k = \{i \in \mathcal{I}_{N_2} \mid \text{lev_to_bin}(i) = k\}, \quad k \in \mathcal{K}_{N_2}. \quad (3.66)$$

3.4.1 Uniform Rovibrational Collisional Model

In the Uniform Rovibrational Collisional (URVC) model (Magin et al. 2010; Panesi et al. 2010; Magin et al. 2012), the population distribution within the energy bins is assumed to be uniform:

$$\frac{n_i}{\tilde{n}_k} = \frac{a_i}{\tilde{a}_k}, \quad k \in \mathcal{K}_{N_2}, \quad i \in \mathcal{I}_{N_2}, \quad (3.67)$$

where the number density and the degeneracy of the energy bin k are defined as:

$$\tilde{n}_k = \sum_{i \in \mathcal{B}_{N_2}^k} n_i, \quad \tilde{a}_k = \sum_{i \in \mathcal{B}_{N_2}^k} a_i, \quad k \in \mathcal{K}_{N_2}. \quad (3.68)$$

Equation (3.67) does not hold in equilibrium conditions. This means that the URVC model introduces modifications, compared to the RVC model, in terms of equilibrium thermodynamic properties. This fact makes the application of

the URVC model less appealing for flows where equilibrium is imposed in some parts of the domain (*i.e.* such as in the reservoir for nozzle flows). This problem can be partially alleviated by increasing the number of energy bins. It is worth to mention that, since the energy levels in the URVC model are sorted by increasing energy, the assumed uniform distribution (3.67) within each bin may mix together energy levels having different vibrational and rotational quantum numbers. This means that the use of eq. (3.67) for the sake of mechanism reduction should not prevent *a priori* to account for rotational non-equilibrium effects.

For a given energy bin k , an average energy \tilde{E}_k is further introduced:

$$\tilde{E}_k = \frac{1}{\tilde{a}_k} \sum_{i \in \mathcal{B}_{N_2}^k} a_i E_i, \quad k \in \mathcal{K}_{N_2}. \quad (3.69)$$

Based on the sub-division into energy bins constructed through eqs. (3.64)-(3.66), it is possible to write the energy E_i of the level i within the energy bin k based on its average energy \tilde{E}_k as:

$$E_i = \tilde{E}_k + \Delta \tilde{E}_k(i), \quad i \in \mathcal{I}_{N_2}, \quad k \in \mathcal{K}_{N_2}. \quad (3.70)$$

The average bin energy \tilde{E}_k and the $\Delta \tilde{E}_k(i)$ contribution are the equivalent of the vibrational and rotational energies as defined through eq. (3.1).

Master Equations The master equations for the URVC model can be obtained from those for the RVC model (3.14) by summing the equations for the i levels over the energy levels contained within each bin (stored in the sets $\mathcal{B}_{N_2}^k$) and by using eq. (3.67):

$$\frac{\partial}{\partial t} \begin{pmatrix} \rho_N \\ \tilde{\rho}_k \\ \rho_e \end{pmatrix} = \begin{pmatrix} \omega_N \\ \tilde{\omega}_k \\ 0 \end{pmatrix}, \quad k \in \mathcal{K}_{N_2}. \quad (3.71)$$

The mass production term and the density of the energy bin k are defined as $\tilde{\omega}_k = \sum_{i \in \mathcal{B}_{N_2}^k} \omega_i$ and $\tilde{\rho}_k = m_{N_2} \tilde{n}_k$, respectively.

Mass Production Terms After some algebra, the mass production terms for N and the energy bins of N_2 in eq. (3.71) can be written as:

$$\omega_N = \sum_{k \in \mathcal{K}_{N_2}} \tilde{\omega}_k^{\text{dis}}, \quad \tilde{\omega}_k = - \left(\tilde{\omega}_k^{\text{dis}} + \tilde{\omega}_k^{\text{in}} \right), \quad k \in \mathcal{K}_{N_2}, \quad (3.72)$$

where the partial production terms due to bin dissociation and inelastic collisional excitation have the following expressions:

$$\tilde{\omega}_k^{\text{dis}} = m_{\text{N}_2} n_{\text{N}} \left[\tilde{n}_k \tilde{k}_k^{\text{dis}}(T) - n_{\text{N}}^2 \tilde{k}_k^{\text{rec}}(T) \right], \quad (3.73)$$

$$\begin{aligned} \tilde{\omega}_k^{\text{in}} = m_{\text{N}_2} n_{\text{N}} & \sum_{\substack{l > k \\ l \in \mathcal{K}_{\text{N}_2}}} \left[\tilde{n}_k \tilde{k}_{k \rightarrow l}^{\text{in}}(T) - \tilde{n}_l \tilde{k}_{l \rightarrow k}^{\text{in}}(T) \right] - \\ & m_{\text{N}_2} n_{\text{N}} \sum_{\substack{l < k \\ l \in \mathcal{K}_{\text{N}_2}}} \left[\tilde{n}_l \tilde{k}_{l \rightarrow k}^{\text{in}}(T) - \tilde{n}_k \tilde{k}_{k \rightarrow l}^{\text{in}}(T) \right], \\ k \in \mathcal{K}_{\text{N}_2}. \end{aligned} \quad (3.74)$$

The bin-averaged (endothermic) rate coefficients for dissociation and inelastic collisional excitation ($\tilde{k}_k^{\text{dis}}(T)$ and $\tilde{k}_{k \rightarrow l}^{\text{in}}(T)$, with $k < l$, respectively) are:

$$\tilde{k}_k^{\text{dis}}(T) = \frac{1}{\tilde{a}_k} \sum_{i \in \mathcal{B}_{\text{N}_2}^k} a_i k_i^{\text{dis}}(T), \quad (3.75)$$

$$\begin{aligned} \tilde{k}_{k \rightarrow l}^{\text{in}}(T) = \frac{1}{\tilde{a}_k} \sum_{i \in \mathcal{B}_{\text{N}_2}^k} \sum_{\substack{j \in \mathcal{B}_{\text{N}_2}^l \\ j > i}} a_i k_{i \rightarrow j}^{\text{in}}(T), \\ k < l, \quad k, l \in \mathcal{K}_{\text{N}_2}. \end{aligned} \quad (3.76)$$

The (exothermic) rate coefficients for recombination and inelastic collisional de-excitation ($\tilde{k}_k^{\text{rec}}(T)$ and $\tilde{k}_{l \rightarrow k}^{\text{in}}(T)$, with $k < l$, respectively) are:

$$\tilde{k}_k^{\text{rec}}(T) = \frac{Z_{\text{N}_2}^{\text{tra}}(T) \tilde{D}_k(T)}{\left[a_{\text{N}} Z_{\text{N}}^{\text{tra}}(T) \right]^2} \exp \left(\frac{2E_{\text{N}} - \tilde{E}_k}{k_{\text{b}} T} \right), \quad (3.77)$$

$$\begin{aligned} \tilde{k}_{l \rightarrow k}^{\text{in}}(T) = \frac{1}{\tilde{a}_l} \sum_{i \in \mathcal{B}_{\text{N}_2}^k} \sum_{\substack{j \in \mathcal{B}_{\text{N}_2}^l \\ j > i}} a_i \exp \left(\frac{E_j - E_i}{k_{\text{b}} T} \right) k_{i \rightarrow j}^{\text{in}}(T), \\ k < l, \quad k, l \in \mathcal{K}_{\text{N}_2}, \end{aligned} \quad (3.78)$$

where quantity $\tilde{D}_k(T)$ is defined as:

$$\tilde{D}_k(T) = \sum_{i \in \mathcal{B}_{\text{N}_2}^k} a_i k_i^{\text{dis}}(T) \exp \left[-\frac{\Delta \tilde{E}_k(i)}{k_{\text{b}} T} \right], \quad k \in \mathcal{K}_{\text{N}_2}. \quad (3.79)$$

Equations (3.77)-(3.78) show that the endothermic and exothermic rate coefficients for the URVC model are not related through a micro-reversibility relation among the energy bins. This is due to the assumed uniform distribution (3.67) within the energy bins.

Thermodynamic Properties The gas number density and pressure are computed based on eq. (3.20), where the number density of N₂ is written as $n_{N_2} = \sum_{k \in \mathcal{K}_{N_2}} \tilde{n}_k$. The gas thermal energy density can be obtained by substituting the assumed uniform population distribution (3.67) within the energy bins in eq. (3.21):

$$\rho e = \frac{3}{2} n k_b T + n_N E_N + \sum_{k \in \mathcal{K}_{N_2}} \tilde{n}_k \tilde{E}_k. \quad (3.80)$$

The formulation of the URVC model is completed with the introduction of an internal temperature T_{int} . This is extracted from the energy bin population as post-processing and defined through the following implicit relation:

$$\frac{\sum_{k \in \mathcal{K}_{N_2}} \tilde{n}_k \tilde{E}_k}{n_{N_2}} = \frac{\sum_{k \in \mathcal{K}_{N_2}} \tilde{E}_k \tilde{a}_k \exp(-\tilde{E}_k/k_b T_{\text{int}})}{\sum_{k \in \mathcal{K}_{N_2}} \tilde{a}_k \exp(-\tilde{E}_k/k_b T_{\text{int}})}. \quad (3.81)$$

3.4.2 Boltzmann Rovibrational Collisional Model

In the Boltzmann Rovibrational Collisional (BRVC) model (Munafò et al. 2011; 2014), it is assumed that the population of the energy levels within each bin follows a Boltzmann distribution at the local translational temperature T :

$$\frac{n_i}{\tilde{n}_k} = \frac{a_i}{\tilde{Z}_k(T)} \exp\left[-\frac{\Delta\tilde{E}_k(i)}{k_b T}\right], \quad i \in \mathcal{I}_{N_2}, \quad k \in \mathcal{K}_{N_2}, \quad (3.82)$$

where the number density and the partition function of the energy bin k are:

$$\tilde{n}_k = \sum_{i \in \mathcal{B}_{N_2}^k} n_i, \quad \tilde{Z}_k(T) = \sum_{i \in \mathcal{B}_{N_2}^k} a_i \exp\left[-\frac{\Delta\tilde{E}_k(i)}{k_b T}\right], \quad k \in \mathcal{K}_{N_2}. \quad (3.83)$$

The energy contribution $\Delta\tilde{E}_k(i)$ is always computed, as for the URVC model, through $E_i = \tilde{E}_k + \Delta\tilde{E}_k(i)$, with the important difference that now \tilde{E}_k represents the energy of the first level within the energy bin k .

The assumption of local equilibrium of the internal levels within each bin is justified by the large reaction rate coefficients for excitation and de-excitation which characterize groups of levels with similar internal energy. This assumption was found to work quite well in the conditions of interest to the present thesis (as it is shown in chs. 4-5). Furthermore, increasing the number of energy bins can easily extend the range of validity of the BRVC model to the strongest non-equilibrium conditions. As for the URVC model, the assumed Boltzmann distribution (3.82) within each bin may mix together energy levels with different vibrational and rotational quantum numbers. Hence, also for the case of the BRVC model, the use of eq. (3.82) for the sake of mechanism reduction should not prevent *a priori* to account for rotational non-equilibrium effects.

Equation (3.82) holds true in equilibrium conditions. This implies that the BRVC model (together with the VC model) does not introduce modifications, when compared with the RVC model, as far as equilibrium thermodynamic properties are concerned. This is not the case for the URVC model. In equilibrium conditions, the energy bin population follows a Boltzmann distribution:

$$\frac{\tilde{n}_k}{n_{N_2}} = \frac{\tilde{Z}_k(T) \exp\left(-\tilde{E}_k/k_b T\right)}{\sum_{k \in \mathcal{K}_{N_2}} \tilde{Z}_k(T) \exp\left(-\tilde{E}_k/k_b T\right)}, \quad k \in \mathcal{K}_{N_2}, \quad (3.84)$$

where the bin partition function plays the role of a degeneracy. Equation (3.84) can be obtained as follows. In equilibrium conditions, the number density of the energy level i is related to that of N_2 through the Boltzmann distribution law (1.36):

$$\frac{n_i}{n_{N_2}} = \frac{a_i}{Z_{N_2}^{\text{int}}(T)} \exp\left(-\frac{E_i}{k_b T}\right), \quad i \in \mathcal{I}_{N_2}. \quad (3.85)$$

The substitution of the eq. (3.85) in eq. (3.82) and the successive use of the energy splitting $E_i = \tilde{E}_k + \Delta\tilde{E}_k(i)$ in the result obtained gives eq. (3.84).

Master Equations The master equations for the BRVC model are obtained based on the same procedure used for the URVC model given in sec. 3.4.1.

$$\frac{\partial}{\partial t} \begin{pmatrix} \rho_N \\ \tilde{\rho}_k \\ \rho_e \end{pmatrix} = \begin{pmatrix} \omega_N \\ \tilde{\omega}_k \\ 0 \end{pmatrix}, \quad k \in \mathcal{K}_{N_2}. \quad (3.86)$$

The mass production term and the density of the energy bin k are always defined as $\tilde{\omega}_k = \sum_{i \in \mathcal{B}_{N_2}^k} \omega_i$ and $\tilde{\rho}_k = m_{N_2} \tilde{n}_k$, respectively.

Mass Production Terms After some algebra, the mass production terms for N and the energy bins of the N_2 in eq. (3.86) can be written as:

$$\omega_N = \sum_{k \in \mathcal{K}_{N_2}} \tilde{\omega}_k^{\text{dis}}, \quad \tilde{\omega}_k = -\left(\tilde{\omega}_k^{\text{dis}} + \tilde{\omega}_k^{\text{in}}\right), \quad k \in \mathcal{K}_{N_2}, \quad (3.87)$$

where the partial production terms due to bin dissociation and inelastic collisional excitation have the following expressions:

$$\tilde{\omega}_k^{\text{dis}} = m_{N_2} n_N \left[\tilde{n}_k \tilde{k}_k^{\text{dis}}(T) - n_N^2 \tilde{k}_k^{\text{rec}}(T) \right], \quad (3.88)$$

$$\begin{aligned} \tilde{\omega}_k^{\text{in}} = m_{N_2} n_N & \sum_{\substack{l > k \\ l \in \mathcal{K}_{N_2}}} \left[\tilde{n}_k \tilde{k}_{k \rightarrow l}^{\text{in}}(T) - \tilde{n}_l \tilde{k}_{l \rightarrow k}^{\text{in}}(T) \right] - \\ & m_{N_2} n_N \sum_{\substack{l < k \\ l \in \mathcal{K}_{N_2}}} \left[\tilde{n}_l \tilde{k}_{l \rightarrow k}^{\text{in}}(T) - \tilde{n}_k \tilde{k}_{k \rightarrow l}^{\text{in}}(T) \right], \end{aligned} \quad (3.89)$$

$$k \in \mathcal{K}_{N_2}.$$

The bin-averaged (endothermic) rate coefficients for dissociation and inelastic collisional excitation ($\tilde{k}_k^{\text{dis}}(T)$ and $\tilde{k}_{k \rightarrow l}^{\text{in}}(T)$, with $k < l$, respectively) are:

$$\tilde{k}_k^{\text{dis}}(T) = \frac{1}{\tilde{Z}_k(T)} \sum_{i \in \mathcal{B}_{N_2}^k} a_i k_i^{\text{dis}}(T) \exp \left[-\frac{\Delta \tilde{E}_k(i)}{k_b T} \right], \quad (3.90)$$

$$\begin{aligned} \tilde{k}_{k \rightarrow l}^{\text{in}}(T) &= \frac{1}{\tilde{Z}_k(T)} \sum_{i \in \mathcal{B}_{N_2}^k} \sum_{\substack{j \in \mathcal{B}_{N_2}^l \\ j > i}} a_i k_{i \rightarrow j}^{\text{in}}(T) \exp \left[-\frac{\Delta \tilde{E}_k(i)}{k_b T} \right], \\ k < l, \quad k, l &\in \mathcal{K}_{N_2}. \end{aligned} \quad (3.91)$$

From the algebraic manipulation needed to obtain the BRVC model, it can be shown that the (exothermic) rate coefficients for recombination and inelastic collisional de-excitation ($\tilde{k}_k^{\text{rec}}(T)$ and $\tilde{k}_{l \rightarrow k}^{\text{in}}(T)$, with $k < l$, respectively) can be computed by applying micro-reversibility among the energy bins:

$$\frac{\tilde{k}_k^{\text{rec}}(T)}{\tilde{k}_k^{\text{dis}}(T)} = \frac{Z_{N_2}^{\text{tra}}(T) \tilde{Z}_k(T)}{\left[a_N Z_N^{\text{tra}}(T) \right]^2} \exp \left(\frac{2E_N - \tilde{E}_k}{k_b T} \right), \quad (3.92)$$

$$\begin{aligned} \frac{\tilde{k}_{l \rightarrow k}^{\text{in}}(T)}{\tilde{k}_{k \rightarrow l}^{\text{in}}(T)} &= \frac{\tilde{Z}_k(T)}{\tilde{Z}_l(T)} \exp \left(\frac{\tilde{E}_l - \tilde{E}_k}{k_b T} \right), \\ k < l, \quad k, l &\in \mathcal{K}_{N_2}. \end{aligned} \quad (3.93)$$

Equations (3.92)-(3.93) are a direct consequence of the assumed Boltzmann distribution (3.82) within the energy bins.

Thermodynamic Properties The gas number density and pressure are computed based on eq. (3.20), where the number density of N_2 is written as $n_{N_2} = \sum_{k \in \mathcal{K}_{N_2}} \tilde{n}_k$. For the BRVC model, the gas thermal energy density can be obtained by substituting the assumed population distribution within the energy bins (eq. (3.82)) in eq. (3.21). After some algebra, one has:

$$\rho e = \frac{3}{2} n k_b T + n_N E_N + \sum_{k \in \mathcal{K}_{N_2}} \tilde{n}_k \left[\tilde{E}_k + k_b T^2 \frac{\partial \ln \tilde{Z}_k(T)}{\partial T} \right]. \quad (3.94)$$

The formulation of the BRVC model is completed with the introduction of an internal temperature T_{int} . This is extracted from the energy bin population as post-processing and defined through the following implicit relation:

$$\frac{\sum_{k \in \mathcal{K}_{N_2}} \tilde{n}_k \tilde{E}_k}{n_{N_2}} = \frac{\sum_{k \in \mathcal{K}_{N_2}} \tilde{E}_k \tilde{Z}_k(T) \exp(-\tilde{E}_k/k_b T_{\text{int}})}{\sum_{k \in \mathcal{K}_{N_2}} \tilde{Z}_k(T) \exp(-\tilde{E}_k/k_b T_{\text{int}})}. \quad (3.95)$$

3.5 Unified Notation

The RVC and coarse-grained models (VC, BRVC and URVC) presented in secs. 3.3-3.4 can be cast into a unified notation. This is convenient when one has to compare the different models as done in chs. 4-5.

The internal states of N₂ considered by a particular model (vibrational, rovibrational and bins) can be indicated by means a generalized index ϵ and stored in the set \mathcal{E}_{N_2} defined as:

$$\mathcal{E}_{N_2} = \begin{cases} \mathcal{V}_{N_2}, & \text{VC,} \\ \mathcal{K}_{N_2}, & \text{BRVC-URVC,} \\ \mathcal{I}_{N_2}, & \text{RVC.} \end{cases} \quad (3.96)$$

As already done before, the generalized set \mathcal{E}_{N_2} can be split into its bound and predissociated subsets ($\mathcal{E}_{N_2}^B$ and $\mathcal{E}_{N_2}^P$, respectively). These satisfy the relations $\mathcal{E}_{N_2}^B \cup \mathcal{E}_{N_2}^P = \mathcal{E}_{N_2}$ and $\mathcal{E}_{N_2}^B \cap \mathcal{E}_{N_2}^P = \emptyset$. In what follows, physical quantities that are related to a generalized internal state of N₂ are indicated with a $\tilde{\cdot}$ over- ϵ . The number of generalized internal energy states of N₂ is indicated with \mathcal{N}_{N_2} .

Master Equations The use of eq. (3.96) allows to write the master equations for the RVC, VC, BRVC and URVC models as:

$$\frac{\partial}{\partial t} \begin{pmatrix} \rho_N \\ \tilde{\rho}_\epsilon \\ \rho_\epsilon \end{pmatrix} = \begin{pmatrix} \omega_N \\ \tilde{\omega}_\epsilon \\ 0 \end{pmatrix}, \quad \epsilon \in \mathcal{E}_{N_2}. \quad (3.97)$$

Mass Production Terms The mass production terms for N and the generalized internal states of N₂ are:

$$\omega_N = \sum_{\epsilon \in \mathcal{E}_{N_2}} \tilde{\omega}_\epsilon^{\text{dis}} + \sum_{\epsilon \in \mathcal{E}_{N_2}^P} \tilde{\omega}_\epsilon^{\text{pre}}, \quad (3.98)$$

$$\tilde{\omega}_\epsilon = - \begin{cases} (\tilde{\omega}_\epsilon^{\text{dis}} + \tilde{\omega}_\epsilon^{\text{in}}), & \epsilon \in \mathcal{E}_{N_2}^B, \\ (\tilde{\omega}_\epsilon^{\text{dis}} + \tilde{\omega}_\epsilon^{\text{pre}} + \tilde{\omega}_\epsilon^{\text{in}}), & \epsilon \in \mathcal{E}_{N_2}^P, \end{cases} \quad (3.99)$$

where the partial production terms due to dissociation, predissociation and inelastic collisional excitation are:

$$\tilde{\omega}_\epsilon^{\text{dis}} = m_{N_2} n_N \left[\tilde{n}_\epsilon \tilde{k}_\epsilon^{\text{dis}}(T) - n_N^2 \tilde{k}_\epsilon^{\text{rec}}(T) \right], \quad \epsilon \in \mathcal{E}_{N_2}, \quad (3.100)$$

$$\tilde{\omega}_\epsilon^{\text{pre}} = m_{N_2} \left[\tilde{n}_\epsilon \tilde{k}_\epsilon^{\text{pre}}(T) - n_N^2 \tilde{k}_\epsilon^{\text{i-pre}}(T) \right], \quad \epsilon \in \mathcal{E}_{N_2}^P, \quad (3.101)$$

$$\tilde{\omega}_\epsilon^{\text{in}} = m_{N_2} n_N \sum_{\substack{\epsilon' > \epsilon \\ \epsilon' \in \mathcal{E}_{N_2}}} \left[\tilde{n}_\epsilon \tilde{k}_{\epsilon \rightarrow \epsilon'}^{\text{in}}(T) - \tilde{n}_{\epsilon'} \tilde{k}_{\epsilon' \rightarrow \epsilon}^{\text{in}}(T) \right] -$$

$$m_{N_2} n_N \sum_{\substack{\epsilon' < \epsilon \\ \epsilon' \in \mathcal{E}_{N_2}}} \left[\tilde{n}_{\epsilon'} \tilde{k}_{\epsilon' \rightarrow \epsilon}^{\text{in}}(T) - \tilde{n}_\epsilon \tilde{k}_{\epsilon \rightarrow \epsilon'}^{\text{in}}(T) \right], \quad \epsilon \in \mathcal{E}_{N_2}. \quad (3.102)$$

Obviously, the production terms related to predissociation in eqs. (3.98)-(3.102) are only non-zero for the RVC model.

Thermodynamic Properties The gas number density and pressure are computed based on eq. (3.20), where the number density of N₂ is written as $n_{N_2} = \sum_{\epsilon \in \mathcal{E}_{N_2}} \tilde{n}_\epsilon$. The generalized expression for the gas thermal energy density is:

$$\rho e = \frac{3}{2} n k_b T + n_N E_N + \sum_{\epsilon \in \mathcal{E}_{N_2}} \tilde{n}_\epsilon \tilde{E}_\epsilon + \begin{cases} 0, & \text{RVC-URVC,} \\ \sum_{\epsilon \in \mathcal{E}_{N_2}} \tilde{n}_\epsilon k_b T^2 \frac{\partial \ln \tilde{Z}_\epsilon(T)}{\partial T}, & \text{VC-BRVC.} \end{cases} \quad (3.103)$$

With the use of the generalized notation introduced here, the thermodynamic properties of N and N₂ (energy, enthalpy and specific heats per unit mass; see eqs. (1.45)-(1.47)) assume the following expressions:

$$e_N(T) = \frac{3}{2} \frac{k_b}{m_N} T + \frac{E_N}{m_N}, \quad (3.104)$$

$$\tilde{e}_\epsilon(T) = \frac{3}{2} \frac{k_b}{m_{N_2}} T + \frac{\tilde{E}_\epsilon}{m_{N_2}} + \begin{cases} 0, & \text{RVC-URVC,} \\ \frac{k_b T^2}{m_{N_2}} \frac{\partial \ln \tilde{Z}_\epsilon(T)}{\partial T}, & \text{VC-BRVC,} \end{cases} \quad (3.105)$$

$$\epsilon \in \mathcal{E}_{N_2},$$

$$h_N(T) = e_N(T) + \frac{k_b}{m_N} T, \quad \tilde{h}_\epsilon(T) = \tilde{e}_\epsilon(T) + \frac{k_b}{m_{N_2}} T, \quad \epsilon \in \mathcal{E}_{N_2}, \quad (3.106)$$

$$c_{vN}(T) = \frac{3}{2} \frac{k_b}{m_N}, \quad (3.107)$$

$$\tilde{c}_{v\epsilon}(T) = \frac{3}{2} \frac{k_b}{m_{N_2}} + \begin{cases} 0, & \text{RVC-URVC,} \\ \frac{\partial}{\partial T} \left[\frac{k_b T^2}{m_{N_2}} \frac{\partial \ln \tilde{Z}_\epsilon(T)}{\partial T} \right], & \text{VC-BRVC,} \end{cases} \quad (3.108)$$

$$\epsilon \in \mathcal{E}_{N_2},$$

$$c_{pN}(T) = c_{vN}(T) + \frac{k_b}{m_N}, \quad \tilde{c}_{p\epsilon}(T) = \tilde{c}_{v\epsilon}(T) + \frac{k_b}{m_{N_2}}, \quad \epsilon \in \mathcal{E}_{N_2}. \quad (3.109)$$

Transport Properties Transport phenomena have not been taken into account while developing the coarse-grained models. However, in view of applications to viscous flows (shown in ch. 5), few words need to be said on how to evaluate transport properties and fluxes.

Based on the contents of sec. 2.4.2, the shear viscosity and the translational thermal conductivity are:

$$\eta = \alpha_N^\eta X_N + \alpha_{N_2}^\eta X_{N_2}, \quad (3.110)$$

$$\lambda^{\text{tra}} = \alpha_N^{\lambda^{\text{tra}}} X_N + \alpha_{N_2}^{\lambda^{\text{tra}}} X_{N_2}, \quad (3.111)$$

where $X_{N_2} = \sum_{\epsilon \in \mathcal{E}_{N_2}} \tilde{X}_\epsilon$. The α coefficients are found by solving the following two-by-two linear (symmetric) transport systems:

$$\begin{pmatrix} G_{NN}^\eta & G_{NN_2}^\eta \\ G_{N_2N}^\eta & G_{N_2N_2}^\eta \end{pmatrix} \begin{pmatrix} \alpha_N^\eta \\ \alpha_{N_2}^\eta \end{pmatrix} = \begin{pmatrix} X_N \\ X_{N_2} \end{pmatrix}, \quad (3.112)$$

$$\begin{pmatrix} G_{NN}^{\lambda^{\text{tra}}} & G_{NN_2}^{\lambda^{\text{tra}}} \\ G_{N_2N}^{\lambda^{\text{tra}}} & G_{N_2N_2}^{\lambda^{\text{tra}}} \end{pmatrix} \begin{pmatrix} \alpha_N^{\lambda^{\text{tra}}} \\ \alpha_{N_2}^{\lambda^{\text{tra}}} \end{pmatrix} = \begin{pmatrix} X_N \\ X_{N_2} \end{pmatrix}. \quad (3.113)$$

The total thermal conductivity is computed by summing the translational and internal contributions, $\lambda = \lambda^{\text{tra}} + \lambda^{\text{int}}$. The internal contribution appears due to the assumed Boltzmann distributions at the translational temperature T in the BRVC and VC models. The internal thermal conductivity is computed based on the generalized Eucken's correction (Magin and Degrez 2004):

$$\lambda^{\text{int}} = \frac{\sum_{\epsilon \in \mathcal{E}_{N_2}} \tilde{\rho}_\epsilon [(3/2)(k_b/m_{N_2}) - \tilde{c}_{v\epsilon}(T_\star)]}{X_N/\mathcal{D}_{N_2N} + X_{N_2}/\mathcal{D}_{N_2N_2}}, \quad (3.114)$$

where the temperature T_\star is extracted from:

$$\frac{\sum_{\epsilon \in \mathcal{E}_{N_2}} \tilde{n}_\epsilon \tilde{E}_\epsilon}{n_{N_2}} = \frac{\sum_{\epsilon \in \mathcal{E}_{N_2}} \tilde{E}_\epsilon \tilde{Z}_\epsilon(T) \exp(-\tilde{E}_\epsilon/k_b T_\star)}{\sum_{\epsilon \in \mathcal{E}_{N_2}} \tilde{Z}_\epsilon(T) \exp(-\tilde{E}_\epsilon/k_b T_\star)}. \quad (3.115)$$

Notice that internal thermal conductivity is zero for the RVC and URVC models. This is consistent with the STS CE method developed in ch. 2.

Thermal diffusion is neglected. The diffusion velocities of N and N_2 are found by solving the Stefan-Maxwell equations (2.74), which, based on the assumption $\mathbf{v}_{N_2}^d = \tilde{\mathbf{v}}_\epsilon^d$ (introduced in sec. 2.4.2), reduce to:

$$\begin{pmatrix} \tilde{G}_{NN}^d & \tilde{G}_{NN_2}^d \\ \tilde{G}_{N_2N}^d & \tilde{G}_{N_2N_2}^d \end{pmatrix} \begin{pmatrix} \mathbf{v}_N^d \\ \mathbf{v}_{N_2}^d \end{pmatrix} = - \begin{pmatrix} \nabla_{\mathbf{x}} X_N \\ \nabla_{\mathbf{x}} X_{N_2} \end{pmatrix}. \quad (3.116)$$

The constitutive relations for the stress tensor and the heat flux vector are always given by eqs. (2.87)-(2.88) (with no thermal diffusion effects):

$$\underline{\tau} = \eta \left[\nabla_{\mathbf{x}} \mathbf{v} + (\nabla_{\mathbf{x}} \mathbf{v})^T - \frac{2}{3} \nabla_{\mathbf{x}} \mathbf{v} \underline{\mathbf{I}} \right], \quad (3.117)$$

$$\mathbf{q} = \rho_N \mathbf{v}_N^d h_N + \sum_{\epsilon \in \mathcal{E}_{N_2}} \tilde{\rho}_\epsilon \tilde{\mathbf{v}}_\epsilon^d \tilde{h}_\epsilon - \lambda \nabla_{\mathbf{x}} T. \quad (3.118)$$

The reduced collision integrals $\overline{Q}_{NN}^{(i,j)}$, $\overline{Q}_{NN_2}^{(i,j)}$ and $\overline{Q}_{N_2N_2}^{(i,j)}$ needed for the evaluation of the transport properties and fluxes are computed by using the curve fits of Gupta et al. (1991).

3.6 Intermediate Conclusions

In this chapter a quantum-chemistry database for the $\text{N}_2(^1\Sigma_g^+)$ - $\text{N}(^4\text{S}_u)$ system, developed at NASA Ames Research Center, has been presented in detail (sec. 3.1). The state-to-state kinetics and thermodynamic data contained in the database have been used for developing a RVC model. The developed RVC model is extremely accurate, as no simplifying assumptions are introduced. However, its use can lead to expensive calculations, due to the fact that almost 10 000 coupled differential equations must be solved simultaneously. For this reason, reduced models have been proposed by increasing complexity (MT, VC, URVC and BRVC). The MT model (sec. 3.2) is a purely macroscopic model, where the continuity equations for N and N_2 are coupled to the rotational and vibrational (or internal only) energy conservation equations. The MT model is the cheapest one, among the reduced models. The VC model (sec. 3.3) has been developed by assuming rotational equilibrium. This hypothesis (which does not hold true for flows behind strong normal shock waves; see ch. 4) allows for an important reduction of the number of equations, as only the vibrational levels of N_2 (61) must be tracked. The URVC and BRVC models are two variants of the Energy Bin model (sec. 3.4). This model has been developed by lumping the energy levels of N_2 in energy bins, where a distribution of the energy levels is assumed. In the URVC model (sec. 3.4.1), the distribution is uniform. In the BRVC model (sec. 3.4.2), a Boltzmann distribution at the local translational temperature is assumed. The mathematical formulation of the BRVC and URVC models is similar, with the important difference that the URVC model does not allow for retrieving equilibrium. The computational cost of the Energy bin model depends on the number of energy bins in use.

The RVC and reduced models have been integrated in hydrodynamic flow solvers developed by the author. Applications to inviscid and viscous flows are treated in chs. 4-5.

Part II

Integration of Coarse-Grained Models in Hydrodynamic Flows

Chapter 4

ODE Solver for Flows Behind Normal Shock Waves

This chapter illustrates the coupling of the RVC and reduced models developed in ch. 3 with an Ordinary Differential Equation (ODE) solver for computing inviscid flows behind normal shock waves. The scope is two-fold: to gain insight on the dynamics of internal energy excitation and dissociation and to compare all the models in terms of accuracy and computational cost. Since the discussion is focused on the kinetics of the considered collisional processes, simplifying assumptions are introduced to make the flow problem more tractable.

The present chapter is structured as follows. In sec. 4.1 the time-dependent and multi-dimensional flow governing equations are reduced to a system of ODEs after the introduction of simplifying assumptions. In the same section, the numerical method is briefly outlined. Applications are first shown for the RVC model in sec. 4.2, where a detailed analysis is performed on both flow quantities and energy level dynamics. After that, the results obtained by means of the reduced models (MT, VC, BRVC and URVC) are introduced and presented by increasing complexity of the reduced models in sec. 4.3. Intermediate conclusions are given in sec. 4.4.

4.1 Governing Equations and Numerical Method

The non-equilibrium flow behind a normal shock wave is computed under the following assumptions:

1. The flow is steady and one-dimensional,
2. The flow is inviscid,
3. The shock wave moves at constant speed.

The flow problem is conveniently studied in the shock reference frame. The shock front is treated as a mathematical discontinuity, where the flow properties experience a sudden jump from their free-stream values. The governing equations for the problem under investigation are the steady, one-dimensional

Euler equations (obtained by applying the adopted simplifying assumptions to eq. (2.82)):

$$\frac{\partial}{\partial x} \begin{pmatrix} \rho_N u \\ \tilde{\rho}_\epsilon u \\ p + \rho u^2 \\ \rho u H \end{pmatrix} = \begin{pmatrix} \omega_N \\ \tilde{\omega}_\epsilon \\ 0 \\ 0 \end{pmatrix}, \quad \epsilon \in \mathcal{E}_{N_2}. \quad (4.1)$$

The mass production terms and the thermodynamic properties in eq. (4.1) are computed based on the contents of secs. 3.2-3.5. The mathematical problem to be solved is an Initial Value Problem (IVP) for a system of ODEs (Gear 1971). The solution initial value is provided by the jump conditions at the shock location. These are computed based on the Rankine-Hugoniot jump relations (Rankine 1870, Hugoniot 1887; 1889) by assuming frozen flow conditions within the shock (no dissociation and no excitation acting).

In order to numerically solve eq. (4.1), it is convenient to perform a transformation from a conservative to a non-conservative canonical form (Thivet 1992):

$$\frac{\partial}{\partial x} \begin{pmatrix} y_N \\ \tilde{y}_\epsilon \\ u \\ T \end{pmatrix} = \begin{pmatrix} s_N \\ \tilde{s}_\epsilon \\ s_u \\ s_T \end{pmatrix}, \quad \epsilon \in \mathcal{E}_{N_2}, \quad (4.2)$$

where the mass fractions of N and the generalized internal state ϵ of N_2 are $y_N = \rho_N/\rho$ and $\tilde{y}_\epsilon = \tilde{\rho}_\epsilon/\rho$, respectively. The expressions of the components of the right-hand-side vector in eq. (4.2) can be obtained from the algebraic manipulation needed to pass from eq. (4.1) to (4.2), and are given in app. B. The IVP represented by eq. (4.2) and its initial condition is usually stiff, due to the wide spectrum of time-scales involved. In view of this, eq. (4.2) is numerically solved by means of the family of Backward Differentiation Formula (BDF) implicit methods (Gear 1971) as implemented in the LSODE FORTRAN library (Radhakrishnan and Hindmarsh 1993).

4.2 Application of the RVC Model

The inviscid flow behind a normal shock wave has been computed by using the free-stream conditions given in tab. 4.1, where the reported free-stream pressure values correspond to 6.67 Pa, 13.33 Pa and 44.4 Pa, respectively. The free-stream flow has been seeded with 2.8 % of N, since only only N_2 -N collisions are considered. Preliminary computations performed by means of multi-temperature models (for $u_\infty = 9, 10$ km/s; Magin et al. 2009; Munafò et al. 2010) have shown that the solution obtained by adopting the present free-stream conditions did not experience an important departure from the results obtained without seeding the free-stream flow and by accounting for N_2 -N and N_2-e^- collisions.

The use of a RVC model in CFD simulations allows for obtaining a great quantity of information concerning flow properties and energy level dynamics. Before analyzing the population distributions, a parametric study on the free-stream conditions/kinetic processes has been initially performed. This has been done for two reasons: to understand the important flow features that must be captured by an accurate reduced model and to select the most appropriate conditions under which testing the reduced models.

p_∞ [torr]	0.05, 0.1 and 0.33
u_∞ [m/s]	6, 7, 8, 9, 10 and 11
T_∞ [K]	300

Table 4.1: Free-stream conditions for normal shock wave studies.

4.2.1 Influence of the Free-Stream Pressure

Figure 4.1 shows the temperature evolution behind the shock wave for different values of the free-stream pressure (both moderate and high-speed conditions are considered). When increasing the free-stream pressure, the flow reaches the post-shock equilibrium conditions faster as a consequence of the enhanced collisional rate between the gas particles.

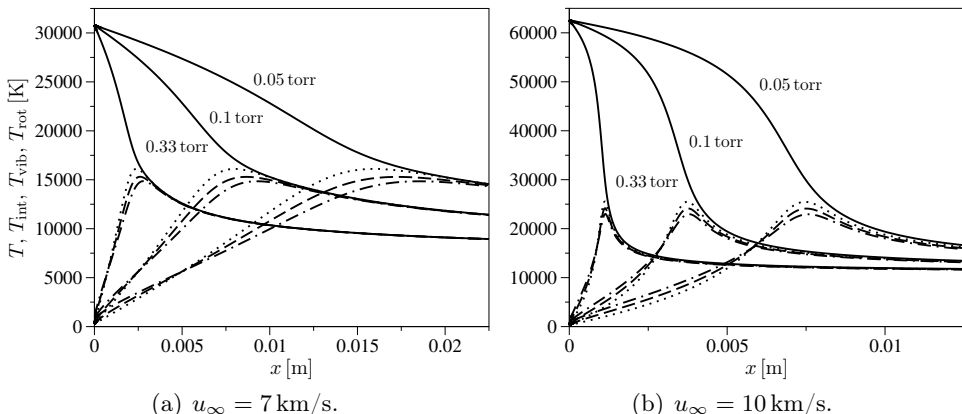


Figure 4.1: RVC model. Temperature evolution behind the shock wave for different values of the free-stream pressure (unbroken lines T , dashed lines T_{int} , dotted-dashed lines T_{vib} , dotted lines T_{rot}).

The internal, vibrational and rotational temperatures shown in fig. 4.1 have been computed based on their definitions given in eqs. (3.34) and (3.35)-(3.38), respectively. It is interesting to notice that the rotational and vibrational temperatures show a very similar behavior. In particular, the vibrational temperature rises faster in the region immediately behind the shock front. The internal temperature always lies between the vibrational and rotational temperatures.

The results obtained indicate that assuming that rotational relaxation proceeds much faster than vibrational relaxation is questionable. The aforementioned approximation is often employed in the aerothermodynamic community (Park 1990), and is usually justified in view of the results obtained when using Parker's model for rotational relaxation (Parker 1959) and in view of experimental data on rotational relaxation times. However, experimental data are mainly available within the temperature range 300-1000 K, which is much lower than that reported in fig. 4.1. Recently, Panesi et al. (2013) have computed rotational relaxation times based on heat-bath calculations by using the same RVC model employed in this thesis. Their results (recalled also in sec. 3.2) show that, at high-temperatures, the rotational and vibrational relaxation times become comparable. This is consistent with the temperature evolution shown in fig. 4.1. The free-stream pressure effect can be also appreciated from the N mole fraction evolution given in fig. 4.2. As expected, increasing the free-stream pressure leads to a faster dissociation due to the enhanced collisional rate among the gas particles.

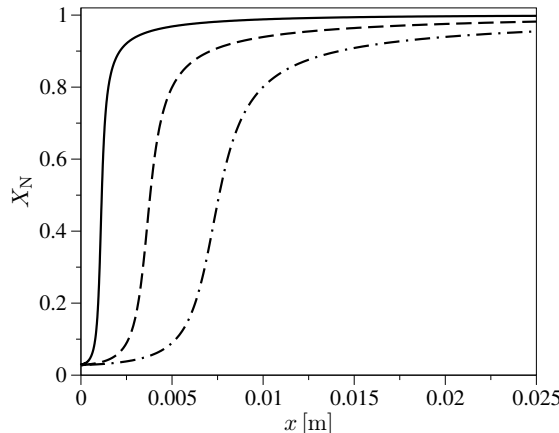


Figure 4.2: RVC model. N mole fraction evolution behind the shock wave for different values of the free-stream pressure ($u_\infty = 10 \text{ km/s}$; unbroken lines $p_\infty = 0.33 \text{ torr}$, dashed lines $p_\infty = 0.1 \text{ torr}$, dotted-dashed lines $p_\infty = 0.05 \text{ torr}$).

4.2.2 Influence of the Free-Stream Velocity

Figure 4.3 shows the temperature and N mole fraction evolution behind the shock wave for different values of the free-stream velocity (the free-stream pressure is 0.1 torr). The increasing of the free-stream velocity has the effect of increasing the amount of translational thermal energy available to the flow in the region immediately behind the shock front. As a consequence, the post-shock values of the gas pressure and translational temperature are increased compared to low-speed conditions (see fig. 4.3(a)). The combined effects of increased pressure and temperature lead to more energetic and frequent collisions,

thereby enhancing the amount of dissociation within the flow (see fig. 4.3(b)). Notice that at low-speed conditions, the distance needed in order to reach the post-shock equilibrium state is higher than that needed for high-speed conditions. This is due to the lowering of the post-shock pressure when decreasing the free-stream velocity.

Some words of caution are needed when analyzing the low-speed results shown in fig. 4.3. Indeed, in view of the limited amount of dissociation (especially for the case $u_\infty = 6 \text{ km/s}$), neglecting the effects of $\text{N}_2\text{-N}_2$ collisions may constitute a less realistic approximation compared to high-speed conditions.

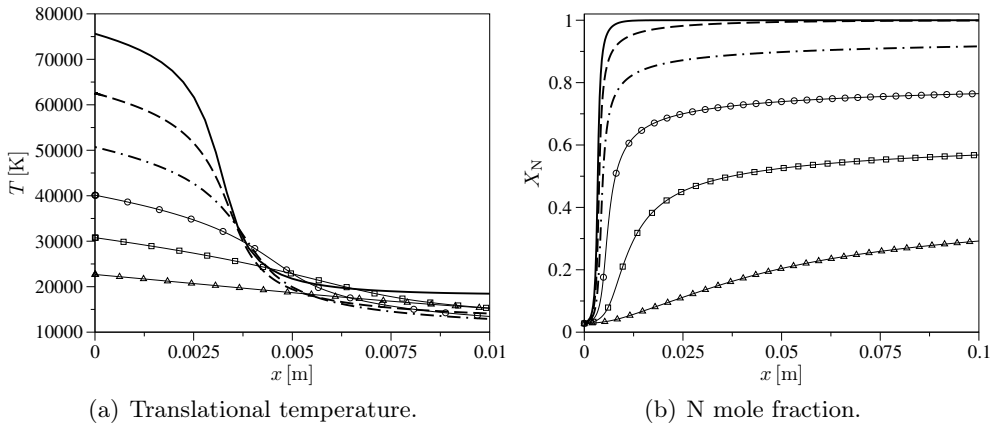


Figure 4.3: *RVC model. Translational temperature and N mole fraction evolution behind the shock wave for different values of the free-stream velocity ($p_\infty = 0.1 \text{ torr}$; unbroken lines $u_\infty = 11 \text{ km/s}$, dashed lines $u_\infty = 10 \text{ km/s}$, dotted-dashed lines $u_\infty = 9 \text{ km/s}$, lines with circles $u_\infty = 8 \text{ km/s}$, lines with squares $u_\infty = 7 \text{ km/s}$, lines with triangles $u_\infty = 6 \text{ km/s}$).*

4.2.3 Influence of Exchange Processes and Predissociation

After studying the effects induced by changing the free-stream pressure and velocity in secs. 4.2.1-4.2.2, a similar study has been performed by including/excluding exchange processes and predissociation. For sake of brevity, only the results obtained by adopting the values of 0.1 torr and 10 km/s for the free-stream pressure and velocity, respectively, are discussed.

Figure 4.4 shows the influence of exchange processes on the temperatures and N mole fraction. The distance at which thermal equilibrium is reached is roughly doubled when exchange processes are not taken into account, as shown in fig. 4.4(a). Neglecting the exchange processes has therefore the effect of lowering the excitation rate of the internal energy of N_2 which, in turn, slows-down the dissociation.

Figure 4.5 shows the influence of predissociation on the temperatures and N mole fraction. Predissociation has the effect of speeding up the dissociation of

N_2 . However, the differences observed between the cases with/without predissociation are negligible compared to those associated with the inclusion/exclusion of exchange processes. The same conclusion holds also for other flow quantities, such as velocity, which are not shown in fig. 4.5.

The findings deduced from figs. 4.4-4.5 apply, in general, to all the cases of tab. 4.1 and confirm the results of Panesi et al. (2013).

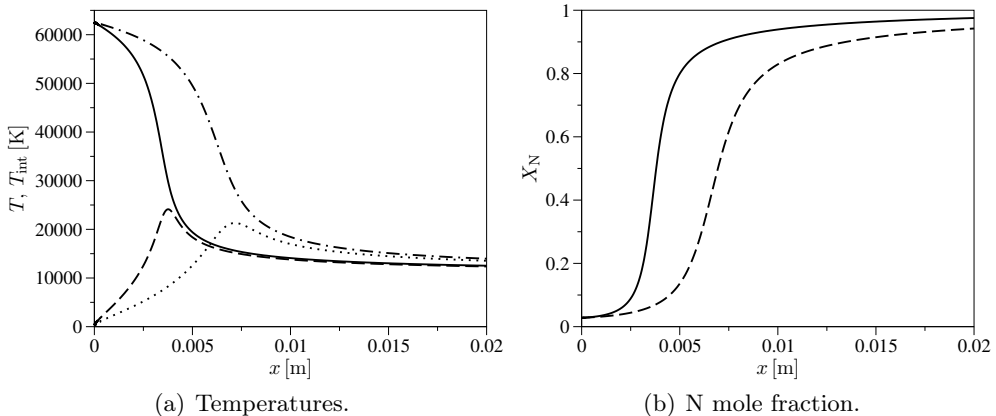


Figure 4.4: RVC model. Temperature and N mole fraction evolution behind the shock wave with/without exchange processes ($p_\infty = 0.1$ torr and $u_\infty = 10$ km/s; in (a) unbroken line T with exchange, dashed line T_{int} with exchange, dotted-dashed line T without exchange, dotted line T_{int} without exchange; in (b) unbroken line with exchange, dashed line without exchange).

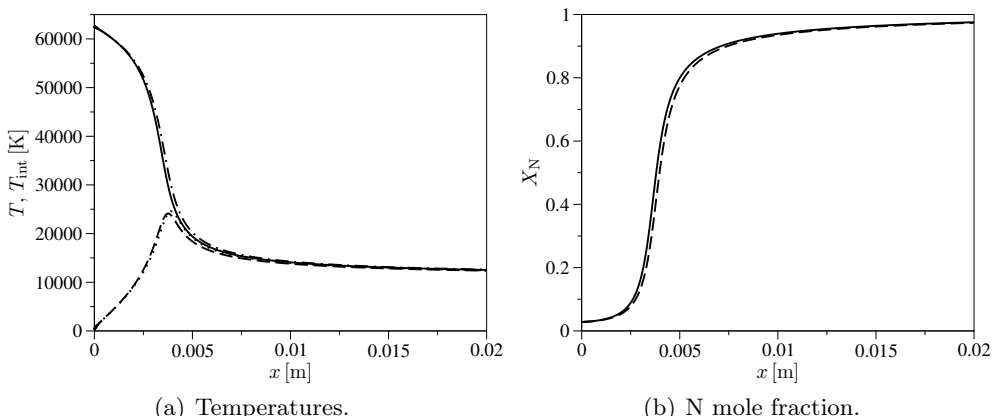


Figure 4.5: RVC model. Temperature and N mole fraction evolution behind the shock wave with/without predissociation ($p_\infty = 0.1$ torr and $u_\infty = 10$ km/s; in (a) unbroken line T with predissociation, dashed line T_{int} with predissociation, dotted-dashed line T without predissociation, dotted line T_{int} without predissociation; in (b) unbroken line with predissociation, dashed line without predissociation).

4.2.4 Findings from the Flowfield Analysis

Before moving to the detailed analysis of the rovibrational energy population distribution (shown in sec. 4.2.5), it is better to summarize the most important observations deduced from the flowfield analysis performed in secs. 4.2.1-4.2.3.

- **Flow quantities.** The temperature evolution in fig. 4.1 suggests that the rates of rotational and vibrational energy relaxation become comparable when the post-shock translational temperature is sufficiently high. This conclusion is consistent with the results obtained by Panesi et al. (2013) for heat-bath calculations. However, the vibrational and rotational temperatures in fig. 4.1 have been obtained as post-processing based on eqs. (3.35)-(3.38). For this reason, the existence and the extent of rotational non-equilibrium effects are further investigated in sec. 4.2.5 by analyzing in detail the evolution of the internal energy population distribution.
- **Kinetic processes.** The results given in fig. 4.4 have shown that exchange processes have an important impact on the flowfield. The opposite conclusion has been found for predissociation (see fig. 4.5), which can be therefore neglected in the development of the reduced models (a conclusion that was already anticipated in sec. 3.2).
- **Free-stream conditions for testing the reduced models.** The parametric study on the free-stream conditions has suggested not to use low values for the free-stream velocity (such as 6 km/s), due to the limited amount of dissociation and the importance of N₂-N₂ collisions for those conditions. In what follows, the free-stream pressure and velocity are kept fixed at 0.1 torr and 10 km/s, respectively.

4.2.5 Energy Level Dynamics

The energy level population distributions have been extracted at eight locations listed in tab. 4.2 (where the corresponding values for the N mole fraction and temperatures are also given).

#	x [m]	X_N	T [K]	T_{int} [K]	T_{vib} [K]	T_{rot} [K]
1	2.5×10^{-5}	2.8×10^{-2}	62 486	473	947	375
2	2.5×10^{-4}	2.9×10^{-2}	61 926	1595	2269	1059
3	2.3×10^{-3}	7.5×10^{-2}	53 205	11 232	11 964	10 367
4	3.2×10^{-3}	2.3×10^{-1}	40 637	19 953	19 275	20 771
5	3.4×10^{-3}	3.2×10^{-1}	36 297	22 291	21 210	23 565
6	3.6×10^{-3}	4.1×10^{-1}	32 481	23 748	22 506	25 185
7	3.9×10^{-3}	5.4×10^{-1}	27 794	23 891	22 850	25 092
8	5.1×10^{-3}	8.1×10^{-1}	18 987	18 016	17 696	18 408

Table 4.2: RVC model. Position, N mole fraction and temperatures for the locations at which the population distributions are extracted.

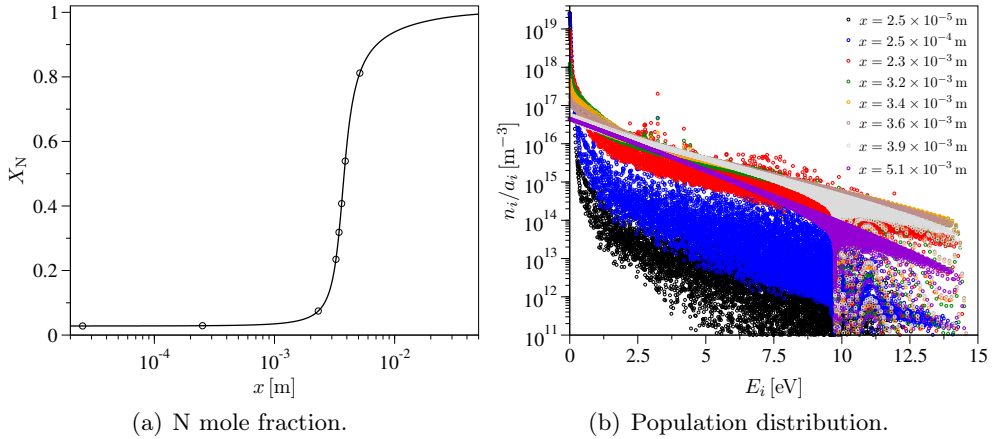


Figure 4.6: RVC model. Comparative evolution of the N mole fraction and rovibrational energy level distribution behind the shock wave ($p_\infty = 0.1$ torr and $u_\infty = 10$ km/s; the symbols in (a) highlight the locations at which the population distributions, plotted in (b), are extracted).

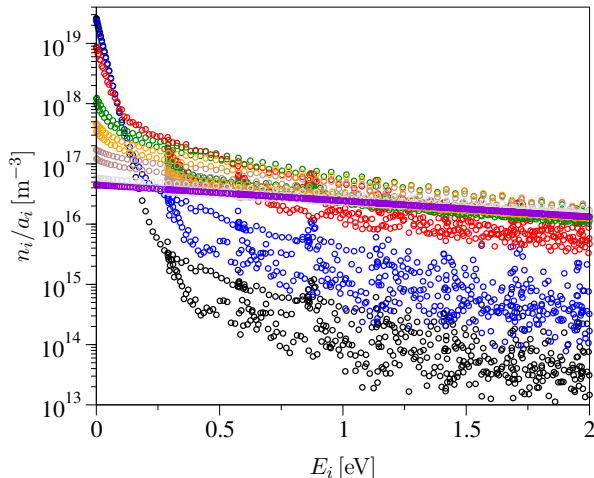


Figure 4.7: RVC model. Evolution behind the shock wave of the population of the rovibrational energy levels lying close to the ground-state ($p_\infty = 0.1$ torr and $u_\infty = 10$ km/s; the locations at which the distributions are plotted are the same as those of fig. 4.6).

Figure 4.6 provides a visual correspondence between the evolution of the N mole fraction and the population distribution behind the shock wave. In the region immediately behind the shock front (locations 1 and 2 of tab. 4.2), the distribution is heavily distorted and experiences strong departures from a Boltzmann distribution. In this zone, the dissociation has not started yet and the medium and high-lying energy levels are poorly populated. Their population progressively increases due to the occurrence of inelastic collisions between N and N₂ (location 3 of tab. 4.2). Moving further downstream, the

inelastic collisions continue to occur and the population distribution assumes a more regular shape. Distortions are more and more localized around the ground state (see fig. 4.7), while the distribution of medium and high-lying energy levels is almost Boltzmann. Once a sufficient degree of excitation reached, the dissociation process starts and, in its initial phase (locations from 2 to 6 of tab. 4.2), occurs through sequences of non-Boltzmann distributions. This feature is still noticeable when more than 40 % of N_2 has already undergone dissociation. The rest of the dissociation (locations 7 and 8 of tab. 4.2), occurs under thermal equilibrium conditions.

Rotational non-equilibrium effects have been investigated by comparing the distributions of the rotational levels (of selected vibrational states) with the Boltzmann distributions at the state-specific rotational temperatures T_{rot}^v . The rotational temperatures T_{rot}^v have been extracted through the following relation:

$$\frac{\sum_{J \in \mathcal{J}_v} \Delta \tilde{E}_v(J) n_{vJ}}{\tilde{n}_v} = \frac{\sum_{J \in \mathcal{J}_v} \Delta \tilde{E}_v(J) a_{vJ} \exp \left[-\Delta \tilde{E}_v(J)/k_b T_{\text{rot}}^v \right]}{\tilde{Z}_v(T_{\text{rot}}^v)}, \quad (4.3)$$

$$v \in \mathcal{V}_{N_2},$$

where the number density and the rotational partition function of the vibrational level v (\tilde{n}_v and \tilde{Z}_v , respectively) are computed based on eq. (3.53). Figure 4.8 shows the results of this comparison for the location 6 of tab. 4.2.

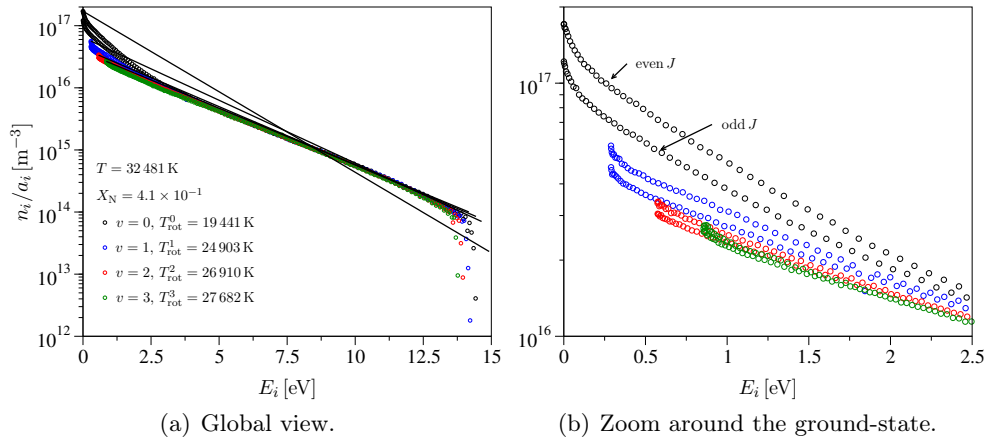


Figure 4.8: RVC model. Rotational energy level distribution for the ground and the first three excited vibrational states at $x = 3.6 \times 10^{-3}$ m ($p_\infty = 0.1$ torr and $u_\infty = 10$ km/s; in (a) the unbroken lines represent the Boltzmann distributions at the rotational temperatures T_{rot}^v).

The numerical values obtained for the rotational temperatures (reported in fig. 4.8(a)) confirm the existence of thermal non-equilibrium between translation and rotation. The reported values further indicate that rotational non-equilibrium effects are more pronounced for low-lying vibrational states. This

is due to the fact that rotational excitation proceeds faster for higher vibrational states as confirmed by fig. 4.8(b) which focuses on the distribution of the rotational levels close to the ground-state. Deviations from a Boltzmann distribution can be observed for low-lying rotational levels of all vibrational states and become more and more pronounced when moving towards the vibrational ground-state. It is interesting to notice that the rotational levels having odd and even rotational quantum number (J) split in two distinct groups. This feature is observed for all vibrational states shown in fig. 4.8(b) and is more evident for the vibrational ground-state.

The assessment of rotational non-equilibrium effects has been completed by tracking the evolution behind the shock wave of the state-specific rotational temperatures T_{rot}^v and by comparing them with the global rotational temperature T_{rot} (see fig. 4.9). All the rotational temperatures, despite the different behaviors, reach the thermal equilibrium condition within the locations $x \simeq 3.5 - 4 \times 10^{-3}$ m. This justifies the use of the global rotational temperature T_{rot} as macroscopic indicator of rotational non-equilibrium effects. The rotational temperature of the vibrational ground-state T_{rot}^0 shows the same trend as T_{rot} , though it rises slower. This is not the case for the rotational temperatures of the excited vibrational states. In the region immediately behind the shock (not shown in fig. 4.9), they quickly rise to values which are much higher than those of T_{rot} and T_{rot}^0 and, at the same time, sensibly lower than the translational temperature. This is consistent with the shape of the rotational level distributions shown in fig. 4.8 and further confirms that rotational excitation proceeds faster for higher vibrational states. The differences between the various rotational temperatures becomes smaller and smaller when the dissociation becomes significant.

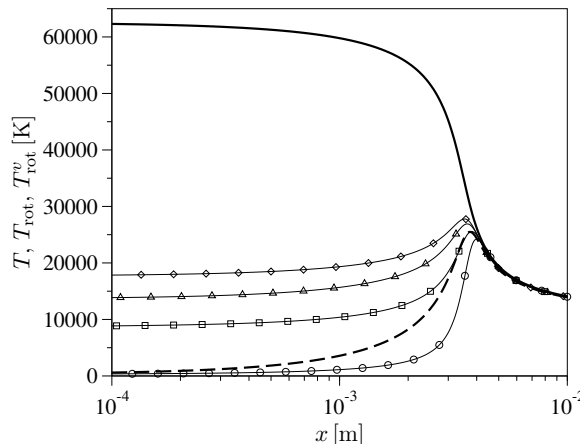


Figure 4.9: RVC model. Translational and rotational temperature evolution behind the shock wave ($p_\infty = 0.1$ torr and $u_\infty = 10$ km/s; unbroken line T , dashed line T_{rot} , line with circles T_{rot}^0 , line with squares T_{rot}^1 , line with triangles T_{rot}^2 , line with diamonds T_{rot}^3).

After completing the study of rotational non-equilibrium effects, the energy level dynamics has been further analyzed by looking at the vibrational and rotational specific population distributions (see fig. 4.10). The rotational specific population, plotted in fig. 4.10(b), is defined as:

$$\tilde{n}_J = \sum_{v \in \mathcal{V}_{N_2}} n_{vJ}, \quad \tilde{E}_J = E_{0J}, \quad J \in \{0, \dots, 279\}. \quad (4.4)$$

The distributions shown in fig. 4.10 share the same features of that of the rovibrational energy levels (fig. 4.6). There is an initial phase in which the medium and high-lying energy levels are being populated through inelastic collisions. This is followed by the onset of dissociation that occurs once the high-lying energy levels are sufficiently populated. The distributions are non-Boltzmann when dissociation starts. This feature disappears after that half of N_2 has undergone dissociation. Notice that, the rotational levels (shown in fig. 4.10(b)) split according to odd and even rotational quantum numbers, as already observed in fig. 4.8(b).

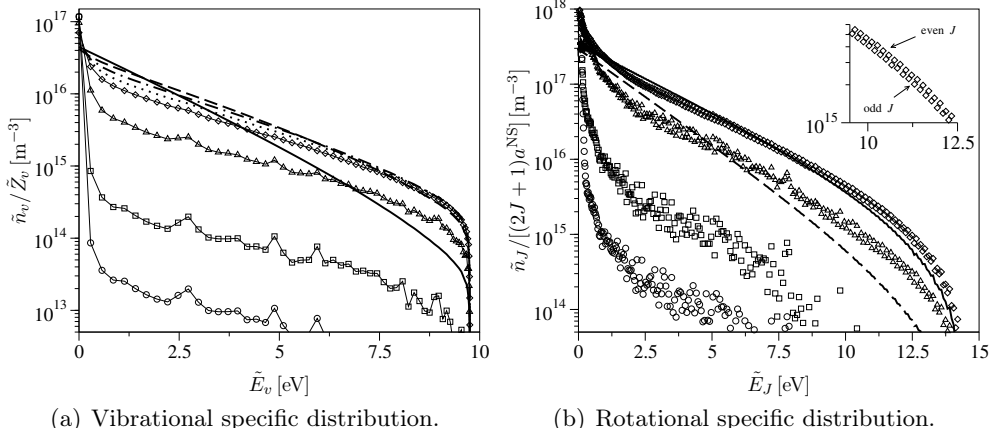


Figure 4.10: RVC model. Evolution of the vibrational and rotational specific population distributions behind the shock wave ($p_\infty = 0.1$ torr and $u_\infty = 10$ km/s; in (a) line with circles $x = 2.5 \times 10^{-5}$ m, line with squares $x = 2.5 \times 10^{-4}$ m, line with triangles $x = 2.3 \times 10^{-3}$ m, line with diamonds $x = 3.2 \times 10^{-3}$ m, dotted line $x = 3.4 \times 10^{-3}$ m, dotted-dashed line $x = 3.6 \times 10^{-3}$ m, dashed line $x = 3.9 \times 10^{-3}$ m, unbroken line $x = 5.1 \times 10^{-3}$ m; in (b) circles $x = 2.5 \times 10^{-5}$ m, squares $x = 2.5 \times 10^{-4}$ m, triangles $x = 2.3 \times 10^{-3}$ m, diamonds $x = 3.2 \times 10^{-3}$ m, unbroken line $x = 3.9 \times 10^{-3}$ m, dashed line $x = 5.1 \times 10^{-3}$ m).

4.3 Application of the Reduced Models (MT, VC, BRVC and URVC)

After completing the analysis of the RVC model solution, the flow behind a normal shock wave has been computed by means of the reduced models (MT, VC, BRVC and URVC) by adopting the free-stream conditions given in tab. 4.1. The results obtained have been then compared with those provided by the RVC model. For reasons that become apparent while analyzing the results, the comparison is shown by increasing complexity of the reduced models.

4.3.1 RVC vs MT

Figure 4.11 compares the RVC and MT model solutions for the temperatures and the N mole fraction behind the shock wave. The two variants of the MT model ($T-T_{\text{int}}$ and $T-T_{\text{vib}}-T_{\text{rot}}$) give practically the same result in terms of chemical composition and translational temperature (in fig. 4.11(a) these quantities are shown only for the $T-T_{\text{vib}}-T_{\text{rot}}$ variant of the MT model).

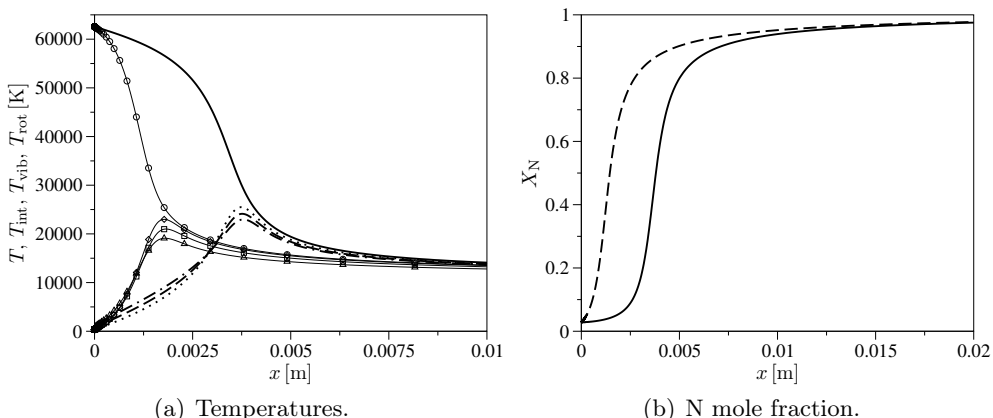


Figure 4.11: RVC and MT model comparison. Temperature and N mole fraction evolution behind the shock wave ($p_\infty = 0.1 \text{ torr}$ and $u_\infty = 10 \text{ km/s}$; in (a) unbroken line T RVC, dashed line T_{int} RVC, dotted-dashed line T_{vib} RVC, dotted line T_{rot} RVC, line with circles T MT, line with squares T_{int} MT, line with triangles T_{vib} MT, line with diamonds T_{rot} MT; in (b) unbroken line RVC, dashed line MT).

The MT model leads to a faster dissociation. This is a general behavior that has been observed for all the cases of tab. 4.1. In order to understand the possible sources for this systematic difference, the mass production and energy transfer terms have been extracted for both the RVC and MT solutions (see fig. 4.12). The results suggest that the MT fails in predicting the correct flow behavior due an overestimation of the macroscopic dissociation rate. On the other hand, the energy transfer seems to be described correctly. This aspect has been further investigated by repeating the calculations without dissociation. Figure 4.13

shows a comparison between the MT and RVC models for the temperatures. The agreement is good, though the MT leads to slightly faster excitation of vibrational and rotational energies. The same conclusion was found for the $T-T_{\text{int}}$ variant of the MT model (not shown in fig. 4.13). The results shown in fig. 4.13 confirm that the disagreement observed in figs. 4.11-4.12 is due to an inaccurate estimation of the macroscopic dissociation rate coefficient in the MT model.

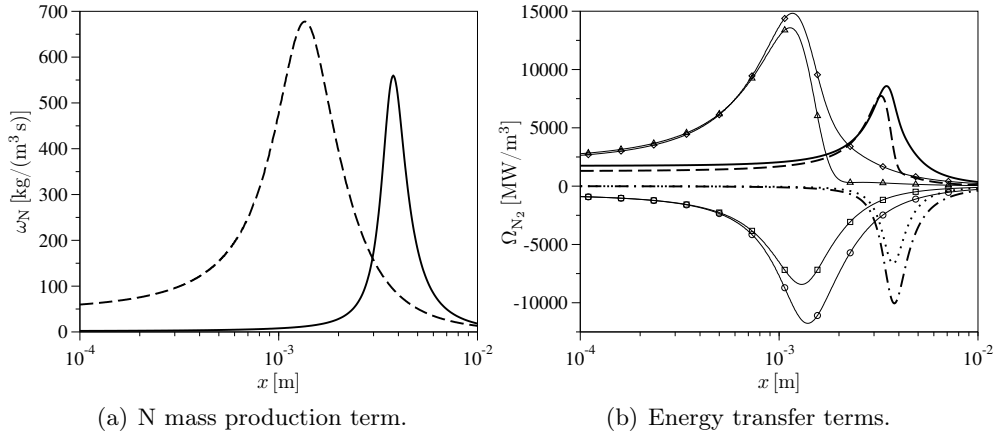


Figure 4.12: RVC and MT model comparison. Mass production and energy transfer term evolution behind the shock wave ($p_\infty = 0.1$ torr and $u_\infty = 10$ km/s; in (a) unbroken line RVC, dashed line MT; in (b) unbroken line $\Omega_{N_2}^{\text{dis-vib}}$ RVC, dashed line $\Omega_{N_2}^{\text{dis-rot}}$ RVC, dotted-dashed line $\Omega_{N_2}^{\text{tra-vib}}$ RVC, dotted line $\Omega_{N_2}^{\text{dis-rot}}$ RVC, line with circles $\Omega_{N_2}^{\text{dis-vib}}$ MT, line with squares $\Omega_{N_2}^{\text{dis-rot}}$ MT, line with diamonds $\Omega_{N_2}^{\text{tra-vib}}$ MT, line with triangles $\Omega_{N_2}^{\text{dis-rot}}$ MT).

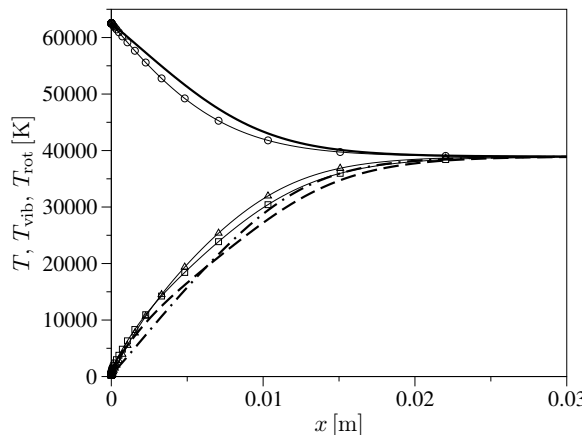


Figure 4.13: RVC and MT model comparison. Temperature evolution behind the shock wave switching off dissociation ($p_\infty = 0.1$ torr and $u_\infty = 10$ km/s; unbroken line T RVC, dashed line T_{vib} RVC, dotted-dashed line T_{rot} RVC, line with circles T MT, line with squares T_{vib} MT, line with triangles T_{rot} MT).

The MT macroscopic dissociation rate coefficient has been computed by Panesi et al. (2013) based on isothermal heat-bath calculations. As it was recalled in sec. 3.2, the one-temperature macroscopic dissociation rate coefficient was determined by taking the QSS value of the following quantity (see also eq. (3.30)):

$$\tilde{k}_{\text{N}_2}^{\text{dis}}(T) = \frac{1}{n_{\text{N}_2}} \sum_{i \in \mathcal{I}_{\text{N}_2}} n_i k_i^{\text{dis}}(T). \quad (4.5)$$

Figure 4.14 is taken from the work of Panesi et al. (2013) and shows the quantity defined in eq. (4.5) as a function of time for different translational temperatures. The QSS period is identified by the existence of a *plateau* region. The results in fig. 4.14 indicate that the duration of the QSS period decreases when increasing the translational temperature. At $T = 40\,000\text{ K}$, the extent of the *plateau* region is so narrow that the existence of QSS becomes questionable. In view of this, one can conclude that the lack of agreement observed between the RVC and MT results is due to the use of a macroscopic dissociation rate coefficient outside of QSS conditions (*i.e.* outside of the range where it is possible to define a macroscopic rate coefficient; Park 1990).

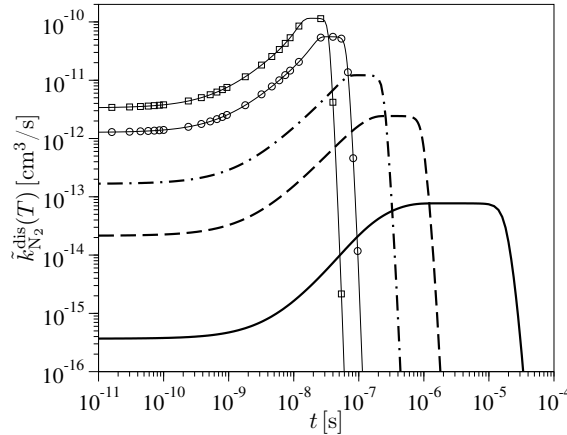


Figure 4.14: RVC model. Time evolution of the macroscopic dissociation rate coefficient (unbroken line $T = 10\,000\text{ K}$, dashed line $T = 15\,000\text{ K}$, dotted-dashed line $T = 20\,000\text{ K}$, line with circles $T = 30\,000\text{ K}$, line with squares $T = 40\,000\text{ K}$).

4.3.2 RVC vs VC, URVC, BRVC and MTP

After assessing the inaccuracy of the MT model, it was decided to test the coarse-grained models (VC, BRVC and URVC) described in secs. 3.3-3.4. For the BRVC and URVC models, the computations have been performed by using different numbers of energy bins (see tab. 4.3). The number of energy bins assigned to the bound region of the internal energy ladder of N_2 ($\mathcal{N}_{\text{N}_2}^{\text{B}}$) has been set, whenever possible, to 75-80 % of the total number of energy bins

(\mathcal{N}_{N_2}) . This choice was motivated by the fact that about 80 % of the internal energy levels of N_2 in the NASA ARC database are bound (see sec. 3.1.1).

#	\mathcal{N}_{N_2}	$\mathcal{N}_{N_2}^B$	$\mathcal{N}_{N_2}^P$
1	2	1	1
2	5	4	1
3	10	8	2
4	20	16	4
5	30	24	6
6	40	32	8
7	50	40	10
8	75	60	15
9	100	80	20
10	500	325	175

Table 4.3: Number of energy bins used for the BRVC and URVC models.

For the sake of completeness, the comparison between the RVC and coarse-grained model solutions has been performed by including also the results obtained by means of the MT model developed by Panesi et al. (2013) and the multi-temperature model developed by Park (MTP; Park 1993). The MTP model has been considered as, at the present time, it represents the model which is most commonly used in aerothermodynamic flow solvers (Gnoffo et al. 1989; Candler and MacCormack 1991; Lani 2009). The MTP model accounts for two distinct temperatures (translational and vibrational; $T-T_{vib}$ model). In this model, the $\Omega_{N_2}^{tra-vib}$ and $\Omega_{N_2}^{dis-vib}$ energy transfer terms are described by using the Landau-Teller model (1936) and the non-preferential dissociation model of Candler and MacCormack (1991), respectively.

Figure 4.15 compares the RVC and reduced model solutions in terms of translational temperature and N mole fraction. The BRVC(50) model (where 50 indicates the number of energy bins) leads to the best agreement with the RVC model solution, as the dissociation is only slightly overestimated. The URVC(50) model solution is also very close to that of the BRVC(50) model. For this reason, it is not shown in fig. 4.15. The MTP model leads to the fastest dissociation. The MT and VC models give very similar results and they both lead to a too fast dissociation. The too fast dissociation of the MT model is due (as shown in sec. 4.3.1) to the lack of QSS conditions. In case of the VC model, the too fast dissociation is instead due to the assumed rotational equilibrium the model is based on. As clearly shown in sec. 4.2.5, the assumption of rotational equilibrium does not hold true for the adopted free-stream conditions (see fig. 4.9). On the other hand, the results obtained for the BRVC(50) and URVC(50) models indicate that these coarse-grained models can account for rotational non-equilibrium effects. Hence, their use should be preferred to the MT and VC models for dissociating flows behind shock waves.

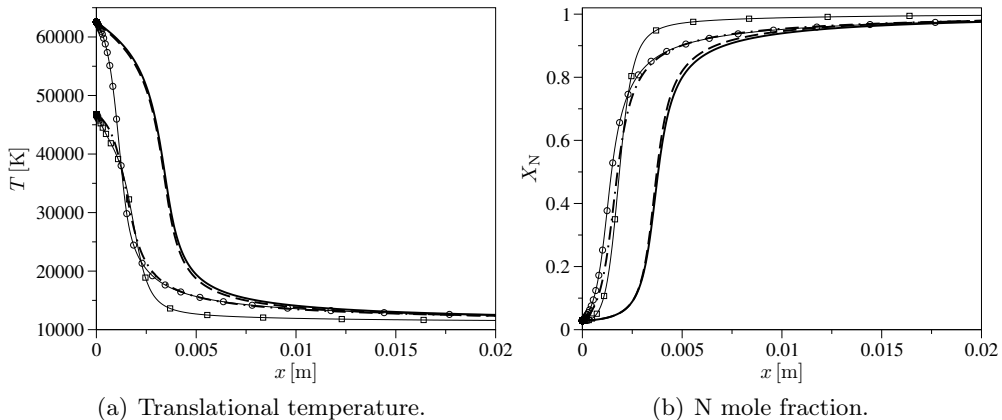


Figure 4.15: *RVC, BRVC(50), VC, MT and MTP model comparison. Translational temperature and N mole fraction evolution behind the shock wave ($p_\infty = 0.1$ torr and $u_\infty = 10$ km/s; unbroken lines RVC, dashed lines BRVC(50), dotted-dashed lines VC, lines with circles MT, lines with squares MTP).*

The sources of the slight discrepancy between the BRVC(50) and RVC models observed in fig. 4.15 have been further investigated by comparing the evolution behind the shock wave of the mass production and energy transfer terms (see fig. 4.16). The results show that the internal energy excitation is perfectly captured by the BRVC(50) model, while the dissociation rate is a bit overestimated. These results are consistent with the N_2 mole fraction evolution shown in fig. 4.15(b).

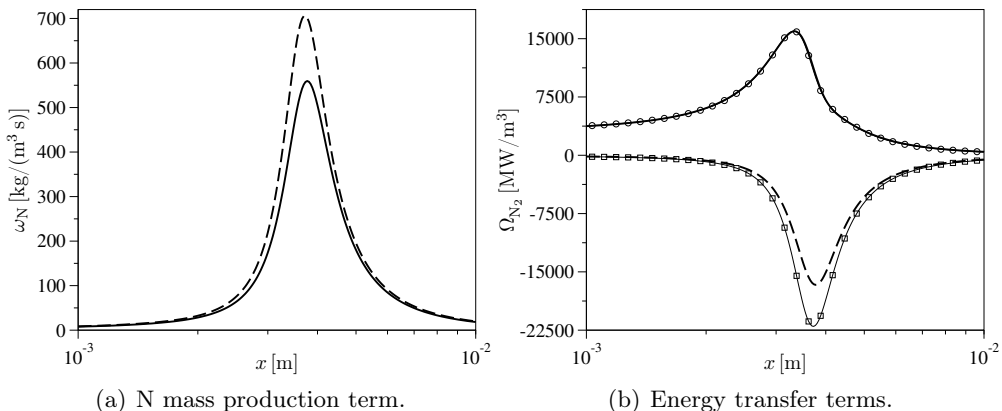


Figure 4.16: *RVC and BRVC(50) model comparison. Mass production and energy transfer term evolution behind the shock wave ($p_\infty = 0.1$ torr and $u_\infty = 10$ km/s; in (a) unbroken line RVC, dashed line BRVC(50); in (b) unbroken line $\Omega_{N_2}^{\text{tra-int}}$ RVC, dashed line $\Omega_{N_2}^{\text{dis-int}}$ RVC, line with circles $\Omega_{N_2}^{\text{tra-int}}$ BRVC(50), line with squares $\Omega_{N_2}^{\text{dis-int}}$ BRVC(50)).*

4.3.3 Bin Number Sensitivity Analysis for the BRVC and URVC Models

The comparison among the reduced models performed in sec. 4.3.2 has demonstrated that the BRVC and URVC models are the most accurate. However, the results shown in figs. 4.15-4.16 refer to a fixed number of energy bins (50). In order to assess the influence of the number of energy bins used on flow quantities, the solutions obtained for the number of energy bins given in tab. 4.3 have been compared with each other.

Figure 4.17 shows the temperatures and N mole fraction evolution behind the shock wave for different numbers of energy bins in the case of the BRVC model. Notice that the post-shock translational temperature depends on the number of energy bins. This is due to the non-linear temperature dependent term in the expression for the gas thermal energy density (see eq. (3.94)). In all the cases, both the translational and internal temperature approach the post-shock equilibrium value. The solutions obtained when using 2 and 5 energy bins tend to overestimate the dissociation rate, implying that a larger number should be used. This behavior could be partly due to the lower value of the post-shock translational temperature. The use of a larger number of energy bins does not introduce appreciable changes as can be seen from the small differences between the 20 and 100 energy bin solutions.

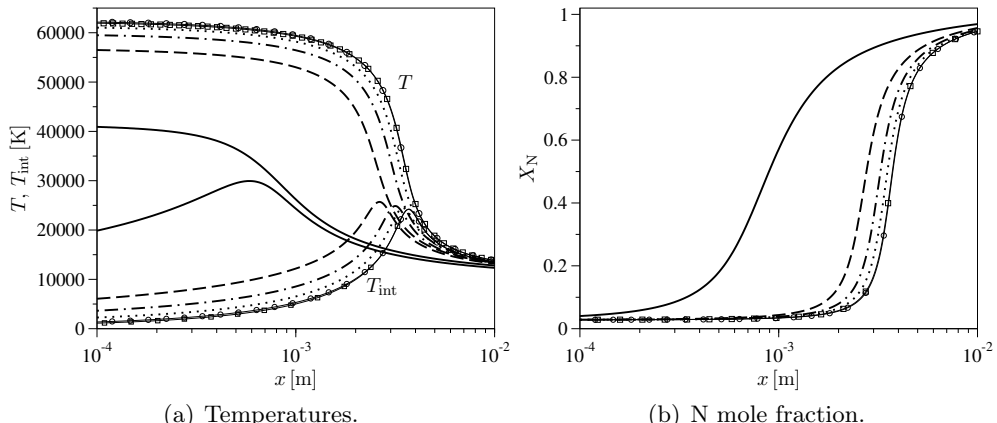


Figure 4.17: BRVC model. Bin number convergence study on the temperatures and the N mole fraction for the flow behind a normal shock wave ($p_\infty = 0.1$ torr and $u_\infty = 10$ km/s; unbroken lines BRVC(2), dashed lines BRVC(5), dotted-dashed lines BRVC(10), dotted lines BVRC(20), lines with circles BRVC(50), lines with squares BRVC(100)).

In the case of the URVC model, the sensitivity of the N mole fraction and translational temperature to the number of energy bins is similar to that observed for the BRVC model (with the difference that the post-shock translational temperature is no-longer bin number dependent). The situation for the internal

temperature is different, as shown in fig. 4.18. When using only 5 energy bins, the value obtained for the URVC model does not converge to the correct post-shock equilibrium value (11 420 K), as opposed to the case of the BVRC model. A higher number of energy bins is needed for obtaining a more physical evolution of the internal temperature. These results are due to the fact that (as shown in sec. 3.4.1) the URVC model does not allow to retrieve the equilibrium state (*i.e.* chemical composition and energy distribution). The present observations lead to the conclusion that the BRVC model should be preferred to the URVC model. This is especially true for computations that require to impose equilibrium conditions in some parts of the computational domain (such as in nozzle flows, shown in ch. 5).

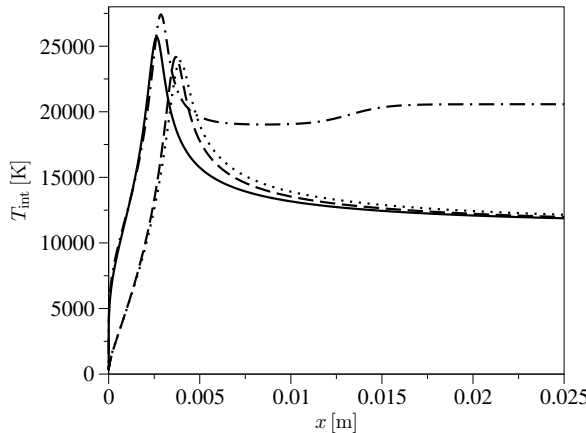


Figure 4.18: BRVC and URVC models. Internal temperature evolution behind the shock wave for different numbers of energy bins ($p_{\infty} = 0.1$ torr and $u_{\infty} = 10$ km/s; unbroken line BRVC(5), dashed line BRVC(50), dotted-dashed line URVC(5), dotted line URVC(50)).

4.4 Intermediate conclusions

This chapter has described the application of the RVC and reduced models (MT, VC, BRVC and URVC) to study non-equilibrium inviscid flows behind normal shock waves.

The numerical solutions obtained by means of the RVC model (sec. 4.2) have highlighted the importance of rotational non-equilibrium effects. In particular, it was found that the rates of vibrational and rotational excitation behind the shock wave become comparable for high-speed conditions. These results are consistent with those of Panesi et al. (2013) who used the RVC model in heat-bath calculations. The results obtained by means of the RVC model have also shown that exchange processes play an important role and cannot be neglected. The opposite behavior was found for predissociation, demonstrating that this process could be neglected for the development of the reduced models.

Rotational non-equilibrium effects have been investigated more in detail by analyzing the rovibrational energy level population distributions at different locations behind the shock (sec. 4.2.5). The extracted state-specific rotational temperatures have confirmed the lack of thermal equilibrium between the N₂ translational and rotational degrees of freedom. A careful inspection of the behavior of the rotational levels close to the ground-state has revealed the existence of a splitting according to odd and even rotational quantum numbers. The splitting was systematically observed for all low-lying vibrational states and was more pronounced for the vibrational ground-state (which experienced the biggest departure from rotational equilibrium).

The RVC model solution has been then compared with those obtained by means of the reduced models (MT, VC, BRVC and URVC). The comparison between the RVC and MT results (sec. 4.3.1) has shown that the MT model leads to a too fast dissociation. This behavior was due to the lack of QSS for the adopted free-stream conditions. After assessing the deficiencies of the MT model, the results obtained by means of the coarse-grained models (VC, BRVC and URVC) have been introduced (sec. 4.3.2). The VC model led to a too fast dissociation, due to the assumed rotational equilibrium. The BRVC and URVC models were in much better agreement with the RVC model, meaning that these coarse-grained models could automatically account for rotational non-equilibrium effects. A sensitivity analysis to the number of energy bins has shown that a correct description of flow quantities could be achieved by using only 20 energy bins. This led to the conclusion that the BRVC and URVC models should be preferred to the VC model for high-speed conditions. The differences between the BRVC and URVC models have been further investigated by looking at the internal temperature evolution (sec. 4.3.3). In the case of the BRVC model, the internal temperature approached the correct post-shock equilibrium value independently on the number of bins in used. A high number (50) was needed for the URVC model. The observed behavior is a direct consequence of the fact the BRVC model allows to retrieve equilibrium, as opposed to the URVC model. The use of the BRVC model should be preferred to the URVC model. The conclusions regarding the performances of the reduced models (MT, VC, BRVC and URVC) have been drawn based on the results obtained in a purely dissociating environment. In view of this, the application domain is enlarged in ch. 5, where the RVC and reduced models are applied to other benchmarks, such as nozzle and stagnation-line flows. This is also done with scope of having a deeper and more accurate understanding of the performances offered by the developed reduced models.

Chapter 5

CFD Solvers for Aerothermodynamic Flows

This chapter illustrates the application of the RVC and reduced models developed in ch. 3 to CFD solvers for aerothermodynamic flows. The scope of the analysis is: to gain insight on the dynamics of internal energy excitation and dissociation and to compare all the models in terms of accuracy and computational cost. The benchmarks considered here constitute a more realistic representation of actual aerothermodynamic flows compared to ch. 4.

The present chapter is structured as follows. Section 5.1 introduces the flow governing equations in conservation law form. The numerical methods are explained in sec. 5.2. After that, computational results are discussed. Section 5.3 focuses on quasi-one-dimensional nozzle flows. In sec. 5.4 the viscous flow along the stagnation line of blunt bodies is analyzed. Multi-dimensional applications are considered in sec. 5.5. Intermediate conclusions are given in sec. 5.6.

5.1 Governing Equations in Conservation Law Form

As shown in ch. 2, a hydrodynamic description of non-equilibrium flows is provided by the time-dependent, three-dimensional Navier-Stokes equations:

$$\frac{\partial \mathbf{U}}{\partial t} + \nabla_{\mathbf{x}} \cdot \underline{\mathcal{F}} - \nabla_{\mathbf{x}} \cdot \underline{\mathcal{F}}^d = \mathbf{S}. \quad (5.1)$$

When adopting the unified notation of sec. 3.5, the conservative variable and source term vectors, and the inviscid and diffusive flux tensors are:

$$\mathbf{U} = [\rho_N \quad \tilde{\rho}_\epsilon \quad \rho \mathbf{v} \quad \rho E]^T, \quad (5.2)$$

$$\mathbf{S} = [\omega_N \quad \omega_\epsilon \quad \mathbf{0}_3 \quad 0]^T, \quad (5.3)$$

$$\underline{\mathcal{F}} = [\rho_N \mathbf{v} \quad \tilde{\rho}_\epsilon \mathbf{v} \quad \rho \mathbf{v} \otimes \mathbf{v} + p \mathbf{I} \quad \rho \mathbf{v} H]^T, \quad (5.4)$$

$$\begin{aligned} \underline{\mathcal{F}}^d &= [-\rho_N \mathbf{v}_N^d \quad -\tilde{\rho}_\epsilon \mathbf{v}_\epsilon^d \quad \boldsymbol{\tau} \quad \boldsymbol{\tau} \mathbf{v} - \mathbf{q}]^T, \\ \epsilon &\in \mathcal{E}_{N_2}. \end{aligned} \quad (5.5)$$

In the Navier-Stokes equations (5.1), the constitutive relations for the stress tensor $\underline{\tau}$ and the heat flux vector \mathbf{q} are given by Newton's and Fourier's laws (3.117)-(3.118), respectively. The diffusion velocities are found by solving the Stefan-Maxwell equations (3.116). The thermodynamic properties, mass production terms and transport properties in eqs. (5.2)-(5.5) can be computed based on the contents of ch. 3.

In the present chapter, the following benchmarks are considered:

- Quasi-one-dimensional flows within converging-diverging nozzles (sec. 5.3),
- Flows along the stagnation line of blunt bodies (sec. 5.4),
- Inviscid axisymmetric flows (sec. 5.5).

Each case in the previous list is studied by applying *ad-hoc* simplifying assumptions to eq. (5.1). When this is done, a simpler form of the flow governing equations (5.1) is obtained. Sections 5.1.1-5.1.3 provide the conservation law form of the simplified governing equations.

5.1.1 Inviscid Quasi-One-Dimensional Nozzle Flows

The governing equations for an inviscid and quasi-one-dimensional flow within a nozzle of cross-sectional area distribution $A = A(x)$ (where x is the position along the nozzle axis), can be obtained based on the Navier-Stokes equations (5.1) by neglecting the transport fluxes and applying the hypothesis of quasi-one-dimensional gas motion. The set of equations obtained by using this procedure can be written in conservation law form as (Hirsch 1990):

$$\frac{\partial \mathbf{U}}{\partial t} + \frac{\partial \mathbf{F}}{\partial x} = \mathbf{S}, \quad (5.6)$$

where the vector \mathbf{F} is the inviscid flux vector. The source term vector is the sum of two distinct contributions:

$$\mathbf{S} = \mathbf{S}^c + \mathbf{S}^k. \quad (5.7)$$

The convective source term vector \mathbf{S}^c accounts for the nozzle cross-sectional area variation. The vector \mathbf{S}^k accounts for the kinetic processes within the flow (internal energy excitation and dissociation). The conservative variable, inviscid flux and source term vectors in eqs. (5.6)-(5.7) are:

$$\mathbf{U} = [\rho_N \ \tilde{\rho}_\epsilon \ \rho u \ \rho E]^T, \quad (5.8)$$

$$\mathbf{F} = [\rho_N u \ \tilde{\rho}_\epsilon u \ p + \rho u^2 \ \rho u H]^T, \quad (5.9)$$

$$\mathbf{S}^c = -\frac{\partial \ln A}{\partial x} [\rho_N u \ \tilde{\rho}_\epsilon u \ \rho u^2 \ \rho u H]^T, \quad (5.10)$$

$$\mathbf{S}^k = [\omega_N \ \tilde{\omega}_\epsilon \ 0 \ 0]^T, \quad (5.11)$$

$$\epsilon \in \mathcal{E}_{N_2}.$$

5.1.2 Stagnation-Line Flows

The flow along the stagnation-line of blunt bodies can be studied by using the quasi-one-dimensional Navier-Stokes equations derived by Klomfass and Müller (1997). The derivation starts by writing eqs. (5.1) in spherical (or cylindrical) coordinates and by assuming a functional dependence for the flow variables:

$$\rho_N = \overline{\rho_N}(r), \quad \tilde{\rho}_\epsilon = \overline{\tilde{\rho}_\epsilon}(r), \quad \epsilon \in \mathcal{E}_{N_2}, \quad (5.12)$$

$$u = \overline{u}(r) \cos \theta, \quad v = \overline{v}(r) \sin \theta, \quad T = \overline{T}(r), \quad p - p_\infty = \overline{p}(r) \cos^2 \theta, \quad (5.13)$$

where quantities u and v are the axial and radial velocity components, respectively, and quantity r is the distance from the stagnation-point. The θ angle is measured with respect to the stagnation-line. The stagnation-line equations are obtained by substituting eqs. (5.12)-(5.13) in eq. (5.1), and taking then the limit $\theta \rightarrow 0$. The obtained set of one-dimensional equations can be written as system of time-dependent hyperbolic-parabolic conservation laws (see below). This is particularly advantageous, as it allows for the use of shock-capturing methods in conjunction with a time-marching approach for reaching steady-state conditions (Hirsch 1990). Depending on the coordinate system in use, two formulations can be obtained: spherical and cylindrical. In this thesis, the spherical formulation has been adopted as it provides a more realistic representation of the flow around the stagnation-point of re-entry vehicles.

Alternative formulations to that of Klomfass and Müller (1997) exist, such as viscous shock-layers (Thivet 1992; Gupta and Lee 1995). In viscous shock layers, the governing equations cannot be cast in a conservative form. This obliges to resort to shock-fitting procedures for computing the jumps in flow variables at the shock location. These reasons explain why the formulation of Klomfass and Müller (1997) was preferred to viscous shock-layers.

The stagnation-line equations obtained by Klomfass and Müller (1997) are:

$$\frac{\partial \mathbf{U}}{\partial t} + \frac{\partial \mathbf{F}}{\partial r} - \frac{\partial \mathbf{F}^d}{\partial r} = \mathbf{S}. \quad (5.14)$$

The conservative variable, inviscid flux and diffusive flux vectors are:

$$\mathbf{U} = [\rho_N \quad \tilde{\rho}_\epsilon \quad \rho u \quad \rho v \quad \rho E]^T, \quad (5.15)$$

$$\mathbf{F} = [\rho_N u \quad \tilde{\rho}_\epsilon u \quad p + \rho u^2 \quad \rho u v \quad \rho u H]^T, \quad (5.16)$$

$$\begin{aligned} \mathbf{F}^d &= [-\rho_N u_N^d \quad -\tilde{\rho}_\epsilon \tilde{u}_\epsilon^d \quad \tau_{rr} \quad \tau_{r\theta} \quad \tau_{rr} u - q]^T, \\ \epsilon &\in \mathcal{E}_{N_2}, \end{aligned} \quad (5.17)$$

where the overbar symbol has been omitted for the sake of clarity. It is important to mention that only the axial velocity component u (\overline{u} in eq. (5.12)) contributes to the gas specific kinetic energy (*i.e.* $e^{\text{kin}} = u^2/2$). This peculiarity results from the procedure leading to the stagnation-line equations and must be taken into account when deriving the eigensystem associated to the hyperbolic part of eq. (5.14) (see app. C for more details).

The source term vector in eq. (5.14) is the sum of three distinct contributions:

$$\mathbf{S} = \mathbf{S}^c + \mathbf{S}^d + \mathbf{S}^k. \quad (5.18)$$

As it was in sec. 5.1.1, the kinetic source term vector \mathbf{S}^k accounts for the kinetic processes within the flow. The convective and diffusive source term vectors (\mathbf{S}^c and \mathbf{S}^d , respectively) are additional source terms resulting from the procedure leading to the stagnation-line equations:

$$\begin{aligned} \mathbf{S}^c = & -\frac{1}{r} \left[\begin{array}{cccc} 2\rho_N(u+v) & 2\tilde{\rho}_\epsilon(u+v) & 2\rho u(u+v) \\ 3\rho v(u+v) - 2(p-p_\infty) & 2\rho(u+v)H \end{array} \right]^T, \end{aligned} \quad (5.19)$$

$$\begin{aligned} \mathbf{S}^d = & -\frac{1}{r} \left[\begin{array}{cccc} 2\rho_N u_N^d & 2\tilde{\rho}_\epsilon \tilde{u}_\epsilon^d & -2(\tau_{rr} + \tau_{r\theta} - \tau_{\theta\theta}) & -(3\tau_{r\theta} - \tau_{\theta\theta}) \\ -2(\tau_{rr}u + \tau_{r\theta}u + \tau_{\theta\theta}v - q) \end{array} \right]^T, \end{aligned} \quad (5.20)$$

$$\begin{aligned} \mathbf{S}^k = & \left[\begin{array}{ccccc} \omega_N & \tilde{\omega}_\epsilon & 0 & 0 & 0 \end{array} \right]^T, \\ \epsilon \in & \mathcal{E}_{N_2}. \end{aligned} \quad (5.21)$$

In the stagnation-line formulation of Klomfass and Müller (1997), the constitutive relations for the stress tensor and the heat flux vector reduce to:

$$\tau_{rr} = \frac{4}{3}\eta \left(\frac{\partial u}{\partial r} - \frac{u+v}{r} \right), \quad (5.22)$$

$$\tau_{r\theta} = \eta \left(\frac{\partial v}{\partial r} - \frac{u+v}{r} \right), \quad (5.23)$$

$$\tau_{\theta\theta} = -\frac{1}{2}\tau_{rr}, \quad (5.24)$$

$$q = \rho_N u_N^d h_N + \sum_{\epsilon \in \mathcal{E}_{N_2}} \tilde{\rho}_\epsilon \tilde{u}_\epsilon^d \tilde{h}_\epsilon - \lambda \frac{\partial T}{\partial r}. \quad (5.25)$$

5.1.3 Inviscid Axisymmetric Flows

The governing equations for inviscid axisymmetric flows can be obtained based on the Navier-Stokes equations (5.1) by neglecting the transport fluxes and by assuming that the flow is axisymmetric. After some algebraic manipulation, the conservation law form of the governing equations is obtained:

$$\frac{\partial y\mathbf{U}}{\partial t} + \frac{\partial y\mathbf{F}}{\partial x} + \frac{\partial y\mathbf{G}}{\partial y} = \mathbf{S}, \quad (5.26)$$

where quantities x and y are the axial and radial coordinates, respectively. The conservative variable and inviscid flux vectors are:

$$\mathbf{U} = \left[\begin{array}{ccccc} \rho_N & \tilde{\rho}_\epsilon & \rho u & \rho v & \rho E \end{array} \right]^T, \quad (5.27)$$

$$\mathbf{F} = \left[\begin{array}{ccccc} \rho_N u & \tilde{\rho}_\epsilon u & p + \rho u^2 & \rho uv & \rho u H \end{array} \right]^T, \quad (5.28)$$

$$\mathbf{G} = \left[\begin{array}{ccccc} \rho_N v & \tilde{\rho}_\epsilon v & \rho uv & p + \rho v^2 & \rho v H \end{array} \right]^T, \quad (5.29)$$

$$\epsilon \in \mathcal{E}_{N_2},$$

where u and v are the axial and radial velocity components, respectively. The source term vector in eq. (5.26) is made of two distinct contributions:

$$\mathbf{S} = \mathbf{S}^c + y\mathbf{S}^k. \quad (5.30)$$

As it was in secs. 5.1.1-5.1.2, the kinetic source term vector \mathbf{S}^k accounts for the kinetic processes within the flow. The convective (or axisymmetric) source term vector \mathbf{S}^c is an additional source term resulting from the procedure leading to the axisymmetric equations (5.26):

$$\mathbf{S}^c = [0 \ \tilde{0}_\epsilon \ 0 \ p \ 0]^T, \quad (5.31)$$

$$\mathbf{S}^k = [\omega_N \ \tilde{\omega}_\epsilon \ 0 \ 0 \ 0]^T, \quad (5.32)$$

$$\epsilon \in \mathcal{E}_{N_2},$$

where the symbol $\tilde{0}_\epsilon$ indicates the component ϵ of the null vector $\mathbf{0}_{\mathcal{N}_{N_2}}$.

5.2 Numerical Methods

5.2.1 1D Flows

The conservation law form of the governing equations (5.6) and (5.14) for quasi-one-dimensional nozzle and stagnation-line flows, respectively, are formally identical except for the presence of diffusive terms (flux and source) in the stagnation-line case. This means that the discretization procedure for the quasi-one-dimensional nozzle flow governing equations can be obtained based on that for the stagnation-line case by neglecting the diffusive terms, and by replacing the r coordinate with the x coordinate.

The numerical procedure used for solving eq. (5.14) is based on the application of the method-of-lines (MOL). The latter consists in separating the spatial and temporal discretization (Hirsch 1990).

Spatial Discretization

The spatial discretization of eq. (5.14) is performed by means of the Finite Volume (FV) method (Hirsch 1990). Its application leads to the following ODE describing the time evolution of the conservative variable vector of the cell i :

$$\frac{\partial \mathbf{U}_i}{\partial t} \Delta r_i + \tilde{\mathbf{F}}_{i+\frac{1}{2}} - \tilde{\mathbf{F}}_{i-\frac{1}{2}} - \left(\mathbf{F}_{i+\frac{1}{2}}^d - \mathbf{F}_{i-\frac{1}{2}}^d \right) = \left(\mathbf{S}_i^c + \mathbf{S}_i^d + \mathbf{S}_i^k \right) \Delta r_i, \quad (5.33)$$

with the cell volume (length) $\Delta r_i = r_{i+1/2} - r_{i-1/2}$. The numerical inviscid flux $\tilde{\mathbf{F}}_{i+1/2}$ is computed by means of Roe's approximate Riemann solver (Roe 1981):

$$\tilde{\mathbf{F}}_{i+\frac{1}{2}} = \frac{1}{2} [\mathbf{F}(\mathbf{U}_{i+1}) + \mathbf{F}(\mathbf{U}_i)] - \frac{1}{2} |\mathbf{A}(\hat{\mathbf{U}})| (\mathbf{U}_{i+1} - \mathbf{U}_i). \quad (5.34)$$

The dissipation matrix $|\mathbf{A}(\hat{\mathbf{U}})|$ is defined as $|\mathbf{A}(\hat{\mathbf{U}})| = \mathbf{R}(\hat{\mathbf{U}})|\boldsymbol{\Lambda}(\hat{\mathbf{U}})|\mathbf{L}(\hat{\mathbf{U}})$, where $\boldsymbol{\Lambda}$, \mathbf{R} and \mathbf{L} are, respectively, the eigenvalue, right eigenvector and left eigenvector matrices associated to the inviscid flux Jacobian matrix $\mathbf{A} = \partial \mathbf{F} / \partial \mathbf{U} = \mathbf{R} \boldsymbol{\Lambda} \mathbf{L}$ (Gnoffo et al. 1989; Hirsch 1990; Candler and MacCormack 1991). The expressions for the matrices $\boldsymbol{\Lambda}$, \mathbf{R} and \mathbf{L} (*i.e.* the eigensystem associated to the Jacobian \mathbf{A}) are provided in app. C. The hat symbol in eq. (5.34) indicates that the conservative variable vector must be evaluated at Roe's averaged state. In the present thesis, Roe's averaged state is computed based on the linearization proposed by Prabhu (1994). The entropy fix of Harten and Hyman (Hirsch 1990) is used in order to prevent the occurrence of expansion shocks.

The diffusive flux and source term ($\mathbf{F}_{i+1/2}^d$ and \mathbf{S}_i^d , respectively) are both evaluated in terms of primitive variables:

$$\mathbf{P} = [\rho_N \quad \tilde{\rho}_\epsilon \quad u \quad v \quad T]^T, \quad \epsilon \in \mathcal{E}_{N_2}. \quad (5.35)$$

In the computation of the diffusive flux $\mathbf{F}_{i+1/2}^d$, the value and the gradient of the generic primitive variable p at the interface $i + 1/2$ are computed according to a weighted average and a central finite difference approximation, respectively:

$$p_{i+\frac{1}{2}} = \frac{p_{i+1}\Delta r_{i+1} + p_i\Delta r_i}{\Delta r_{i+1} + \Delta r_i}, \quad \left(\frac{\partial p}{\partial r} \right)_{i+\frac{1}{2}} = 2 \left(\frac{p_{i+1} - p_i}{\Delta r_{i+1} + \Delta r_i} \right). \quad (5.36)$$

In the computation of the diffusive source term \mathbf{S}_i^d , the gradient of the generic primitive variable p at the centroid location of the cell i is computed according to a two point central finite-difference approximation:

$$\left(\frac{\partial p}{\partial r} \right)_i = 2 \left(\frac{p_{i+1} - p_{i-1}}{\Delta r_{i+1} + 2\Delta r_i + \Delta r_{i-1}} \right). \quad (5.37)$$

Boundary Conditions and Reconstruction

Boundary conditions are implemented through ghost cells (Hirsch 1990) and are imposed in terms of primitive variables (5.35).

Second order accuracy in space is achieved through an upwind variable reconstruction at cell interface. For the sake of robustness, the reconstruction is performed on primitive variables (Candler and MacCormack 1991). The reconstructed values of the generic primitive variable p at the left (L) and right (R) sides of the interface $i + 1/2$ are computed by means of the Monotone Upstream Centered Schemes for Conservation Laws (MUSCL) method of van Leer (1979):

$$p_{i+1/2}^L = p_i + \frac{1}{2} \phi(r_i^L) (p_i - p_{i-1}), \quad (5.38)$$

$$p_{i+1/2}^R = p_{i+1} - \frac{1}{2} \phi(1/r_{i+1}^R) (p_{i+2} - p_{i+1}), \quad (5.39)$$

where $\phi = \phi(r)$ is a slope limiter function (van Leer 1979; Hirsch 1990). The left and right ratios of consecutive differences are computed as:

$$r_i^L = \frac{p_{i+1} - p_i}{p_i - p_{i-1}}, \quad r_{i+1}^R = \frac{p_{i+2} - p_{i+1}}{p_{i+1} - p_i}. \quad (5.40)$$

In the present thesis, the slope limiter of van Albada et al. (1982) has been used. After applying eqs. (5.38)-(5.40), the reconstructed left and right conservative variables ($\mathbf{U}_{i+1/2}^L$ and $\mathbf{U}_{i+1/2}^R$, respectively) are found, and the second-order numerical flux is then computed as $\tilde{\mathbf{F}}_{i+1/2} = \tilde{\mathbf{F}}_{i+1/2}(\mathbf{U}_{i+1/2}^L, \mathbf{U}_{i+1/2}^R)$.

Temporal Discretization

Equation (5.33) is integrated in time by means of the implicit Backward-Euler (BE) method (Gear 1971; Hirsch 1990):

$$\frac{\delta \mathbf{U}_i^n}{\Delta t_i} \Delta r_i + \tilde{\mathbf{F}}_{i+\frac{1}{2}}^{n+1} - \tilde{\mathbf{F}}_{i-\frac{1}{2}}^{n+1} - \left(\mathbf{F}_{i+\frac{1}{2}}^{d,n+1} - \mathbf{F}_{i-\frac{1}{2}}^{d,n+1} \right) = \left(\mathbf{S}_i^{c,n+1} + \mathbf{S}_i^{d,n+1} + \mathbf{S}_i^{k,n+1} \right) \Delta r_i, \quad (5.41)$$

with $\delta \mathbf{U}_i^n = \mathbf{U}_i^{n+1} - \mathbf{U}_i^n$. The local time-step Δt_i is computed based on the Courant-Friedrichs-Lowy (CFL) number according to (Blazek 2006):

$$\Delta t_i = \frac{\text{CFL } \Delta r_i}{\left[|u| + c + \frac{1}{\Delta r} \max \left(\frac{4\eta}{3\rho}, \frac{\lambda}{C_v} \right) \right]_i}, \quad (5.42)$$

where the quantities c and C_v are the gas frozen speed of sound and the gas volumetric specific heat at constant volume, respectively (their expressions are given in app. C). The viscous contribution to the time-step (given by the second term at the denominator of eq. (5.42)) is needed in order prevent numerical instabilities in zones such as boundary layers, where the diffusive part of eq. (5.14) becomes dominant. Equation (5.42) has been derived based on heuristic considerations and alternative formulation can be found in the literature (Hirsch 1990; Plectcher et al. 2011). In order to advance the solution from the time-level n to the time-level $n + 1$, the flux and source terms in eq. (5.41) are linearized around the solution at the time-level n by means of a Taylor-series expansion. For the sake of robustness, the effects of the reconstruction are not considered while performing the linearization. Depending on the terms that are retained in the linearization process, two time-integration methods result: a) fully implicit method and b) point-implicit method.

Fully Implicit Method The numerical inviscid flux is linearized according to the formulation of Liou and van Leer (1988):

$$\tilde{\mathbf{F}}_{i+\frac{1}{2}}^{n+1} \simeq \tilde{\mathbf{F}}_{i+\frac{1}{2}}^n + \mathbf{A}_i^{+,n} \delta \mathbf{U}_i^n + \mathbf{A}_{i+1}^{-,n} \delta \mathbf{U}_{i+1}^n, \quad (5.43)$$

where the positive-negative split Jacobians are $\mathbf{A}^\pm = \mathbf{R} \boldsymbol{\Lambda}^\pm \mathbf{L}$ (Liou and van Leer 1988; Hirsch 1990) and their expressions are given in app. D. A popular alternative to eq. (5.43) is the approximation proposed by Jameson and Yoon (1987) where the matrices \mathbf{A}^\pm are replaced with the simpler expression

$1/2 [\mathbf{A} \pm (|u| + c)\mathbf{I}]$, where \mathbf{I} is the identity matrix. However, calculations of both nozzle and stagnation-line flows have shown that eq. (5.43) enables to obtain a significant convergence speed-up compared to the approximation of Jameson and Yoon (1987).

The linearization of the convective and kinetic source terms is straightforward:

$$\mathbf{S}_i^{c\,n+1} \simeq \mathbf{S}_i^{c\,n} + \frac{\partial \mathbf{S}_i^{c\,n}}{\partial \mathbf{U}_i} \delta \mathbf{U}_i^n, \quad (5.44)$$

$$\mathbf{S}_i^{k\,n+1} \simeq \mathbf{S}_i^{k\,n} + \frac{\partial \mathbf{S}_i^{k\,n}}{\partial \mathbf{U}_i} \delta \mathbf{U}_i^n. \quad (5.45)$$

The Jacobian matrices $\partial \mathbf{S}^c / \partial \mathbf{U}$ and $\partial \mathbf{S}^k / \partial \mathbf{U}$ are evaluated analytically in order to enhance stability. Their expressions are given in app. E.

The linearization of the diffusive flux and source term is more delicate and is performed in two steps. The first step consists in writing the diffusive flux and source term as the sum of a first term, which depends linearly on the gradient of conservative variables, and a second non-linear term as:

$$\mathbf{F}_{i+\frac{1}{2}}^{d\,n} = \mathbf{A}_{i+\frac{1}{2}}^{d\,n} \left(\frac{\partial \mathbf{U}}{\partial r} \right)_{i+\frac{1}{2}}^n + \mathbf{B}_{i+\frac{1}{2}}^{d\,n}, \quad (5.46)$$

$$\mathbf{S}_i^{d\,n} = \mathbf{A}_{s\,i}^{d\,n} \left(\frac{\partial \mathbf{U}}{\partial r} \right)_i^n + \mathbf{B}_{s\,i}^{d\,n}. \quad (5.47)$$

To facilitate the linearization procedure, the matrices \mathbf{A}^d and \mathbf{A}_s^d are computed by assuming a Fickian diffusion model based on self-consistent effective diffusion coefficients (Ramshaw and Chang 1996). The expressions for the matrices \mathbf{A}^d and \mathbf{A}_s^d and the vectors \mathbf{B}^d and \mathbf{B}_s^d are given in app. F. The gradients of the conservative variables in eqs. (5.46)-(5.47) are computed according to eqs. (5.36)-(5.37). The expressions obtained are then linearized around the time-level n as follows:

$$\mathbf{F}_{i+\frac{1}{2}}^{d\,n+1} \simeq \mathbf{F}_{i+\frac{1}{2}}^{d\,n} + 2\mathbf{A}_{i+\frac{1}{2}}^{d\,n} \left(\frac{\delta \mathbf{U}_{i+1}^n - \delta \mathbf{U}_i^n}{\Delta r_{i+1} + \Delta r_i} \right) + \frac{\partial \mathbf{B}_{i+1/2}^{d\,n}}{\partial \mathbf{U}_i^n} \delta \mathbf{U}_i^n + \frac{\partial \mathbf{B}_{i+1/2}^{d\,n}}{\partial \mathbf{U}_{i+1}^n} \delta \mathbf{U}_{i+1}^n, \quad (5.48)$$

$$\mathbf{S}_i^{d\,n+1} \simeq \mathbf{S}_i^{d\,n} + 2\mathbf{A}_{s\,i}^{d\,n} \left(\frac{\delta \mathbf{U}_{i+1}^n - \delta \mathbf{U}_{i-1}^n}{\Delta r_{i+1} + 2\Delta r_i + \Delta r_{i-1}} \right) + \frac{\partial \mathbf{B}_{s\,i}^{d\,n}}{\partial \mathbf{U}_i^n} \delta \mathbf{U}_i^n. \quad (5.49)$$

Notice that the matrices \mathbf{A}^d and \mathbf{A}_s^d are kept frozen while performing the linearization. In eq. (5.48), the last two terms on the right-hand-side are further approximated to:

$$\frac{\partial \mathbf{B}_{i+1/2}^{d\,n}}{\partial \mathbf{U}_i^n} \simeq \frac{\partial \mathbf{B}_i^{d\,n}}{\partial \mathbf{U}_i^n}, \quad \frac{\partial \mathbf{B}_{i+1/2}^{d\,n}}{\partial \mathbf{U}_{i+1}^n} \simeq \frac{\partial \mathbf{B}_{i+1}^{d\,n}}{\partial \mathbf{U}_{i+1}^n}. \quad (5.50)$$

The substitution of eqs. (5.43)-(5.50) in eq. (5.41) leads to a block-tridiagonal linear algebraic system to be solved at each time-step:

$$\mathbf{M}_{L\,i}^n \delta \mathbf{U}_{i-1}^n + \mathbf{M}_{C\,i}^n \delta \mathbf{U}_i^n + \mathbf{M}_{R\,i}^n \delta \mathbf{U}_{i+1}^n = -\tilde{\mathbf{R}}_i^n, \quad (5.51)$$

where the left, center and right block matrices, and the right-hand-side residual have the following expressions:

$$\mathbf{M}_{L,i} = \frac{2\Delta r_i \mathbf{A}_{s,i}^d}{(\Delta r_{i+1} + 2\Delta r_i + \Delta r_{i-1})} - \frac{2\mathbf{A}_{i-1/2}^d}{(\Delta r_i + \Delta r_{i-1})} + \frac{\partial \mathbf{B}_{i-1}^d}{\partial \mathbf{U}_{i-1}} - \mathbf{A}_{i-1}^+, \quad (5.52)$$

$$\begin{aligned} \mathbf{M}_{C,i} = & \left[\frac{\mathbf{I}}{\Delta t_i} - \left(\frac{\partial \mathbf{S}_i^k}{\partial \mathbf{U}_i} + \frac{\partial \mathbf{S}_i^c}{\partial \mathbf{U}_i} + \frac{\partial \mathbf{B}_{s,i}^d}{\partial \mathbf{U}_i} \right) \right] \Delta r_i + |\mathbf{A}_i| + \\ & \frac{2\mathbf{A}_{i+1/2}^d}{(\Delta r_{i+1} + \Delta r_i)} + \frac{2\mathbf{A}_{i-1/2}^d}{(\Delta r_i + \Delta r_{i-1})}, \end{aligned} \quad (5.53)$$

$$\mathbf{M}_{R,i} = -\frac{2\Delta r_i \mathbf{A}_{s,i}^d}{(\Delta r_{i+1} + 2\Delta r_i + \Delta r_{i-1})} - \frac{2\mathbf{A}_{i+1/2}^d}{(\Delta r_{i+1} + \Delta r_i)} - \frac{\partial \mathbf{B}_{i+1}^d}{\partial \mathbf{U}_{i+1}} + \mathbf{A}_{i+1}^-, \quad (5.54)$$

$$\tilde{\mathbf{R}}_i = \tilde{\mathbf{F}}_{i+\frac{1}{2}} - \tilde{\mathbf{F}}_{i-\frac{1}{2}} - \left(\mathbf{F}_{i+\frac{1}{2}}^d - \mathbf{F}_{i-\frac{1}{2}}^d \right) - \left(\mathbf{S}_i^c + \mathbf{S}_i^d + \mathbf{S}_i^k \right) \Delta r_i. \quad (5.55)$$

The folding of the boundary conditions in the block matrices $\mathbf{M}_{L,i}$, $\mathbf{M}_{C,i}$ and $\mathbf{M}_{R,i}$ is performed as suggested by Candler and MacCormack (1991). The block-tridiagonal system in eq. (5.51) is solved by means of Thomas' algorithm (Hirsch 1990) and the solution updated at the time-level $n + 1$:

$$\mathbf{U}_i^{n+1} = \mathbf{U}_i^n + \delta \mathbf{U}_i^n. \quad (5.56)$$

This process is continued until steady-state is not reached.

Point-Implicit Method In the case of a point-implicit method, only the Jacobian matrices associated to the cell i are retained while performing the linearization. This is equivalent to set to zero the matrices $\mathbf{M}_{L,i}$ and $\mathbf{M}_{R,i}$ in eq. (5.51). In this way, at each time-step, the solution variation $\delta \mathbf{U}_i$ can be computed independently for each cell according to:

$$\mathbf{M}_{C,i}^n \delta \mathbf{U}_i^n = -\tilde{\mathbf{R}}_i^n. \quad (5.57)$$

Once eq. (5.57) applied for each cell, the solution update readily follows from eq. (5.56). The advantage of a point-implicit method lies in its low memory requirements compared to a fully implicit method. This property is used for applications of the RVC model to expanding flows in sec. 5.3.1. Moreover, a point-implicit method is also less demanding in terms of programming efforts, compared to a fully implicit method. This is due to the fact the solution update in a point-implicit method does not involve the solution of a linear algebraic system (*i.e.* only a local matrix inversion is required). These positive aspects are counterbalanced by more stringent stability limits which become quite severe for viscous flows. Indeed, the CFL number cannot exceed, in general, values of the order of 1-2 and 0.1-0.5 for inviscid and viscous flows, respectively.

5.2.2 2D Flows

Numerical solutions of eq. (5.26) are obtained by means of a 2D structured, multi-block and parallel inviscid FV solver developed by Kapper (2009). Even in this case, the MOL is used. Only the main characteristics of the solver are given in this section. For more details the reader is referred to the PhD thesis of Kapper (2009) and to the papers of Kapper and Cambier (2011a; 2011b).

Spatial Discretization

The computational domain is discretized by using structured grids. Figure 5.1 provides the node and cell ordering convention.

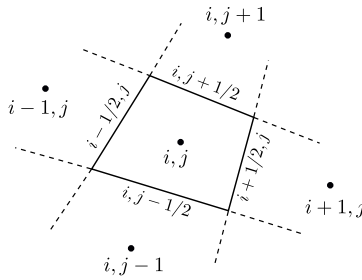


Figure 5.1: Node and cell ordering convention in the 2D structured grid code in use.

The spatial discretization of eq. (5.26) is performed by applying the FV method to each i, j cell of the domain. This leads to the following ODE for the time evolution of the conservative variable vector of the cell i, j :

$$\frac{\partial \mathbf{U}_{i,j}}{\partial t} A_{i,j} = -\tilde{\mathbf{R}}_{i,j}, \quad (5.58)$$

with $A_{i,j}$ being the cell volume (area). The right-hand-side residual can be split as $\tilde{\mathbf{R}}^{i,j} = \tilde{\mathbf{R}}_{c,i,j} + \tilde{\mathbf{R}}_{s,i,j}$, where the convective and source term contributions are:

$$\tilde{\mathbf{R}}_{c,i,j} = \left(ly \tilde{\mathbf{F}}_n \right)_{i+\frac{1}{2},j} + \left(ly \tilde{\mathbf{F}}_n \right)_{i-\frac{1}{2},j} + \left(ly \tilde{\mathbf{F}}_n \right)_{i,j+\frac{1}{2}} + \left(ly \tilde{\mathbf{F}}_n \right)_{i,j-\frac{1}{2}}, \quad (5.59)$$

$$\tilde{\mathbf{R}}_{s,i,j} = -\mathbf{S}_{i,j} A_{i,j}, \quad \mathbf{S}_{i,j} = \left(\mathbf{S}^c + y \mathbf{S}^k \right)_{i,j}, \quad (5.60)$$

where the symbol l is used to indicate the cell face area (length). The numerical inviscid flux $\tilde{\mathbf{F}}_{n,i+1/2,j}$ is computed by means of Roe's approximate Riemann solver (Roe 1981):

$$\tilde{\mathbf{F}}_{n,i+\frac{1}{2},j} = \frac{1}{2} [\mathbf{F}_n(\mathbf{U}_{i+1,j}) + \mathbf{F}_n(\mathbf{U}_{i,j})] - \frac{1}{2} |\mathbf{A}_n(\hat{\mathbf{U}})| (\mathbf{U}_{i+1,j} - \mathbf{U}_{i,j}). \quad (5.61)$$

The normal inviscid flux is given by $\mathbf{F}_n = \mathbf{F}_n x + \mathbf{G}_n y$, where n_x and n_y are the x and y components of the outward unit normal vector \mathbf{n} of the interface $i+1/2, j$, respectively. The dissipation matrix is $|\mathbf{A}_n(\hat{\mathbf{U}})| = \mathbf{R}_n(\hat{\mathbf{U}}) |\Lambda_n(\hat{\mathbf{U}})| \mathbf{L}_n(\hat{\mathbf{U}})$, where

Λ_n , \mathbf{R}_n and \mathbf{L}_n are, respectively, the eigenvalue, right eigenvector and left eigenvector matrices of the projected inviscid flux Jacobian matrix $\mathbf{A}_n = \partial \mathbf{F}_n / \partial \mathbf{U} = \mathbf{R}_n \Lambda_n \mathbf{L}_n$. The Roe averaged state is computed, as in sec. 5.2.1, based on the linearization of Prabhu (1994). Multi-dimensional applications of Roe's approximate Riemann solver can potentially lead to undesired effects, such as the carbuncle phenomenon and odd-even decoupling (Quirk 1994). These may be cured by *ad-hoc* fixes. In the present work, a different approach has been used. As recognized by Quirk (1994), the previous shortcomings can be avoided through a targeted application of the Harten-Lax-van Leer-Einfeldt (HLLE) approximate Riemann solver (Einfeldt et al. 1991):

$$\tilde{\mathbf{F}}_{n,i+\frac{1}{2},j} = \frac{b^+ \mathbf{F}_n(\mathbf{U}_{i+1,j}) - b^- \mathbf{F}_n(\mathbf{U}_{i,j})}{b^+ - b^-} + \frac{b^+ b^-}{b^+ - b^-} (\mathbf{U}_{i+1,j} - \mathbf{U}_{i,j}). \quad (5.62)$$

The upwind wave speeds are defined as:

$$b^+ = \max \left[0, (V_n + c)_{i+1,j}, \hat{V}_n + \hat{c} \right], \quad (5.63)$$

$$b^- = \min \left[0, (V_n - c)_{i,j}, \hat{V}_n - \hat{c} \right], \quad (5.64)$$

where the normal velocity is $V_n = u n_x + v n_y$. The use of the HLLE numerical flux is activated when the interface non-dimensional pressure difference $|p_{i+1,j} - p_{i,j}| / \min(p_{i+1,j}, p_{i,j})$ is greater than a threshold critical value (Quirk 1994). For a more detailed discussion, the reader is referred to the paper of Quirk (1994) and the PhD thesis of Kapper (2009).

Boundary Conditions and Reconstruction

Boundary conditions are implemented through ghost cells (Hirsch 1990) and are imposed in terms of primitive variables.

High-order spatial resolution is achieved by evaluating the inviscid flux at a reconstructed state at cell interface. The reconstruction is performed on characteristic variables $\mathbf{W} = \mathbf{LU}$ through a parabolic interpolation (Suresh and Huynh 1997). Referring to the a one-dimensional and uniform mesh example, the reconstructed characteristic variables at the interfaces $i \pm 1/2$ are found via:

$$\mathbf{W}_{i-\frac{1}{2}} = \frac{1}{6}(2\mathbf{W}_{i-1} + 5\mathbf{W}_i - \mathbf{W}_{i+1}), \quad (5.65)$$

$$\mathbf{W}_{i+\frac{1}{2}} = \frac{1}{6}(2\mathbf{W}_{i+1} + 5\mathbf{W}_i - \mathbf{W}_{i-1}). \quad (5.66)$$

The use of eqs. (5.65)-(5.66) makes the scheme third-order accurate in space. In order to prevent the occurrence of instabilities, a limiting procedure is required and the reconstructed characteristic variables are modified according to:

$$\mathbf{W}_{i-\frac{1}{2}} \leftarrow \text{median}(\mathbf{W}_{i-\frac{1}{2}}, \mathbf{W}_i, \mathbf{W}_i^{\text{MP}}), \quad (5.67)$$

$$\mathbf{W}_{i+\frac{1}{2}} \leftarrow \text{median}(\mathbf{W}_{i+\frac{1}{2}}, \mathbf{W}_{i+1}, \mathbf{W}_{i+1}^{\text{MP}}). \quad (5.68)$$

The monotonicity-preserving (MP) limits of the interfaces $i \pm 1/2$ are:

$$\mathbf{W}_i^{\text{MP}} = \mathbf{W}_i + \text{minmod}[\mathbf{W}_{i+1} - \mathbf{W}_i, \alpha(\mathbf{W}_i - \mathbf{W}_{i-1})], \quad (5.69)$$

$$\mathbf{W}_{i+1}^{\text{MP}} = \mathbf{W}_{i+1} + \text{minmod}[\mathbf{W}_{i+2} - \mathbf{W}_{i+1}, \alpha(\mathbf{W}_{i+1} - \mathbf{W}_i)], \quad (5.70)$$

with $\text{minmod}(a, b) = \frac{1}{2}(\text{sgn}(a) + \text{sgn}(b))\min(\text{abs}(a), \text{abs}(b))$. In the present thesis, the parameter α has been set to 2. Once eqs. (5.67)-(5.68) applied, the reconstructed conservative variables are found through $\mathbf{U} = \mathbf{L}^{-1}\mathbf{W}$. Then the numerical inviscid fluxes $\tilde{\mathbf{F}}_{i\pm 1/2}$ are then evaluated as $\tilde{\mathbf{F}}_{i\pm 1/2} = \mathbf{F}(\mathbf{U}_{i\pm 1/2})$. Details regarding the multi-dimensional version of the reconstruction procedure on non-uniform/uniform meshes can be found in the PhD thesis of Kapper (2009).

Temporal Discretization

The temporal discretization is realized as follows. Given the numerical solution at the time-level n , the update at the time-level $n + 1$ is computed as:

$$\mathbf{U}_{i,j}^{n+1} = \mathbf{U}_{i,j}^n + \delta_c \mathbf{U}_{i,j}^n + \delta_s \mathbf{U}_{i,j}^n. \quad (5.71)$$

The convective and source contributions to the solution update ($\delta_c \mathbf{U}$ and $\delta_s \mathbf{U}$, respectively) are computed independently as explained below.

During the convective step, the presence of source terms is neglected and the solution update is computed explicitly according to:

$$\delta_c \mathbf{U}_{i,j}^n = -\frac{\Delta t_{c,i,j}}{A_{i,j}} \tilde{\mathbf{R}}_{c,i,j}^n. \quad (5.72)$$

The convective time-step Δt_c is computed based on the CFL criterion for 2D structured grids (see for instance Hirsch 1990; Blazek 2006).

The source step is performed by neglecting the flux contributions. In this case the solution update is performed in an implicit manner:

$$\delta_s \mathbf{U}_{i,j}^n = \left(\frac{\mathbf{I}}{\Delta t_{s,i,j}} - \frac{\partial \mathbf{S}_{i,j}^n}{\partial \mathbf{U}_{i,j}} \right)^{-1} \mathbf{S}_{i,j}^n. \quad (5.73)$$

For the purpose of enhancing stability and reducing the computational time, the Jacobian matrices involved in the computation of $\partial \mathbf{S} / \partial \mathbf{U}$ are evaluated analytically (their expressions are given in app. E). The source time-step Δt_s should be computed based on a stability analysis of the ODE system $\partial \mathbf{U} / \partial t = \mathbf{S}$, and not based on the CFL number. However, it was found that the assumption $\Delta t_c = \Delta t_s$ did not lead to severe convergence problems.

The approach used here for the temporal discretization is known as operator splitting. The use of operator splitting can be be advantageous in multi-dimensional applications, at it avoids the solution of large linear systems which arise for implicit methods (Hirsch 1990). This nice feature comes at the price of a narrower stability domain. A possible improvement in this aspect can be obtained with the use of multi-stage time-stepping schemes (such as the second order two-stage Adams-Bashforth method; Kapper 2009).

5.3 Quasi-One-Dimensional Nozzle Flows

This section investigates non-equilibrium recombination in quasi-one-dimensional flows within realistic nozzle geometries. In the case of the RVC model, steady-state solutions of the nozzle flow governing equations (5.6) have been obtained by means of the point-implicit method described in sec. 5.2.1. For the other models, the fully implicit method described in the same section has been used.

5.3.1 Application of the RVC Model to the Flow within the Nozzle of the EAST Facility

The study of non-equilibrium recombination within nozzles has considered, as first application, the flow within the nozzle of the Electric Arc Shock Tube (EAST) facility at NASA ARC. Figure 5.2 shows the normalized area distribution of the EAST facility nozzle. For the RVC model, predissociation has not been accounted for (due to its limited impact on flow quantities as observed in sec. 4.2.3 for flows behind shock waves). The nozzle has been truncated at the location $x = 5 \times 10^{-2}$ m in order to avoid numerical problems due to the low-temperature extrapolation of the elementary rate coefficients. This issue was not faced in the case of the VC and BRVC models and can be explained by the fact that the rate coefficients for these coarse-grained models are computed through weighted averages over the energy levels (eqs. (3.58)-(3.61) and eqs. (3.90)-(3.93)). This operation tends to smooth and attenuate an eventual irregular behavior of the elementary rate coefficients at low temperatures.

The nozzle flowfield has been computed by assuming Local Thermodynamic Equilibrium (LTE) at the nozzle inlet. The inlet static pressure and temperature have been set to 101 325 Pa and 10 000 K, respectively. The corresponding mole fractions of N and N₂ are 0.993 and 0.07, respectively. These conditions have been selected, so that N₂-N collisions are the dominant mechanism in the flow.

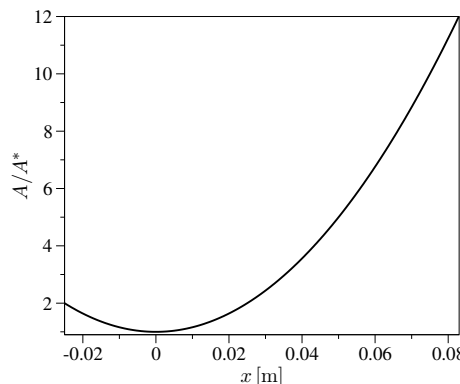


Figure 5.2: Normalized area distribution of the EAST facility nozzle (inlet $x = -0.025$ m, throat $x = 0$ m, outlet $x = 0.083$ m).

Flowfield Analysis

Figure 5.3 shows the evolution along the nozzle axis of the N_2 mole fraction and the temperatures. The temperature evolution shows that rotational non-equilibrium effects are quite limited. This is not the case for the vibrational energy mode, whose temperature is sensibly higher than the translational and rotational temperatures at the nozzle outlet. The internal temperature always lies in between the rotational and vibrational ones (as observed in sec. 4.2.1 for flows behind shock waves). The results shown in fig. 5.3 suggest that, for the expanding case, a VC model should lead to an accurate description. This is indeed confirmed by the results shown later.

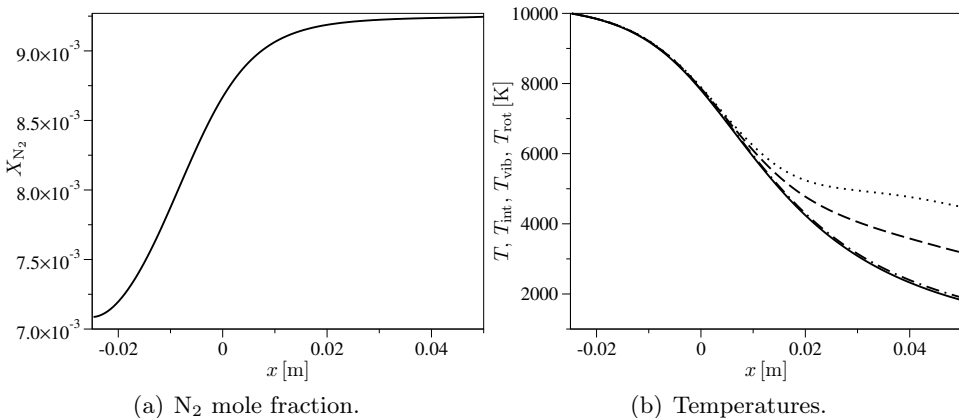


Figure 5.3: RVC Model. N_2 mole fraction and temperature evolution along the axis of the EAST facility nozzle (in (b) unbroken line T , dashed line T_{int} , dotted line T_{vib} , dotted-dashed line T_{rot}).

Energy Level Dynamics

The internal energy level population distributions have been extracted at 7 locations listed in tab. 5.1.

#	x [m]	X_{N_2}	T [K]	T_{int} [K]	T_{vib} [K]	T_{rot} [K]
1	-2.5×10^{-2}	7.09×10^{-3}	10000	10000	10000	10000
2	1.1×10^{-4}	8.67×10^{-3}	7794	7848	7879	7815
3	1×10^{-2}	9.07×10^{-3}	5846	6032	6173	5884
4	2×10^{-2}	9.19×10^{-3}	4232	4767	5237	4285
5	3×10^{-2}	9.22×10^{-3}	3052	4036	4945	3116
6	4×10^{-2}	9.24×10^{-3}	2322	3578	4763	2391
7	5×10^{-2}	9.25×10^{-3}	1809	3166	4468	1885

Table 5.1: RVC model. Position, N_2 mole fraction and temperatures for the locations at which the population distributions are extracted.

Figure 5.4 provides a visual correspondence between the evolution of the N_2 mole fraction and the population distribution along the nozzle axis. At the nozzle inlet the energy level population distribution is Boltzmann, due to assumed LTE conditions. Moving along the nozzle axis, recombination starts to occur. This leads to a progressive overpopulation in the high-energy regions of the population distribution, due to the preferential recombination in high-lying energy levels. It is interesting to notice that, in the zone close to the dissociation limit ($\simeq 9.735$ eV), a local overpopulation peak is formed.

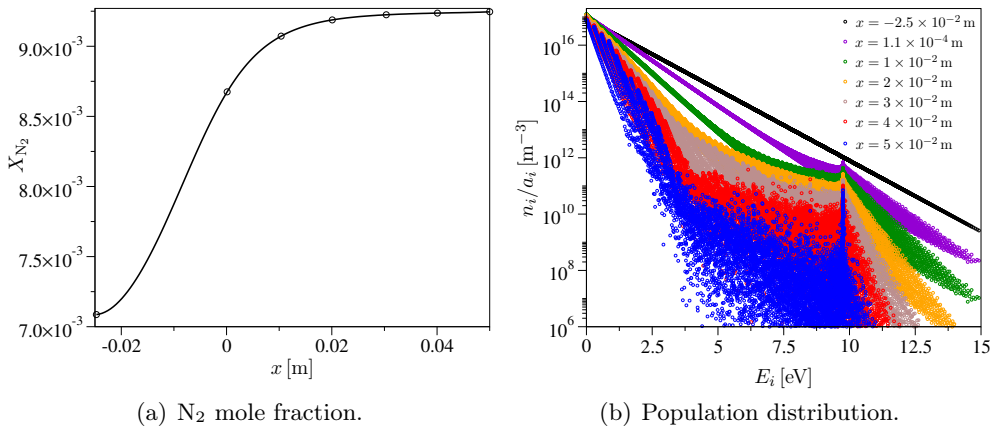


Figure 5.4: *RVC model. Comparative evolution of the N_2 mole fraction and the rovibrational energy level distribution along the axis of the EAST facility nozzle (the symbols in (a) highlight the locations at which the population distributions, plotted in (b), are extracted).*

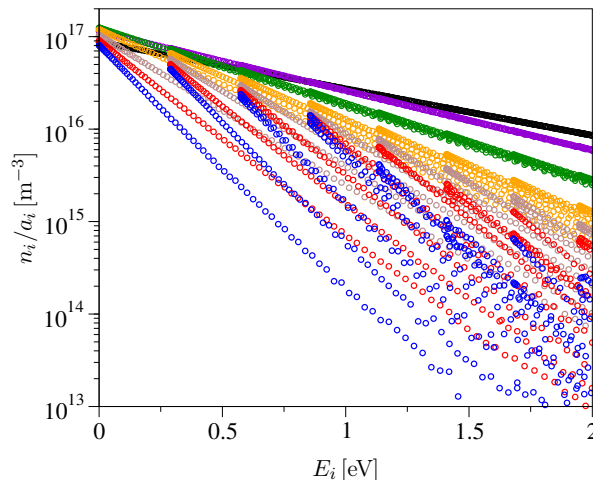


Figure 5.5: *RVC model. Evolution along the axis of the EAST facility nozzle of the population of the rovibrational energy levels lying close to the ground-state (the locations at which the distributions are plotted are the same as those of fig. 5.4).*

The extension of the overpopulation peak becomes bigger and bigger while approaching the nozzle outlet. This result shows that the dynamical behavior of the energy levels lying close to the dissociation limit is quite different from that of the others. In particular, it seems to suggest the existence of a preferential channel for recombination.

When the temperature decreases (due to the expansion process), the population distribution separates into distinct straight lines in the region close to the ground-state (see fig. 5.5). These correspond to the rotational levels of the ground and the first excited vibrational states as shown in fig. 5.6 for the location 7 of tab. 5.1. The fact that the rotational levels close to the ground-state lie along a straight line, indicates that they are in thermal equilibrium at their own temperature. Numerical values for this temperature for each vibrational level shown in fig. 5.6 have been extracted based on eq. (4.3) and are reported in fig. 5.6(a). The values obtained are very close to that of the translational temperature and confirm that the rotational energy mode is in thermal equilibrium with translation (as anticipated before). A more detailed investigation of the rotational level distribution in fig. 5.6(b) reveals the existence of a splitting between energy levels having odd and even rotational quantum numbers (J). This feature was already observed before when studying flows behind shock waves (sec. 4.2.5; see fig. 4.8(b)). However, for a recombining nozzle expansion, the splitting is barely noticeable for the ground and the first excited vibrational states, while it becomes more and more evident when moving towards higher vibrational states. This result shows that the assumption of rotational equilibrium is less appropriate for these states.

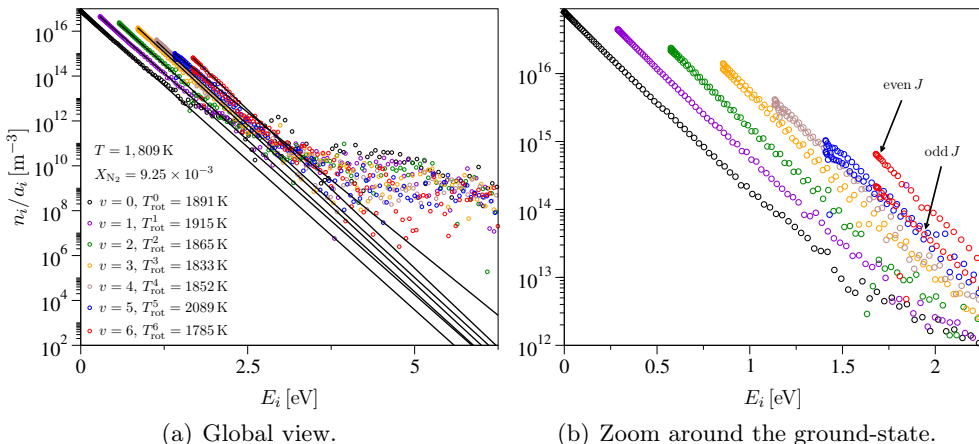


Figure 5.6: RVC model. Rotational energy level distribution for the ground and the first five excited vibrational states at the location $x = 5 \times 10^{-2}$ m along the axis of the EAST facility nozzle (the unbroken lines in (a) represent the Boltzmann distributions at the rotational temperatures T_{rot}^v).

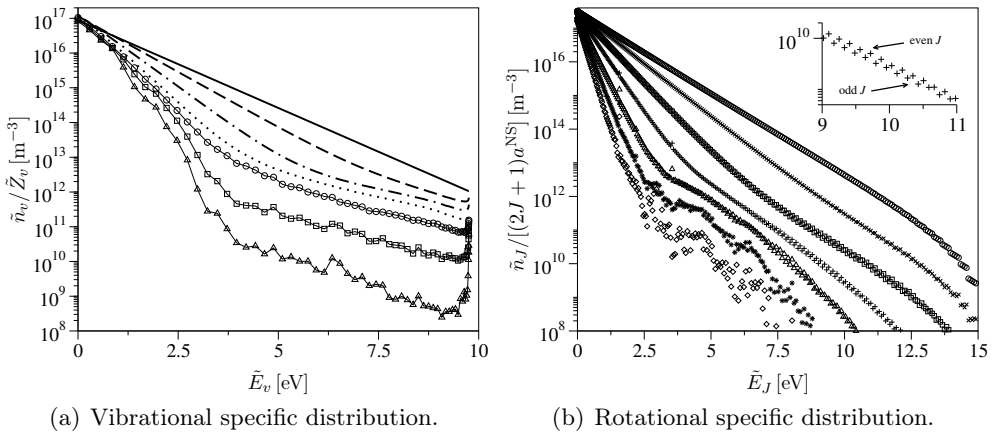


Figure 5.7: RVC model. Evolution of the vibrational and rotational specific population distributions along the axis of the EAST facility nozzle (in (a) unbroken line $x = -2.5 \times 10^{-2}$ m, dashed line $x = 1.1 \times 10^{-4}$ m, dotted-dashed line $x = 1 \times 10^{-2}$ m, dotted line $x = 2 \times 10^{-2}$ m, line with circles $x = 3 \times 10^{-2}$ m, line with squares $x = 4 \times 10^{-2}$ m, line with triangles $x = 5 \times 10^{-2}$ m; in (b) circles $x = -2.5 \times 10^{-2}$ m, crosses $x = 1.1 \times 10^{-4}$ m, squares $x = 1 \times 10^{-2}$ m, plus $x = 2 \times 10^{-2}$ m, triangles $x = 3 \times 10^{-2}$ m, stars $x = 4 \times 10^{-2}$ m, diamonds $x = 5 \times 10^{-2}$ m).

The energy level dynamics can also be studied by looking at vibrational and rotational specific population distributions (fig. 5.7). The observed over-population illustrates again the existence of a preferential recombination in high-lying energy levels. In the region where the distribution deviates from a Boltzmann-like shape, the rotational levels split according to odd and even rotational quantum numbers (as observed in fig. 5.5).

Comparison with the VC, BRVC and MTP Models

After a detailed investigation of the RVC model solution, the nozzle flowfield has been computed by means of the BRVC(50), VC and MTP models. Figure 5.8 compares all the models in terms of the N₂ mole fraction. The BRVC(50) and VC model solutions are very close to that obtained by means of the RVC model. On the other hand, the MTP leads to an excessive amount of recombination.

Model	X_{N_2}	T [K]	u [m/s]
RVC	9.25×10^{-3}	1809	5041
BRVC(50)	9.69×10^{-3}	1822	5045
VC	9.42×10^{-3}	1808	5042
MTP	1.35×10^{-2}	1896	5072

Table 5.2: RVC, BRVC(50), VC and MTP model comparison. Outlet values for the N₂ mole fraction, translational temperature and velocity (EAST facility nozzle).

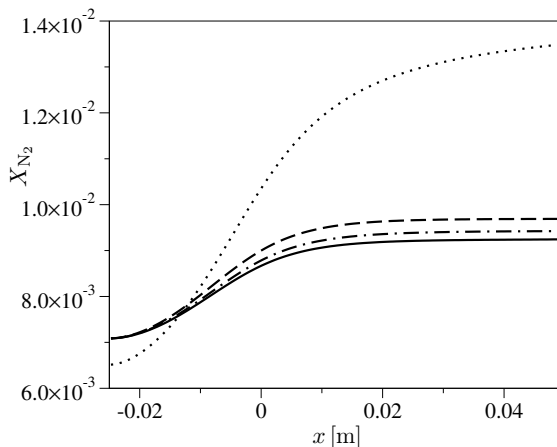


Figure 5.8: *RVC, BRVC(50), VC and MTP model comparison. N₂ mole fraction evolution along the axis of the EAST facility nozzle (unbroken line RVC, dashed line BRVC(50), dotted-dashed line VC, dotted line MTP).*

Due to the limited amount of recombination, flow quantities such as temperature and velocity do not experience noticeable variations among the models. This can be seen from tab. 5.2 reporting the outlet values of the N₂ mole fraction, translational temperature and velocity. The translational temperature and velocity values obtained in the case of the MTP are slightly higher than those obtained by means of the RVC, BRVC(50) and VC models. This is consistent with the higher values for the N₂ mole fraction observed in fig. 5.8. The relative errors on the outlet values of the N₂ mole fraction for the BRVC(50), VC and MTP are 4.76 percent, 1.84 percent and 45.95 %, respectively. In the present situation, the VC model performs slightly better than the BRVC model (as opposed to what observed in sec. 4.3.2 for flows behind shock waves). The better agreement observed in the case of the VC model is probably due to the fact that the assumed rotational equilibrium distribution (3.52) is naturally suggested by the observed energy level dynamics. The analysis of the rovibrational distributions given in figs. 5.4(b)-5.7 has shown that the assumption of rotational equilibrium is indeed appropriate for the low-lying rotational levels of the vibrational ground-state and the first excited vibrational states.

Figures 5.9 and 5.10 show the evolution along the nozzle axis of the mass production and energy transfer terms, respectively. The VC model solution is the one leading to the better agreement with the RVC model. This result is consistent with the N₂ mole fraction evolution given in fig. 5.8. The differences observed between the BRVC(50) and RVC model solutions put in evidence that the BRVC model slightly overestimates not only the dissociation rate, but also the rate at which the translational-internal energy transfer occurs. This result is in contrast with those obtained in sec. 4.3.2 while investigating non-equilibrium effects behind shock waves (see fig. 4.16). The disagreement observed in the rate of translational-internal energy transfer is probably an indication that the

BRVC model is most suited for high-temperature conditions. However, it is worth to recall that, even in the present low-temperature conditions, the departure from the VC model solution is quite limited.

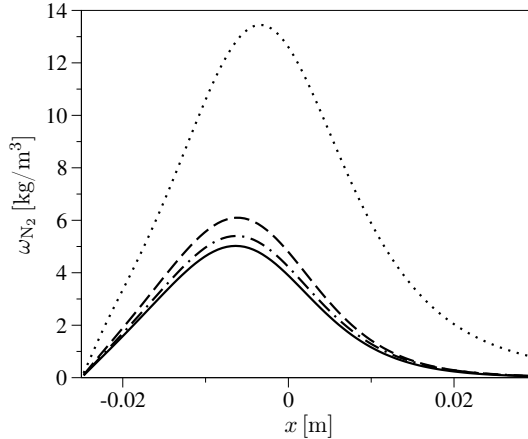


Figure 5.9: RVC, BRVC(50), VC and MTP model comparison. N_2 mass production term evolution along the axis of the EAST facility nozzle (unbroken line RVC, dashed line BRVC(50), dotted-dashed line VC, dotted line MTP).

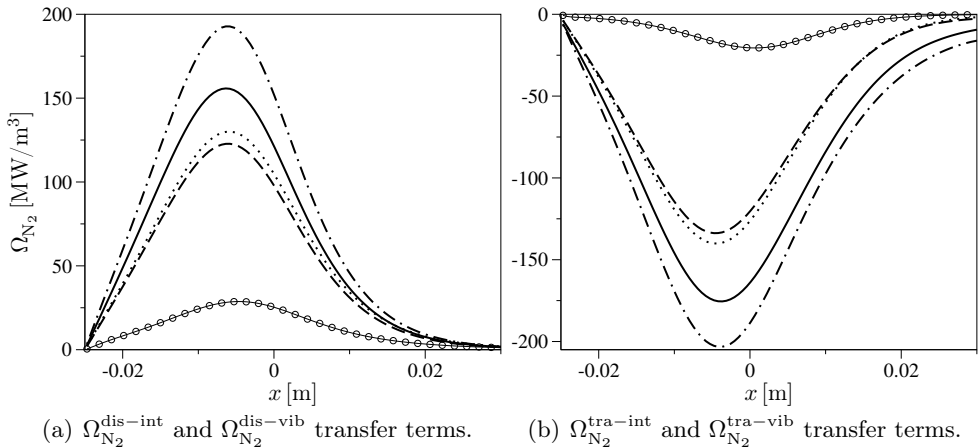


Figure 5.10: RVC, BRVC(50), VC and MTP model comparison. Energy transfer term evolution along the axis of the EAST facility nozzle (in (a) unbroken line $\Omega_{N_2}^{\text{dis-int}}$ RVC, dashed line $\Omega_{N_2}^{\text{dis-vib}}$ RVC, dotted-dashed line $\Omega_{N_2}^{\text{dis-int}}$ BRVC(50), dotted-line line $\Omega_{N_2}^{\text{dis-vib}}$ VC, line with circles $\Omega_{N_2}^{\text{dis-vib}}$ MTP; in (b) unbroken line $\Omega_{N_2}^{\text{tra-int}}$ RVC, dashed line $\Omega_{N_2}^{\text{tra-vib}}$ RVC; dotted-dashed line $\Omega_{N_2}^{\text{tra-int}}$ BRVC(50), dotted-line line $\Omega_{N_2}^{\text{tra-vib}}$ VC, line with circles $\Omega_{N_2}^{\text{tra-vib}}$ MTP).

The small discrepancy observed between the RVC and VC model solutions have been investigated more in detail by looking at the vibrational specific population distributions along the nozzle axis. Figure 5.11 compares the vibrational specific population distributions for the two models at the locations 2-7 of tab. 5.1.

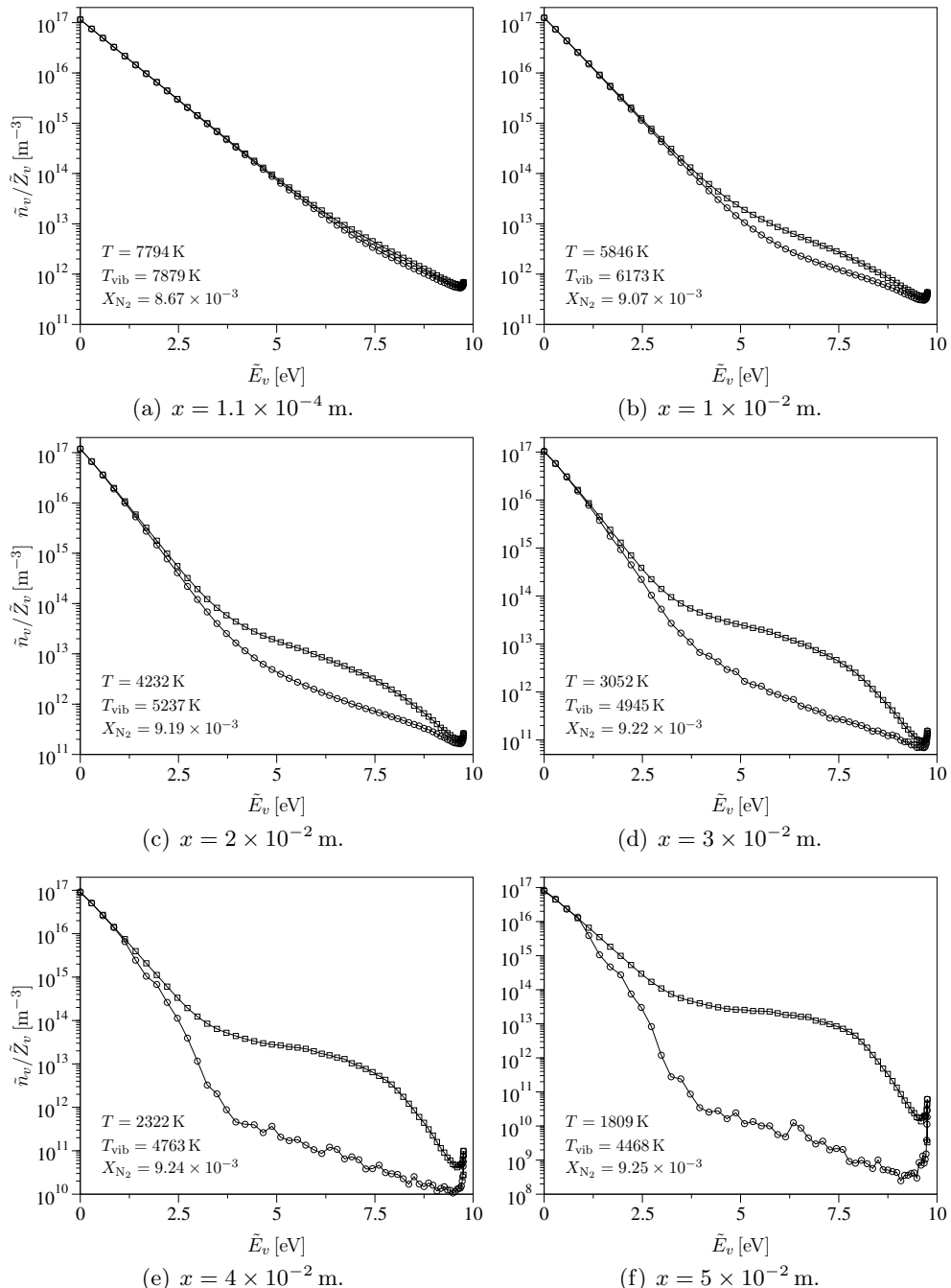


Figure 5.11: RVC and VC model comparison. Vibrational specific population distributions along the axis of the EAST facility nozzle (lines with circles RVC, lines with squares VC; the reported values for the N₂ mole fraction, translational and vibrational temperatures refer to the RVC model solution).

For both models, the recombination (which occurs around the nozzle throat as shown in fig. 5.8) leads to an overpopulation of high-lying vibrational states. The agreement between the RVC and VC model solutions is very good at the nozzle throat (location 2; fig. 5.11(a)). Moving further downstream, some differences start to arise in the high-energy portion of the distribution (locations 3-4; figs. 5.11(b)-5.11(c)). These differences become more and more enhanced towards the nozzle exit (location 7; fig. 5.11(f)) where the agreement between the RVC and VC solutions is good only for the vibrational ground-state and the first four excited vibrational states. For higher vibrational states, the population predicted by the RVC model is lower than that of the VC model. This result is consistent with the rotational level distributions at location 7 which have been investigated before (fig. 5.6). The previous analysis of the rotational distributions has highlighted the existence of an odd-even splitting of rotational levels (with the consequent lack of rotational non-equilibrium) starting from the fourth excited vibrational state. From this analysis, one can conclude that the observed differences between the RVC and VC model solutions are due to the lack of rotational equilibrium throughout the whole rovibrational ladder (see figs. 5.4(b)-5.7).

5.3.2 Application of the BRVC Model to the Flow within the F4 and Scirocco Nozzles

The performances of the BRVC model have been further tested by computing the non-equilibrium flow within the following realistic geometries:

- F4 (ONERA; France),
- Scirocco (CIRA; Italy).

Figure 5.12 provides their normalized area distributions.

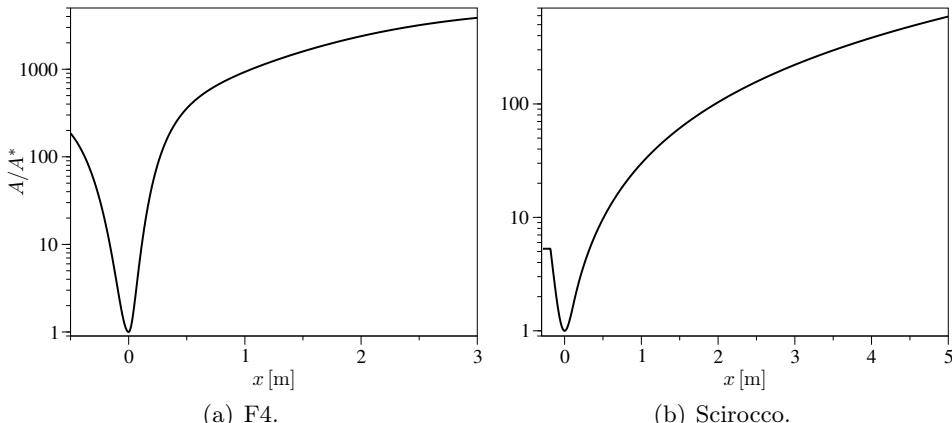


Figure 5.12: Normalized area distributions of the F4 and Scirocco nozzles (in (a) inlet $x = -0.5$ m, throat $x = 0$ m, outlet $x = 3$ m; in (b) inlet $x = -0.28$ m, throat $x = 0$ m, outlet $x = 5$ m).

The nozzle geometries considered in this section have been chosen as, due to the high outlet/throat area ratio, they lead to a more significant expansion compared to the EAST facility nozzle. Computations have been performed by using the same inlet conditions as in sec. 5.3.1.

Comparison with the VC and MTP Models

Figure 5.13 shows the N_2 mole fraction, velocity and temperature evolution along the axis of the F4 and Scirocco nozzles for the BRVC(50), VC and MTP models. The corresponding outlet values are provided in tab. 5.3.

Model	F4			Scirocco		
	X_{N_2}	T [K]	u [m/s]	X_{N_2}	T [K]	u [m/s]
BRVC(50)	1.40×10^{-2}	21.3	5520	1.74×10^{-2}	781	5556
VC	1.34×10^{-2}	21.03	5509	1.67×10^{-2}	762	5543
MTP	2.11×10^{-2}	25.7	5599	3.37×10^{-2}	133	5718

Table 5.3: BRVC(50), VC and MTP model comparison. Outlet values for the N_2 mole fraction, translational temperature and velocity (F4 and Scirocco nozzles).

The spatial evolution of the flow quantities shown in fig. 5.13 confirms that the expansion in the F4 and Scirocco nozzles is much more severe compared to the case of the EAST facility nozzle (as anticipated before). In particular, the outlet values of the translational temperature are decreased by almost two orders of magnitude. Despite this, the outlet values of the N_2 mole fraction are only roughly doubled. This is due to the freezing of recombination which occurs around the throat location (figs. 5.13(a)-5.13(b)).

For both nozzle geometries, the evolution of the N_2 mole fraction (figs. 5.13(a)-5.13(b)) shows that the use of the VC model leads to a slightly lower recombination than the BRVC(50) model. This trend is consistent with the results obtained for the EAST facility nozzle (see fig. 5.8). As demonstrated in sec. 5.3.1, the VC model solution can be considered as the exact solution of the problem under investigation (as far as the flow properties are concerned) due to the limited influence of rotational non-equilibrium effects. In this case, the relative errors on the outlet value of the N_2 mole fraction when using the BRVC(50) model are 4.48 % and 4.19 % for the F4 and Scirocco nozzles, respectively. The approximation introduced by the use of the BRVC(50) model is therefore contained within acceptable limits. In the case of the MTP model, the recombination is overestimated and the relative error on the outlet values of the N_2 mole fraction are much higher (more than 100 % for the Scirocco nozzle). Due to the higher recombination in the adopted nozzles, the differences in terms of velocity and translational temperature between the VC (or BRVC(50)) and MTP models are more pronounced compared to the case of the EAST facility nozzle (see tab. 5.2).

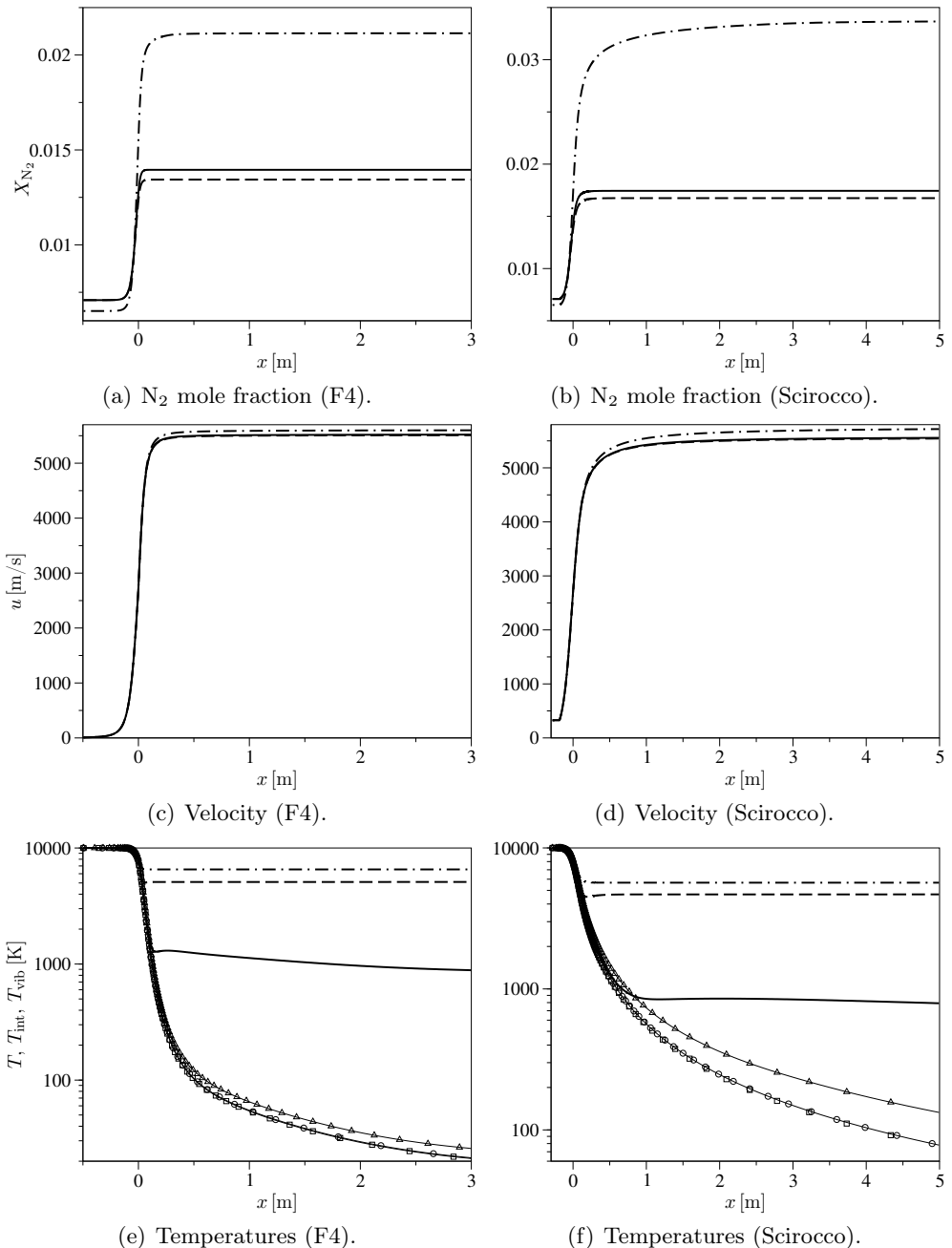


Figure 5.13: BRVC(50), VC and MTP model comparison. N₂ mole fraction, velocity and temperature evolution along the axis of the F4 and Scirocco nozzles (in (a)-(d) unbroken lines BRVC(50), dashed lines VC, dotted-dashed lines MTP; in (e)-(f) lines with circles T BRVC(50), lines with squares T_{int} VC, lines with triangles T_{vib} MTP, unbroken lines T_{int} BRVC(50), dashed lines T_{vib} VC, dotted-dashed lines T_{vib} MTP).

Energy Bin Dynamics

The energy bin population distributions have been extracted at 9 nine locations along the axis of the Scirocco nozzle (with the corresponding values for position, N₂ mole fraction and temperatures provided in tab. 5.4).

#	x [m]	X_{N_2}	T [K]	T_{int} [K]
1	-3×10^{-1}	7.09×10^{-3}	10 000	10 000
2	-4.03×10^{-2}	1.14×10^{-2}	8969	8977
3	3.46×10^{-2}	1.59×10^{-2}	6719	6736
4	8.46×10^{-2}	1.69×10^{-2}	5051	5072
5	1.35×10^{-1}	1.73×10^{-2}	3803	3829
6	2.85×10^{-1}	1.74×10^{-2}	2082	2118
7	3.5×10^{-1}	1.74×10^{-2}	1721	1763
8	5.29×10^{-1}	1.74×10^{-2}	1160	1229
9	6.94×10^{-1}	1.74×10^{-2}	852	977

Table 5.4: BRVC(50) model. Position, N₂ mole fraction and temperatures for the locations at which the energy bin population distributions are extracted (Scirocco nozzle).

Figure 5.14 provides a visual correspondence between the evolution of the N₂ mole fraction and the energy bin population distribution along the nozzle axis. The population is Boltzmann at the nozzle inlet, as a result of the LTE assumption. Deviations from a Boltzmann distribution start occurring in the throat region, due to preferential recombination in high-lying energy bins. Moving towards the nozzle outlet, the distribution is highly distorted putting forward differences in the dynamics of bound and predissociated energy bins.

Figure 5.15 focuses on the population distribution at the locations 6 and 9 of tab. 5.4. Three regions can be identified. The first comprises the energy bins close to ground-state. The second includes the medium and high-lying bound energy bins, while the third region contains all the predissociated energy bins. Boltzmann distributions at the internal and translational temperature are superimposed on the first and third regions, respectively. The good agreement observed between the actual and the Boltzmann distributions indicates that the bound energy bins close to the ground-state are in partial equilibrium at the internal temperature, while the predissociated energy bins are in partial equilibrium at the translational temperature (*i.e.* they are in chemical equilibrium with the free state). The observed behavior of the energy bins is analogous to that of the electronic states of atoms and molecules in recombining plasmas. In that situation the electronic levels close to the ground-state are partial equilibrium at the free-electron temperature while those close to the ionization limit are in chemical (Saha) equilibrium with the free state (Panesi et al. 2011; Munafò et al. 2013). The energy bin population distributions along the axis of the F4 nozzle (not shown) share the same features observed in fig. 5.15.

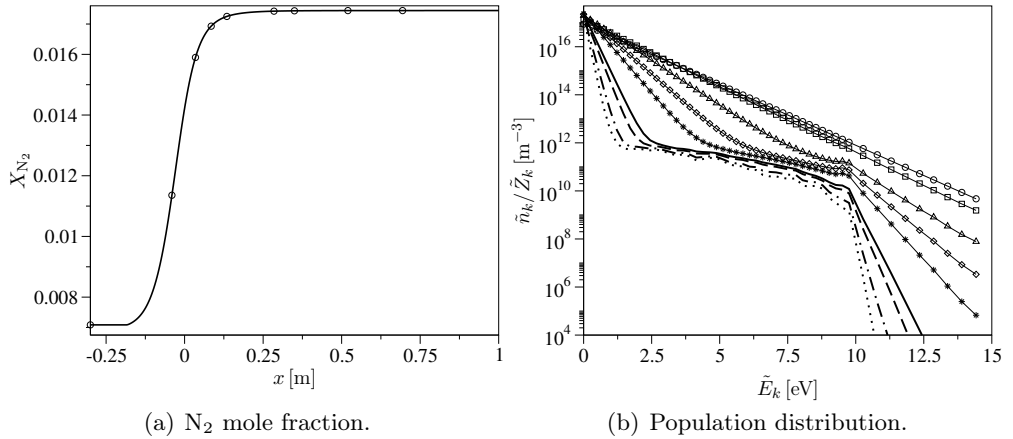


Figure 5.14: *BRVC(50) model. Comparative evolution of the N_2 mole fraction and the energy bin population distribution along the axis of the Scirocco nozzle (the symbols in (a) highlight the locations where the population distributions, plotted in (b), are extracted; in (b) line with circles $x = -3 \times 10^{-1}$ m, line with squares $x = -4.03 \times 10^{-3}$ m, line with triangles $x = 3.46 \times 10^{-2}$ m, line with diamonds $x = 8.46 \times 10^{-2}$ m, line with stars $x = 1.35 \times 10^{-1}$ m, unbroken line $x = 2.85 \times 10^{-1}$ m, dashed line $x = 3.5 \times 10^{-1}$ m, dotted-dashed line $x = 5.29 \times 10^{-1}$ m, dotted line $x = 6.94 \times 10^{-1}$ m).*

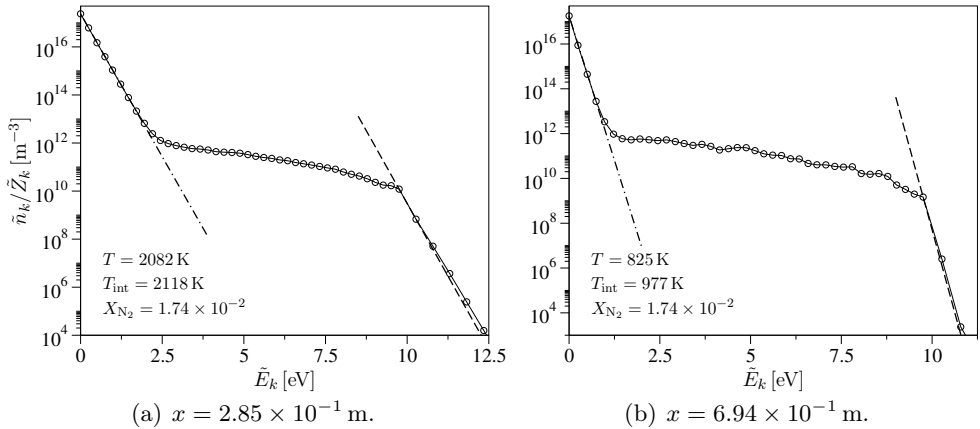


Figure 5.15: *BRVC(50) model. Energy bin population distributions at the locations $x = 2.85 \times 10^{-1}$ m and $x = 6.94 \times 10^{-1}$ m along the axis of the Scirocco nozzle (the dashed and the dotted-dashed lines indicate the Boltzmann distributions at the translational and internal temperature, respectively).*

Bin Number Sensitivity Analysis

The computational results obtained by means of the BRVC model have considered so far only a fixed number of energy bins (50). In order to assess the sensitivity of the solution to the number of energy bins, the same strategy

adopted in sec. 4.3.3 for flows behind shock waves has been used. Hence, the computation of the non-equilibrium flows within the F4 and Scirocco nozzles has been repeated by using different numbers of energy bins (listed in tab. 4.3). Figure 5.16 shows the N_2 mole fraction evolution along the axis of the F4 and Scirocco nozzles for different numbers of energy bins. For sake of completeness, the solution obtained by means of the VC and MTP models are also reported. As expected, the solution accuracy improves by increasing the number of energy bins. It is interesting to notice that, even in the case of 2-5 energy bins, the BRVC solution is quite close to that of the VC model. The computational cost of the numerical solutions obtained by using 2-5 energy bins is of the same order as that of the MTP model. This means that, in a comparison with conventional multi-temperature models, the BRVC model allows for a more accurate description of the recombination dynamics without incurring in an excessive increase of the computational cost. This fact becomes particularly important in view of possible multi-dimensional CFD applications of the proposed coarse-grain models.

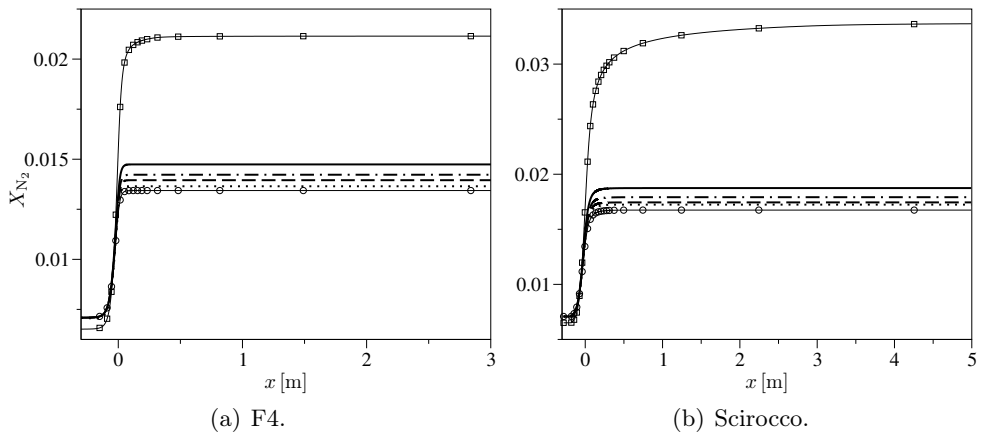


Figure 5.16: *BRVC model. Influence of the number of energy bins on the N_2 mole fraction evolution along the axis of the F4 and Scirocco nozzles (unbroken lines BRVC(2), dotted-broken lines BRVC(10), dashed lines BRVC(50), dotted lines BRVC(500), lines with circles VC, lines with squares MTP).*

Table 5.5 provides the outlet values of the N_2 mole fraction for different numbers of energy bins. In the same Table, the relative errors on the N_2 fraction are also given. This is estimated by considering the VC model solution as the exact solution of the problem under investigation. The numerical error on the outlet value of the N_2 fraction is already quite contained (between 5 percent and 7 %) when using only 10-20 energy bins. The increase of the number of energy bins leads only to a slight improvement of the solution accuracy at the price of a much higher computational cost. These results are consistent with those obtained in sec. 4.3.3 for flows behind shock waves.

\mathcal{N}_{N_2}	F4		Scirocco	
	X_{N_2}	err. $X_{\text{N}_2} \%$	X_{N_2}	err. $X_{\text{N}_2} \%$
2	1.87×10^{-2}	11.98	1.47×10^{-1}	9.701
5	1.85×10^{-2}	10.78	1.45×10^{-1}	8.209
10	1.79×10^{-2}	7.19	1.42×10^{-1}	5.97
20	1.76×10^{-3}	5.39	1.405×10^{-1}	4.85
50	1.74×10^{-2}	4.19	1.395×10^{-1}	4.104
100	1.74×10^{-2}	4.19	1.39×10^{-1}	3.73
500	1.72×10^{-2}	2.99	1.36×10^{-1}	1.49

Table 5.5: BRVC model. Outlet values of the N_2 mole fraction and related relative error for different number of energy bins (the relative error on the N_2 mole fraction is estimated by taking the VC model solution as the exact solution).

The influence of the number of energy bins can also be observed at the microscopic level. This is done in fig. 5.17 showing the energy bin population distribution at the location 6 of tab. 5.4 for the Scirocco nozzle. The analysis of fig. 5.17 shows that a minimum number of 10-20 energy bins is needed in order to obtain a proper resolution of the main features of the distribution.

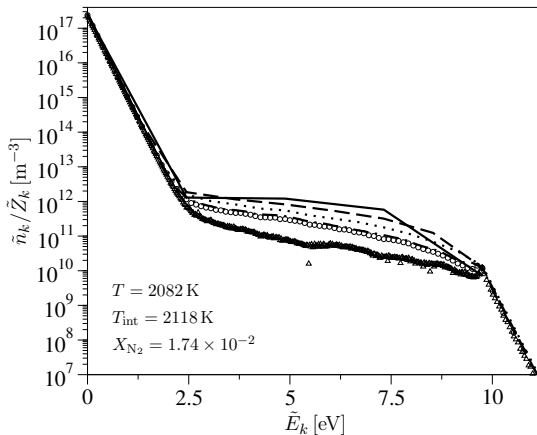


Figure 5.17: BRVC model. Energy bin population distribution at the location $x = 2.85 \times 10^{-1} \text{ m}$ along the axis of the Scirocco nozzle for different numbers of energy bins (unbroken line BRVC(5), dashed line BRVC(10), dotted line BRVC(20), dotted-dashed line BVVC(50), circles BRVC(100), triangles BRVC(500); the reported values for the N_2 mole fraction, translational and internal temperatures refer to the BRVC(50) model solution).

5.4 Stagnation-Line Flows

This section presents the results on non-equilibrium stagnation-line flows. The steady-state solutions to the stagnation-line governing equations (5.14) have been obtained by means of the fully implicit method described in sec. 5.2.1. Computations have been performed by means of the BRVC model. This was motivated by the higher flexibility and lower computational cost of the BRVC model compared to the VC model, as obtained from the investigation of flows behind normal shock waves (sec. 4.3) and within nozzles (sec. 5.3).

The nose radius has been set to $r = 0.4\text{ m}$. The free-stream pressure and temperature have been set to the same values used in secs. 4.2-4.3 for studying inviscid flows behind shock waves ($p_\infty = 0.05\text{ torr}$, 0.1 torr , 0.33 torr and $T_\infty = 300\text{ K}$, respectively). The free-stream velocity has been kept fixed at 10 km/s . As done in secs. 4.2-4.3, the free-stream flow is seeded with 2.8% of N since only N₂-N collisions are considered. At the wall a no-slip boundary condition is applied. The wall has been considered non-catalytic and its temperature set to 2000 K .

5.4.1 Flowfield analysis

Figure 5.18 shows the temperature and N mole fraction along the stagnation-line for different values of the free-stream pressure. The results shown have been obtained by means of the BRVC(20) model. In the high-pressure case ($p_\infty = 0.33\text{ torr}$), three regions can be identified in the flowfield: a) The shock wave, b) an intermediate post-shock area where the flow reaches local equilibrium conditions and c) the boundary layer. When the free-stream pressure is decreased, regions b) and c) mix together leading to the formation of a so called merged-layer flow (Gnoffo 1999).

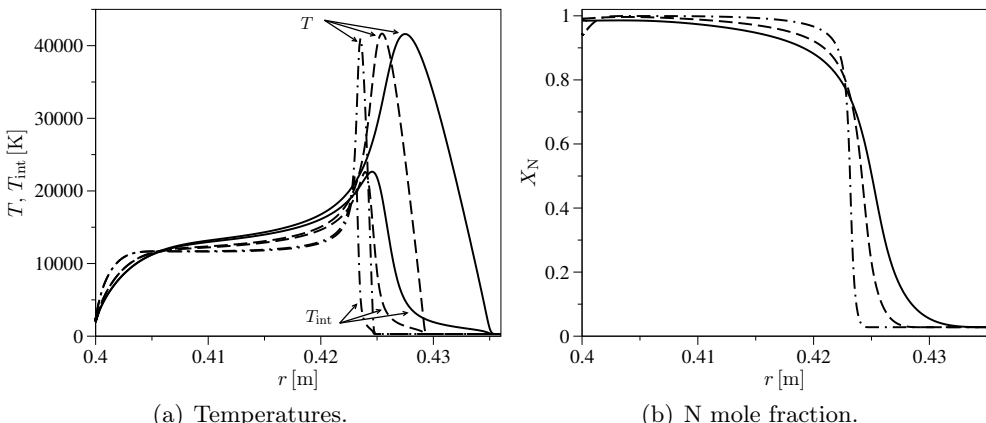


Figure 5.18: BRVC(20) model. Temperature and N mole fraction evolution along the stagnation-line for different values of the free-stream pressure (unbroken lines $p_\infty = 0.05\text{ torr}$, dashed lines $p_\infty = 0.1\text{ torr}$, dotted-dashed lines $p_\infty = 0.33\text{ torr}$).

Moreover, the thickness of the shock wave and the boundary layer regions increase and decrease, respectively. This is due to the lowering of the collision rate among the gas particles which also affects the recombination and the temperature gradients at the wall. Notice that for the lowest free-stream pressure value ($p_\infty = 0.05$ torr), the flow is still undergoing dissociation when it suddenly hits the wall. This is the reason why the wall value of the N mole fraction is lower compared to the case $p_\infty = 0.1$ torr.

Figure 5.19 shows the heat flux evolution along the stagnation-line. The corresponding wall values are reported in tab. 5.6 (together with pressure, N mole fraction and internal temperature). Increasing the free-stream pressure induces higher wall heat flux values, which is consistent with the results shown fig. 5.18 on temperature and chemical composition.

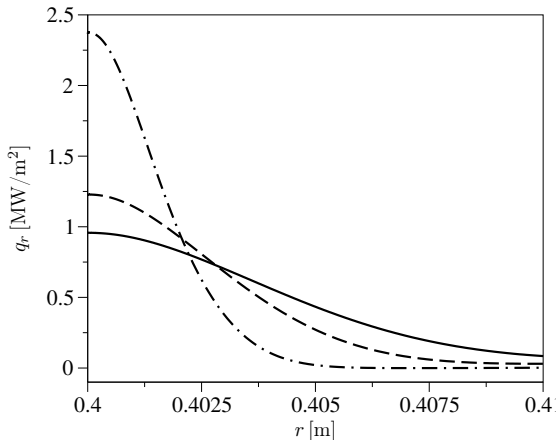


Figure 5.19: BRVC(20) model. Heat flux evolution along the stagnation-line for different values of the free-stream pressure (unbroken line $p_\infty = 0.05$ torr, dashed line $p_\infty = 0.1$ torr, dotted-dashed line $p_\infty = 0.33$ torr).

The reported values for the internal temperature at the wall (given in tab. 5.20) are higher than the imposed translational temperature value (2000 K) and indicate the existence of thermal non-equilibrium between the translational and the internal energy mode in the boundary layer.

p_∞ [torr]	p [torr]	X_N	q_r [MW/m ²]	T_{int} [K]
0.05	52.643	0.985	0.96	2118.901
0.1	105.75	0.991	1.23	2372.34
0.33	350.98	0.941	2.38	2181.57

Table 5.6: BRVC(20) model. Wall pressure, N mole fraction, heat flux and internal temperature for different values of the free-stream pressure.

This aspect has been investigated more in detail by looking at the temperature profiles within the boundary layer as done in fig. 5.20. The results show that, during recombination, the internal temperature is systematically higher than

the translational one. This is analogous to what observed in sec. 5.3 for recombining nozzle flows. In the present situation, however, the differences observed between the two temperatures are quite small compared to the nozzle case. This is due to the fact that, in a boundary layer, the gas pressure is constant, while in a nozzle expansion it may decrease of several orders of magnitude along the nozzle axis.

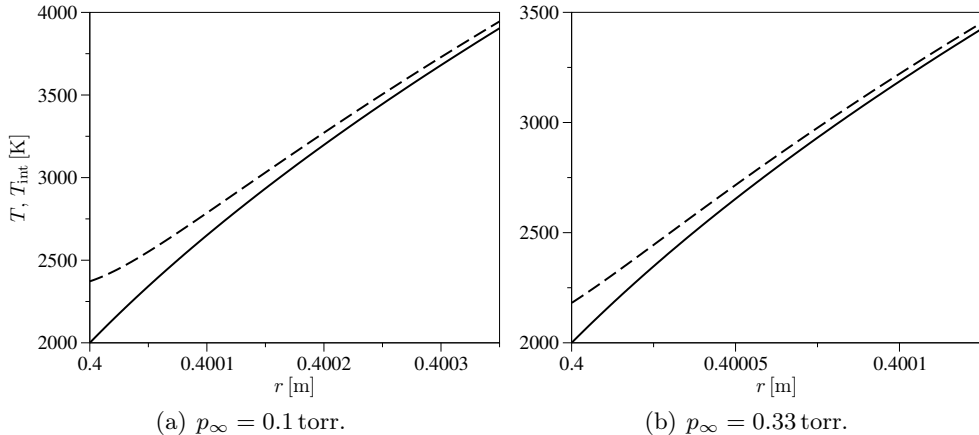


Figure 5.20: BRVC(20) model. Translational and internal temperature profiles within the boundary layer for different values of the free-stream pressure (unbroken lines T , dashed lines T_{int}).

The observed lack of thermal equilibrium in the boundary layer is consistent with the results obtained by Armenise et al. (1994) who studied boundary layer flows by means of vibrational collisional models. It is worth to recall that, in multi-dimensional CFD codes employing conventional multi-temperature models (such as that of Park 1993), the possible existence of thermal non-equilibrium effects at the wall is usually neglected. This choice is often motivated by the lack of theoretical information concerning the non-equilibrium state of the gas at the wall. On the other hand, the use of detailed collisional models (as done this section) allows to circumvent this problem as the internal temperature at the wall does not need to be specified and is obtained as a result of the calculation.

5.4.2 Energy Bin Dynamics

The computation of stagnation-line non-equilibrium flows allows to study, in the same testcase, the detailed dynamics of both dissociation and recombination which have been so far investigated separately in inviscid flows behind shock waves and within nozzles (sects. 4.2-4.3 and 5.3, respectively). This aspect reveals the completeness, in terms of physical description, of the testcase considered in this section.

Figures 5.21-5.23 shows a comparative evolution between the N mole frac-

tion and the energy bin population distributions across the three flowfield regions outlined before: a) shock-wave (fig. 5.21), b) post-shock equilibrium area (fig. 5.22) and c) boundary layer (fig. 5.23).

The dynamics of dissociation in fig. 5.21 proceeds as observed in sec. 4.2.5. There is an initial phase where inelastic collisions lead to an increase of the population of high-lying energy bins. This induces strong distortions in the population distribution which considerably deviates from a Boltzmann-like shape. Once a sufficient degree of excitation reached, N_2 begins to dissociate. The dissociation initially occurs through sequences of non-Boltzmann distributions with evident distortions around the ground-state. These progressively disappear and the final part of the dissociation occurs in thermal equilibrium conditions. After that, the flow enters the post-shock relaxation area (fig. 5.22). The population distribution remains Boltzmann with slope given by the post-shock equilibrium temperature. In this region of the flowfield, the population of the energy bins increases due to the rise of the gas pressure while approaching the wall. The recombination in the boundary layer occurs in a similar manner to that observed in sec. 5.3.2 for nozzle flows. Initially, the distribution is Boltzmann and changes its slope due to the cooling of the flow. Distortions are then progressively induced by preferential recombination in high-lying energy bins. At the wall and in the points immediately upstream, the population distributions splits into three distinct regions as already observed in sec. 5.3.2 (fig. 5.15) for the non-equilibrium flow within the Scirocco nozzle.

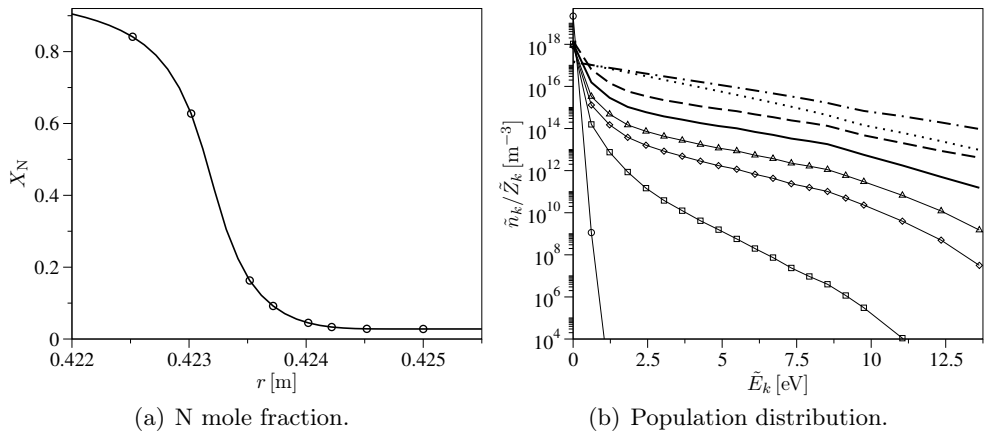


Figure 5.21: BRVC(20) model. Comparative evolution of the N mole fraction and the energy bin population distribution across the shock wave. The circles in fig. 5.21(a) indicate the locations at which the population distributions, plotted in fig. 5.21(b), are extracted (in fig. 5.21(b) line with circles $r = 0.425$ m, line with squares $r = 0.4245$ m, line with diamonds $r = 0.4242$ m, line with triangles $r = 0.424$ m, unbroken line $r = 0.4237$ m, dashed line $r = 0.4235$ m, dotted-dashed line $r = 0.423$ m, dotted line $r = 0.4225$ m).

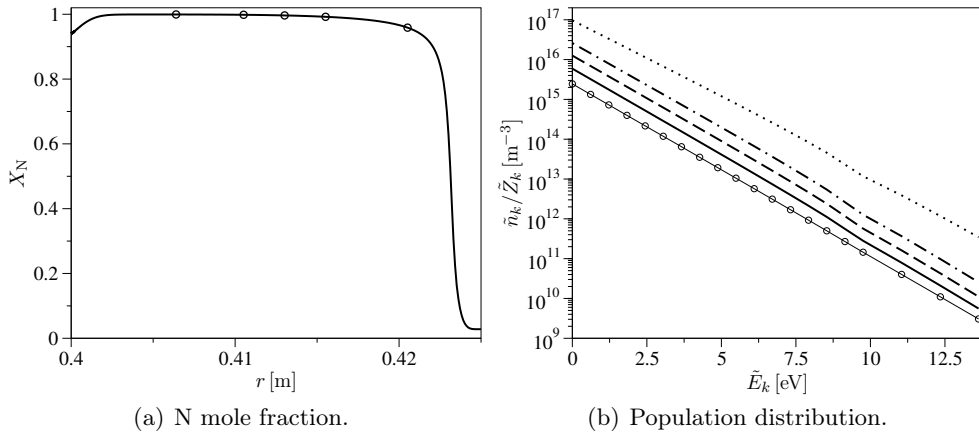


Figure 5.22: BRVC(20) model. Comparative evolution of the N mole fraction and the energy bin population distribution in the post-shock equilibrium area. The circles in (a) indicate the locations at which the population distributions, plotted in (b), are extracted (in (b) line with circles $r = 0.421$ m, unbroken line $r = 0.416$ m , dashed line $r = 0.413$ m , dotted-dashed line $r = 0.411$ m, dotted line $r = 0.406$ m).

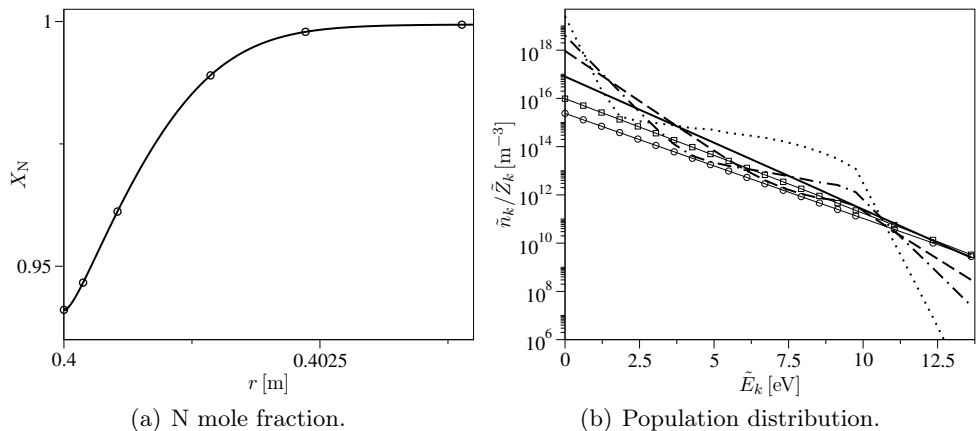


Figure 5.23: BRVC(20) model. Comparative evolution of the N mole fraction and the energy bin population distribution in the boundary layer. The circles in (a) indicate the locations at which the population distributions, plotted in (b), are extracted (in (b) line with circles $r = 0.404$ m, line with squares $r = 0.402$ m, unbroken line $r = 0.401$ m, dashed line $r = 0.4005$ m, dotted-dashed line $r = 0.4002$ m , dotted line $r = 0.4$ m)

Figure 5.24 focuses on the energy bin population distribution at the locations $r = 0.4$ m (wall) and $r = 0.402$ m. The results confirm that the bound energy bins close to the ground-state and the predissociated bins are in Boltzmann equilibrium at the internal and translational temperature, respectively.

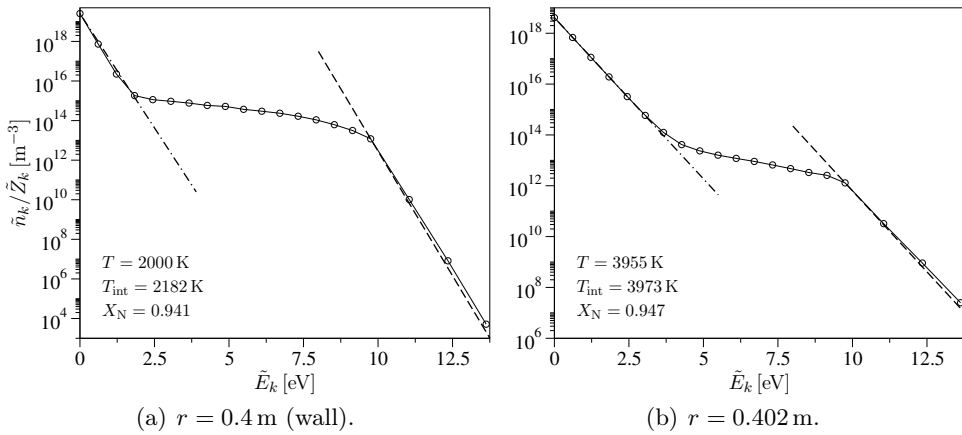


Figure 5.24: BRVC(20) model. Energy bin population distributions at the locations $r = 0.4$ m (wall) and $r = 0.402$ m in the boundary layer (the dashed and the dotted-dashed lines indicate the Boltzmann distributions at the translational and internal temperature, respectively).

5.4.3 Comparison with the MTP Model

The results obtained by means of the BRVC(20) model have been compared with the MTP model solution. Figure 5.25 compares the two models in terms of temperature and N mole fraction for the adopted values of free-stream pressure. In all the cases, it is observed that the shock stand-off distance is slightly underpredicted by the MTP model. The evolution of the N mole fraction along the stagnation-line clearly shows that the MTP model leads to a faster dissociation across the shock wave and to a higher recombination in the boundary layer. These results are consistent with those obtained in sects. 4.3.2 and 5.3.2 for inviscid shock and nozzle flows, respectively.

The differences between the two models, in terms of recombination in the boundary layer, become more and more enhanced when increasing the free-stream pressure. This can also be seen from tab. 5.7, reporting the wall values for the heat flux and the N mole fraction, and from fig. 5.26 showing the heat flux evolution along the stagnation-line. Notice that for the high pressure case ($p_\infty = 0.33$ torr), the wall heat flux predicted by the MTP model is almost twice the value predicted by the BRVC(20) model. The observed discrepancy is quite high and underlines the importance of accounting for non-Boltzmann distribution effects in the computation of stagnation-line, and more in general, aerothermodynamic flows. One may object that a more realistic heat flux comparison should also account for N_2-N_2 collisions. However, it should be recalled that the comparison between the BRVC(20) and the MTP models is performed consistently, by excluding in both cases N_2-N_2 and other types of collisions. Hence, the heat flux overestimation obtained in the case of the MTP model can be considered as a valid proof of its lack of accuracy.

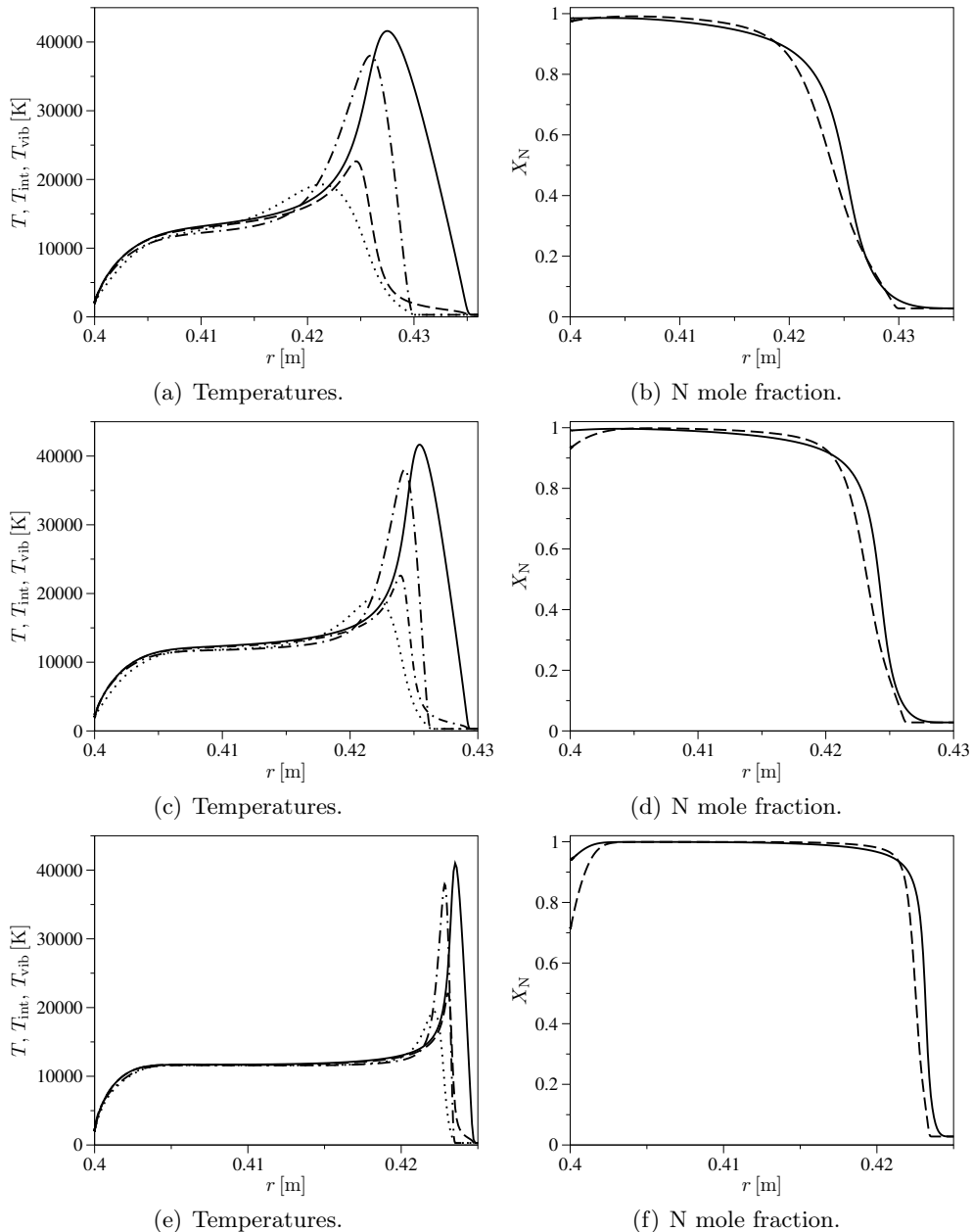


Figure 5.25: BRVC(20) and MTP model comparison. Temperature and N mole fraction evolution along the stagnation-line for different values of the free-stream pressure ((a)-(b) $p_\infty = 0.05$ torr, (c)-(d) $p_\infty = 0.1$ torr, (e)-(f) $p_\infty = 0.33$ torr; in (a), (c) and (e) unbroken lines T BRVC(20), dashed lines T_{int} BRVC(20), dotted-dashed lines T MTP, dotted lines T_{vib} MTP; in (b), (d) and (f) unbroken lines BRVC(20), dashed lines MTP).

p_∞	0.05 torr		0.1 torr		0.33 torr	
Model	q_r [MW/m ²]	X_N	q_r [MW/m ²]	X_N	q_r [MW/m ²]	X_N
BRVC(20)	0.958	0.985	1.23	0.991	2.38	0.941
MTP	0.948	0.975	1.47	0.933	4.13	0.714

Table 5.7: BRVC(20) and MTP model. Wall heat flux and N mole fraction values.

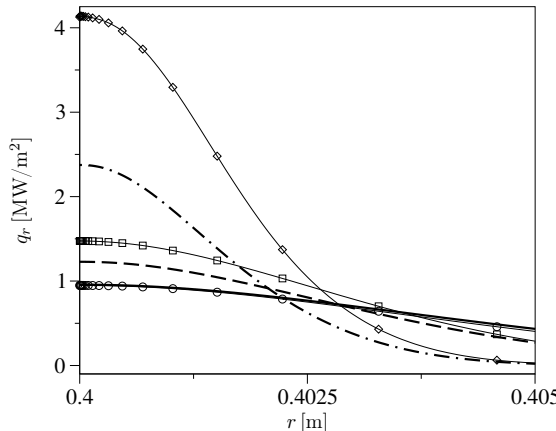


Figure 5.26: BRVC(20) and MTP model comparison. Heat flux evolution along the stagnation-line for different values of the free-stream pressure (unbroken line BRVC(20) $p_\infty = 0.05$ torr, dashed line BRVC(20) $p_\infty = 0.1$ torr, dotted-dashed line BRVC(20) $p_\infty = 0.33$ torr, line with circles MTP $p_\infty = 0.05$ torr, line with squares MTP $p_\infty = 0.1$ torr, line with diamonds MTP $p_\infty = 0.33$ torr).

5.4.4 Bin number Sensitivity Analysis

The sensitivity analysis performed in sects. 4.3.3 and 5.3.2 for inviscid flows behind shock waves and within nozzles indicated that, for the BRVC model, 20 energy bins guaranteed an accurate resolution of dissociation and recombination. This conclusion has been further investigated in the case of stagnation-line flows by repeating the calculations of sec. 5.4.1 with 10 and 100 energy bins. Figure 5.27 compares the BRVC(10), BRVC(20) and BRVC(100) model solutions in terms of translational temperature and N mole fraction. The dissociation and recombination within the shock and the boundary layer, respectively, are already well captured with only 10 energy bins. Using a higher number does not lead to appreciable changes in flowfield and it only allows for a better resolution of the temperature profile across the shock wave. This is further confirmed by the wall heat flux values reported in tab. 5.8. It is interesting to notice that the differences between the three solutions are much less pronounced than what observed in sec. 4.3.3 for inviscid flows behind shock waves (see fig. 4.17). This is due to dissipation phenomena which lead to a smooth temperature rise across the shock wave with a consequent lower sensitivity of the post-shock conditions to the number of energy bins.

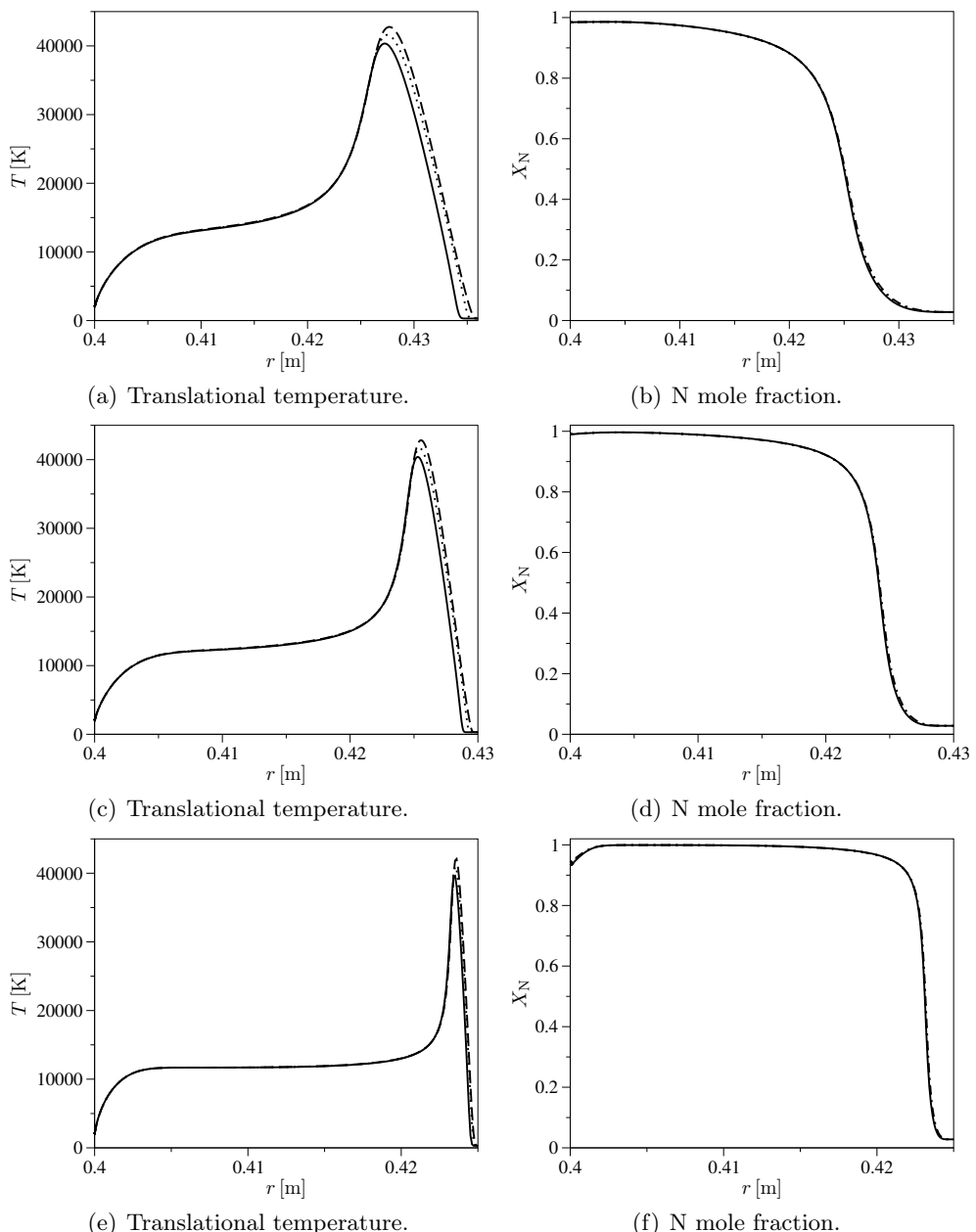


Figure 5.27: BRVC model. Translational temperature and N mole fraction evolution along the stagnation-line for different numbers of energy bins ((a)-(b) $p_\infty = 0.05$ torr, (c)-(d) $p_\infty = 0.1$ torr, (e)-(f) $p_\infty = 0.33$ torr; unbroken lines BRVC(10), dotted lines BRVC(20), dashed lines BRVC(100)).

p_∞	0.05 torr		0.1 torr		0.33 torr	
\mathcal{N}_{N_2}	$q_r[\text{MW/m}^2]$	X_{N}	$q_r[\text{MW/m}^2]$	X_{N}	$q_r[\text{MW/m}^2]$	X_{N}
10	-0.954	0.985	-1.23	0.9902	-2.42	0.934
20	-0.958	0.985	-1.23	0.991	-2.38	0.941
100	-0.961	0.985	-1.23	0.991	-2.35	0.944

Table 5.8: BRVC model. Wall heat flux and N mole fraction for different numbers of energy bins.

5.5 Inviscid Axisymmetric Flows

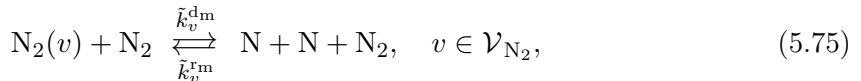
The coarse-grained models developed in ch. 3 have been applied to inviscid axisymmetric flows by solving the flow governing equations (5.26) as explained in sec. 5.2.2. The aim of the investigation was two-fold: to illustrate the feasibility of multi-dimensional simulations by means of collisional models, and to validate the models through comparison with experiments.

A comparison with experiments would require accounting for $\text{N}_2\text{-N}_2$ collisions. Since the NASA ARC database provides kinetic data only for a limited set of all the $\text{N}_2\text{-N}_2$ rovibrational transitions (Panesi et al. 2013), the simulations have been performed by means of an enriched VC model accounting for the following $\text{N}_2\text{-N}$ and $\text{N}_2\text{-N}_2$ interactions (Munafò et al. 2012):

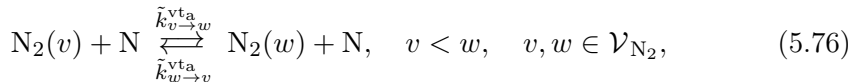
- Atomic impact dissociation/recombination (d_a and r_a):



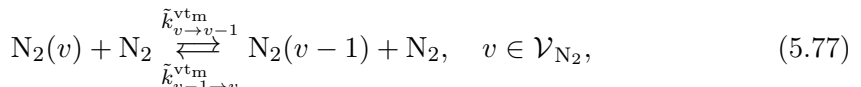
- Molecular impact dissociation/recombination (d_m and r_m):



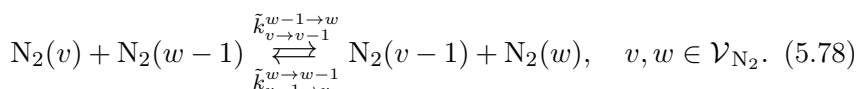
- Atomic impact vibrational-translational energy transfer (vt_a):



- Molecular impact vibrational-translational energy transfer (vt_m):



- Vibrational-vibrational energy transfer (vv):



The direct rate coefficients for the d_a and vt_a processes ($\tilde{k}_v^{d_a}$ and $\tilde{k}_{v \rightarrow w}^{vt_a}$, respectively) have been taken from the VC model developed in sec. 3.3 (see eqs. (3.58)-(3.59)). The direct rate coefficients for the d_m , vt_m and vv processes ($\tilde{k}_v^{d_m}$, $\tilde{k}_{v \rightarrow v-1}^{vt_m}$ and $\tilde{k}_{v \rightarrow v-1}^{w-1 \rightarrow w}$, respectively) have been taken from the available literature (Armenise et al. 1994; Capitelli et al. 2000; Colonna et al. 2006). The inverse process rate coefficients are computed by means of micro-reversibility. The enriched VC model given by eqs. (5.74)-(5.78) has been also applied to quasi-one-dimensional nozzle flows by Munafò et al. (2012). In the same reference, a comparison has been performed with the results obtained by using the d_a and vt_a rate coefficients computed by Esposito (1999; 2006).

5.5.1 Flow within the Nozzle of the EAST Facility

The enriched VC model has been applied to compute the inviscid axisymmetric flow within the nozzle of the EAST facility (whose area distribution is given in fig. 5.2). The throat area value has been taken from Sharma et al. (1993).

The flow is supposed to be in LTE conditions at the nozzle inlet. The related values for total pressure and temperature have been set to 10 132 500 Pa and 5600 K, respectively. These values have chosen been because: a) they correspond to actual operative conditions of the EAST facility and b) for these conditions, Sharma et al. (1993) have measured the population of vibrational levels by means of Raman spectroscopy. The inlet N and N_2 mole fractions (as obtained from the simulation) are 0.005 and 0.9995, respectively.

Calculations have been run by using a 4-block structured mesh where each block consisted of a 50×50 grid (see fig. 5.28). A grid convergence study has been performed by computing the nozzle flowfield on a finer grid obtained by doubling the number of nodes in both the radial and axial directions. The numerical solution obtained on the refined mesh did not show appreciable differences compared to that obtained on the initial one. Hence, the numerical solution obtained on the 50×50 grid could be considered grid-converged.

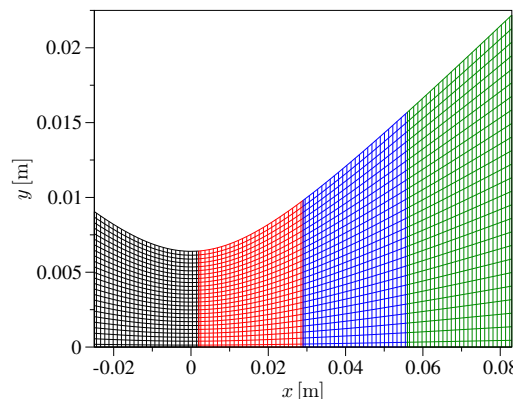


Figure 5.28: VC model. Mesh used for the EAST facility nozzle (4 blocks, 200×50 cells; one node over two is plotted along both the axial and radial directions).

Figure 5.29 shows the density and velocity magnitude fields. Figure 5.30 focuses on the temperature and mole fraction evolution along the axis. Due to the low temperature conditions at the nozzle inlet, the recombination of N is extremely limited (though its effects are noticeable when looking at the vibrational level populations as shown later in this section). The flow remains in thermal equilibrium for all the converging portion of the nozzle. Once the nozzle throat is past, the expansion becomes significant and non-equilibrium effects appear. These are caused by the combination of: a) decrease of the flow macroscopic time-scale (due to the velocity increase) and b) increase of the kinetic time-scale (due to the temperature decrease). In the diverging portion of the nozzle, the translational and vibrational temperatures deviate from each other, with the latter becoming frozen around the location $x \simeq 4 \times 10^{-2}$ m. Moving further downstream, the flow continues to expand as if the recombination and inelastic vt_a , vt_m and vv collisional processes were not occurring.

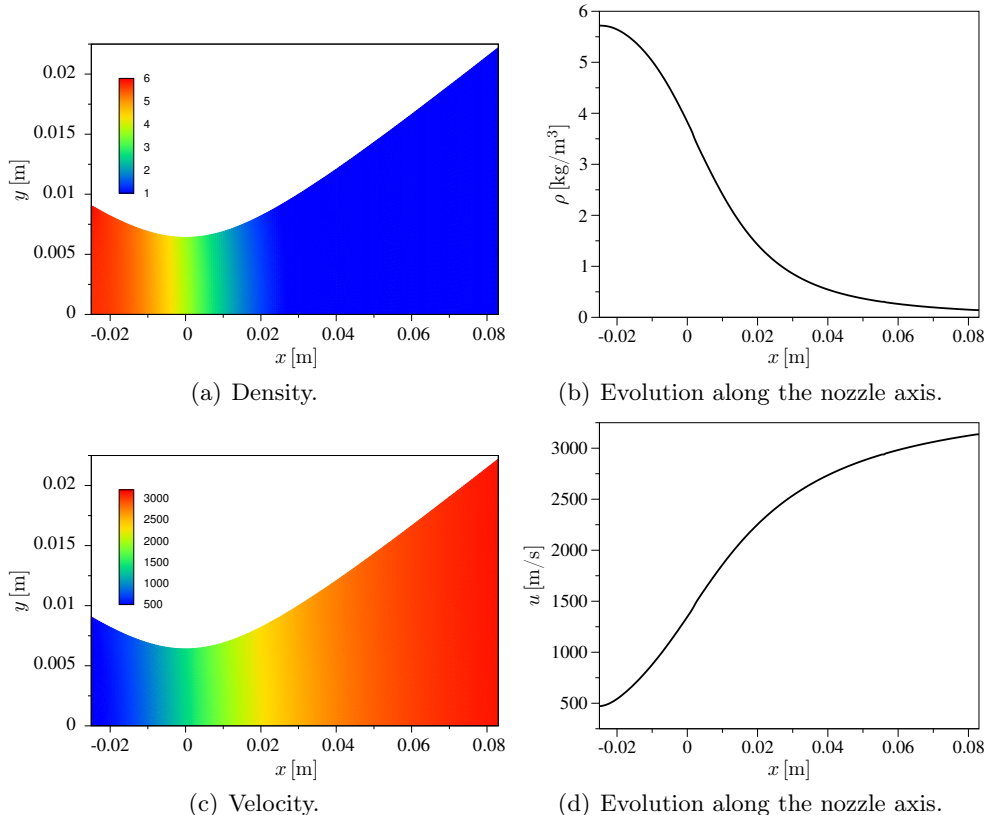


Figure 5.29: VC model. Density and velocity distributions within the EAST facility nozzle.

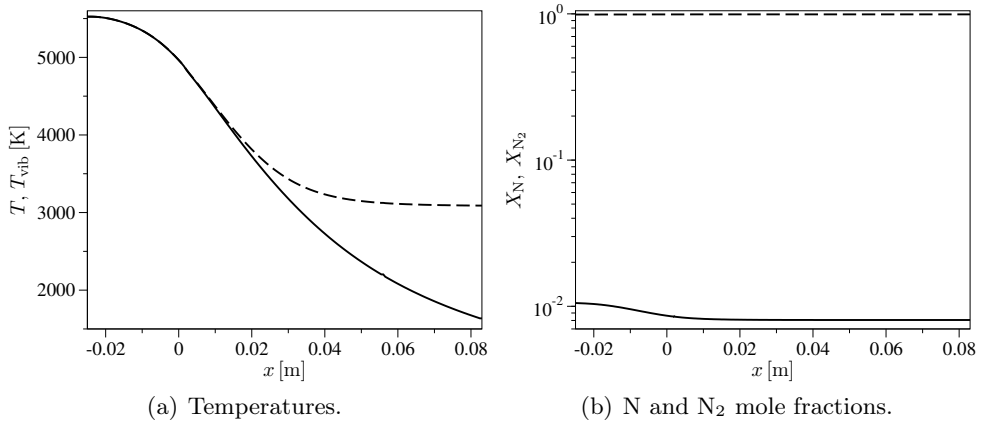


Figure 5.30: *VC model. Temperature and mole fraction evolution along the axis of the EAST facility nozzle (in (a) unbroken line T , dashed line T_{vib} ; in (b) unbroken line N, dashed line N_2).*

Figure 5.31 shows the evolution of the population distribution along the nozzle axis. At the nozzle inlet, the distribution is Boltzmann due to assumed LTE conditions. When the flow expands, the shape of the distribution remains initially the same. Only its slope changes as an effect of the cooling. The recombination causes an overpopulation in high-lying energy levels which becomes more and more pronounced moving along the nozzle axis. At the nozzle outlet, the ground-state and low-lying levels lie along a straight line (whose slope is given by the vibrational temperature previously shown) while high-lying energy levels are overpopulated.

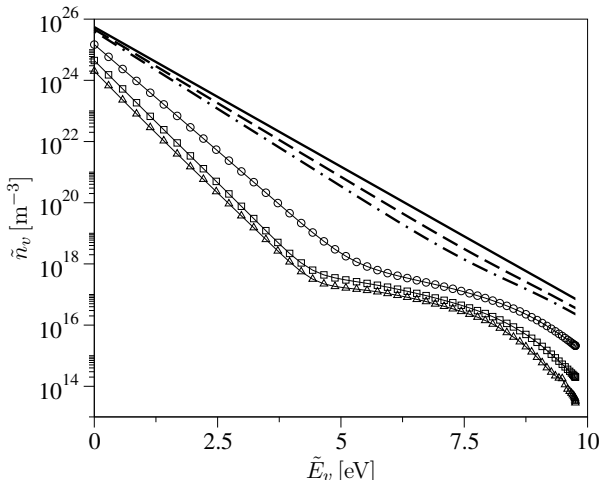


Figure 5.31: *VC model. Evolution of the vibrational population distribution along the axis of the EAST facility nozzle (unbroken line $x = -2.5 \times 10^{-2}$ m, dashed line $x = -6 \times 10^{-3}$ m, dotted-dashed line $x = 0$ m, line with circles $x = 2.4 \times 10^{-2}$ m, line with squares $x = 5.4 \times 10^{-2}$ m, line with triangles $x = 8.3 \times 10^{-2}$ m).*

The computed population distributions have been compared with the experimental data of Sharma et al. (1993) who performed Raman spectroscopy measurements at the locations $x = -6 \times 10^{-3}$ m, 2.4×10^{-2} m and 5.4×10^{-2} m. Figure 5.32 compares the computed and experimental normalized population distributions for the first 10 vibrational levels. The agreement is excellent at the first location, where the flow is close to equilibrium. At the second and third locations, some discrepancies appear for higher vibrational states. In this zone (where measurement errors are more significant), the simulation predicts a Boltzmann distribution at the vibrational temperature, while an overpopulation appears in the experimental data. The latter could be due to non-equilibrium at the nozzle inlet. This possibility has been neglected in the computations, due to assumed LTE conditions at the nozzle inlet. Moreover, the actual flow in the facility is unsteady and viscous. None of these features has been taken into account. In view of this, the comparison between computational and experimental results can be considered satisfactory.

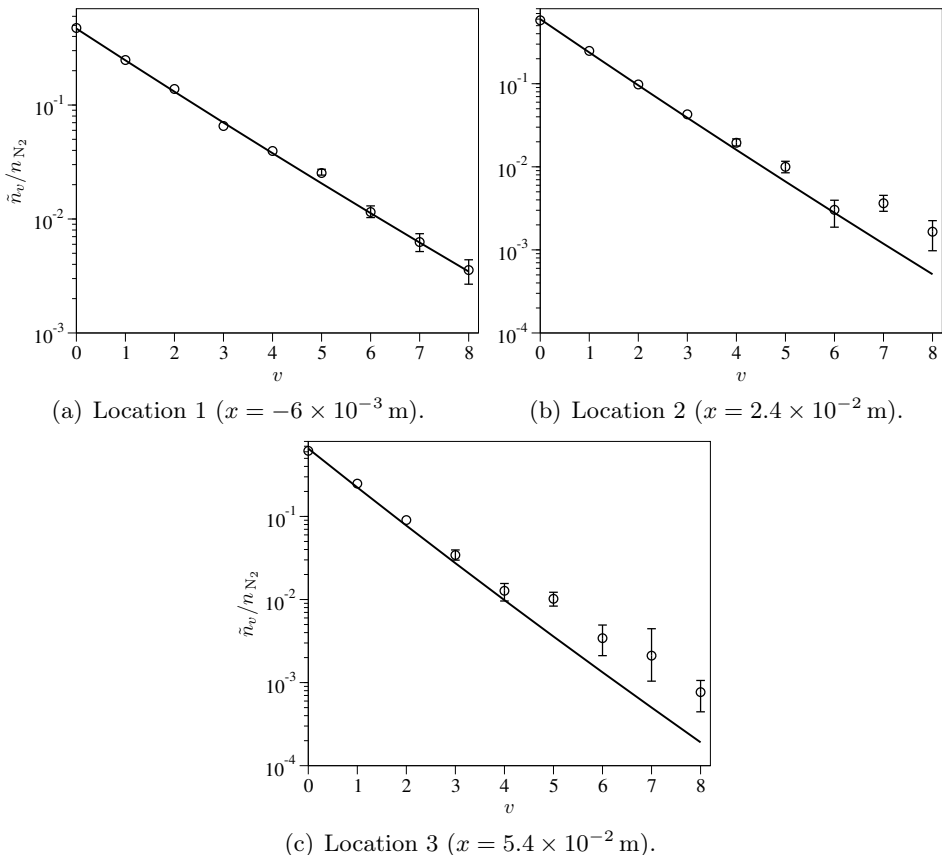


Figure 5.32: VC model. Comparison between the computed and experimental normalized vibrational population distributions for the EAST facility nozzle (unbroken lines calculations, circles experiments).

5.5.2 Flow over a Sphere

The second application of the enriched VC model described before has considered the inviscid and axisymmetric flow over a sphere with radius $r = 0.5$ m. The free-stream pressure, temperature and velocity have been set to 0.1 torr, 300 K and 9 km/s, respectively. Since N₂-N₂ collisions are now taken into account, there was no need for seeding the free-stream with some small amount of N. Calculations have been run by using a 12-block structured mesh, where each block consisted of a 90×30 grid (see fig. 5.33). As done in sec. 5.5.1 for the EAST facility nozzle flow, a grid convergence study has been performed by computing the flowfield around the sphere on a finer grid obtained by doubling the number of nodes in both radial and axial directions. The numerical solution obtained on the refined mesh did not show appreciable differences compared to that obtained on the initial one. Hence, the numerical solution obtained on the 90×30 grid could be considered grid-converged.

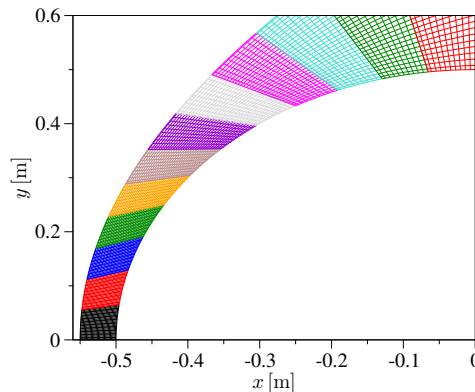


Figure 5.33: VC model. Mesh used for the flow over a sphere (12 blocks, 90×360 cells; one node over three is plotted along both the axial and radial directions).

Figure 5.34 shows the temperature N mole fraction distributions around the sphere, while the related evolutions along the stagnation-line are given in fig. 5.35. At the shock location, the vibrational temperature is frozen and maintains its free-stream value. Behind the shock, excitation initially occurs through v_{t_m} processes. This leads to a steep rise of the vibrational temperature (obtained based on eq. (3.63)) behind the shock. Once molecules are excited, they start to dissociate and, as soon as some N is formed, v_{t_a} processes start to occur as well. In this phase, dissociation occurs at the expense of vibrational energy causing a decrease of the vibrational temperature. Since the flow is inviscid, no boundary layer is formed at the wall. At the wall, the gas temperature assumes the value corresponding to the post-shock equilibrium conditions. It is worth to notice that, as opposed to what observed when using conventional multi-temperature models (Park 1990), the vibrational temperature behind the shock is always lower than the translational one.

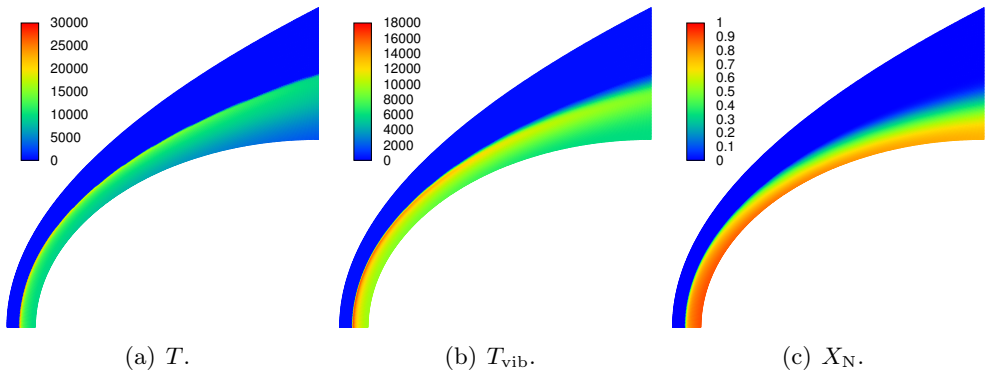


Figure 5.34: VC model. Temperature and N mole fraction distributions around the sphere.

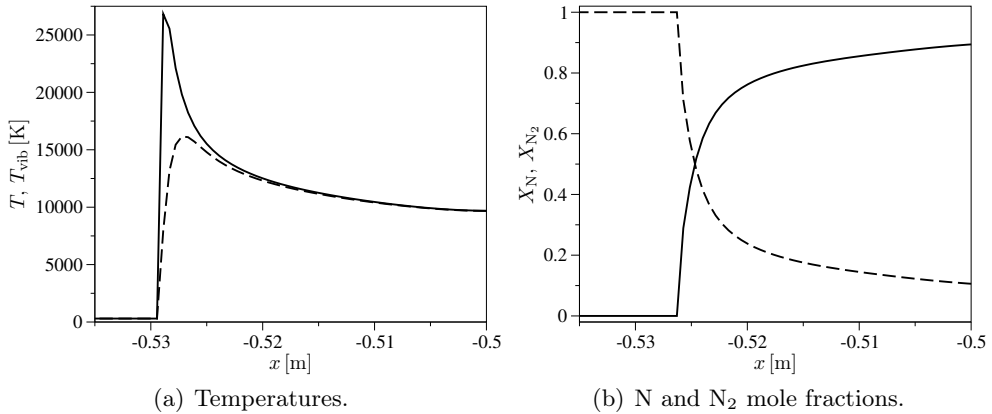


Figure 5.35: VC model. Temperature and N mole fraction evolution along the stagnation-line (in (a) unbroken line T , dashed line T_{vib} ; in (b) unbroken line N , dashed line N_2).

The dynamics of the dissociation and internal energy excitation can also be studied at the microscopic level. This is done in fig. 5.36 showing the evolution along the stagnation-line of the mole fractions of the first 10 vibrational states of N₂ (fig. 5.36(a)) and the vibrational level population distribution (fig. 5.36(b)). The results indicates that macroscopic dissociation proceeds through an initial stage of excitation followed by a second phase where dissociation from all vibrational levels occurs. The evolution of the population distribution in fig. 5.36(b) shares the same features observed in sects. 4.2.5 and 5.4.2 for inviscid flows behind shock waves and viscous stagnation-line flows, respectively. When the flow crosses the shock, the free-stream Boltzmann distribution is progressively distorted due to collisional excitation processes that populate high-lying energy levels. Then, the dissociation of N₂ starts and, in its final phase, it occurs under thermal equilibrium conditions.

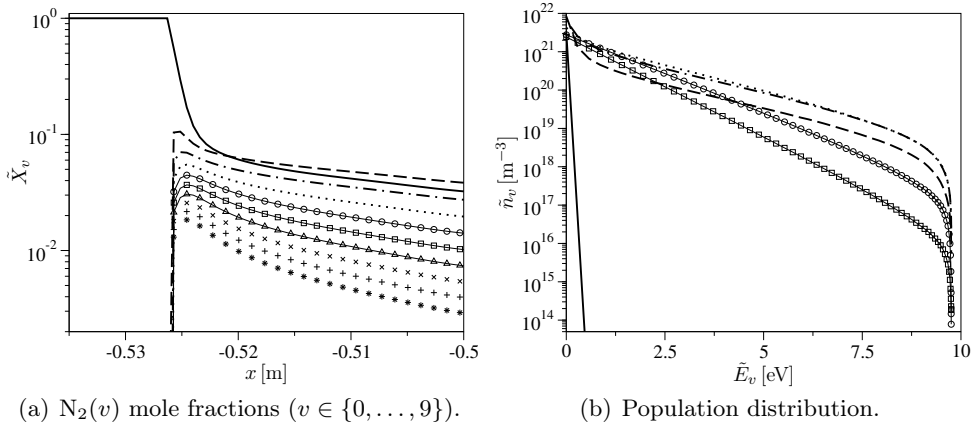


Figure 5.36: VC model. Evolution of the $\text{N}_2(v)$ mole fractions and the vibrational population distribution along the stagnation-line (in (a) unbroken line $\text{N}_2(0)$, dashed line $\text{N}_2(1)$, dotted-dashed line $\text{N}_2(2)$, dotted line $\text{N}_2(3)$, line with circles $\text{N}_2(4)$, line with squares $\text{N}_2(5)$, line with triangles $\text{N}_2(6)$, crosses $\text{N}_2(7)$, plus $\text{N}_2(8)$, stars $\text{N}_2(9)$; in (b) unbroken line $x = -0.55$ m, dashed line $x = -0.53$ m, dotted-dashed line $x = -0.525$ m, dotted line $x = -0.52$ m, line with circles $x = -0.515$ m, line with squares $x = -0.5$ m).

5.6 Intermediate Conclusions

This chapter has described the integration of the RVC, BRVC and VC models in CFD solvers for aerothermodynamic flows. Applications have considered inviscid quasi-one-dimensional flows within converging-diverging nozzles (sec. 5.3), viscous stagnation-line flows (sec. 5.4), and inviscid axisymmetric flows (sec. 5.5). In all the cases, with the exception of sec. 5.5, the computational results have been also compared with those obtained by means of the MTP model.

5.6.1 Nozzle Flows

The RVC model has been applied to investigate the non-equilibrium flow within the nozzle of the EAST facility in sec. 5.3.1. The results obtained have shown that rotational non-equilibrium effects have a small influence on flow quantities. This was confirmed by the good agreement between the RVC and VC model solutions. A comparison of the vibrational specific distributions obtained by means of the RVC and VC models has shown that the VC model tends to overestimate the population of high-lying vibrational states (due to the assumption of rotational equilibrium). However, these high-lying states contribute to a negligible extent to the bulk vibrational energy.

The analysis of the rovibrational energy level population distributions for the EAST facility nozzle, has shown that the rotational levels of the ground and the low-lying vibrational states are in thermal equilibrium with translation. This is not the case for higher states. A careful investigation of the rotational

level distributions has revealed the presence of an odd-even rotational quantum number splitting for those levels close to the ground-state. This feature (already observed in sec. 4.2.5 for flows behind shock waves) was more noticeable for higher vibrational states, which experienced a bigger departure from the local thermal equilibrium.

Both the BRVC and VC models have shown to be in good agreement with the RVC model. The VC model was slightly more accurate, as opposed to what observed in sec. 4.3.2 for flows behind shock waves. This result could be explained by the fact that the adoption of a VC model is naturally suggested by the observed rotational equilibrium for the low-lying vibrational states.

The BRVC model has been then applied to investigate the non-equilibrium flow within the F4 and Scirocco nozzles in sec. 5.3.2. These simulations were also performed for a further investigation of the discrepancies observed between the BRVC and VC model solutions in sec. 5.3.1. The results obtained have shown that, even with 10-20 energy bins, the numerical solutions are very close to those obtained by means of the VC model. For both nozzle geometries, the relative error on the outlet values of the N₂ mole fraction have been estimated by assuming the VC model as the exact solution. The error was lower than 5% when using 20 energy bins. Moreover, for the case of 2-5 energy bins, the results did not show an excessive departure from the VC model solution and provided also a much more accurate description than the MTP model. This facts make the BRVC model more appealing for multi-dimensional CFD applications. This is the reason why the investigation of viscous stagnation-line flows (sec. 5.4) has been performed by considering only the BRVC model among all the coarse-grained models developed in the present thesis.

5.6.2 Stagnation-line Flows

Based on the conclusions drawn from the investigation of nozzle flows, the analysis of viscous stagnation-line flows (sec. 5.4) has been carried out by means of the BRVC model. This test-case revealed to be particularly rich, in terms of physico-chemical modeling, as it allowed to account for both recombination and dissociation in the same benchmark.

The detailed analysis of the energy bin dynamics (sec. 5.4.2) has shown that the recombination in the boundary layer occurs through sequences of non-Boltzmann distributions. The comparison between the BRVC and MTP model solutions (sec. 5.4.3) has shown that the MTP model overestimates the wall heat flux, due to an inaccurate description of recombination within the boundary layer. The sensitivity study on the number of energy bins (sec. 5.4.4) has shown that, when dissipation phenomena are considered, the flowfield solution is less dependent on the number of energy bins, compared to what observed for the inviscid flow results discussed in sects. 4.3.3 and 5.3.2. Indeed, for the adopted free-stream conditions, even 10 energy bins could be used for achieving an accurate flow description.

5.6.3 Inviscid Axisymmetric Flows

Multi-dimensional applications to inviscid and axisymmetric non-equilibrium flows (sec. 5.5) have been performed in order to show their feasibility and to validate the models developed in the present thesis. In order to accomplish validation, the numerical simulations have been performed by means of an enriched VC model, accounting for both N₂-N and N₂-N₂ interactions. The rate coefficients for N₂-N₂ interactions have been taken from the available literature. The use of the BRVC model has not been considered, due to the limited set of rovibrational kinetic data for N₂-N₂ interactions in the NASA ARC database. The enriched VC model has been applied to compute the steady flows within the nozzle of the EAST facility (sec. 5.5.1) and around a sphere (sec. 5.5.2). In the case of the flow within the nozzle of the EAST facility, the computed vibrational population distributions have been compared with the Raman spectroscopy measurements of Sharma et al. (1993). A fair agreement has been observed, allowing for a partial validation of the enriched VC model used in the simulations.

For the sake of completeness, it should be said that the promising multi-dimensional results obtained in this chapter are preliminary, due to the lack of “2D effects” caused by the neglecting of the transport fluxes in the flow governing equations.

Part III

Development of a Deterministic Kinetic Flow Solver

Chapter 6

Extension of a Conservative Spectral-Lagrangian Method to Multi-Component Gases and Inelastic Collisions

This chapter describes a spectral-Lagrangian method for solving the Boltzmann equation for multi-component gases with internal energy (Munafò et al. 2014). Reactive collisions, such as dissociation, are not accounted for. The spectral-Lagrangian method is an extension of that developed by Gamba and Tharkabhushanam (2009) for a mono-component gas without internal energy. The present chapter is structured as follows. Section 6.1 introduces the weak form of the partial collision operators. The development of the numerical method starts in sec. 6.2 with the derivation of the weighted convolution structure of the Fourier transformed Boltzmann equation. The computational procedure for the discrete evaluation of the collision operators is given in sec. 6.3, where the discretization of the phase-space is also detailed.

6.1 The Weak Form of The Partial Collision Operators

In the case of a multi-component gas with internal energy (where the effects of reactive collisions are neglected), the Boltzmann equation (1.5) reduces to:

$$\mathfrak{D}_{s_i} f_{s_i} = Q_{s_i}^{\text{el}} + Q_{s_i}^{\text{in}}, \quad s \in \mathcal{S}, \quad i \in \mathcal{I}_s, \quad (6.1)$$

where the elastic and inelastic collision operators are:

$$Q_{s_i}^{\text{el}} = \sum_{\substack{p \in \mathcal{S} \\ j \in \mathcal{I}_p}} Q_{s_i p_j}, \quad Q_{s_i}^{\text{in}} = \sum_{\substack{(p_j, s_k, p_l) \\ \in \mathcal{C}_{s_i}^{\text{in}}}} Q_{s_i p_j}^{s_k p_l}, \quad s \in \mathcal{S}, \quad i \in \mathcal{I}_s. \quad (6.2)$$

The expressions for the partial elastic and inelastic collision operators (given in eqs. (1.7) and (1.11), respectively) are repeated here for the sake of clarity:

$$Q_{s_i p_j} = \iint_{\mathcal{S}^2 \times \mathbb{R}^3} \left(f'_{s_i} f'_{p_j} - f_{s_i} f_{p_j} \right) \sigma_{s_i p_j} g d\omega' d\mathbf{c}_{p_j}, \quad (6.3)$$

$$s, p \in \mathcal{S}, \quad i \in \mathcal{I}_s, \quad j \in \mathcal{I}_p,$$

$$Q_{s_i p_l}^{s_k p_l} = \iint_{\mathcal{S}^2 \times \mathbb{R}^3} \left[\left(\frac{\beta_{s_k} \beta_{p_l}}{\beta_{s_i} \beta_{p_j}} \right) f'_{s_k} f'_{p_l} - f_{s_i} f_{p_j} \right] \sigma_{s_i p_l}^{s_k p_l} g d\omega' d\mathbf{c}_{p_l}, \quad (6.4)$$

$$(p_j, s_k, p_l) \in \mathcal{C}_{s_i}^{\text{in}}, \quad s \in \mathcal{S}, \quad i \in \mathcal{I}_s.$$

The weak form of the partial collision operators can be obtained through multiplication of eqs. (6.3)-(6.4) by a smooth test function $\varphi_{s_i} = \varphi_{s_i}(\mathbf{c}_{s_i})$ and integration over the velocity space:

$$\int_{\mathbb{R}^3} Q_{s_i p_j} \varphi_{s_i} d\mathbf{c}_{s_i} = \iiint_{\mathcal{S}^2 \times \mathbb{R}^3 \times \mathbb{R}^3} (\varphi'_{s_i} - \varphi_{s_i}) f_{s_i} f_{p_j} \sigma_{s_i p_j} g d\omega' d\mathbf{c}_{p_j} d\mathbf{c}_{s_i}, \quad (6.5)$$

$$s, p \in \mathcal{S}, \quad i \in \mathcal{I}_s, \quad j \in \mathcal{I}_p,$$

$$\begin{aligned} \int_{\mathbb{R}^3} Q_{s_i p_j}^{s_k p_l} \varphi_{s_i} d\mathbf{c}_{s_i} &= \iiint_{\mathcal{S}^2 \times \mathbb{R}^3 \times \mathbb{R}^3} \varphi_{s_i} f'_{s_k} f'_{p_l} \sigma_{s_k p_l}^{s_i p_j} g' d\omega d\mathbf{c}'_{s_k} d\mathbf{c}'_{p_l} - \\ &\quad \iiint_{\mathcal{S}^2 \times \mathbb{R}^3 \times \mathbb{R}^3} \varphi_{s_i} f_{s_i} f_{p_j} \sigma_{s_i p_j}^{s_k p_l} g d\omega' d\mathbf{c}_{s_i} d\mathbf{c}_{p_j}, \end{aligned} \quad (6.6)$$

$$(p_j, s_k, p_l) \in \mathcal{C}_{s_i}^{\text{in}}, \quad s \in \mathcal{S}, \quad i \in \mathcal{I}_s,$$

where $\varphi'_{s_i} = \varphi_{s_i}(\mathbf{c}'_{s_i})$. In obtaining eqs. (6.5)-(6.6) the micro-reversibility relations (1.8) and (1.12) for elastic and inelastic collisions, respectively, have been used. For the partial elastic collision operator the weak form is obtained by applying the usual technique of swapping between primed and unprimed variables in the integral and by exploiting micro-reversibility (eq. (1.8)). Since in elastic collisions there are no transitions between the internal energy levels, swapping between primed and unprimed variables has no effect on the species index. This allows for casting the weak form into a unique integral involving the species velocity distribution function in the pre-collisional state. The same result cannot be obtained in the case of inelastic collisions (swapping between primed and unprimed variables is associated to a species index change). The weak form of the partial inelastic collision operator is obtained by applying micro-reversibility (eq. (1.12)) to the gain part of the operator, while the loss part is left unchanged. As discussed by Dellacherie (2003), alternative expressions to that given in eq. (6.6) can be obtained. However, the one given in eq. (6.6) is the most suited for the work presented in this thesis.

6.2 The Fourier Transform of the Partial Collision Operators

The numerical method proposed in sec. 6.3 makes use of the Fourier transform of the partial collision operators. This can be obtained by using a Fourier velocity mode $(2\pi)^{-3/2} \exp(-i\zeta \cdot \mathbf{c}_{s_i})$ as test function in the weak form given in eqs. (6.5)-(6.6) (Bobylev 1988; Gamba and Tharkabhushanam 2009).

The Fourier transform of the partial collision operators satisfy the following properties (Munafò et al. 2014).

Proposition 6.2.1. *The Fourier transform of the partial elastic and inelastic collision operators can be written as weighted convolutions in Fourier space:*

$$\hat{Q}_{s_ip_j}(\zeta) = \int_{\mathbb{R}^3} \hat{f}_{s_i}(\zeta - \xi) \hat{f}_{p_j}(\xi) \hat{W}_{s_ip_j}(\zeta, \xi) d\xi, \quad (6.7)$$

$$\begin{aligned} \hat{Q}_{s_ip_j}^{s_k p_l}(\zeta) &= \int_{\mathbb{R}^3} \hat{f}_{s_k}(\zeta - \xi) \hat{f}_{p_l}(\xi) \hat{G}_{s_ip_j}^{s_k p_l}(\zeta, \xi) d\xi - \\ &\quad \int_{\mathbb{R}^3} \hat{f}_{s_i}(\zeta - \xi) \hat{f}_{p_j}(\xi) \hat{L}_{s_ip_j}^{s_k p_l}(\xi) d\xi, \\ &(p_j, s_k, p_l) \in \mathcal{C}_{s_i}^{\text{in}}, \quad s \in \mathcal{S}, \quad i \in \mathcal{I}_s. \end{aligned} \quad (6.8)$$

Quantities \hat{f}_{s_i} , \hat{f}_{s_k} , \hat{f}_{p_j} and \hat{f}_{p_l} are the Fourier transform of the velocity distribution function of the species s_i , s_k , p_j and p_l , respectively. The functions $\hat{W}_{s_ip_j}(\zeta, \xi)$, $\hat{G}_{s_ip_j}^{s_k p_l}(\zeta, \xi)$ and $\hat{L}_{s_ip_j}^{s_k p_l}(\zeta, \xi)$ are convolution weights defined as:

$$\begin{aligned} \hat{W}_{s_ip_j}(\zeta, \xi) &= \frac{1}{(2\pi)^{3/2}} \iint_{\mathcal{S}^2 \times \mathbb{R}^3} g \sigma_{s_ip_j} \left\{ \exp \left[-i \frac{\mu_{sp}}{m_s} (\mathbf{g}' - \mathbf{g}) \cdot \zeta \right] - 1 \right\} \times \\ &\quad \exp(-i \mathbf{g} \cdot \xi) d\omega' d\mathbf{g}, \quad s, p \in \mathcal{S}, \quad i \in \mathcal{I}_s, \quad j \in \mathcal{I}_p, \end{aligned} \quad (6.9)$$

$$\begin{aligned} \hat{G}_{s_ip_j}^{s_k p_l}(\zeta, \xi) &= \frac{1}{(2\pi)^{3/2}} \iint_{\mathcal{S}^2 \times \mathbb{R}^3} g' \sigma_{s_k p_l}^{s_i p_j} \exp \left[-i \frac{\mu_{sp}}{m_s} (\mathbf{g} - \mathbf{g}') \cdot \zeta \right] \times \\ &\quad \exp(-i \mathbf{g}' \cdot \xi) d\omega d\mathbf{g}', \end{aligned} \quad (6.10)$$

$$\hat{L}_{s_ip_j}^{s_k p_l}(\xi) = \frac{1}{(2\pi)^{3/2}} \iint_{\mathcal{S}^2 \times \mathbb{R}^3} g \sigma_{s_ip_j}^{s_k p_l} \exp(-i \mathbf{g} \cdot \xi) d\omega' d\mathbf{g}, \quad (6.11)$$

$$(p_j, s_k, p_l) \in \mathcal{C}_{s_i}^{\text{in}}, \quad s \in \mathcal{S}, \quad i \in \mathcal{I}_s,$$

where the pre and post-collisional relative velocity vectors are $\mathbf{g} = g\omega$ and $\mathbf{g}' = g'\omega'$, respectively.

Proof. The direct substitution of $\varphi_{s_i}(\mathbf{c}_{s_i}) = (2\pi)^{-3/2} \exp(-i\zeta \cdot \mathbf{c}_{s_i})$ in eqs. (6.5)-(6.6) gives, after some algebra, the thesis. The mathematical details of the proof can be found in app. G. \square

From Proposition 6.2.1, the following observations can be made:

1. The convolution weights depend only on the differential cross-section. No dependence on the velocity distribution function occurs. This finding can be exploited to develop a computational method that uses eqs. (6.7)-(6.8) for the discrete evaluation of the collision operators (*i.e.* the weights associated to each interaction can be pre-computed).
2. The convolution weights $\hat{G}_{s_ip_j}^{s_k p_l}(\zeta, \xi)$ and $\hat{L}_{s_ip_j}^{s_k p_l}(\zeta, \xi)$ are associated, respectively, to the gain and loss part of the partial inelastic collision operator and cannot be directly summed to give a unique convolution weight. This is possible only for elastic collisions, for which case it can be shown that $\hat{W}_{s_ip_j}(\zeta, \xi) = \hat{G}_{s_ip_j}^{s_k p_j}(\zeta, \xi) - \hat{L}_{s_ip_j}^{s_k p_j}(\zeta, \xi)$
3. Since no assumption is introduced on the cross-section, anisotropic interactions can naturally be taken into account.

Proposition 6.2.2. *The expressions for the convolution weights reduce to one-dimensional integrals on the pre and post-collisional relative velocity magnitudes in the case of isotropic interactions (differential cross-section depending only on the relative velocity magnitude):*

$$\hat{W}_{s_ip_j}(\zeta, \xi) = 4\sqrt{2\pi} \int_0^{+\infty} \sigma_{s_ip_j} \left[j_0 \left(\frac{\mu_{sp}}{m_s} g \zeta \right) j_0 \left(g \left| \xi - \zeta \frac{\mu_{sp}}{m_s} \right| \right) - j_0(g\xi) \right] \times g^3 dg, \quad s, p \in \mathcal{S}, \quad i \in \mathcal{I}_s, \quad j \in \mathcal{I}_p, \quad (6.12)$$

$$\begin{aligned} \hat{G}_{s_ip_j}^{s_k p_l}(\zeta, \xi) &= 4\sqrt{2\pi} \int_{\mathcal{G}'_{s_k p_l}}^{+\infty} \sigma_{s_ip_j}^{s_k p_l} j_0 \left(\frac{\mu_{sp}}{m_s} \sqrt{g'^2 + 2 \frac{\Delta E_{s_ip_j}^{s_k p_l}}{\mu_{sp}}} \zeta \right) \times \\ &\quad j_0 \left(g' \left| \xi - \zeta \frac{\mu_{sp}}{m_s} \right| \right) g'^3 dg', \end{aligned} \quad (6.13)$$

$$\hat{L}_{s_ip_j}^{s_k p_l}(\xi) = 4\sqrt{2\pi} \int_{\mathcal{G}_{s_ip_j}^{s_k p_l}}^{+\infty} \sigma_{s_ip_j}^{s_k p_l} j_0(g\xi) g^3 dg, \quad (6.14)$$

$$(p_j, s_k, p_l) \in \mathcal{C}_{s_i}^{\text{in}}, \quad s \in \mathcal{S}, \quad i \in \mathcal{I}_s,$$

where the lower relative velocity limits $\mathcal{G}'_{s_k p_l}$ and $\mathcal{G}_{s_ip_j}^{s_k p_l}$ in the integrals defining the gain and loss inelastic isotropic convolution weights are:

$$\mathcal{G}'_{s_k p_l} = \begin{cases} \sqrt{-\frac{2 \Delta E_{s_ip_j}^{s_k p_l}}{\mu_{sp}}} & \text{if } \Delta E_{s_ip_j}^{s_k p_l} < 0, \\ 0 & \text{if } \Delta E_{s_ip_j}^{s_k p_l} \geq 0, \end{cases} \quad (6.15)$$

$$\mathcal{G}_{s_ip_j}^{s_k p_l} = \begin{cases} \sqrt{\frac{2 \Delta E_{s_ip_j}^{s_k p_l}}{\mu_{sp}}} & \text{if } \Delta E_{s_ip_j}^{s_k p_l} > 0, \\ 0 & \text{if } \Delta E_{s_ip_j}^{s_k p_l} \leq 0, \end{cases} \quad (6.16)$$

$$(p_j, s_k, p_l) \in \mathcal{C}_{s_i}^{\text{in}}, \quad s \in \mathcal{S}, \quad i \in \mathcal{I}_s.$$

The function $j_0(x) = \sin(x)/x$ is the zeroth-order spherical Bessel function of first kind (or, in alternative, un-normalized sinc function; Abramovitz and Stegun 1972). Quantities ζ and ξ are the magnitudes of the vectors ζ and ξ , respectively.

Proof. The use of a spherical coordinate system in the integrals over \mathbf{g} , \mathbf{g}' , ω and ω' in eqs. (6.9)-(6.11) gives, after some algebra, the thesis. As an example, the integral over ω' in eq. (6.9) can be computed by adopting a spherical coordinate system for the vector ω' with the pole aligned along the direction of the vector ζ . A similar procedure can be used for the other integrals. The mathematical details of the proof can be found in app. H. \square

6.3 Numerical Method

The numerical method proposed for solving the Boltzmann equation (6.1) exploits the particularly simple structure assumed by the Fourier transform of the partial elastic and inelastic collision operators (weighted convolution in Fourier space; eqs. (6.7)-(6.8)). The velocity space is always kept three-dimensional and only zero/one-dimensional flow problems are considered. This is justified in view of the fact that the main purpose of the thesis work was the development of a conservative algorithm for the evaluation of the collision operators in the case of multi-component gases with discrete internal energy levels. The extension of the proposed method to multi-dimensional flows is trivial, as the aforementioned algorithm remains the same whether the flow is multi-dimensional or not.

When the flow is one-dimensional and its direction is aligned with the x axis of a Cartesian reference frame $(O; x, y, z)$, the Boltzmann equation (6.1) becomes:

$$\frac{\partial f_{s_i}}{\partial t} + c_{s_i} x \frac{\partial f_{s_i}}{\partial x} = Q_{s_i}^{\text{el}} + Q_{s_i}^{\text{in}}, \quad s \in \mathcal{S}, \quad i \in \mathcal{I}_s. \quad (6.17)$$

In order obtain numerical solutions to eq. (6.17), the following steps have to be taken:

1. Discretization of the phase-space,
2. Discretization of the streaming and collision operators (in both time and position domains),
3. Development of a computational algorithm for an efficient evaluation of the elastic and inelastic collision operators allowing to satisfy the conservation requirements stated in eqs. (1.24) and (1.26):

$$\sum_{\substack{s \in \mathcal{S} \\ i \in \mathcal{I}_s}} \int_{\mathfrak{R}^3} \psi_{s_i}^{\text{el}\nu} Q_{s_i}^{\text{el}} d\mathbf{c}_{s_i} = 0, \quad \nu \in \mathcal{I}^{\text{el}}, \quad \sum_{\substack{s \in \mathcal{S} \\ i \in \mathcal{I}_s}} \int_{\mathfrak{R}^3} \psi_{s_i}^{\text{in}\nu} Q_{s_i}^{\text{in}} d\mathbf{c}_{s_i} = 0, \quad \nu \in \mathcal{I}^{\text{in}}. \quad (6.18)$$

All the items of the previous list are described in secs. 6.3.1-6.3.2

6.3.1 Discretization of the Phase-Space

A Cartesian reference frame $(O; c_x, c_y, c_z)$ is introduced for the velocity space of all species. The former is discretized by considering points falling inside a cube, having side semi-length equal to L_c and centered at the origin O :

$$\mathcal{V}_c = \{\mathbf{c} = (c_x, c_y, c_z) \in \Re^3 \mid c_\alpha \in [-L_c, L_c], \alpha \in \{x, y, z\}\}. \quad (6.19)$$

The individual discrete velocity nodes belonging to the set \mathcal{V}_c are obtained as follows. Let Δc be the velocity mesh spacing, defined as:

$$\Delta c = \frac{2L_c}{N_c}, \quad (6.20)$$

where N_c is the number of velocity nodes along the c_x , c_y and c_z directions, let $\mathbf{h} = (h_x, h_y, h_z)$ be the vector of indices associated to the discrete velocity node $\mathbf{c}_h = (c_{hx}, c_{hy}, c_{hz})$ and let \mathcal{H} be the set $\mathcal{H} = \{0, \dots, N_c - 1\}$. The discrete velocity node \mathbf{c}_h belonging to the set \mathcal{V}_c is computed as follows:

$$\mathbf{c}_h = -L_c (\mathbf{i}_{c_x} + \mathbf{i}_{c_y} + \mathbf{i}_{c_z}) + \mathbf{h} \Delta c, \quad \mathbf{h} = (h_x, h_y, h_z) \in \mathcal{H}^3. \quad (6.21)$$

The vectors \mathbf{i}_{c_x} , \mathbf{i}_{c_y} and \mathbf{i}_{c_z} are, respectively, the unit vectors of the c_x , c_y and c_z axes of the Cartesian frame $(O; c_x, c_y, c_z)$, and the set \mathcal{H}^3 is defined as $\mathcal{H} \times \mathcal{H} \times \mathcal{H}$. A vector of integration weights $\mathbf{w}_h = (w_{hx}, w_{hy}, w_{hz})$ is introduced and associated to each discrete velocity node \mathbf{c}_h . In the present work, trapezoidal-rule weights are used:

$$w_{h\alpha} = \begin{cases} 1/2 & \text{if } h_\alpha = 0, N_c - 1, \\ 1 & \text{otherwise,} \end{cases} \quad \alpha \in \{x, y, z\}. \quad (6.22)$$

The global integration weight associated to the discrete velocity node \mathbf{c}_h is computed as $w_h = w_{hx} w_{hy} w_{hz}$.

As anticipated before in this section, the algorithm proposed for the evaluation of the collision operators (described in sec. 6.3.2) is based on their Fourier transform. This is the reason why a Fourier velocity space (associated to the velocity space described above) is introduced and discretized as follows. A Cartesian reference frame $(O; \zeta_x, \zeta_y, \zeta_z)$ in the Fourier velocity space is introduced and the points falling inside a cube, having semi-length equal to L_ζ and centered at the origin O , are considered:

$$\mathcal{V}_\zeta = \{\zeta = (\zeta_x, \zeta_y, \zeta_z) \in \Re^3 \mid \zeta_\alpha \in [-L_\zeta, L_\zeta], \alpha \in \{x, y, z\}\}. \quad (6.23)$$

The coordinates of the discrete Fourier velocity nodes, belonging to the set \mathcal{V}_ζ , are obtained in the same manner as done for the physical velocity nodes in eq. (6.21). Thus:

$$\zeta_\eta = -L_\zeta (\mathbf{i}_{\zeta_x} + \mathbf{i}_{\zeta_y} + \mathbf{i}_{\zeta_z}) + \boldsymbol{\eta} \Delta \zeta, \quad \boldsymbol{\eta} = (\eta_x, \eta_y, \eta_z) \in \mathcal{H}^3, \quad (6.24)$$

where the vectors \mathbf{i}_{ζ_x} , \mathbf{i}_{ζ_y} and \mathbf{i}_{ζ_z} are, respectively, the unit vectors of the ζ_x , ζ_y and ζ_z axes of the Cartesian frame $(O; \zeta_x, \zeta_y, \zeta_z)$. A vector of trapezoidal-rule weights is also associated to each discrete Fourier velocity node, $\mathbf{w}_\eta = (w_{\eta_x}, w_{\eta_y}, w_{\eta_z})$ (with the related global weight being $w_\eta = w_{\eta_x} w_{\eta_y} w_{\eta_z}$). The mesh size in the Fourier velocity space is computed as:

$$\Delta\zeta = \frac{2L_\zeta}{N_c}. \quad (6.25)$$

In the proposed numerical method, the semi-length L_c and the number of nodes N_c along each direction of the velocity space are input parameters. The velocity mesh spacing Δc is then computed through eq. (6.20). The semi-length L_ζ and the mesh spacing $\Delta\zeta$ of the Fourier velocity space are found by imposing in eq. (6.25) the condition:

$$\Delta\zeta \Delta c = \frac{2\pi}{N_c}. \quad (6.26)$$

The substitution of the expressions for Δc and $\Delta\zeta$ (given in eqs. (6.20) and (6.25), respectively) in eq. (6.26) allows to obtain a relation for L_ζ depending only on the input parameters (N_c and L_c):

$$L_\zeta = \frac{\pi N_c}{2L_c}. \quad (6.27)$$

Once L_ζ computed, the Fourier velocity mesh spacing $\Delta\zeta$ is then found from eq. (6.25). The choice of a uniform mesh along each direction of the velocity spaces (physical and Fourier) and of the condition given in eq. (6.26) are due to the use of the Fast-Fourier-Transform (FFT) algorithm for the evaluation of the Fourier and the inverse Fourier transforms (Gamba and Tharkabhushanam 2009; 2010).

The position space is discretized by considering points belonging to the following subset \mathcal{X} of the x axis:

$$\mathcal{X} = \{(x, 0, 0) \in \Re \mid x \in [-L_x^-, L_x^+]\}, \quad (6.28)$$

where quantities L_x^- and L_x^+ are both positive. A finite volume grid can be defined based on eq. (6.28). Let N_x be the number of nodes in the position space, j the index corresponding to a generic cell in the discretized position space, $x_{j-1/2}$ and $x_{j+1/2}$ the coordinates of the related left and right nodes, respectively, and \mathcal{J} the set $\mathcal{J} = \{0, \dots, N_x - 2\}$. The centroid location x_j and the volume (length) Δx_j of the cell j are computed as:

$$x_j = \frac{1}{2}(x_{j+1/2} + x_{j-1/2}), \quad \Delta x_j = x_{j+1/2} - x_{j-1/2}, \quad j \in \mathcal{J}. \quad (6.29)$$

The time domain is discretized as follows. Let N_t be the number time-steps, Δt^n the time-step value associated to the time-level t^n and \mathcal{N} the set $\mathcal{N} =$

$\{0, \dots, N_t\}$. The set of nodes of the discretized time-domain is then:

$$\mathcal{T} = \left\{ t^n = \sum_{m \leq n} \Delta t_m \in \Re \mid n, m \in \mathcal{N} \right\}. \quad (6.30)$$

For the sake of later convenience, it is useful to introduce the compact notation $f_{s_i \mathbf{h}_j}^n = f_{s_i}(x_j, \mathbf{c}_h, t^n)$ to indicate the value of the velocity distribution function of the species s_i at the point (x_j, \mathbf{c}_h) of the discretized phase-space at the discrete time-level t^n .

6.3.2 Numerical Integration of the Boltzmann Equation

Numerical solutions to the Boltzmann equation (6.17) are obtained by means of the MOL. A second-order FV method is firstly applied in order to perform the discretization in the position space. Secondly, the semi-discrete set of equations obtained is integrated in time. In the present work, explicit time-integration methods are considered due their ease of implementation and low memory requirements compared to implicit methods (Mieussens 2000; Mieussens and Struchtrup 2004).

Spatial Discretization

The application of the FV method to the Boltzmann equation (6.17) (written for the discrete velocity node \mathbf{c}_h) leads to the following semi-discrete equation for the cell j :

$$\Delta x_j \left(\frac{\partial f_{s_i}}{\partial t} \right)_{\mathbf{h}_j} + \Phi_{s_i \mathbf{h}_{j+1/2}} - \Phi_{s_i \mathbf{h}_{j-1/2}} = \Delta x_j Q_{s_i \mathbf{h}_j}, \quad (6.31)$$

$$s \in \mathcal{S}, \quad j \in \mathcal{I}_s, \quad j \in \mathcal{J}, \quad \mathbf{h} \in \mathcal{H}^3,$$

where $\Phi_{s_i \mathbf{h}_{j-1/2}}$ and $\Phi_{s_i \mathbf{h}_{j+1/2}}$ are, respectively, the numerical fluxes at the interfaces $j - 1/2$ and $j + 1/2$ of the cell j , respectively, while $Q_{s_i \mathbf{h}_j}$ represents the sum of the elastic and inelastic collision operators for the species s_i evaluated at the node (x_j, \mathbf{c}_h) of the discretized phase-space (the algorithm for its evaluation is described later in this section). The numerical flux is computed by means of a second order slope-limited upwind scheme (Hirsch 1990):

$$\Phi_{s_i \mathbf{h}_{j+1/2}} = c_{\mathbf{h}}^+ f_{s_i \mathbf{h}_j}^L + c_{\mathbf{h}}^- f_{s_i \mathbf{h}_{j+1}}^R, \quad (6.32)$$

$$s \in \mathcal{S}, \quad i \in \mathcal{I}_s, \quad j \in \mathcal{J}, \quad \mathbf{h} \in \mathcal{H}^3,$$

where the upwind wave speeds are $c_{\mathbf{h}}^{\pm} = (c_{h_x} \pm |c_{h_x}|)/2$. In analogy with what done for the CFD solvers described in ch. 5 (see eqs. (5.38)-(5.40)), the reconstructed values of the distribution function at the left and right sides of

the interface $j + 1/2$ are obtained based on a limited MUSCL reconstruction:

$$f_{s_i \mathbf{h} j}^L = f_{s_i \mathbf{h} j} + \frac{1}{2} \phi(r_j^L) (f_{s_i \mathbf{h} j} - f_{s_i \mathbf{h} j-1}), \quad (6.33)$$

$$f_{s_i \mathbf{h} j+1}^R = f_{s_i \mathbf{h} j+1} - \frac{1}{2} \phi(1/r_{j+1}^R) (f_{s_i \mathbf{h} j+2} - f_{s_i \mathbf{h} j+1}), \quad (6.34)$$

$$s \in \mathcal{S}, \quad i \in \mathcal{I}_s, \quad j \in \mathcal{J}, \quad \mathbf{h} \in \mathcal{H}^3,$$

where $\phi = \phi(r)$ is a slope limiter function (van Leer 1979; Hirsch 1990). The left and right ratios of consecutive differences are computed as:

$$r_j^L = \frac{f_{s_i \mathbf{h} j+1} - f_{s_i \mathbf{h} j}}{f_{s_i \mathbf{h} j} - f_{s_i \mathbf{h} j-1}}, \quad (6.35)$$

$$r_{j+1}^R = \frac{f_{s_i \mathbf{h} j+2} - f_{s_i \mathbf{h} j+1}}{f_{s_i \mathbf{h} j+1} - f_{s_i \mathbf{h} j}}, \quad (6.36)$$

$$s \in \mathcal{S}, \quad i \in \mathcal{I}_s, \quad j \in \mathcal{J}, \quad \mathbf{h} \in \mathcal{H}^3.$$

Temporal Discretization

Equation (6.31) is integrated in time by means of the Forward-Euler (FE) method (Hirsch 1990):

$$f_{s_i \mathbf{h} j}^{n+1} = f_{s_i \mathbf{h} j}^n - \frac{\Delta t_j}{\Delta x_j} \left[\left(\Phi_{s_i \mathbf{h} j+\frac{1}{2}}^n - \Phi_{s_i \mathbf{h} j-\frac{1}{2}}^n \right) - \Delta x_j Q_{s_i \mathbf{h} j}^n \right], \quad (6.37)$$

$$s \in \mathcal{S}, \quad i \in \mathcal{I}_s, \quad j \in \mathcal{J}, \quad \mathbf{h} \in \mathcal{H}^3, \quad n \in \mathcal{N}.$$

The time-step is computed according to (Mieussens 2000):

$$\Delta t_j = \frac{\text{CFL}}{\frac{1}{\Delta t^c} + \frac{L_c}{\Delta x_j}}, \quad j \in \mathcal{J}, \quad (6.38)$$

where Δt^c is the collision time-step. Equation (6.38) has been derived based on a model Boltzmann equation with a BGK collision operator (Mieussens 2000). However, its use did not lead to particular problems while performing the calculations presented in ch. 7.

As alternative to the FE method, multi-stage time-stepping schemes (such as Runge-Kutta methods; Hirsch 1990) could be considered. Similarly, one might use high-order FV schemes for the streaming operator (as done by Filbet and Russo 2003) which would give the advantage of requiring less cells in the position space at which to evaluate the collision operators. However, the main focus of this thesis was the development of a computational algorithm for the discrete evaluation of the elastic and inelastic collision operators. For this reason, it was chosen to use a simple slope-limited MUSCL scheme in conjunction with the FE method outlined above. Boundary conditions are applied through ghost cells (Hirsch 1990).

Conservative Discrete Evaluation of the Collision Operators

The elastic and inelastic collision operators are evaluated (on the discrete velocity nodes given by eq. (6.21)) by means of the following algorithms.

For the elastic collision $s_i + p_j = s_i + p_j$, the related partial collision operator is computed as:

Algorithm 6.3.1 *Evaluation of the partial elastic collision operator $Q_{s_ip_j}$*

```

for all  $\eta \in \mathcal{H}^3$  do
    compute  $\hat{f}_{s_i}(\zeta_\eta)$ ,  $\hat{f}_{p_j}(\zeta_\eta)$ ;
end for
for all  $\eta \in \mathcal{H}^3$  do
    compute  $\hat{Q}_{s_ip_j}(\zeta_\eta)$  through eq. (6.7);
end for
for all  $\mathbf{h} \in \mathcal{H}^3$  do
    compute  $\tilde{Q}_{s_ip_j}(\mathbf{c}_h)$  by inverting the Fourier transform  $\hat{Q}_{s_ip_j}$ ;
end for
for all  $\mathbf{h} \in \mathcal{H}^3$  do
    Enforce conservation through the solution of a constrained optimization
    problem:  $Q_{s_ip_j}(\mathbf{c}_h) = \text{Opt}(\tilde{Q}_{s_ip_j}(\mathbf{c}_h))$ ;
end for

```

For the inelastic collision $s_i + p_j = s_k + p_l$, the related partial collision operator is computed as:

Algorithm 6.3.2 *Evaluation of the partial inelastic collision operator $Q_{s_ip_j}^{s_k p_l}$*

```

for all  $\eta \in \mathcal{H}^3$  do
    compute  $\hat{f}_{s_i}(\zeta_\eta)$ ,  $\hat{f}_{s_k}(\zeta_\eta)$ ,  $\hat{f}_{p_j}(\zeta_\eta)$ ,  $\hat{f}_{p_l}(\zeta_\eta)$ 
end for
for all  $\eta \in \mathcal{H}^3$  do
    compute  $\hat{Q}_{s_ip_j}^{s_k p_l}(\zeta_\eta)$  through eq. (6.8);
end for
for all  $\mathbf{h} \in \mathcal{H}^3$  do
    compute  $\tilde{Q}_{s_ip_j}^{s_k p_l}(\mathbf{c}_h)$  by inverting the Fourier transform  $\hat{Q}_{s_ip_j}^{s_k p_l}$ ;
end for
for all  $\mathbf{h} \in \mathcal{H}^3$  do
    Enforce conservation through the solution of a constrained optimization
    problem:  $Q_{s_ip_j}^{s_k p_l}(\mathbf{c}_h) = \text{Opt}(\tilde{Q}_{s_ip_j}^{s_k p_l}(\mathbf{c}_h))$ ;
end for

```

The details related to numerical approximation of the Fourier transform and the weighted convolution are provided in app. I. The global cost of the algorithms 6.3.1-6.3.2 is $O(N_c^6)$ and the last step is performed in order to ensure conservation of mass, momentum and energy during collisions as stated in eq. (6.18).

This approach was originally proposed and formulated by Gamba and Tharkabhushanam (2009; 2010) for the case of a mono-component gas without internal energy. In this thesis, an extension of the original method to multi-component gases with discrete internal energy levels is proposed. Due to the existence of separate sets of collisional invariants (elastic and inelastic), the conservation of mass, momentum and energy during collisions is enforced through two separate constrained optimization problems (Munafò et al. 2014).

Elastic collisions:

$$\mathcal{P}_{\text{el}} = \left\{ \min \left(\sum_{\substack{s \in \mathcal{S} \\ i \in \mathcal{I}_s}} \sum_{j \in \mathcal{I}_p} \left| \tilde{\mathbf{Q}}_{s_i p_j} - \mathbf{Q}_{s_i p_j} \right|^2 \right), \quad \sum_{\substack{s \in \mathcal{S} \\ i \in \mathcal{I}_s}} \sum_{j \in \mathcal{I}_p} \Psi_{s_i}^{\text{el}} \mathbf{Q}_{s_i p_j} = \mathbf{0}_{\mathcal{N}_s + 4} \right\}. \quad (6.39)$$

Inelastic collisions:

$$\mathcal{P}_{\text{in}} = \left\{ \min \left(\sum_{\substack{s \in \mathcal{S} \\ i \in \mathcal{I}_s}} \sum_{\substack{(p_j, s_k, p_l) \\ \in \mathcal{C}_{s_i}^{\text{in}}} \left| \tilde{\mathbf{Q}}_{s_i p_j}^{s_k p_l} - \mathbf{Q}_{s_i p_j}^{s_k p_l} \right|^2 \right), \quad \sum_{\substack{s \in \mathcal{S} \\ i \in \mathcal{I}_s}} \sum_{\substack{(p_j, s_k, p_l) \\ \in \mathcal{C}_{s_i}^{\text{in}}} \Psi_{s_i}^{\text{in}} \mathbf{Q}_{s_i p_j}^{s_k p_l} = \mathbf{0}_{\mathcal{N}_c + 4} \right\}. \quad (6.40)$$

The vectors $\mathbf{Q}_{s_i p_j}$, $\tilde{\mathbf{Q}}_{s_i p_j}$, $\mathbf{Q}_{s_i p_j}^{s_k p_l}$ and $\tilde{\mathbf{Q}}_{s_i p_j}^{s_k p_l}$ store the values of the partial collision operators $Q_{s_i p_j}$ and $Q_{s_i p_j}^{s_k p_l}$, respectively, on the discrete velocity nodes given by eq. (6.21), where the tilde symbol is used to indicate the values obtained after the inversion of the Fourier transform that do not satisfy conservation. The constraints imposed represent the conservation requirements (as stated in eq. (6.18)) that the collision operators must satisfy. In view of the discretization introduced for the velocity space, this operation is realized at discrete level through multiplication with the elastic and inelastic integration matrices ($\Psi_{s_i}^{\text{el}}$ and $\Psi_{s_i}^{\text{in}}$, respectively). The columns of these matrices are precisely given by the elastic and inelastic collisional invariants (eqs. (1.23) and (1.25), respectively) evaluated at the discrete velocity nodes given by eq. (6.21). Hence, for the columns associated to the discrete velocity node \mathbf{c}_h one has:

$$(\Psi_{s_i}^{\text{el}})_{\mathbf{h}} = \Delta c^3 w_h \begin{bmatrix} m_s \boldsymbol{\delta}_{s_i} & m_s \mathbf{c}_h & \frac{1}{2} m_s c_h^2 + E_{s_i} \end{bmatrix}^T, \quad (6.41)$$

$$(\Psi_{s_i}^{\text{in}})_{\mathbf{h}} = \Delta c^3 w_h \begin{bmatrix} m_s \boldsymbol{\delta}_s & m_s \mathbf{c}_h & \frac{1}{2} m_s c_h^2 + E_{s_i} \end{bmatrix}^T, \quad (6.42)$$

$$s \in \mathcal{S}, \quad i \in \mathcal{I}_s, \quad \mathbf{c}_h \in \mathcal{V}_c, \quad \mathbf{h} \in \mathcal{H}^3,$$

where $c_h^2 = \mathbf{c}_h \cdot \mathbf{c}_h$. The vector $\boldsymbol{\delta}_{s_i}$ has \mathcal{N}_s components and that relative to the internal energy level j of the chemical component p is $\delta_{sp} \delta_{ij}$. The vector $\boldsymbol{\delta}_s$ has \mathcal{N}_c components and that relative to the chemical component p is δ_{sp} .

Proposition 6.3.1. *The solution of the constrained optimization problem \mathcal{P}_{el} for elastic collisions is:*

$$\mathbf{Q}_{s_i p_j} = \tilde{\mathbf{Q}}_{s_i p_j} - (\Psi_{s_i}^{\text{el}})^T (\tilde{\Psi}^{\text{el}})^{-1} \tilde{\mathbf{Q}}^{\text{el}}, \quad s, p \in \mathcal{S}, \quad i \in \mathcal{I}_s, \quad j \in \mathcal{I}_p, \quad (6.43)$$

where the matrix $\tilde{\Psi}^{\text{el}}$ and the vector $\tilde{\mathbf{Q}}^{\text{el}}$ are defined as:

$$\tilde{\Psi}^{\text{el}} = \mathcal{N}_s \sum_{\substack{s \in \mathcal{S} \\ i \in \mathcal{I}_s}} \Psi_{s_i}^{\text{el}} (\Psi_{s_i}^{\text{el}})^T, \quad (6.44)$$

$$\tilde{\mathbf{Q}}^{\text{el}} = \sum_{\substack{s \in \mathcal{S} \\ i \in \mathcal{I}_s}} \sum_{\substack{p \in \mathcal{S} \\ j \in \mathcal{I}_p}} \Psi_{s_i}^{\text{el}} \tilde{\mathbf{Q}}_{s_i p_j}. \quad (6.45)$$

Proof. The solution is found by writing down the Lagrangian associated to the problem \mathcal{P}_{el} and then looking for its stationary points. The mathematical details of the proof can be found in app. J. \square

Equation (6.43) reduces to the original result obtained by Gamba and Tharkab-hushanam (2009; 2010) for the case of a mono-component gas without internal energy:

$$\mathbf{Q} = \tilde{\mathbf{Q}} - \Psi^T (\Psi \Psi^T)^{-1} \Psi \tilde{\mathbf{Q}}, \quad (6.46)$$

where the (elastic) integration matrix is obtained from eq. (6.41) when $\mathcal{N}_s = \mathcal{N}_c = 1$:

$$(\Psi)_{\mathbf{h}} = \Delta c^3 w_h \begin{bmatrix} m & m \mathbf{c}_h & \frac{1}{2} m c_h^2 \end{bmatrix}^T, \quad \mathbf{c}_h \in \mathcal{V}_c, \quad \mathbf{h} \in \mathcal{H}^3. \quad (6.47)$$

Proposition 6.3.2. *The solution of the constrained optimization problem \mathcal{P}_{in} for inelastic collisions is:*

$$\mathbf{Q}_{s_i p_j}^{s_k p_l} = \tilde{\mathbf{Q}}_{s_i p_j}^{s_k p_l} - (\Psi_{s_i}^{\text{in}})^T (\tilde{\Psi}^{\text{in}})^{-1} \tilde{\mathbf{Q}}^{\text{in}}, \quad (6.48)$$

$$s \in \mathcal{S}, \quad i \in \mathcal{I}_s, \quad (p_j, s_k, p_l) \in \mathcal{C}_{s_i}^{\text{in}},$$

where the matrix $\tilde{\Psi}_{s_i}^{\text{in}}$ and the vector $\tilde{\mathbf{Q}}^{\text{in}}$ are defined as:

$$\tilde{\Psi}^{\text{in}} = \sum_{\substack{s \in \mathcal{S} \\ i \in \mathcal{I}_s}} \mathcal{N}_{s_i}^{\text{in}} \Psi_{s_i}^{\text{in}} (\Psi_{s_i}^{\text{in}})^T, \quad (6.49)$$

$$\tilde{\mathbf{Q}}^{\text{in}} = \sum_{\substack{s \in \mathcal{S} \\ i \in \mathcal{I}_s}} \sum_{\substack{(p_j, s_k, p_l) \\ \in \mathcal{C}_{s_i}^{\text{in}}}} \Psi_{s_i}^{\text{in}} \tilde{\mathbf{Q}}_{s_i p_j}^{s_k p_l}. \quad (6.50)$$

Quantity $\mathcal{N}_{s_i}^{\text{in}}$ is equal to $\#(\mathcal{C}_{s_i}^{\text{in}})$. In the case of a mono-component gas ($\mathcal{N}_c = 1$) where all the possible inelastic transitions $s_i + s_j = s_k + s_l$ are accounted for, quantity $\mathcal{N}_{s_i}^{\text{in}}$ reduces to $\mathcal{N}_s (\mathcal{N}_s^2 - 1)$.

Proof. The solution is found by writing down the Lagrangian associated to the problem \mathcal{P}_{in} and then looking for its stationary points. The mathematical details of the proof can be found in app. J. \square

6.4 Intermediate Conclusions

In this chapter, an existing spectral-Lagrangian method for the Boltzmann equation for a mono-component gas without internal energy has been extended to multi-component gases with discrete internal energy levels. Both elastic and inelastic collisions have been taken into account, while reactive collisions have been neglected.

The numerical integration of the Boltzmann equation is realized through the MOL, where the streaming operator is discretized by means of a second-order upwind FV scheme in conjunction with an explicit time-integrator. The procedure in use for computing the collision operators is based on the convolution structure of the Fourier transformed Boltzmann equation. The latter shows that the Fourier transform of the partial elastic and inelastic collision operators can be written as weighted convolutions in Fourier space. Based on these results, an algorithm has been developed for evaluating the collision operators on a discretized phase-space. The conservation of mass, momentum and energy during collisions is enforced through two separate constrained optimization problems (one for elastic collisions and the other for inelastic collisions). The two constrained optimization problems are formulated in a consistent manner with the elastic and inelastic collisional invariants. Applications to zero/one-dimensional problems are shown in ch. 7.

Chapter 7

Applications of the BEST code

This chapter shows applications of the conservative spectral-Lagrangian method presented in ch. 6. The numerical method has been implemented in a parallel code (BEST; Boltzmann Equation Spectral-Lagrangian Solver) written in C programming language. Parallelization has been performed by means of the OpenMP library (Chapman et al. 2008). The Fastest-Fourier-Transform in the West (FFTW) (2005; 2012) and the GNU-Scientific Library (GSL) (2013) packages have been used for the evaluation of FFTs and vector/matrix manipulation, respectively.

The present chapter is structured as follows. Section 7.1 assesses the accuracy of the original formulation of the numerical method. Then, the extended formulation is tested on both space homogeneous/inhomogeneous benchmarks involving multi-component gases (sec. 7.2) and inelastic collisions (sec. 7.3). In all the cases, the macroscopic moments are compared with the DSMC results obtained by Torres (2012). The numerical approximation of the integrals defining the macroscopic moments are given in app. K.

7.1 Gas without Internal Energy: Flow across a Normal Shock Wave in Ar

In the work of Gamba and Tharkabhushanam (2009; 2010), research efforts were mostly devoted towards the analysis of the properties of the spectral-Lagrangian method, such as conservation and numerical error on macroscopic moments. Computational results were never compared with the DSMC predictions. Moreover, the calculations were performed by considering only Maxwell or hard-sphere (HS) cross-section models. These models provide an unrealistic description of collisions in dilute gases (Bird 1994). In view of these aspects, it was decided to assess the accuracy of the original spectral-Lagrangian method by comparing the results for the flow across a normal shock wave in Ar with those obtained by means of the DSMC method provided by Torres (2012). In order to both show the method flexibility and perform a validation through

comparison with experiments, the calculations have been run by using the more realistic variable-hard-sphere (VHS) cross-section model (Bird 1994).

The gas is made of Ar (with mass 6.63×10^{-26} kg). The excited electronic states of Ar are neglected and only elastic collisions are accounted for. Collisions are described by means of the VHS cross-section model. The former can be formulated as a HS cross-section model where the diameter d is a function of the relative velocity magnitude g :

$$\sigma = \frac{d^2(g)}{4}, \quad d^2(g) = \frac{15}{8} \left[\frac{(\pi m k_b)^{1/2} (4k_b/m)^{\omega-1/2} T_{\text{ref}}^\omega}{\Gamma(9/2 - \omega) \pi \eta_{\text{ref}}} \right] g^{1-2\omega}, \quad (7.1)$$

where the symbol Γ stands for the Gamma function. Quantities T_{ref} and η_{ref} are the reference values for the temperature and the shear viscosity, respectively, and quantity ω is the exponent of the assumed viscosity law:

$$\eta = \eta_{\text{ref}} \left(\frac{T}{T_{\text{ref}}} \right)^\omega. \quad (7.2)$$

The flow across the shock wave is computed by solving the Boltzmann equation (6.1) in the shock frame. The free-stream (∞) density and temperature are 1×10^{-4} kg/m³ and 300 K, respectively. Four different values for the free-stream Mach number have been considered. These are provided in tab. 7.1 which reports also the post-shock (ps) conditions (computed based on the Rankine-Hugoniot jump relations) and the VHS model parameters.

#	M_∞	ρ_{ps} [kg/m ³]	u_{ps} [m/s]	T_{ps} [K]	T_{ref} [K]	η_{ref} [Pa s]	ω
1	1.55	1.78×10^{-4}	281.01	464.32	380	2.75×10^{-5}	0.791
2	3.38	3.17×10^{-4}	344.17	1328.61	820	4.84×10^{-5}	0.716
3	6.5	3.74×10^{-4}	561.43	4222.11	2300	9.72×10^{-5}	0.685
4	9	3.86×10^{-4}	752.71	7855.56	4100	1.44×10^{-4}	0.683

Table 7.1: Flow across a normal shock wave in Ar. Post-shock conditions and VHS model parameters.

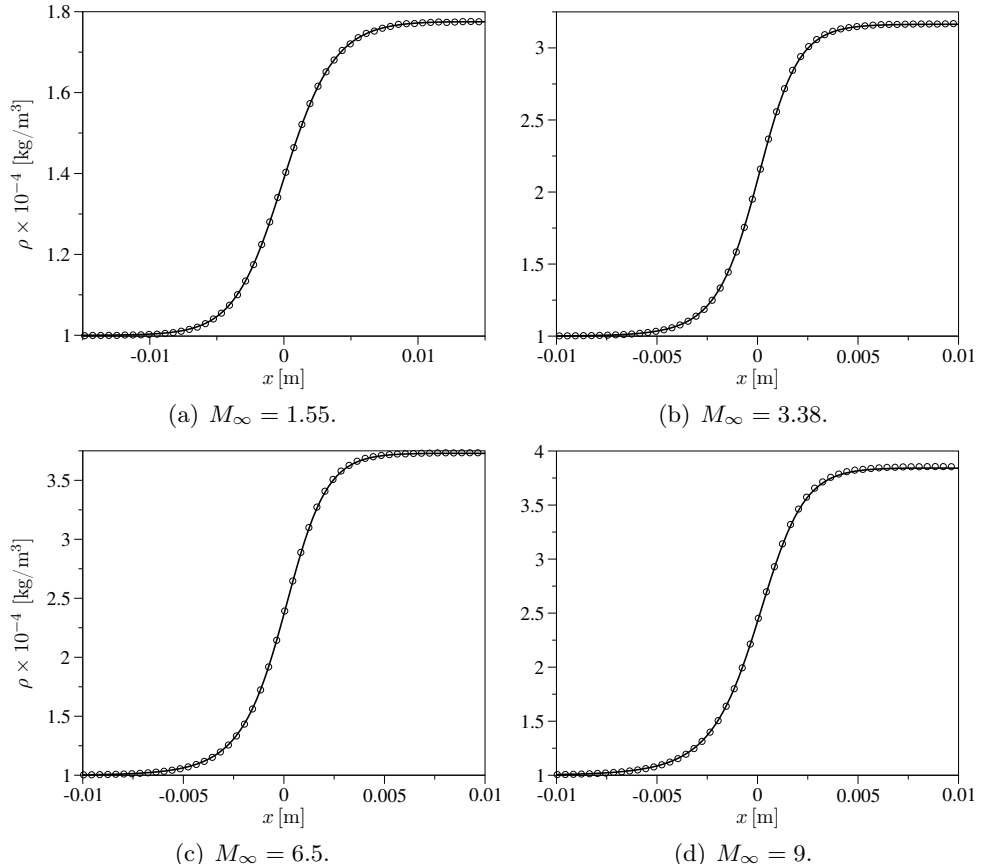
The values of the VHS model parameters have been determined as follows. The reference temperature has been set to the arithmetic average between the free-stream and post-shock values. The shear viscosity reference value and the viscosity law exponent have been obtained by fitting the viscosity data for Ar (taken from Svehla 1995) with eq. (7.2).

Table 7.2 provides the simulation parameters. The position space is discretized by using a uniform FV grid. The gas flow is directed along the positive direction of the x axis. At the boundaries $x = -L_x^-$ and $x = L_x^+$, the pre and post-shock Maxwell-Boltzmann velocity distribution functions are imposed, respectively. These velocity distribution functions are also used for initializing the numerical solution in the intervals $-L_x^- \leq x \leq 0$ and $0 < x \leq L_x^+$, respectively. The time-marching method described in sec. 6.3.2 is then applied until the steady-state is reached.

#	N_c	L_c [m/s]	N_x	L_x^- [m]	L_x^+ [m]	Δt^c [s]	CFL	Limiter
1	24	2200	201	2×10^{-2}	2×10^{-2}	1×10^{-8}	0.5	van Albada
2	32	3700	201	2×10^{-2}	2×10^{-2}	1×10^{-8}	0.5	van Albada
3	40	6200	201	2×10^{-2}	2×10^{-2}	1×10^{-8}	0.5	van Albada
4	46	6800	201	2×10^{-2}	2×10^{-2}	1×10^{-8}	0.5	van Albada

Table 7.2: Flow across a normal shock wave in Ar. Simulation parameters.**Macroscopic Moments: BEST vs DSMC**

In order to perform a meaningful comparison with the DSMC results, a common origin has to be determined for the numerical solutions. This has been taken at the location where the normalized density $(\rho - \rho_\infty)/(\rho_{ps} - \rho_\infty)$ is equal to 0.5 (Bird 1994). This procedure is also applied to the shock wave results shown in secs. 7.2-7.3.

**Figure 7.1:** Flow across a normal shock wave in Ar. Density evolution for different values of the free-stream Mach number (lines BEST, symbols DSMC(Torres)).

Figures 7.1-7.2 show, respectively, the density and temperature evolution across the shock wave for the adopted free-stream conditions. The parallel temperature (T_x) experiences an overshoot, reaches a local maximum and then relaxes towards the value corresponding to the post-shock conditions. This flowfield feature (observed for the first time in DSMC simulations; Bird 1994) is more and more enhanced when increasing the free-stream Mach number and is directly related to the distortion (along the c_x velocity axis) that the velocity distribution function experiences while the flow crosses the shock wave (see later in this section). On the other hand, the kinetic and transverse temperatures (T and T_y , respectively), show a monotone increase from the pre-shock till the post-shock value. For all the cases shown in figs. 7.1-7.2 the agreement with the DSMC results is excellent. The same conclusion holds also when looking at higher order moments such as heat flux and normal viscous stress shown in figs. 7.3-7.4, respectively.

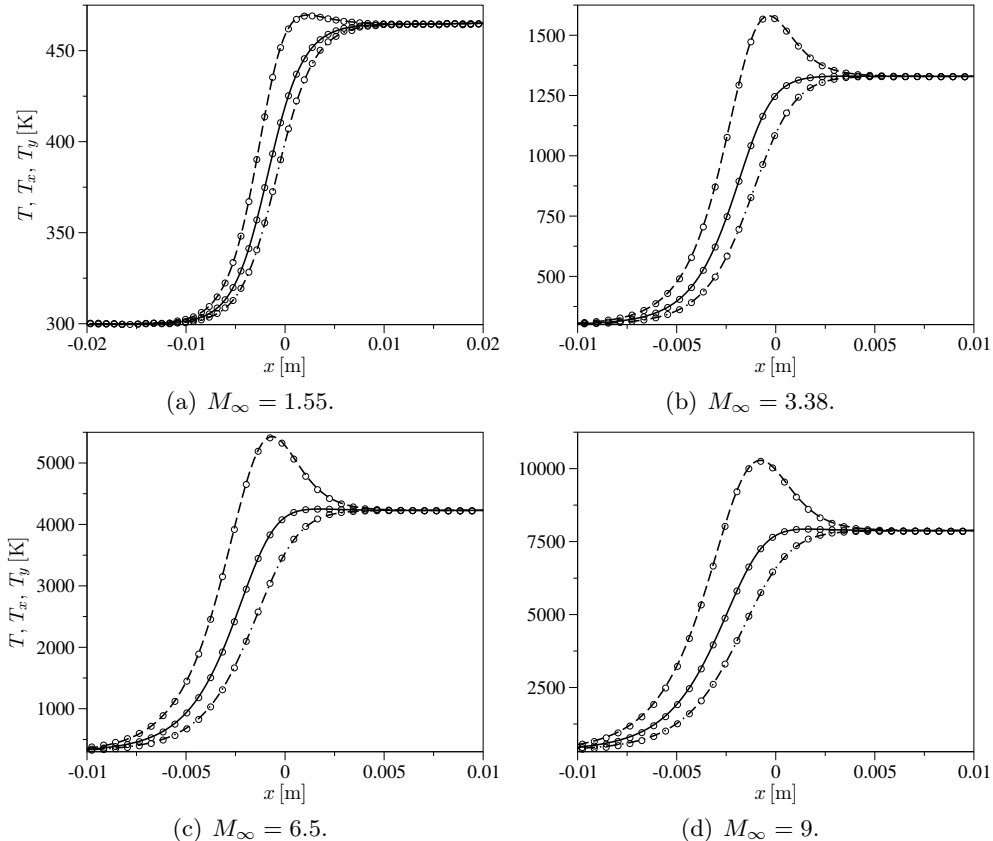


Figure 7.2: Flow across a normal shock wave in Ar. Temperature evolution for different values of the free-stream Mach number (unbroken lines T BEST, dashed lines T_x BEST, dotted-dashed lines T_y BEST, symbols DSMC(Torres)).

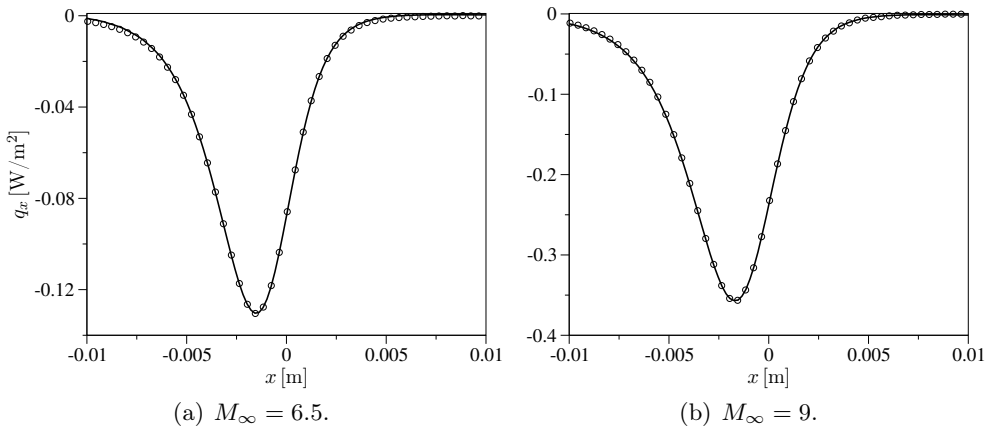


Figure 7.3: Flow across a normal shock wave in Ar. Heat flux evolution for different values of the free-stream Mach number (lines BEST, symbols DSMC(Torres)).

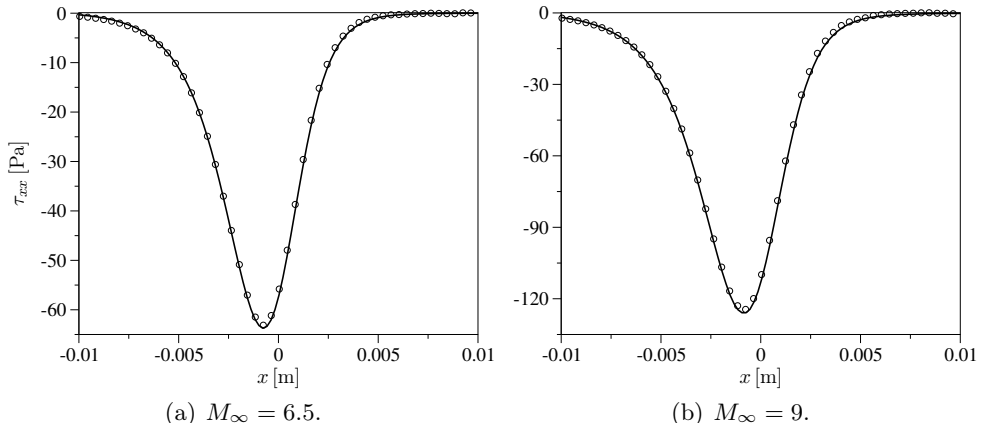


Figure 7.4: Flow across a normal shock wave in Ar. Normal viscous stress evolution for different values of the free-stream Mach number (lines BEST, symbols DSMC(Torres)).

Analysis of the Velocity Distribution Function

Figure 7.5 shows a visual correspondence between the density and the c_x axis component of the velocity distribution function across the shock wave when $M_\infty = 6.5$. Due to the smooth compression in the front region of the shock, the velocity distribution function initially evolves by deviating little from the pre-shock Maxwellian. When the gas compression becomes significant, distortions start to appear and become more and more pronounced. These are particularly evident in the mid region of the shock wave where the velocity distribution function assumes a bimodal shape. Once this portion of the shock passed, the rate of compression decreases and the distortions in the velocity distribution function progressively disappear while the gas approaches the

post-shock equilibrium state. The evolution of the velocity distribution can also be appreciated in fig. 7.6 showing its projection on the (c_x, c_y) plane (*i.e.* $f(c_x, c_y, 0)$) at different locations across the shock wave.

The same features observed in figs. 7.5-7.6 are also found for the cases $M_\infty = 3.38$ and 9 (not shown), with the difference that the observed distortions are, respectively, less and more pronounced compared to the case $M_\infty = 6.5$. On the other hand, the results obtained when $M_\infty = 1.55$ (not shown) show that the velocity distribution function evolves smoothly with no appreciable shape distortions.

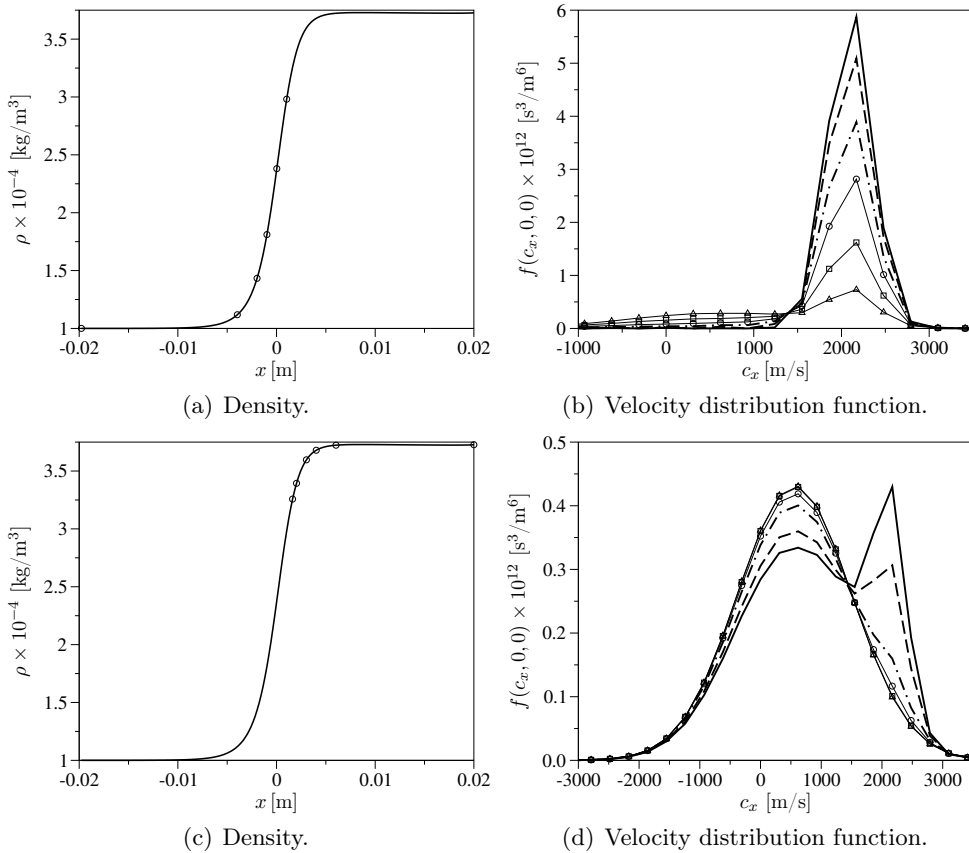


Figure 7.5: Flow across a normal shock wave in Ar. Comparative evolution of the density and the c_x axis component of the velocity distribution function ($M_\infty = 6.5$; the symbols in (a) and (c) highlight the locations at which the velocity distribution function, plotted in (b) and (d), is extracted; in (b) unbroken line $x = -2 \times 10^{-2}$ m, dashed line $x = -4 \times 10^{-3}$ m, dotted-dashed line $x = -2 \times 10^{-3}$ m, line with circles $x = -1 \times 10^{-3}$ m, line with squares $x = 0$ m, line with triangles $x = 1 \times 10^{-3}$ m; in (d) unbroken line $x = 1.6 \times 10^{-3}$ m, dashed line $x = 2 \times 10^{-3}$ m, dotted-dashed line $x = 3 \times 10^{-3}$ m, line with circles $x = 4 \times 10^{-3}$ m, line with squares $x = 6 \times 10^{-3}$ m, line with triangles $x = 2 \times 10^{-2}$ m).

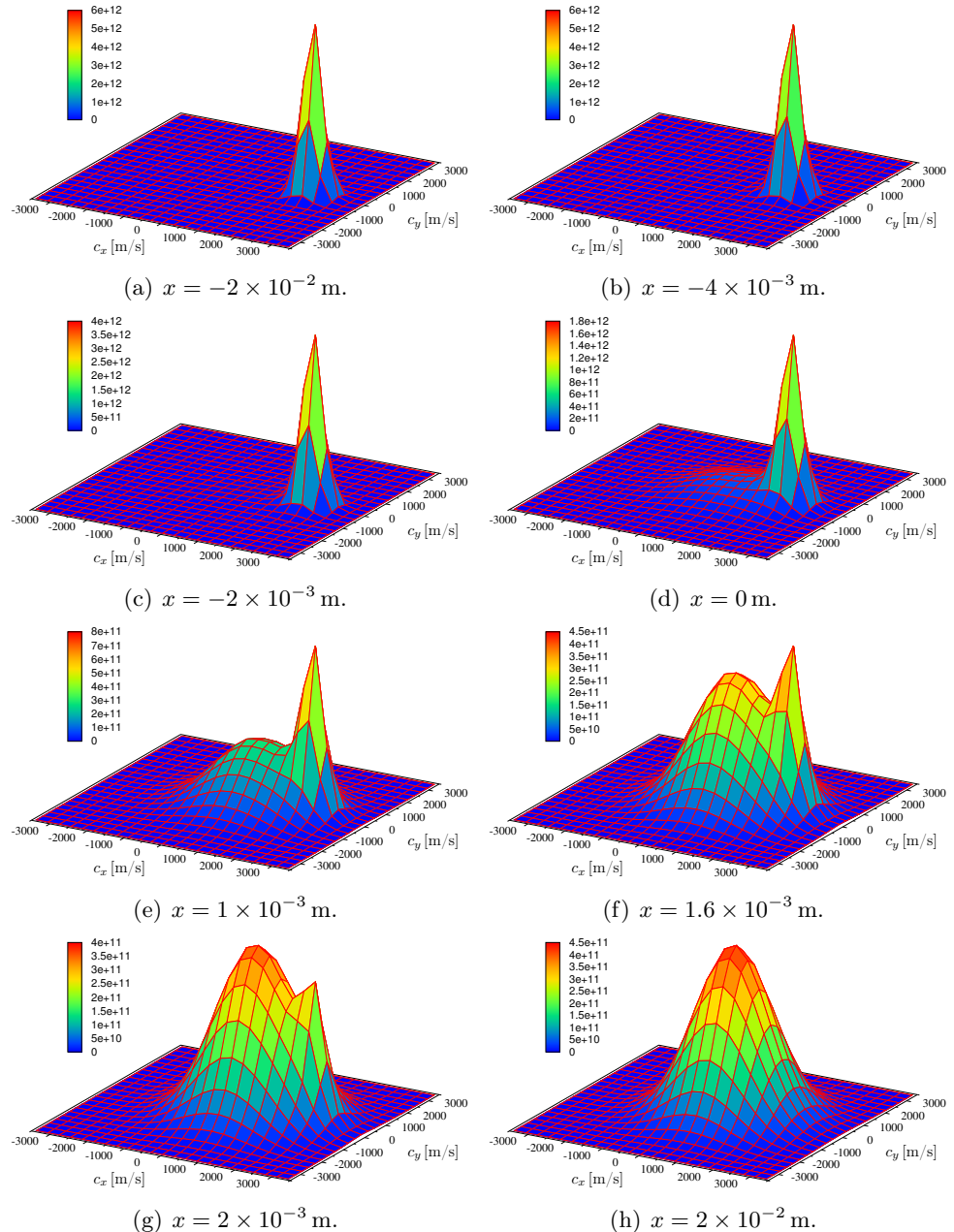


Figure 7.6: Flow across a normal shock wave in Ar. Evolution of the projection on the (c_x, c_y) plane of the velocity distribution function ($M_\infty = 6.5$).

Comparison with Experimental Density Profiles

The computed density profiles have been compared with those determined experimentally by Alsmeyer (1976) (see fig. 7.7). The normalized density profiles are plotted as a function of the non-dimensional distance x/λ_∞ , where the free-stream mean free path λ_∞ has been set to the value indicated in the paper of Alsmeyer ($\lambda_\infty = 1.098 \times 10^{-3}$ m).

The agreement between the computed and experimental density profiles is fairly good, though some discrepancies arise. In all the cases, these are found in the initial part of the shock front (and also in the post-shock region for the case $M_\infty = 1.55$). In that zone, due to moderate values of the thermal speed (caused by low temperatures), collisions between the gas particles are strongly affected by medium-range attractive forces (Hirschfelder et al. 1964). The effects of medium-range attractive forces are completely neglected by the VHS cross-section model, which is purely repulsive, and this could then explain the systematic disagreement observed.

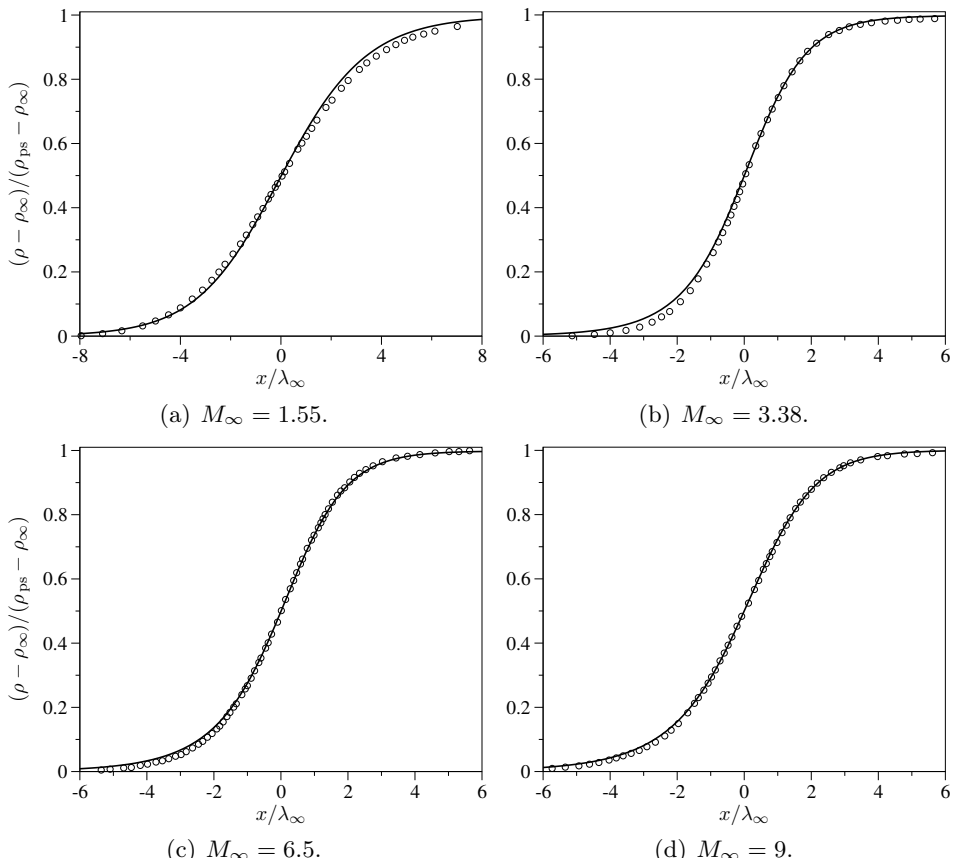


Figure 7.7: Flow across a normal shock wave in Ar. Comparison between the computed and experimental density profiles for different values of the free-stream Mach number (unbroken lines BEST, symbols experiments).

This aspect has been investigated more in detail. The case $M_\infty = 3.38$ has been recomputed by using cross-section models based on interaction potentials accounting for both repulsive and attractive forces. In this situation one should normally account for the anisotropic character of the cross-section (which can be done with the numerical method in use; see sec. 6.2). Despite that, a simplified approach has been considered. The cross-section is always written as a HS cross-section with a velocity dependent diameter. For a given interaction potential, the velocity dependent diameter is determined from the total viscosity cross section $\sigma_\eta = (2/3)\pi d^2$, which is computed from the classical elastic scattering theory (Hirschfelder et al. 1964; Ferziger and Kaper 1972). More details can be found in Munafò et al. (2013). In the present work, the viscosity cross-sections computed by using a Lennard-Jones (LJ) interaction potential (Hirschfelder et al. 1964; Ferziger and Kaper 1972) and that provided by Phelps et al. (2000) (PL), who applied the WKB theory to the elastic Ar-Ar scattering, have been considered. Figure 7.8 shows the comparison between the experimental density profiles and those computed by means of the LJ, VHS and PL cross-section models. The LJ and PL results are in slightly better agreement with the experiments in the front part of the shock, though the differences between all the models are quite small.

It is worth to recall that the VHS cross-section model parameters (ω , η_{ref} and T_{ref}) have to be computed for each value of the free-stream Mach number by some appropriate tuning approach (as explained before), if a reasonable agreement with experiments is wished. This is not needed when using cross-sections based on realistic interaction potentials (such as LJ and PL).

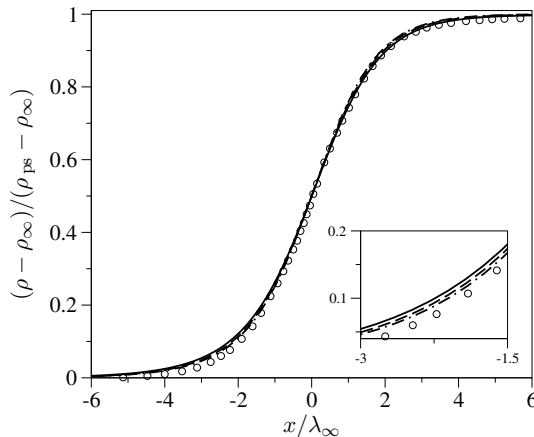


Figure 7.8: Flow across a normal shock wave in Ar. Comparison between the computed and experimental density profiles for different cross-section models ($M_\infty = 3.38$; unbroken line VHS, dashed line LJ, dotted-dashed line PL, symbols experiments).

Comparison with the Navier-Stokes Solution

Before moving to applications of the extended spectral-Lagrangian method, it was decided to complete the accuracy assessment of the original numerical method by comparing the computed density profiles with those obtained by solving the Navier-Stokes equations in the case of the VHS model (see fig. 7.9). This has been also done in order to have an estimation of the approximation introduced when using a hydrodynamic description beyond its range of applicability. For the sake of consistency, in obtaining the Navier-Stokes (NS) solution, the transport properties have been evaluated by using the VHS model parameters given in tab. 7.2. The density profiles in fig. 7.9 show that the Navier-Stokes solution is qualitatively correct and not too far from the Boltzmann equation solution. However, the accuracy of the Navier-Stokes solution progressively deteriorates when increasing the free-stream Mach number. In particular, the shock thickness is systematically underestimated (Bird 1994).

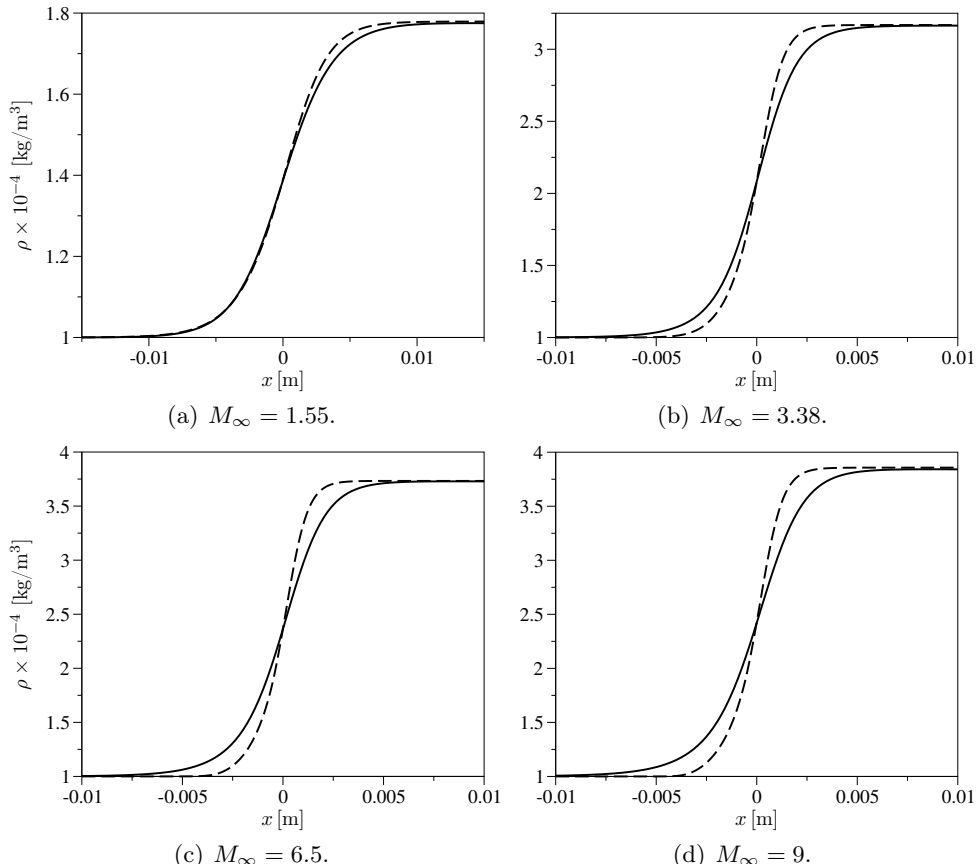


Figure 7.9: Flow across a normal shock wave in Ar. Comparison of the density profiles obtained by solving the Boltzmann and the Navier-Stokes equations for different values of the free-stream Mach number (unbroken lines BEST, dashed lines NS).

7.2 Multi-Component Gas without Internal Energy

After assessing the accuracy of the spectral-Lagrangian method of Gamba and Tharkabhushanam (2009; 2010), its extension to multi-component gases without internal energy has been tested on space homogeneous and inhomogeneous problems. The former consists in studying the time-evolution of a isochoric gaseous system initially set in a non-equilibrium state, while the latter consists in computing the steady flow across a normal shock wave.

The multi-component gas considered here is made of Ne and Ar (whose relative amounts are case dependent). The electronic energy of the atoms is assumed to be negligible. Only elastic collisions are accounted for. The HS collision model is used for the differential cross-section:

$$\sigma_{sp} = \frac{(d_s + d_p)^2}{16}, \quad s, p \in \{\text{Ne, Ar}\}. \quad (7.3)$$

The numerical values for the Ne and Ar diameters have been taken from Bird (1994) and are reported in tab. 7.3.

s	$m_s [\text{kg}]$	$d_s [\text{m}]$
Ne	3.35×10^{-26}	2.77×10^{-10}
Ar	6.63×10^{-26}	4.17×10^{-10}

Table 7.3: Masses and diameters of Ne and Ar.

7.2.1 Isochoric Equilibrium Relaxation of a Ne-Ar gas

The gas is composed of 83 % and of Ne and 17 % of Ar. The corresponding mass fractions are 0.71 and 0.29, respectively. The gas has a density of $7 \times 10^{-3} \text{ kg/m}^3$ and is set in an initial non-equilibrium state where Ne and Ar follow a Maxwell-Boltzmann velocity distribution function at 300 K and 500 K, respectively. The latter corresponds to a gas temperature of 333.63 K.

The velocity space is discretized by adopting 24 velocity nodes and by setting its semi-length to 3000 m/s ($N_c = 24$ and $L_c = 3000 \text{ m/s}$, respectively). The collision time-step Δt^c is set to $1 \times 10^{-9} \text{ s}$ in order to have a value lower than the mean collision time. The number of partial elastic collision operators to be evaluated at each time-step is equal to 4. The simulation was stopped after 300 time-steps. The CPU time required was approximately 3 minutes when using 4 OpenMP threads.

Macroscopic Moments: BEST vs DSMC

Once the simulation is started, collisions bring the system from its initial non-equilibrium condition to the final equilibrium state. Since the system is isochoric and no external mass, momentum and energy sources are present, the following statements hold:

- The density of each species is constant and maintains its initial value. The same holds true for the gas density.
- The species and gas hydrodynamic velocities are constant and maintains their initial values (zero).
- The gas temperature is constant and maintains its initial value. On the other hand, the temperature of each species experiences variation and approaches the equilibrium temperature value.

The above statements follow directly from the laws of mass, momentum and energy conservation and should be obtained as a result if the numerical method used is conservative. This has been assessed by monitoring the time-evolution of the species and gas densities, and temperatures (see fig. 7.10). The species and the gas densities retain their initial value and do not show any variation. The same holds true for the gas temperature and velocity (not shown), while the species temperatures evolve towards the correct equilibrium value. The results confirm that the extension of the original spectral-Lagrangian method to multi-component gases without internal energy is conservative. The agreement with the DSMC results is excellent.

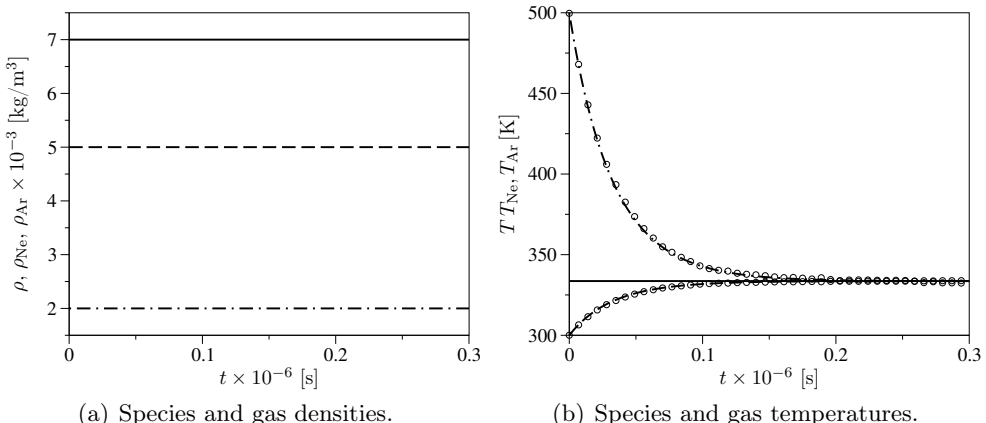


Figure 7.10: Isochoric equilibrium relaxation of a Ne-Ar gas. Time-evolution of the species and gas density and temperature (unbroken line gas BEST, dashed line Ne BEST, dotted-dashed line Ar BEST, symbols DSMC(Torres)).

Analysis of the Species Velocity Distribution Functions

Figure 7.11 shows the time-evolution of the c_x axis component of the species velocity distribution functions (the c_y and c_z axis components are not shown because they are practically identical to the c_x component). The results obtained show that the evolution towards the equilibrium state occurs through sequences of Maxwell-Boltzmann velocity distribution functions.

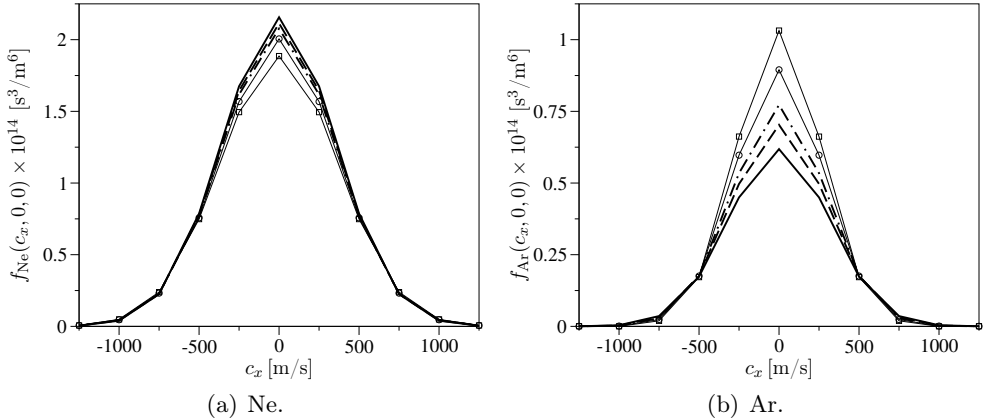


Figure 7.11: Isochoric equilibrium relaxation of a Ne-Ar gas. Time-evolution of the c_x axis component of the species velocity distribution functions (unbroken lines $t = 5 \times 10^{-9}$ s, dashed lines $t = 1.4 \times 10^{-8}$ s, dotted-dashed lines $t = 2.4 \times 10^{-8}$ s, lines with circles $t = 5.0 \times 10^{-8}$ s, lines with squares $t = 1.5 \times 10^{-7}$ s).

Sensitivity Study: Number of Velocity Nodes and Conservation Constraint

In order to asses the influence of the number of velocity nodes N_c and the enforcement of conservation on the solution, the benchmark presented in this section has been re-run by adopting the number of nodes reported in tab. 7.4 with and without enforcing conservation. In tab. 7.4, the L_1 and L_2 norms of the error on the gas temperature are also provided (see also fig. 7.12).

#	N_c	E_1 (with cons.)	E_2 (with cons.)	E_1 (w/o cons.)	E_2 (w/o cons.)
1	8	0.84×10^2	0.49×10^1	0.61×10^3	0.402×10^2
2	10	0.12×10^2	0.71	0.19×10^3	0.12×10^2
3	12	0.12×10^1	0.67×10^{-1}	0.12×10^3	0.82×10^1
4	14	0.68×10^{-1}	0.39×10^{-2}	0.27×10^2	0.18×10^1
5	16	0.52×10^{-2}	0.31×10^{-3}	0.73×10^1	0.507
6	18	0.12×10^{-2}	0.77×10^{-4}	0.15×10^1	0.106
7	20	0.31×10^{-3}	0.21×10^{-4}	0.304	0.208×10^{-1}
8	22	0.63×10^{-4}	0.43×10^{-5}	0.68×10^{-1}	0.44×10^{-2}
9	24	0.104×10^{-4}	0.72×10^{-6}	0.17×10^{-1}	0.108×10^{-2}

Table 7.4: Isochoric equilibrium relaxation of a Ne-Ar gas. Number of velocity nodes and related L_1 and L_2 norms of the error on the gas temperature ($N_t = 300$).

The error norms have been computed according to:

$$E_p = \left(\sum_{n=0}^{N_t} \left| \frac{T^n - T}{T} \right|^p \right)^{1/p}, \quad p \in \{1, 2\}, \quad (7.4)$$

where the number of time-steps is $N_t = 300$ and the gas temperature is $T = 333.63\text{ K}$ (see before). The error values reported in tab. 7.4 and shown in fig. 7.13 demonstrate the importance of the conservation constraint on the quality of the numerical solution.

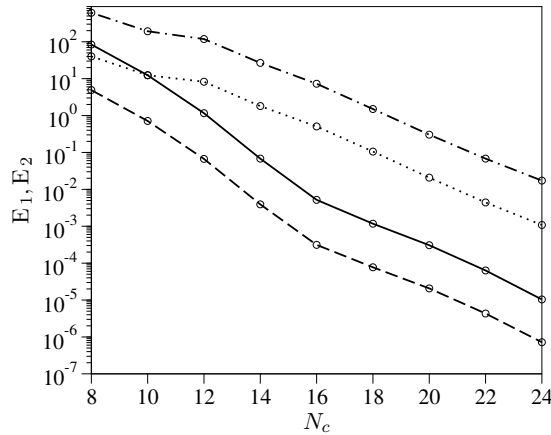


Figure 7.12: Isochoric equilibrium relaxation of a Ne-Ar gas. L_1 and L_2 norms of the error on the gas temperature with and without conservation constraint (unbroken line E_1 with conservation, dashed line E_2 with conservation, dotted-dashed line E_1 without conservation, dotted line E_2 without conservation; circles are added to highlight the number of velocity nodes used).

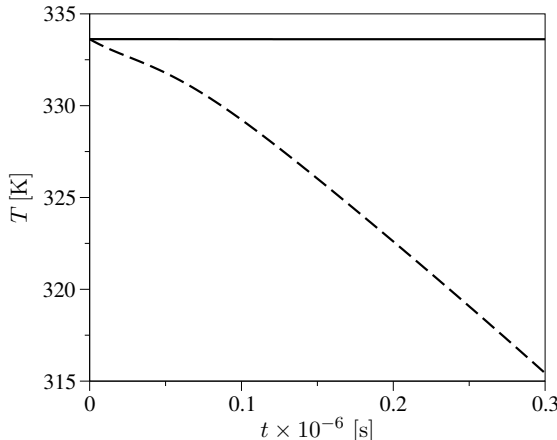


Figure 7.13: Isochoric equilibrium relaxation of a Ne-Ar gas. Time-evolution of the gas temperature with and without conservation constraint ($N_c = 16$; unbroken line with conservation, dashed line without conservation).

The numerical errors obtained when applying the conservation constraint are orders of magnitude lower than those obtained when conservation is not enforced. The differences are less pronounced when using a low number of velocity nodes (e.g. 8, 10). This can be explained by the fact that 8 or 10 velocity

nodes are not enough to obtain an accurate estimate of second-order moments (such as the gas temperature) of the initial velocity distribution function. When the number of velocity nodes is increased, the error in the solution obtained by enforcing conservation becomes substantially the sum over all time-steps of the quadrature rule error when evaluating the gas initial temperature. This is not the case when conservation is not enforced. In this situation, the error is dominated by the lack of conservation. An evidence of this is given in fig. 7.13 showing the time-evolution of the gas temperature with and without conservation constraint for 16 velocity nodes.

7.2.2 Flow Across a Normal Shock Wave in a Ne-Ar gas

The steady-state flow across a normal shock wave in a Ne-Ar gas has been studied, as done in sec. 7.1, in the shock wave reference frame. A peculiar aspect of the present benchmark is the species separation occurring within the shock. The separation is due to the mass difference between the two species with the lighter species experiencing the compression sooner than the heavier one (Center 1967; Bird 1994).

The gas is composed of 50 % of Ne and 50 % of Ar. The corresponding mass fractions are 0.34 and 0.66, respectively. The gas free-stream density, temperature and velocity are $1 \times 10^{-4} \text{ kg/m}^3$, 300 K and 744 m/s, respectively. The latter correspond to a free-stream Mach number equal to 2. Post-shock values for the gas density, velocity and temperature (computed based on the Rankine-Hugoniot jump relations) are $2.29 \times 10^{-4} \text{ kg/m}^3$, 623.44 K and 325.45 m/s, respectively.

The simulation parameters are provided in tab. 7.5. As already done in sec. 7.1, the position is discretized by means of a uniform FV grid. At the boundaries $x = -L_x^-$ and $x = L_x^+$, a Maxwell-Boltzmann velocity distribution function corresponding, respectively, to the pre and post-shock conditions are imposed for the two species. The steady-state flow across the shock wave has been computed by using the same procedure as of sec. 7.1. The memory required for this test-case is the same as that of sec. 7.2.1

N_c	L_c [m/s]	N_x	L_x^- [m]	L_x^+ [m]	Δt^c [s]	CFL	Limiter
22	3200	201	2×10^{-2}	2×10^{-2}	1×10^{-8}	0.5	van Albada

Table 7.5: Flow across a normal shock wave in a Ne-Ar gas. Simulation parameters.

Macroscopic Moments: BEST vs DSMC

Figure 7.14 shows the evolution across the shock wave of the species hydrodynamic velocity and parallel temperature. The results confirm, as expected, that the Ne experiences the compression before the Ar. This effect progressively disappears while the flow approaches the post-shock equilibrium state (where

no species separation exists). In analogy with what observed in sec. 7.1, the parallel temperature of both species reaches a maximum, and then approaches the post-shock equilibrium value. This is again due the distortion experienced by the velocity distribution function while the flow crosses the shock wave. Notice that the peak is more pronounced for the heavier component (Ar). The comparison with the DSMC results is again excellent. This is further confirmed by fig. 7.15 showing the evolution across the shock wave of the gas density and temperature (and the related parallel and transverse components).

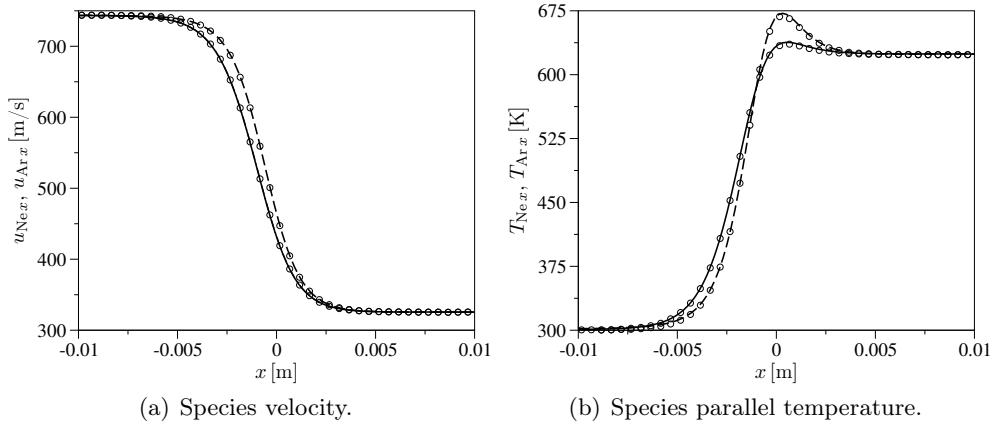


Figure 7.14: Flow across a normal shock wave in a Ne-Ar gas. Evolution of the species hydrodynamic velocity and parallel temperature ($M_\infty = 2$; unbroken lines Ne BEST, dashed line Ar BEST, symbols DSMC(Torres)).

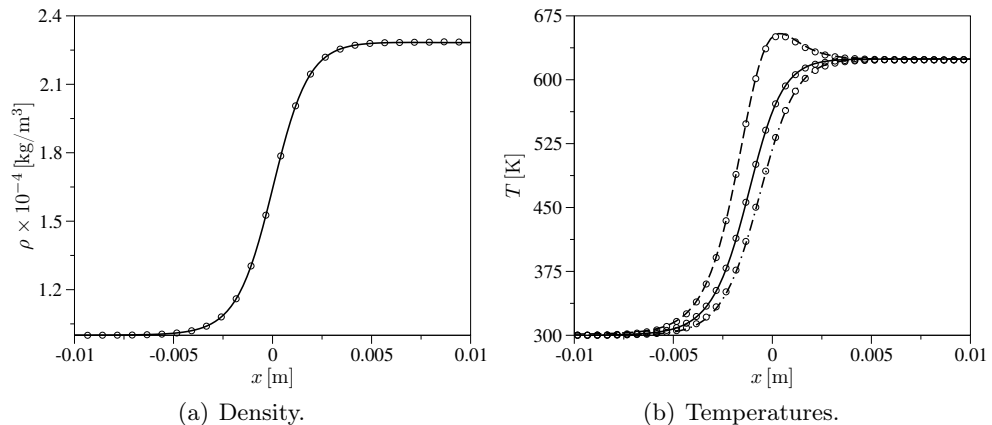


Figure 7.15: Flow across a normal shock wave in a Ne-Ar gas. Evolution of the gas density, temperature and related parallel and transverse components ($M_\infty = 2$; lines BEST, symbols DSMC(Torres); in (b) unbroken line T , dashed line T_x , dotted-dashed line T_y).

Analysis of the Species Velocity Distribution Functions

Figure 7.16 shows a visual correspondence between the density and the c_x axis component of the velocity distribution function of Ne and Ar across the shock wave. Due to the low value of the free-stream Mach number, small deviations from a Maxwellian shape are observed. This justifies, in turn, the moderate maxima reached by the species parallel temperature in fig. 7.14(b). The evolution across the shock wave of the c_y and c_z axis components of the species velocity distribution functions (not shown here) occurs through a sequence of Maxwell-Boltzmann velocity distribution functions.

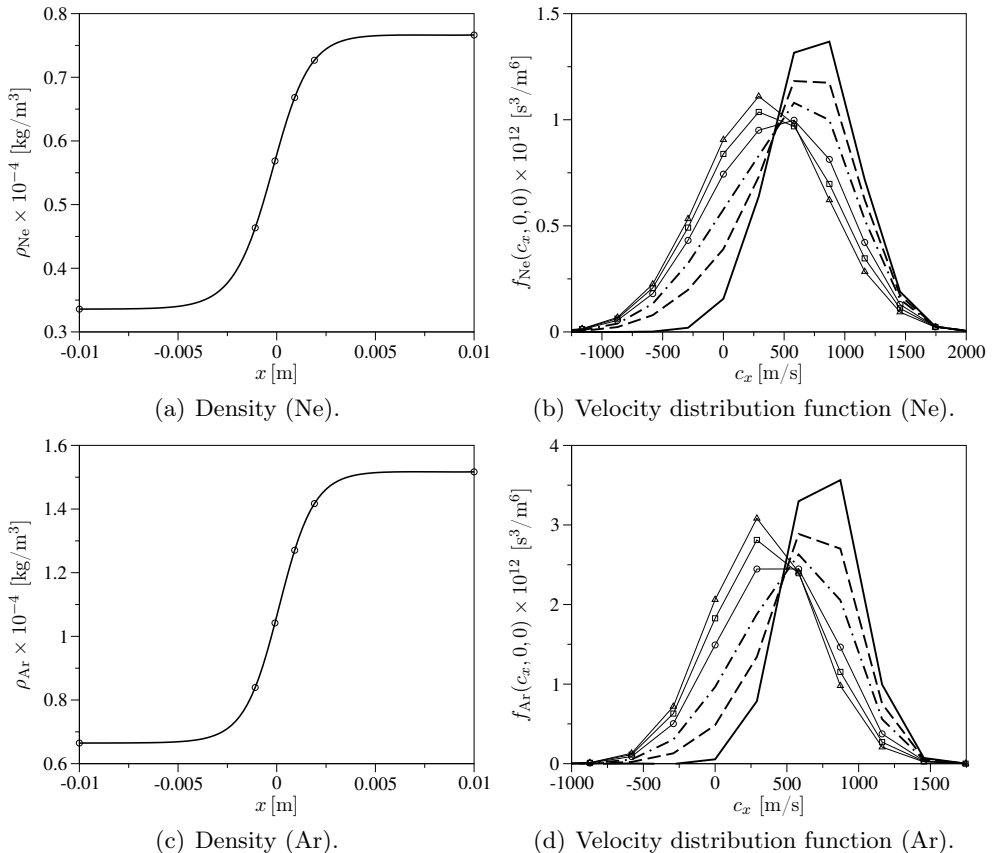


Figure 7.16: Flow across a normal shock wave in a Ne-Ar gas. Comparative evolution of the density and the c_x axis component of the velocity distribution functions of Ne and Ar ($M_\infty = 2$; the symbols in (a) and (c) highlight the locations at which the species velocity distribution functions, plotted in (b) and (d), are extracted; in (b) and (d) unbroken lines $x = -1 \times 10^{-2}$ m, dashed lines $x = -1.1 \times 10^{-3}$ m, dotted-dashed lines $x = -1 \times 10^{-4}$ m, lines with circles $x = 9 \times 10^{-4}$ m, lines with squares $x = 1.9 \times 10^{-3}$ m, lines with triangles $x = 1 \times 10^{-2}$ m).

7.3 Gas with Internal Energy

The extension of the spectral-Lagrangian method of Gamba and Tharkab-hushanam (2009; 2010) to multi-component gases with discrete internal energy levels has been tested on the same kind of benchmarks considered in sec. 7.2. Despite the generality of the formulation described in ch. 6, the results shown in this section refer to a gaseous system made of one component (Ar) with discrete internal energy levels. For this reason, the chemical component index is dropped in what follows.

The value of the Ar mass m is the same as that used in secs. 7.1-7.2, while its diameter d is set equal to 3×10^{-10} m. The number of internal energy levels taken into account (and the related values of degeneracy and energy) are case dependent. Both elastic and inelastic collisions are allowed to occur:

$$i + j = k + l, \quad i, j, k, l \in \mathcal{I}, \quad (7.5)$$

where the set \mathcal{I} stores the internal energy levels. For the evaluation of the differential cross-section for the collision $i + j = k + l$, the model proposed by Anderson et al. (1986) has been considered. According to this model, the differential cross-section is written as a product between a HS differential cross-section $d^2/4$ and a transition probability I_{ij}^{kl} , that is, $\sigma_{ij}^{kl} = (d^2/4)I_{ij}^{kl}$. The transition probability only depends on the pre-collisional relative velocity magnitude g and has the following expression:

$$I_{ij}^{kl} = \frac{\max(\mu g^2 - \Delta E_{ij}^{kl}, 0)}{\sum_{m,n \in \mathcal{I}} \max(\mu g^2 - \Delta E_{ij}^{mn}, 0)}, \quad i, j, k, l \in \mathcal{I}, \quad (7.6)$$

where the reduced mass of the colliding particles μ is equal to $m/2$. Notice that eq. (7.6) comprises also the case of elastic collisions ($i = k$ and $j = l$).

An internal temperature T_{int} is extracted from the level population (in analogy with what done in chs. 4-5 through the use of eq. (3.34)) by solving the following non-linear equation:

$$\frac{\sum_{i \in \mathcal{I}} n_i E_i}{n} = \frac{\sum_{i \in \mathcal{I}} a_i E_i \exp(-E_i/k_b T_{\text{int}})}{\sum_{i \in \mathcal{I}} a_i \exp(-E_i/k_b T_{\text{int}})}, \quad (7.7)$$

where the gas number density is $n = \sum_{i \in \mathcal{I}} n_i$.

7.3.1 Isochoric Equilibrium Relaxation

The isochoric equilibrium relaxation of a multi-energy level gas has been studied by considering 5 internal energy levels. The related values of degeneracy and energy (taken from Anderson et al. 1986) are reported in tab. 7.6.

The initial state of the system corresponds to a partial equilibrium condition. The velocity distribution functions of all levels (species) is a two temperature (translational T and internal T_{int}) Maxwell-Boltzmann velocity distribution

function with zero bulk velocity, obtained by assuming that the population of the internal energy levels is Boltzmann at T_{int} (see eq. (1.36)).

The gas has a density of 1 kg/m^3 . The initial values of the gas translational and internal temperatures are 1000 K and 100 K , respectively. The initial condition of the system approximates the state of the gas immediately behind a normal shock wave when this is treated as a discontinuity (as done in ch. 4).

i	a_i	$E_i [\text{J}]$
1	1	0
2	1	8.30×10^{-21}
3	1	1.66×10^{-20}
4	1	2.50×10^{-20}
5	1	3.30×10^{-20}

Table 7.6: Isochoric equilibrium relaxation of a multi-energy level gas. Level degeneracies and energies.

The velocity space is discretized by adopting 16 velocity nodes and by setting its semi-length to 3000 m/s ($N_c = 16$ and $L_c = 3000 \text{ m/s}$, respectively). The collision time-step Δt^c is set to $1 \times 10^{-12} \text{ s}$ in order to have a value lower than the mean collision time (based on a HS collision model). The number of partial collision operators to be evaluated at each time-step is equal to 625 (25 elastic and 600 inelastic). The simulation was stopped after 2500 time-steps. The CPU time required was approximately 2 hours when using 12 threads. The memory required was approximately 88 GB. This high value is due to the fact that 625 convolution weights must be stored.

Macroscopic Moments: BEST vs DSMC

As for the case studied in sec. 7.2.1, when the simulation is started, collisions bring the system to equilibrium. However, due to the presence of inelastic collisions, some differences arise:

- The gas density is constant and maintains its initial value. On the other hand, the density of each level changes in time and evolves from the initial non-equilibrium state to its final equilibrium value.
- The level and gas hydrodynamic velocities are constant and maintain their initial values (zero).
- The gas temperature changes in time and evolves from the initial non-equilibrium state to its final equilibrium value.

The value of the temperature at equilibrium can be computed from the energy balance between the initial and the final (equilibrium) states. For the present simulation, the value of 723.5 K is obtained. Once the equilibrium temperature determined, it is possible to compute the equilibrium values of the level densities by means of the Boltzmann distribution law (1.36).

In order to assess the conservation properties of the proposed spectral-Lagrangian method for the case of a multi-energy level gas, the time-evolution of the density of each level and the translational and internal temperatures have been monitored (see fig. 7.17). The results given in fig. 7.17 confirm the previous considerations regarding the behavior of the system. In particular, the population of the ground-state decreases while those of the upper states increase. The translational temperature decreases till the equilibrium value is reached. The opposite behavior is observed for the internal temperature. This demonstrates the existence of a net macroscopic energy transfer from the translational to the internal degree of freedom of the gas. The level and gas hydrodynamic velocities retain their initial values (zero) and are not shown in fig. 7.17. The agreement with the DSMC solution is again excellent.

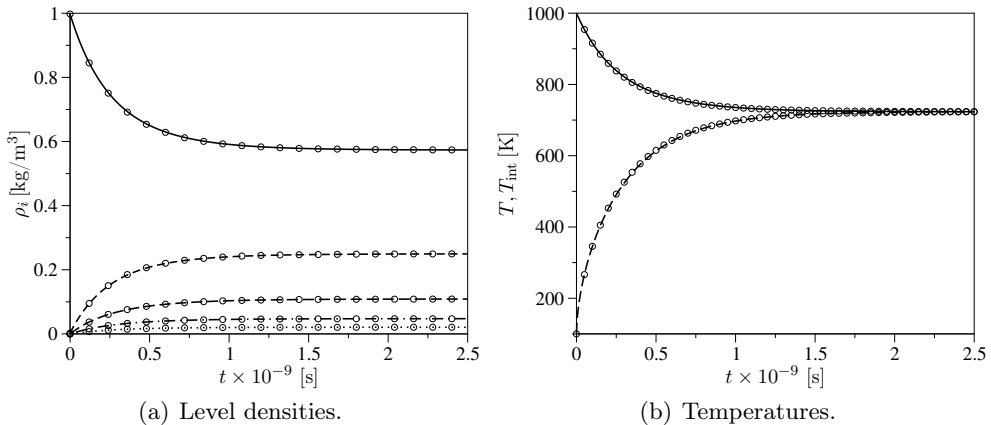


Figure 7.17: Isochoric equilibrium relaxation of a multi-energy level gas. Time-evolution of the level densities and temperatures (lines BEST, symbols DSMC(Torres); in (a) unbroken line ρ_1 , short dashed line ρ_2 , long dashed line ρ_3 , dotted-dashed line ρ_4 , dotted line ρ_5 ; in (b) unbroken line T , dashed line T_{int}).

Table 7.7 compares the final values of the temperature and the level densities as obtained from the simulation with those determined by means of equilibrium calculations. The agreement between the two data sets is very good. This further confirms the conservation properties of the extended spectral-Lagrangian method when both elastic and inelastic collisions are taken into account.

	T [K]	ρ_1 [kg/m ³]	ρ_2 [kg/m ³]	ρ_3 [kg/m ³]	ρ_4 [kg/m ³]	ρ_5 [kg/m ³]
BEST	723.4029	0.573	0.245	0.1088	0.0474	0.02069
Eq.	723.543	0.573	0.245	0.1089	0.0474	0.02064

Table 7.7: Isochoric equilibrium relaxation of a multi-energy level gas. Final values of temperature and level densities (comparison between simulation and equilibrium calculations).

7.3.2 Flow Across a Normal Shock Wave

The steady-state flow across a normal shock wave of a multi-energy level gas has been studied by accounting for 2 internal energy levels. The related values of degeneracy and energy (taken from Josyula et al. 2011) are given in tab. 7.8. In this situation, the total number of partial collision operators to be evaluated reduces to 16 (4 elastic and 12 inelastic).

i	a_i	E_i [J]
1	1	0
2	1	4.14×10^{-21}

Table 7.8: *Flow across a normal shock wave in a multi-energy level gas. Level degeneracies and energies.*

The free-stream values of the gas density, temperature and velocity are set to 1.068×10^{-4} kg/m³, 300 K and 945.33 m/s, respectively. The latter correspond to a free-stream Mach number equal to 3. Post-shock conditions have been obtained by means of the technique suggested by Anderson (1989).¹ The values obtained for the post-shock density, temperature and velocity are 3.25×10^{-4} kg/m³, 1046.2 K and 311.07 m/s, respectively.

The simulation parameters are provided in tab. 7.9. As already done in sects. 7.1 and 7.2.2, the position space is discretized by means of a uniform FV grid. At the boundaries $x = -L_x^-$ and $x = L_x^+$, a Maxwell-Boltzmann velocity distribution function corresponding, respectively, to the pre and post-shock conditions, is imposed for each level. The steady-state flow across the shock wave has been computed by means of the same procedure used in sects. 7.1 and 7.2.2. The memory required for this test-case was approximately 30 GB.

N_c	L_c [m/s]	N_x	L_x^- [m]	L_x^+ [m]	Δt^c [s]	CFL	Limiter
30	3400	201	2×10^{-2}	2×10^{-2}	1×10^{-8}	0.5	van Albada

Table 7.9: *Flow across a normal shock wave in a multi-energy level gas. Simulation parameters.*

Macroscopic Moments: BEST vs DMSC

Figure 7.18 shows the evolution across the shock wave of the level mass fractions, diffusion velocities, velocities and temperatures. The population of the energy levels changes due to the occurrence of inelastic collisions. This creates spatial gradients of the chemical composition that, in turn, lead to a mass diffusion flux for both levels. Species separation occurs within the shock, as it can also be seen from the velocity and temperature evolution. However, in a

¹The Rankine-Hugoniot jump relations cannot be applied in this case, as they are valid only for a calorically perfect gas (Rankine 1870, Hugoniot 1887; 1889)

comparison with sec. 7.2.2, some differences arise. In the present situation, the separation is the result of chemical composition gradients caused by inelastic collisions. In the case of sec. 7.2.2, the separation is due to the mass disparity between the two species that leads to accumulation of the atoms of the lighter species in the initial part of the shock front.

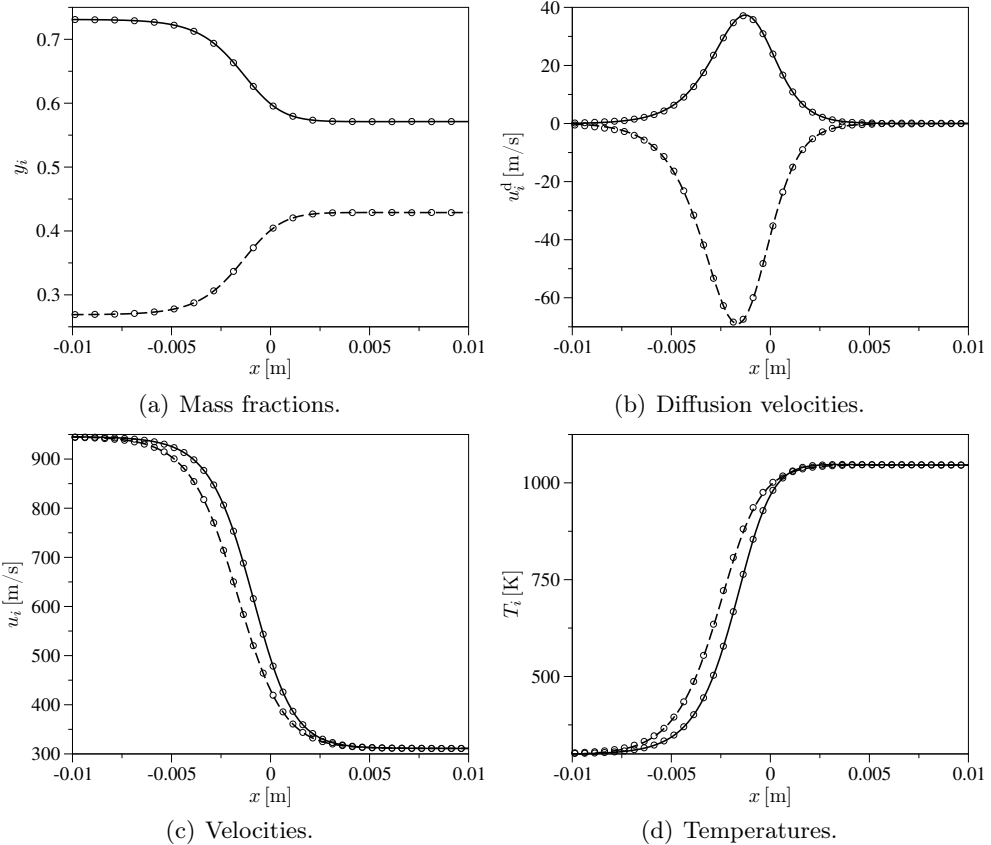


Figure 7.18: Flow across a normal shock wave in a multi-energy level gas. Evolution of the level mass fractions, diffusion velocities, velocities and temperatures ($M_\infty = 3$; unbroken lines level 1 BEST, dashed lines level 2 BEST, symbols DSMC(Torres)).

The comparison with the DSMC results is again excellent. The same conclusion can be drawn when looking at gas quantities (*i.e.* pressure and temperatures) as done in fig. 7.19. Notice that the internal temperature lags very little behind the translational temperature (as opposed to what observed ch. 4). This behavior, though physically correct, is due both to the use of a very simple gas model (*i.e.* one excited internal energy level lying close to the ground-state) and to the use of the Anderson model, which tends to overestimate the probability of inelastic transitions (as shown by Torres and Magin 2012). This does not represent a problem, as the purpose of the thesis work was to assess the accuracy and the conservation properties of the extended spectral-Lagrangian method.

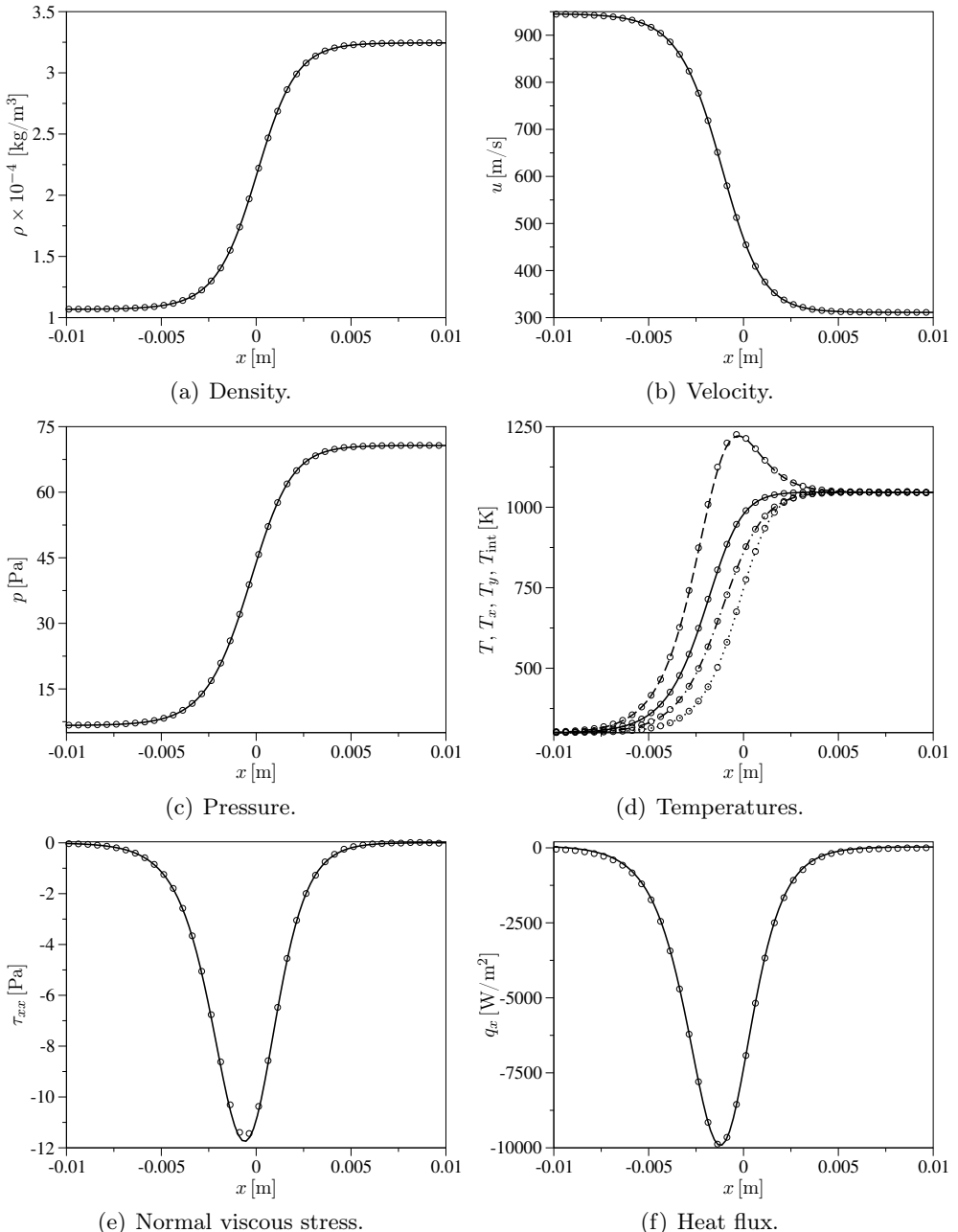


Figure 7.19: Flow across a normal shock wave in a multi-energy level gas. Evolution of the gas density, pressure, velocity, translational temperature and related parallel and transverse components, internal temperature, normal viscous stress and heat flux ($M_\infty = 3$; lines BEST, symbols DSMC(Torres); in (d) unbroken line T , dashed line T_x , dotted-dashed line T_y , dotted line T_{int}).

Analysis of the Level Velocity Distribution Functions

Figure 7.20 shows a visual correspondence between the evolution of the level densities and the related c_x axis component of the velocity distribution functions. The distortions around the location $x = 0$ m are the responsible for the observed maximum in the gas parallel temperature in fig. 7.19(d). The evolution across the shock wave of the c_y and c_z axis components (not shown) occurs through a sequence of Maxwell-Boltzmann velocity distribution functions.

The evolution of the level velocity distributions can also be appreciated in figs. 7.21-7.22 showing their projections on the (c_x, c_y) plane at the same locations as of fig. 7.20.

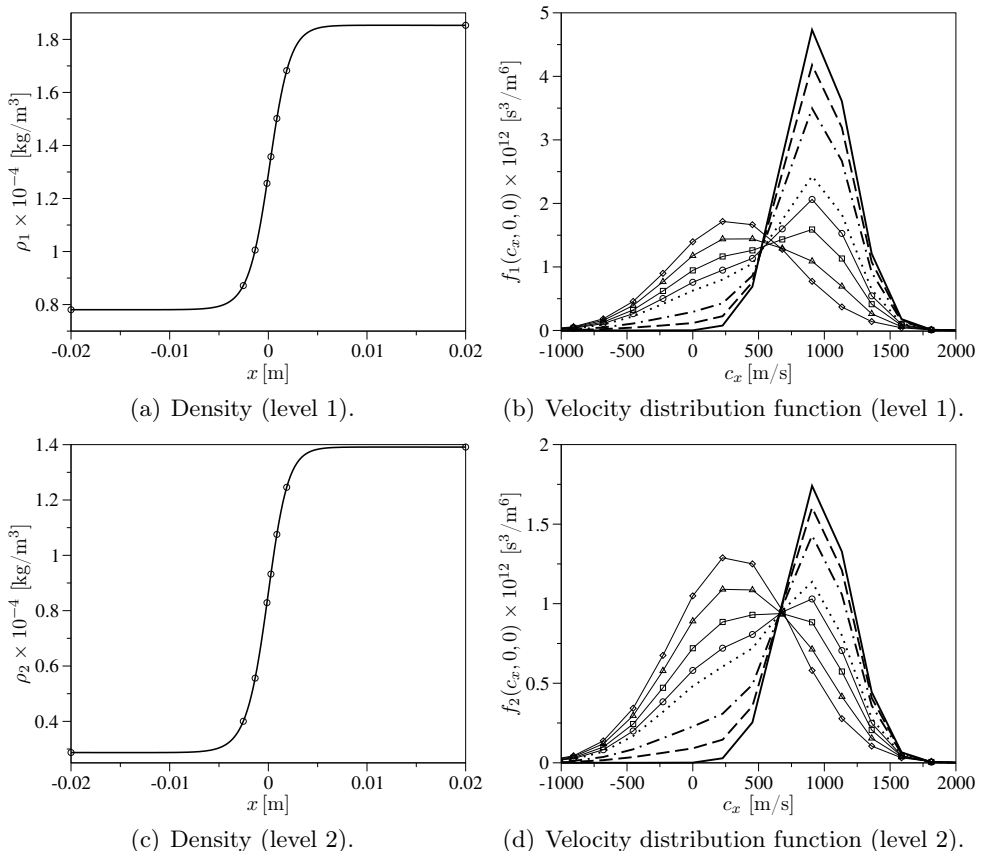


Figure 7.20: Flow across a normal shock wave in a multi-energy level gas. Comparative evolution of the level densities and the related c_x axis component of the velocity distribution functions ($M_\infty = 3$; the symbols in (a) and (c) highlight the locations at which the level velocity distribution functions, plotted in (b) and (d), are extracted; in (b) and (d) unbroken lines $x = -2 \times 10^{-2}$ m, dashed lines $x = -2.5 \times 10^{-3}$ m, dotted-dashed lines $x = -1 \times 10^{-3}$ m, dotted lines $x = -1 \times 10^{-4}$ m, lines with circles $x = 3 \times 10^{-4}$ m, lines with squares $x = 9 \times 10^{-4}$ m, lines with triangles $x = 1.9 \times 10^{-3}$ m, lines with diamonds $x = 2 \times 10^{-2}$ m).

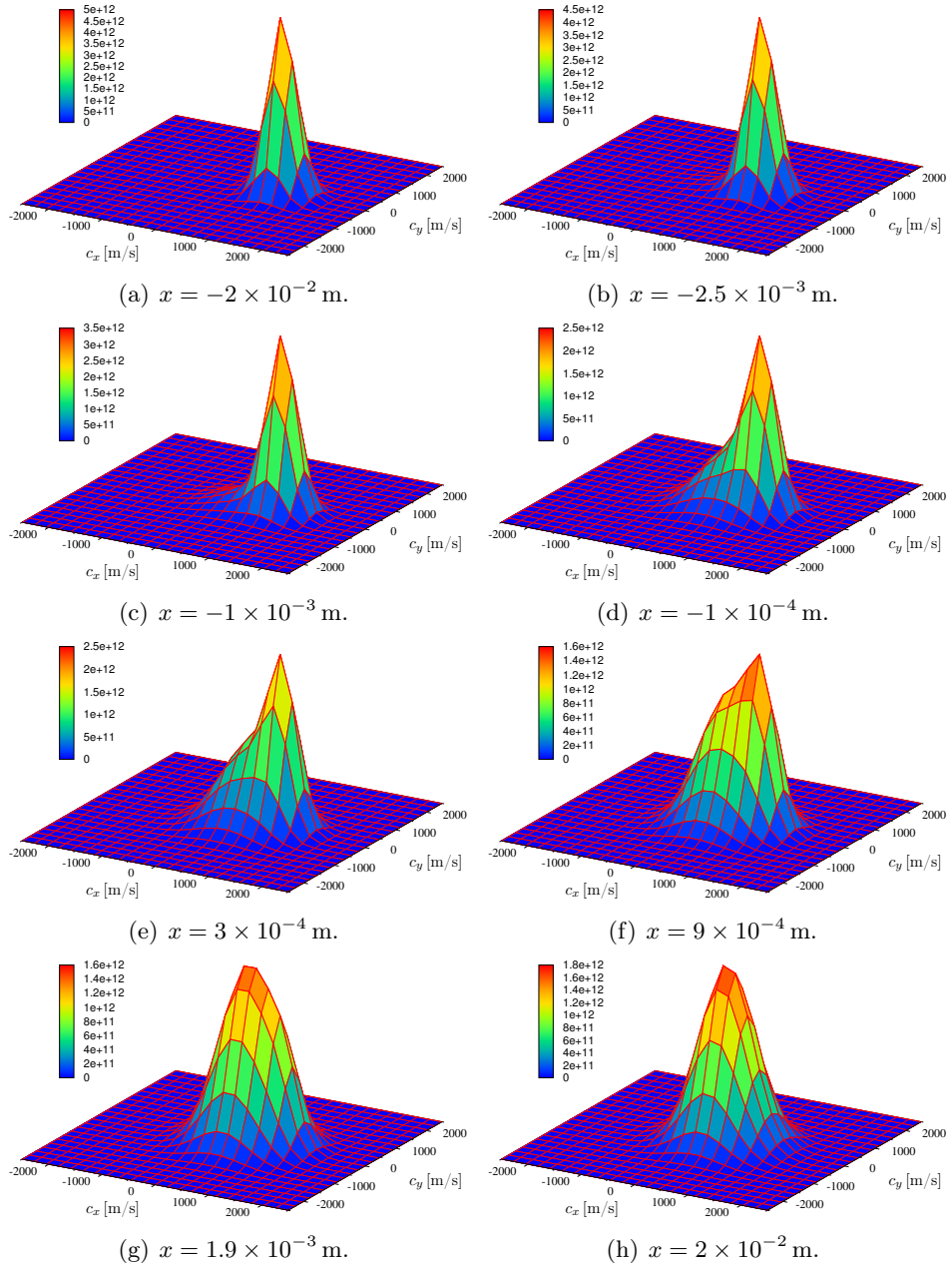


Figure 7.21: Flow across a normal shock wave in a multi-energy level gas. Evolution of the projection on the (c_x, c_y) plane of the velocity distribution function of level 1 ($M_\infty = 3$).

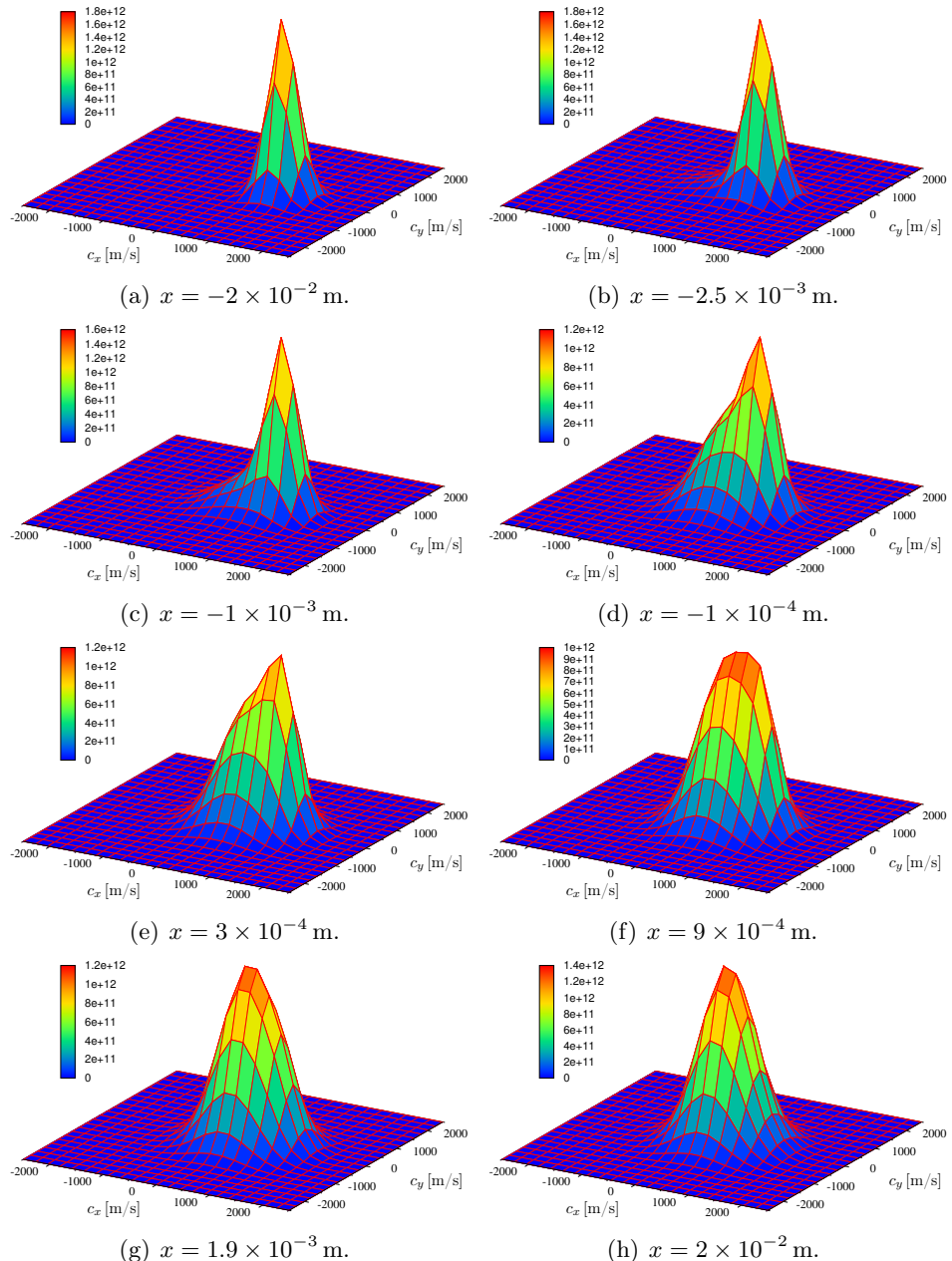


Figure 7.22: Flow across a normal shock wave in a multi-energy level gas. Evolution of the projection on the (c_x, c_y) plane of the velocity distribution function of level 2 ($M_\infty = 3$).

7.4 Intermediate Conclusions

In this chapter applications of the extended spectral-Lagrangian method described in ch. 6 have been shown.

At the beginning (sec. 7.1), the accuracy of the original formulation (valid for a mono-component gas without internal energy) has been assessed by comparing with DSMC the results for the flow across a normal shock wave in Ar. An excellent agreement has been observed. The calculations have been run by using a tunable VHS cross-section model in order to perform a comparison with experimental density profiles. The good agreement obtained allowed for a first-step validation of the computational tool developed (BEST).

After that, the extended formulation of the spectral-Lagrangian method has been tested on benchmarks involving multi-component gases (sec. 7.2) and inelastic collisions (sec. 7.2). In both situations, two cases have been studied in detail: a) isochoric equilibrium relaxation (space homogeneous) and b) steady flow across a normal shock wave (space inhomogeneous). The space homogeneous testcases were chosen as, due to the absence of convective transport, they allowed for testing alone the procedure for the discrete evaluation of the collision operators (*i.e.* the conservation properties of the numerical method). The results obtained in sects. 7.2.1 and 7.3.1 proved that the proposed extension of the spectral-Lagrangian method is indeed conservative. For the case of a multi-component gas without internal energy, the importance of the application of the conservation constraint has been also studied (sec. 7.2.1). The results clearly indicated that, if conservation is not enforced, the solution is unphysical and numerical errors remain high even when using a high number of velocity nodes. The accuracy of the solutions has been assessed by comparing macroscopic moments with the DSMC method results. As for the original formulation, the comparison led to an excellent agreement. The same conclusion was found when analyzing the results obtained for flows across normal shock waves in sects. 7.2.2 and 7.3.2. In these two sections, the evolution of the species velocity distribution functions across the shock wave have been also analyzed.

Conclusions

The present chapter draws general conclusions based on the results presented in this thesis.

Multi-Scale Models

The work on multi-scale models has focused on the $\text{N}_2(^1\Sigma_g^+)$ - $\text{N}(^4\text{S}_u)$ system by using the *ab-initio* database developed by the Computational Quantum Chemistry Group at NASA Ames Research Center. The set of state-to-state kinetics and thermodynamic data provided in this database have been used for building a RVC model and a suite of reduced models for CFD applications: MT, VC, BRVC and URVC.

Applications of the RVC model to flows behind shock waves and within converging-diverging nozzles have allowed for a detailed investigation of the energy level dynamics, and related assessment of rotational non-equilibrium effects, usually not taken into account in conventional CFD solvers. For flows behind shock waves, the results indicated that the assumption of rotational non-equilibrium becomes questionable at high speed conditions. On the other hand, in recombining nozzle flows, the gas expansion occurs under rotational equilibrium conditions, as non-Boltzmann distributions are appreciable only for rotational levels of high-lying vibrational states. The analysis of the rovibrational distributions has revealed the existence of a splitting of rotational levels according to even and odd rotational quantum numbers. In dissociating flows behind shock waves, this feature of the distribution is more and more significant from the high-lying vibrational states to the ground-state, due to the faster rotational excitation of high-lying vibrational states. For nozzle flows, the observed behavior was completely opposite.

The predictions of the RVC model have been compared with those obtained by means of the reduced models. For the sake of completeness, in the comparison, the conventional multi-temperature Park (MTP) model has been also considered, as it represents the standard model used in CFD solvers.

The results obtained for flows behind shock waves indicated that the BRVC and URVC models could reproduce the correct dynamical evolution of flow quantities (such as temperature and chemical composition) with only 20 energy bins. The MT and VC models led to a faster dissociation, due to the lack of QSS

conditions and assumed rotational equilibrium, respectively. The MTP model provided the less accurate description, thereby illustrating the inadequacy of the physico-chemical models currently used in CFD solvers. A sensitivity analysis to the number of energy bins indicated that the BRVC model should be preferred to the URVC model, due to the impossibility of retrieving the post-shock equilibrium conditions with the URVC model (unless a high number of energy bins is used).

For nozzle flows, both the VC and BRVC models were in good agreement with the RVC model predictions. The VC model led to a slightly more accurate description. This is not surprising, as the assumption of rotational equilibrium, on which the VC is built, was found to hold true for expanding flows. The departure between the BRVC and VC model results has been further investigated by performing a sensitivity analysis to the number of energy bins. The analysis revealed that, for the same computational cost of the MTP model (*i.e.* 2-5 energy bins), the BRVC model solution was already quite close to the VC model prediction. Indeed, the relative error on the outlet value of the N₂ mole fraction was around 10 %, while it was more than 100 % for the MTP model. These results suggested that, for CFD applications, the BRVC model should be preferred to the VC model, due to the possibility of achieving an accurate flowfield description at a much lower computational cost.

The BRVC and MTP models have been further compared in the computation of the viscous flow along the stagnation-line of blunt bodies. As observed for nozzle flows, the MTP model overestimated the recombination in the boundary layer, thereby leading to higher wall heat flux values. The sensitivity analysis to the number of energy bins (for the BRVC model) revealed that 10 energy bins were enough to obtain an accurate evolution of the flow quantities and the transport fluxes at the wall.

Computational Methods

The research on computational methods for rarefied flows has led to the extension of an existing spectral-Lagrangian method for the Boltzmann equation (valid for a mono-component gas without internal energy) to multi-component gases and inelastic collisions. The proposed numerical method is based on the convolution structure of the Fourier transformed Boltzmann equation, which shows that the Fourier transform of the partial collision operators (elastic and inelastic) can be written as weighted convolutions in Fourier space. The convolution weights only depend on the cross-section model. Hence, they can be pre-computed to reduce the computational cost. This fact has been exploited in the algorithms developed for the discrete evaluation of the collision operators. The conservation of mass, momentum and energy during collisions has been enforced through the solution of two constrained optimization problems (one for elastic collisions and the other for inelastic collisions). The constrained optimization problems have been formulated in a consistent manner with the elastic

and inelastic collisional invariants.

The extended spectral-Lagrangian method has been implemented in a parallel computational tool. Applications have considered both space homogeneous/inhomogeneous problems. Initially, the accuracy of the original spectral-Lagrangian method has been assessed by comparing the results for the flow across a normal shock wave in Ar with the DSMC predictions. An excellent agreement has been observed. For this benchmark, a comparison with experimental density profiles (which led to a fair agreement) has been also performed for the sake of validation. Later, the extended formulation of the method has been tested on isochoric relaxation and normal shock wave flow benchmarks. Even in these cases, an excellent agreement with the DSMC results has been observed. The conservation properties of the proposed numerical method have been studied in detail for the isochoric relaxation benchmarks. The result obtained have shown that conservation enforcement was mandatory to obtain accurate and physically correct solutions.

Perspectives

This chapter suggests possible further developments of the research work presented in this thesis.

Multi-Scale Models

The applications to inviscid and viscous flows of the proposed reduced models have shown that the BRVC model enables to obtain an accurate flow description, with a computational cost of the same order as that of conventional multi-temperature models. However, the results obtained were limited to the $\text{N}_2(^1\Sigma_g^+)$ - $\text{N}(^4\text{S}_u)$ system. Moreover, phenomena such as ionization and radiation have not been taken into account. The next natural step of the work presented here would be to include, in the BRVC mechanism reduction, the most important rovibrational transitions of the $\text{N}_2(^1\Sigma_g^+)$ - $\text{N}_2(^1\Sigma_g^+)$ system and collisional processes involving electrons (such as electron impact dissociation/ionization and associative ionization). The additional set of N_2 - N_2 rovibrational rate coefficients could be also added to the current RVC model. This would allow for a more accurate assessment of rotational non-equilibrium effects behind shock waves, as the flowfield could be computed in more realistic conditions (*i.e.* without seeding the free-stream flow with a small amount of N). Preliminary results of the application of the N_2 - N_2 system state-to-state kinetics data have been recently presented by Panesi et al. (2013). Other possible topics for future work are multi-dimensional viscous flow applications and accuracy improvement of the BRVC model. Indeed, the results obtained seem to suggest that a higher accuracy could be achieved by reducing the number of energy bins and, at the same time, by assuming that the distribution of the energy levels within a bin is Boltzmann at its own (or global) internal temperature (*i.e.* multi-temperature formulation of the BRVC model). This approach has been successfully employed by Guy et al. (2013) for developing multi-internal-temperature models based on FHO vibrational state-to-state rate coefficients. Due to the importance of radiation phenomena for high-speed entry conditions, future research efforts should be also spent on including radiative transitions and electronically excited states of atoms and molecules in the developed physical models. Further possible developments are the formulation of a more rigorous treatment of transport phenomena (to properly account

for the effects of excited states on the transport fluxes) and the possible re-derivation of the reduced models presented in this thesis based on the Kinetic Theory of Gases and Linear Irreversible Thermodynamics.

Computational Methods

The applications of the extended spectral-Lagrangian method to space homogeneous/inhomogeneous problems involving multi-component gases and inelastic collisions have led to an excellent agreement with the DSMC predictions. Moreover, the results obtained indicated that the proposed numerical method is conservative. The current formulation of the spectral-Lagrangian method does not account for reactive collisions and uses a unique velocity grid for all the species. In order to account for reactive collisions, such as three-body dissociation/recombination, the weighted convolution structure of the reactive collision operator must be established. The use alternative phase-space representations (such as momentum and energy spaces) could be considered in order to deal with collisions between particles having very disparate masses (such atom-electron or molecule-electron collisions). Other possible topics for future work are the use of more accurate cross-section models (based on realistic interaction potentials), multi-dimensional applications and reduction of the computational cost. The latter could be achieved by exploiting eventual symmetries (in the velocity space) of the velocity distribution function.

Appendix A

Fitting Expressions for MT Models

Macroscopic Dissociation Rate Coefficient

$$\tilde{k}_{\text{N}_2}^{\text{dis}}(T) = a_0 T^{a_1} \exp\left(-\frac{a_2}{T}\right), \quad [\text{cm}^3/\text{s}], \quad (\text{A.1})$$

with $a_0 = 1.6017 \times 10^{-5} \text{ cm}^3/\text{s}$, $a_1 = -0.8467$ and $a_2 = 1.134 \times 10^5 \text{ K}$.

Relaxation Times

$$\tau_{\text{N}-\text{N}_2}^{\text{tra-int}} p_{\text{N}} = \exp[b_0(T^{-1/3} - b_1)] + \exp[b_2(T^{-1/3} - b_3)], \quad [\text{s atm}], \quad (\text{A.2})$$

$$\tau_{\text{N}-\text{N}_2}^{\text{tra-vib}} p_{\text{N}} = \exp[b_0(T^{-1/3} - b_1)] + \exp[b_2(T^{-1/3} - b_3)], \quad [\text{s atm}], \quad (\text{A.3})$$

$$\tau_{\text{N}-\text{N}_2}^{\text{tra-rot}} p_{\text{N}} = \exp[b_0(T^{-1/3} + b_1)] - \exp[b_2(T^{-1/3} + b_3)], \quad [\text{s atm}]. \quad (\text{A.4})$$

	b_0	b_1	b_2	b_3
$\tau_{\text{N}-\text{N}_2}^{\text{tra-int}}$	23.354	0.809 88	225.692	0.1335
$\tau_{\text{N}-\text{N}_2}^{\text{tra-vib}}$	246.747	0.119 30	46.9888	0.417 14
$\tau_{\text{N}-\text{N}_2}^{\text{tra-rot}}$	-60.202	0.262 45	-138.875	0.105 01

Table A.1: Relaxation time fitting parameters.

Chemistry Coupling Factors

$$C_{\text{N}_2}^{\text{dis-int}} = c_0 T^{c_1}, \quad (\text{A.5})$$

$$C_{\text{N}_2}^{\text{dis-vib}} = c_0 T^{c_1}, \quad (\text{A.6})$$

$$C_{\text{N}_2}^{\text{dis-rot}} = c_0 + c_1 \ln(T). \quad (\text{A.7})$$

	c_0	c_1
$C_{\text{N}_2}^{\text{dis-int}}$	1.1334	−0.024 714
$C_{\text{N}_2}^{\text{dis-vib}}$	5.867	−0.233 41
$C_{\text{N}_2}^{\text{dis-rot}}$	−0.991 38	0.130 29

Table A.2: *Chemistry coupling factor fitting parameters.*

Appendix B

ODE sets in Canonical Form

In this appendix, and also in those that follow, the temperature dependence of thermodynamic properties is made implicit for the sake of brevity.

B.1 RVC, VC, BRVC and URVC models

The ODE set to be solved is:

$$\frac{\partial}{\partial x} \begin{pmatrix} y_N \\ \tilde{y}_\epsilon \\ u \\ T \end{pmatrix} = \begin{pmatrix} s_N \\ \tilde{s}_\epsilon \\ s_u \\ s_T \end{pmatrix}, \quad \epsilon \in \mathcal{E}_{N_2}. \quad (\text{B.1})$$

After introducing the (constant) mass flux $\dot{m} = \rho u$ and the two-component vector \mathbf{b} , defined as:

$$\mathbf{b} = -\frac{1}{\dot{m}} \left[\frac{k_b}{m_{N_2}} \frac{\omega_N T}{u} \quad \omega_N h_N + \sum_{\epsilon \in \mathcal{E}_{N_2}} \tilde{\omega}_\epsilon \tilde{h}_\epsilon \right]^T, \quad (\text{B.2})$$

it is possible to express the right-hand-side vector of eq. (B.1) as:

$$\begin{pmatrix} s_N \\ \tilde{s}_\epsilon \\ s_u \\ s_T \end{pmatrix} = \begin{pmatrix} \omega_N / \dot{m} \\ \tilde{\omega}_\epsilon / \dot{m} \\ \det(\mathbf{A}_1) / \det(\mathbf{A}) \\ \det(\mathbf{A}_2) / \det(\mathbf{A}) \end{pmatrix}, \quad \epsilon \in \mathcal{E}_{N_2}. \quad (\text{B.3})$$

Quantity \mathbf{A} is a two-by-two matrix, defined as:

$$\mathbf{A} = \begin{pmatrix} 1 - \frac{k_b}{m_{N_2}} \frac{(1+y_N)T}{u^2} & \frac{k_b}{m_{N_2}} \frac{(1+y_N)}{u} \\ u & y_N c_{pN} + \sum_{\epsilon \in \mathcal{E}_{N_2}} \tilde{y}_\epsilon \tilde{c}_{p\epsilon} \end{pmatrix}. \quad (\text{B.4})$$

In eq. (B.3), the notation \mathbf{A}_i indicates the matrix formed by replacing the i -th column of the matrix \mathbf{A} by the vector \mathbf{b} .

B.2 MT models

B.2.1 T - T_{int} Model

The ODE set to be solved is:

$$\frac{\partial}{\partial x} \begin{pmatrix} y_N \\ y_{N_2} \\ u \\ T \\ T_{\text{int}} \end{pmatrix} = \begin{pmatrix} s_N \\ s_{N_2} \\ s_u \\ s_T \\ s_{T_{\text{int}}} \end{pmatrix}. \quad (\text{B.5})$$

By applying the same procedure as of sec. B.1, the right-hand-side vector of eq. (B.5) becomes:

$$\begin{pmatrix} s_N \\ s_{N_2} \\ s_u \\ s_T \\ s_{T_{\text{int}}} \end{pmatrix} = \begin{pmatrix} \omega_N/\dot{m} \\ \omega_{N_2}/\dot{m} \\ \det(\mathbf{A}_1)/\det(\mathbf{A}) \\ \det(\mathbf{A}_2)/\det(\mathbf{A}) \\ (\Omega_{N_2}^{\text{tra-int}} + \Omega_{N_2}^{\text{dis-int}} - e_{N_2}^{\text{int}} \omega_{N_2}) / (\dot{m} y_{N_2} c_{vN_2}^{\text{int}}) \end{pmatrix}. \quad (\text{B.6})$$

The determinants needed to form the components s_u and s_T are computed by means of the same procedure as of sec. B.1 by replacing the matrix \mathbf{A} and the vector \mathbf{b} with the following expressions:

$$\mathbf{A} = \begin{pmatrix} 1 - \frac{k_b}{m_{N_2}} \frac{(1+y_N)T}{u^2} & \frac{k_b}{m_{N_2}} \frac{(1+y_N)}{u} \\ u & c_{pN_2}^{\text{tra}} (1+y_N) \end{pmatrix}, \quad (\text{B.7})$$

$$\mathbf{b} = -\frac{1}{\dot{m}} \left[\frac{k_b}{m_{N_2}} \frac{\omega_N T}{u} \quad \omega_N (h_N - h_{N_2}^{\text{tra}}) + \Omega_{N_2}^{\text{tra-int}} + \Omega_{N_2}^{\text{dis-int}} \right]^T. \quad (\text{B.8})$$

B.2.2 T - T_{vib} - T_{rot} Model

The ODE set to be solved is:

$$\frac{\partial}{\partial x} \begin{pmatrix} y_N \\ y_{N_2} \\ u \\ T \\ T_{\text{vib}} \\ T_{\text{rot}} \end{pmatrix} = \begin{pmatrix} s_N \\ s_{N_2} \\ s_u \\ s_T \\ s_{T_{\text{vib}}} \\ s_{T_{\text{rot}}} \end{pmatrix}. \quad (\text{B.9})$$

By applying the same procedure as of sec. B.1, and after introducing the two-by-two matrix \mathbf{B} and the two-component vector \mathbf{d} , defined as:

$$\mathbf{B} = \begin{pmatrix} \frac{\partial e_{N_2}^{\text{vib}}}{\partial T_{\text{vib}}} & \frac{\partial e_{N_2}^{\text{vib}}}{\partial T_{\text{rot}}} \\ \frac{\partial e_{N_2}^{\text{rot}}}{\partial T_{\text{vib}}} & \frac{\partial e_{N_2}^{\text{rot}}}{\partial T_{\text{rot}}} \end{pmatrix}, \quad (\text{B.10})$$

$$\mathbf{d} = \left[\frac{\Omega_{N_2}^{\text{tra-vib}} + \Omega_{N_2}^{\text{dis-vib}} - e_{N_2}^{\text{vib}} \omega_{N_2}}{\dot{m} y_{N_2}} \quad \frac{\Omega_{N_2}^{\text{tra-rot}} + \Omega_{N_2}^{\text{dis-rot}} - e_{N_2}^{\text{rot}} \omega_{N_2}}{\dot{m} y_{N_2}} \right]^T, \quad (\text{B.11})$$

the right-hand-side vector of eq. (B.9) becomes:

$$\begin{pmatrix} s_N \\ s_{N_2} \\ s_u \\ s_T \\ s_{T_{\text{vib}}} \\ s_{T_{\text{rot}}} \end{pmatrix} = \begin{pmatrix} \omega_N / \dot{m} \\ \omega_{N_2} / \dot{m} \\ \det(\mathbf{A}_1) / \det(\mathbf{A}) \\ \det(\mathbf{A}_2) / \det(\mathbf{A}) \\ \det(\mathbf{B}_1) / \det(\mathbf{B}) \\ \det(\mathbf{B}_2) / \det(\mathbf{B}) \end{pmatrix}. \quad (\text{B.12})$$

The notation \mathbf{B}_i indicates the matrix formed by replacing the i -th column of the matrix \mathbf{B} by the vector \mathbf{d} . The determinants needed to form the components s_u and s_T are computed by means of the same procedure as of sec. B.1 by replacing the matrix \mathbf{A} and the vector \mathbf{b} with the following expressions:

$$\mathbf{A} = \begin{pmatrix} 1 - \frac{k_b}{m_{N_2}} \frac{(1+y_N)T}{u^2} & \frac{k_b}{m_{N_2}} \frac{(1+y_N)}{u} \\ u & c_{pN_2}^{\text{tra}} (1+y_N) \end{pmatrix}, \quad (\text{B.13})$$

$$\mathbf{b} = -\frac{1}{\dot{m}} \left[\frac{k_b}{m_{N_2}} \frac{\omega_N T}{u} \quad \omega_N (h_N - h_{N_2}) + y_{N_2} (\delta_{\text{vib}} s_{T_{\text{vib}}} + \delta_{\text{rot}} s_{T_{\text{rot}}}) \right]^T, \quad (\text{B.14})$$

where quantities δ_{vib} and δ_{rot} are:

$$\delta_{\text{vib}} = \frac{\partial e_{N_2}^{\text{vib}}}{\partial T_{\text{vib}}} + \frac{\partial e_{N_2}^{\text{rot}}}{\partial T_{\text{vib}}}, \quad (\text{B.15})$$

$$\delta_{\text{rot}} = \frac{\partial e_{N_2}^{\text{vib}}}{\partial T_{\text{rot}}} + \frac{\partial e_{N_2}^{\text{rot}}}{\partial T_{\text{rot}}}. \quad (\text{B.16})$$

Appendix C

Eigensystems

C.1 Two-Dimensional Flows

The eigensystem of the two-dimensional equations (5.26) is made of the eigenvalue, right eigenvector and left eigenvector matrices (indicated with \mathbf{A}_n , \mathbf{R}_n and \mathbf{L}_n , respectively) of the Jacobian $\mathbf{A}_n = \mathbf{A}n_x + \mathbf{B}n_y$. The Jacobians \mathbf{A} and \mathbf{B} are defined as $\mathbf{A} = \partial\mathbf{F}/\partial\mathbf{U}$ and $\mathbf{B} = \partial\mathbf{G}/\partial\mathbf{U}$, where the expressions for the inviscid flux vectors \mathbf{F} and \mathbf{G} are given in eqs. (5.28)-(5.29).

The derivation of the eigensystem starts with the computation of the pressure derivatives:

$$\frac{\partial p}{\partial \rho_N} = \Phi_N, \quad \frac{\partial p}{\partial \tilde{\rho}_\epsilon} = \tilde{\Phi}_\epsilon, \quad \epsilon \in \mathcal{E}_{N_2}, \quad (\text{C.1})$$

$$\frac{\partial p}{\partial \rho u} = -(\gamma - 1) u, \quad \frac{\partial p}{\partial \rho v} = -(\gamma - 1) v, \quad (\text{C.2})$$

$$\frac{\partial p}{\partial \rho E} = (\gamma - 1). \quad (\text{C.3})$$

Quantities Φ_N and $\tilde{\Phi}_\epsilon$ are defined as:

$$\Phi_N = \frac{k_b}{m_N} T + (\gamma - 1) \left(e^{\text{kin}} - e_N \right), \quad (\text{C.4})$$

$$\tilde{\Phi}_\epsilon = \frac{k_b}{m_{N_2}} T + (\gamma - 1) \left(e^{\text{kin}} - \tilde{e}_\epsilon \right), \quad \epsilon \in \mathcal{E}_{N_2}, \quad (\text{C.5})$$

where the kinetic energy per unit mass is $e^{\text{kin}} = (u^2 + v^2)/2$. The frozen specific heat ratio γ is given by the ratio of the volumetric constant pressure and constant volume frozen specific heats ($\gamma = C_p/C_v$), which are defined as:

$$C_v = \rho_N c_{vN} + \sum_{\epsilon \in \mathcal{E}_{N_2}} \tilde{\rho}_\epsilon \tilde{c}_{v\epsilon}, \quad (\text{C.6})$$

$$C_p = \rho_N c_{pN} + \sum_{\epsilon \in \mathcal{E}_{N_2}} \tilde{\rho}_\epsilon \tilde{c}_{p\epsilon}. \quad (\text{C.7})$$

Using the pressure derivatives (C.1)-(C.3), it is possible to compute the Jacobian matrices $\mathbf{A} = \partial\mathbf{F}/\partial\mathbf{U}$ and $\mathbf{B} = \partial\mathbf{G}/\partial\mathbf{U}$:

$$\mathbf{A} = \begin{pmatrix} (1 - y_N)u & -y_N u & y_N & 0 & 0 \\ -\tilde{y}_\epsilon u & (\delta_{\epsilon\epsilon'} - \tilde{y}_\epsilon)u & \tilde{y}_\epsilon & 0 & 0 \\ \Phi_N - u^2 & \tilde{\Phi}_{\epsilon'} - u^2 & (3 - \gamma)u & -\bar{\gamma}v & \bar{\gamma} \\ -uv & -uv & v & u & 0 \\ (\Phi_N - H)u & (\tilde{\Phi}_{\epsilon'} - H)u & H - \bar{\gamma}u^2 & -\bar{\gamma}uv & \bar{\gamma}u \end{pmatrix}, \quad (\text{C.8})$$

$$\mathbf{B} = \begin{pmatrix} (1 - y_N)v & -y_N v & 0 & y_N & 0 \\ -\tilde{y}_\epsilon v & (\delta_{\epsilon\epsilon'} - \tilde{y}_\epsilon)v & 0 & \tilde{y}_\epsilon & 0 \\ -uv & -uv & v & u & 0 \\ \Phi_N - v^2 & \tilde{\Phi}_{\epsilon'} - v^2 & -\bar{\gamma}u & (3 - \gamma)v & \bar{\gamma} \\ (\Phi_N - H)v & (\tilde{\Phi}_{\epsilon'} - H)v & -\bar{\gamma}uv & H - \bar{\gamma}v^2 & \bar{\gamma}v \end{pmatrix}, \quad (\text{C.9})$$

$$\epsilon, \epsilon' \in \mathcal{E}_{N_2},$$

where the contracted notation $\bar{\gamma} = \gamma - 1$ has been introduced for the sake of later convenience. From eqs. (C.8)-(C.9) the Jacobian $\mathbf{A}_n = \mathbf{A}\mathbf{n}_x + \mathbf{B}\mathbf{n}_y$ can be formed:

$$\mathbf{A}_n = \begin{pmatrix} (1 - y_N)V_n & -y_N V_n & y_N n_x & y_N n_y & 0 \\ -\tilde{y}_\epsilon V_n & (\delta_{\epsilon\epsilon'} - \tilde{y}_\epsilon)V_n & \tilde{y}_\epsilon n_x & \tilde{y}_\epsilon n_y & 0 \\ \Phi_N n_x - uV_n & \tilde{\Phi}_{\epsilon'} n_x - uV_n & V_n + (2 - \gamma)un_x & un_y - \bar{\gamma}vn_x & \bar{\gamma}n_x \\ \Phi_N n_y - vV_n & \tilde{\Phi}_{\epsilon'} n_y - vV_n & vn_x - \bar{\gamma}un_y & V_n + (2 - \gamma)vn_y & \bar{\gamma}n_y \\ (\Phi_N - H)V_n & (\tilde{\Phi}_{\epsilon'} - H)V_n & Hn_x - \bar{\gamma}uV_n & Hn_y - \bar{\gamma}vV_n & \bar{\gamma}V_n \end{pmatrix},$$

$$\epsilon, \epsilon' \in \mathcal{E}_{N_2}, \quad (\text{C.10})$$

where the normal velocity is $V_n = un_x + vn_y$. To facilitate the diagonalization of \mathbf{A}_n the natural variables \mathbf{V} are introduced (Candler and MacCormack 1991):

$$\mathbf{V} = [\rho_N \quad \tilde{\rho}_\epsilon \quad u \quad v \quad p]^T, \quad \epsilon \in \mathcal{E}_{N_2}. \quad (\text{C.11})$$

The natural variables \mathbf{V} are related to the conservative variables \mathbf{U} via the transformation matrices $\mathbf{M} = \partial\mathbf{U}/\partial\mathbf{V}$ and $\mathbf{N} = \partial\mathbf{V}/\partial\mathbf{U}$. Using the chain rule, the Jacobian \mathbf{A}_n can be re-expressed as:

$$\mathbf{A}_n = \frac{\partial\mathbf{U}}{\partial\mathbf{V}} \frac{\partial\mathbf{V}}{\partial\mathbf{U}} \frac{\partial\mathbf{F}_n}{\partial\mathbf{U}} = \mathbf{M}\mathbf{A}_n^v\mathbf{N}, \quad (\text{C.12})$$

where the matrix \mathbf{A}_n^v is defined as $\mathbf{A}_n^v = \mathbf{N}\tilde{\mathbf{A}}_n$ (with $\tilde{\mathbf{A}}_n = \partial\mathbf{F}_n/\partial\mathbf{V}$). The matrices \mathbf{A}_n and \mathbf{A}_n^v have the same eigenvalues, as they are related through a similarity transformation. Moreover, the left and right eigenvector matrices of \mathbf{A}_n^v and \mathbf{A}_n satisfy the relations $\mathbf{R}_n = \mathbf{M}\mathbf{R}_n^v$ and $\mathbf{L}_n = \mathbf{L}_n^v\mathbf{N}$.

Based on eq. (C.12), one can derive the eigensystem of \mathbf{A}_n as follows. First, the transformation matrices (\mathbf{M} and \mathbf{N}) are evaluated. Then, after computing the

Jacobian $\tilde{\mathbf{A}}_n$, the matrix \mathbf{A}_n^v is formed via $\mathbf{A}_n^v = \mathbf{N}\tilde{\mathbf{A}}_n$. As it is shown below, the matrix \mathbf{A}_n^v can be easily diagonalized to obtain the related eigensystem (the matrices \mathbf{A}_n , \mathbf{R}_n^v and \mathbf{L}_n^v). Once this done, the conservative eigenvector matrices are obtained by means of $\mathbf{R}_n = \mathbf{M}\mathbf{R}_n^v$ and $\mathbf{L}_n = \mathbf{L}_n^v\mathbf{N}$.

The transformation matrices \mathbf{M} and \mathbf{N} are:

$$\mathbf{M} = \begin{pmatrix} 1 & 0 & 0 & 0 & 0 \\ 0 & \delta_{\epsilon\epsilon'} & 0 & 0 & 0 \\ u & u & \rho & 0 & 0 \\ v & v & 0 & \rho & 0 \\ \Theta_N & \tilde{\Theta}_{\epsilon'} & \rho u & \rho v & \frac{1}{\gamma} \end{pmatrix}, \quad (\text{C.13})$$

$$\mathbf{N} = \begin{pmatrix} 1 & 0 & 0 & 0 & 0 \\ 0 & \delta_{\epsilon\epsilon'} & 0 & 0 & 0 \\ -\frac{u}{\rho} & -\frac{u}{\rho} & \frac{1}{\rho} & 0 & 0 \\ -\frac{v}{\rho} & -\frac{v}{\rho} & 0 & \frac{1}{\rho} & 0 \\ \Phi_N & \tilde{\Phi}_{\epsilon'} & -\bar{\gamma}u & -\bar{\gamma}v & \bar{\gamma} \end{pmatrix}, \quad (\text{C.14})$$

$$\epsilon, \epsilon' \in \mathcal{E}_{N_2},$$

where quantities Θ_N and $\tilde{\Theta}_\epsilon$ are defined as:

$$\Theta_N = e_N + e^{\text{kin}} - \frac{k_b}{m_N} \frac{T}{\bar{\gamma}}, \quad (\text{C.15})$$

$$\tilde{\Theta}_\epsilon = \tilde{e}_\epsilon + e^{\text{kin}} - \frac{k_b}{m_{N_2}} \frac{T}{\bar{\gamma}}, \quad \epsilon \in \mathcal{E}_{N_2}. \quad (\text{C.16})$$

The Jacobian matrix $\tilde{\mathbf{A}}_n$ is defined as $\tilde{\mathbf{A}}_n = \tilde{\mathbf{A}}_{n_x} + \tilde{\mathbf{B}}_{n_y}$, where $\tilde{\mathbf{A}} = \partial \mathbf{F} / \partial \mathbf{V}$ and $\tilde{\mathbf{B}} = \partial \mathbf{G} / \partial \mathbf{V}$. The Jacobians $\tilde{\mathbf{A}}$ and $\tilde{\mathbf{B}}$ are:

$$\tilde{\mathbf{A}} = \begin{pmatrix} u & 0 & \rho_N & 0 & 0 \\ 0 & \delta_{\epsilon\epsilon'} u & \tilde{\rho}_\epsilon & 0 & 0 \\ u^2 & u^2 & 2\rho u & 0 & 1 \\ uv & uv & \rho v & \rho u & 0 \\ \Theta_N u & \tilde{\Theta}_{\epsilon'} u & \rho(H + u^2) & \rho u v & \frac{\gamma u}{\bar{\gamma}} \end{pmatrix}, \quad (\text{C.17})$$

$$\tilde{\mathbf{B}} = \begin{pmatrix} v & 0 & 0 & \rho_N & 0 \\ 0 & \delta_{\epsilon\epsilon'} v & 0 & \tilde{\rho}_\epsilon & 0 \\ uv & uv & \rho v & \rho u & 0 \\ v^2 & v^2 & 0 & 2\rho v & 1 \\ \Theta_N v & \tilde{\Theta}_{\epsilon'} v & \rho u v & \rho(H + v^2) & \frac{\gamma v}{\bar{\gamma}} \end{pmatrix}, \quad (\text{C.18})$$

$$\epsilon, \epsilon' \in \mathcal{E}_{N_2},$$

from which the matrix $\tilde{\mathbf{A}}_n = \tilde{\mathbf{A}}_{n_x} + \tilde{\mathbf{B}}_{n_y}$ readily follows:

$$\tilde{\mathbf{A}} = \begin{pmatrix} V_n & 0 & \rho_N n_x & \rho_N n_y & 0 \\ 0 & \delta_{\epsilon\epsilon'} V_n & \tilde{\rho}_\epsilon n_x & \tilde{\rho}_\epsilon n_y & 0 \\ uV_n & uV_n & \rho(un_x + V_n) & \rho un_y & n_x \\ vV_n & vV_n & \rho vn_x & \rho(vn_y + V_n) & n_y \\ \Theta_N V_n & \tilde{\Theta}_{\epsilon'} V_n & \rho(Hn_x + uV_n) & \rho(Hn_y + vV_n) & \frac{\gamma V_n}{\bar{\gamma}} \end{pmatrix}, \quad (\text{C.19})$$

$\epsilon, \epsilon' \in \mathcal{E}_{N_2}.$

The evaluation of the product $\mathbf{N}\tilde{\mathbf{A}}_n$ gives the matrix \mathbf{A}_n^v :

$$\mathbf{A}_n^v = \begin{pmatrix} V_n & 0 & \rho_N n_x & \rho_N n_y & 0 \\ 0 & \delta_{\epsilon\epsilon'} V_n & \tilde{\rho}_\epsilon n_x & \tilde{\rho}_\epsilon n_y & 0 \\ 0 & 0 & V_n & 0 & \frac{n_x}{\rho} \\ 0 & 0 & 0 & V_n & \frac{n_y}{\rho} \\ 0 & 0 & \rho c^2 n_x & \rho c^2 n_y & V_n \end{pmatrix}, \quad \epsilon, \epsilon' \in \mathcal{E}_{N_2}, \quad (\text{C.20})$$

where the frozen speed of sound is $c = \sqrt{\gamma p / \rho}$. As anticipated before, the matrix \mathbf{A}_n^v has a much simpler structure compared to that of the conservative Jacobian (C.10). A straightforward calculation shows that the eigenvalues of \mathbf{A}_n^v are the solution of the secular equation:

$$(V_n - \lambda)^{\mathcal{N}_{N_2} + 2} [(V_n - \lambda)^2 - c^2] = 0. \quad (\text{C.21})$$

The solution of the secular equation (C.21) is:

$$\lambda = \begin{cases} V_n & \mathcal{N}_{N_2} + 2 \text{ times,} \\ V_n - c, \\ V_n + c. \end{cases} \quad (\text{C.22})$$

The eigenvalues $V_n \pm c$ are the acoustic waves, while the eigenvalue V_n (with multiplicity equal to $\mathcal{N}_{N_2} + 2$, *i.e.* the number of species plus one) represent the effect of entropy and shear waves (Hirsch 1990; Leveque 2008). The eigenvalues (C.22) are stored in the eigenvalue matrix Λ_n :

$$\Lambda_n = \begin{pmatrix} V_n & 0 & 0 & 0 & 0 \\ 0 & \delta_{\epsilon\epsilon'} V_n & 0 & 0 & 0 \\ 0 & 0 & V_n - c & 0 & 0 \\ 0 & 0 & 0 & V_n & 0 \\ 0 & 0 & 0 & 0 & V_n + c \end{pmatrix}, \quad \epsilon, \epsilon' \in \mathcal{E}_{N_2}. \quad (\text{C.23})$$

The right and left eigenvector matrices associated to \mathbf{A}_n^v can be found based on their definitions:

$$\mathbf{A}_n^v \mathbf{R}_n^v = \mathbf{R}_n^v \Lambda_n, \quad \mathbf{L}_n^v \mathbf{A}_n^v = \Lambda_n \mathbf{L}_n^v. \quad (\text{C.24})$$

After some algebra one can obtain the expressions for \mathbf{R}_n^v and \mathbf{L}_n^v :

$$\mathbf{R}_n^v = \begin{pmatrix} 1 & 0 & y_N & 0 & y_N \\ 0 & \delta_{\epsilon\epsilon'} & \tilde{y}_\epsilon & 0 & \tilde{y}_\epsilon \\ 0 & 0 & -\frac{c n_x}{\rho} & t_x & \frac{c n_x}{\rho} \\ 0 & 0 & -\frac{c n_y}{\rho} & t_y & \frac{c n_y}{\rho} \\ 0 & 0 & c^2 & 0 & c^2 \end{pmatrix}, \quad (\text{C.25})$$

$$\mathbf{L}_n^v = \begin{pmatrix} 1 & 0 & 0 & 0 & -\frac{y_N}{2c^2} \\ 0 & \delta_{\epsilon\epsilon'} & 0 & 0 & -\frac{\tilde{y}_\epsilon}{2c^2} \\ 0 & 0 & -\frac{\rho n_x}{2c} & -\frac{\rho n_y}{2c} & \frac{1}{2c^2} \\ 0 & 0 & t_x & t_y & 0 \\ 0 & 0 & \frac{\rho n_x}{2c} & \frac{\rho n_y}{2c} & \frac{1}{2c^2} \end{pmatrix}, \quad (\text{C.26})$$

$$\epsilon, \epsilon' \in \mathcal{E}_{N_2}.$$

Quantities t_x and t_y represent the components along the x and y axes, respectively, of the tangential unit vector $\mathbf{t} = [t_x \ t_y]^T$ which is, by definition, orthogonal to the unit normal vector \mathbf{n} (i.e. $\mathbf{t} \cdot \mathbf{n} = 0$, $|\mathbf{t} \times \mathbf{n}| = 1$). The tangential unit vector \mathbf{t} is introduced to ensure the linear independence of the right and left eigenvectors (Gnoffo et al. 1989). The evaluation of the matrix products \mathbf{MR}_n^v and $\mathbf{L}_n^v \mathbf{N}$ gives the conservative right and left eigenvector matrices:

$$\mathbf{R}_n = \begin{pmatrix} 1 & 0 & y_N & 0 & y_N \\ 0 & \delta_{\epsilon\epsilon'} & \tilde{y}_\epsilon & 0 & \tilde{y}_\epsilon \\ u & u & u - c n_x & \rho t_x & u + c n_x \\ v & v & v - c n_y & \rho t_y & v + c n_y \\ \Theta_N & \tilde{\Theta}_{\epsilon'} & H - c V_n & \rho V_t & H + c V_n \end{pmatrix}, \quad (\text{C.27})$$

$$\mathbf{L}_n = \begin{pmatrix} 1 - \frac{y_N \Phi_N}{2c^2} & -\frac{y_N \Phi_{\epsilon'}}{2c^2} & \frac{y_N \bar{\gamma} u}{2c^2} & \frac{y_N \bar{\gamma} v}{2c^2} & -\frac{y_N \bar{\gamma}}{2c^2} \\ -\frac{\tilde{y}_\epsilon \Phi_N}{2c^2} & \delta_{\epsilon\epsilon'} - \frac{\tilde{y}_\epsilon \Phi_{\epsilon'}}{2c^2} & \frac{\tilde{y}_\epsilon \bar{\gamma} u}{2c^2} & \frac{\tilde{y}_\epsilon \bar{\gamma} v}{2c^2} & -\frac{\tilde{y}_\epsilon \bar{\gamma}}{2c^2} \\ \frac{\Phi_N + c V_n}{2c^2} & \frac{\tilde{\Phi}_{\epsilon'} + c V_n}{2c^2} & -\frac{c n_x + \bar{\gamma} u}{2c^2} & -\frac{c n_y + \bar{\gamma} v}{2c^2} & \frac{\bar{\gamma}}{2c^2} \\ -\frac{V_t}{\rho} & -\frac{V_t}{\rho} & \frac{t_x}{\rho} & \frac{t_y}{\rho} & 0 \\ \frac{\Phi_N - c V_n}{2c^2} & \frac{\tilde{\Phi}_{\epsilon'} - c V_n}{2c^2} & \frac{c n_x - \bar{\gamma} u}{2c^2} & \frac{c n_y - \bar{\gamma} v}{2c^2} & \frac{\bar{\gamma}}{2c^2} \end{pmatrix},$$

$$\epsilon, \epsilon' \in \mathcal{E}_{N_2}, \quad (\text{C.28})$$

where the tangential velocity is $V_t = u t_x + v t_y$.

C.2 One-Dimensional Flows

The eigensystem for the one-dimensional equations (5.6) can be obtained by neglecting specific terms in the two-dimensional expressions (C.23) and (C.27)-(C.28). In alternative, one may proceed by repeating the straightforward (but lengthly) algebraic procedure detailed in sec. C.1.

In the one-dimensional case, the pressure derivatives (C.1)-(C.3) reduce to:

$$\frac{\partial p}{\partial \rho_N} = \Phi_N, \quad \frac{\partial p}{\partial \tilde{\rho}_\epsilon} = \tilde{\Phi}_\epsilon, \quad \epsilon \in \mathcal{E}_{N_2}, \quad (\text{C.29})$$

$$\frac{\partial p}{\partial \rho u} = -\bar{\gamma}u, \quad (\text{C.30})$$

$$\frac{\partial p}{\partial \rho E} = \bar{\gamma}, \quad (\text{C.31})$$

and the Jacobian $\mathbf{A} = \partial \mathbf{F} / \partial \mathbf{U}$ (where \mathbf{F} is given by eq. (5.9)) is:

$$\mathbf{A} = \begin{pmatrix} (1 - y_N)u & -y_N u & y_N & 0 \\ -\tilde{y}_\epsilon u & (\delta_{\epsilon\epsilon'} - \tilde{y}_\epsilon)u & \tilde{y}_\epsilon & 0 \\ \Phi_N - u^2 & \tilde{\Phi}_{\epsilon'} - u^2 & (3 - \bar{\gamma})u & \bar{\gamma} \\ (\Phi_N - H)u & (\tilde{\Phi}_{\epsilon'} - H)u & H - \bar{\gamma}u^2 & \gamma u \end{pmatrix}, \quad \epsilon, \epsilon' \in \mathcal{E}_{N_2}. \quad (\text{C.32})$$

The expressions for quantities Φ_N and $\tilde{\Phi}_\epsilon$, Θ_N and $\tilde{\Theta}_\epsilon$ are obtained based on eqs. (C.4)-(C.5) and (C.15)-(C.16), respectively, where the kinetic energy per unit mass must be replaced with $e^{\text{kin}} = u^2/2$.

The eigensystem associated to \mathbf{A} can be obtained by neglecting the rows and the columns related to the y -direction momentum in eqs. (C.23) and (C.27)-(C.28) and by setting $n_x = 1$:

$$\mathbf{\Lambda} = \begin{pmatrix} u & 0 & 0 & 0 \\ 0 & \delta_{\epsilon\epsilon'} u & 0 & 0 \\ 0 & 0 & u - c & 0 \\ 0 & 0 & 0 & u + c \end{pmatrix}, \quad (\text{C.33})$$

$$\mathbf{R} = \begin{pmatrix} 1 & 0 & y_N & y_N \\ 0 & \delta_{\epsilon\epsilon'} & \tilde{y}_\epsilon & \tilde{y}_\epsilon \\ u & u & u - c & u + c \\ \Theta_N & \tilde{\Theta}_{\epsilon'} & H - cu & H + cu \end{pmatrix}, \quad (\text{C.34})$$

$$\mathbf{L} = \begin{pmatrix} 1 - \frac{y_N \Phi_N}{2c^2} & -\frac{y_N \tilde{\Phi}_{\epsilon'}}{2c^2} & \frac{y_N \bar{\gamma}u}{2c^2} & -\frac{y_N \bar{\gamma}}{2c^2} \\ -\frac{\tilde{y}_\epsilon \Phi_N}{2c^2} & \delta_{\epsilon\epsilon'} - \frac{\tilde{y}_\epsilon \tilde{\Phi}_{\epsilon'}}{2c^2} & \frac{\tilde{y}_\epsilon \bar{\gamma}u}{2c^2} & -\frac{\tilde{y}_\epsilon \bar{\gamma}}{2c^2} \\ \frac{\Phi_N + cu}{2c^2} & \frac{\tilde{\Phi}_{\epsilon'} + cu}{2c^2} & -\frac{c + \bar{\gamma}u}{2c^2} & \frac{\bar{\gamma}}{2c^2} \\ \frac{\Phi_N - cu}{2c^2} & \frac{\tilde{\Phi}_{\epsilon'} - cu}{2c^2} & \frac{c - \bar{\gamma}u}{2c^2} & \frac{\bar{\gamma}}{2c^2} \end{pmatrix}, \quad (\text{C.35})$$

$\epsilon, \epsilon' \in \mathcal{E}_{N_2}$.

C.3 Stagnation-line Flows

The eigensystem for the stagnation-line equations (5.14) cannot be deduced from the two-dimensional case. The reason is the modification of the pressure derivatives, due to the fact that $e^{\text{kin}} = u^2/2$. In this situation, one has:

$$\frac{\partial p}{\partial \rho_N} = \Phi_N, \quad \frac{\partial p}{\partial \tilde{\rho}_\epsilon} = \tilde{\Phi}_\epsilon, \quad \epsilon \in \mathcal{E}_{N_2}, \quad (\text{C.36})$$

$$\frac{\partial p}{\partial \rho u} = -\bar{\gamma}u, \quad \frac{\partial p}{\partial \rho v} = 0, \quad (\text{C.37})$$

$$\frac{\partial p}{\partial \rho E} = \bar{\gamma}. \quad (\text{C.38})$$

Using eqs. (C.36)-(C.38), the Jacobian $\mathbf{A} = \partial \mathbf{F} / \partial \mathbf{U}$ (where \mathbf{F} is given by eq. (5.16)) reads:

$$\mathbf{A} = \begin{pmatrix} (1 - y_N)u & -y_N u & y_N & 0 & 0 \\ -\tilde{y}_\epsilon u & (\delta_{\epsilon\epsilon'} - \tilde{y}_\epsilon)u & \tilde{y}_\epsilon & 0 & 0 \\ \Phi_N - u^2 & \tilde{\Phi}_{\epsilon'} - u^2 & (3 - \gamma)u & 0 & \bar{\gamma} \\ -uv & -uv & v & u & 0 \\ (\Phi_N - H)u & (\tilde{\Phi}_{\epsilon'} - H)u & H - \bar{\gamma}u^2 & 0 & \gamma u \end{pmatrix}, \quad (\text{C.39})$$

$\epsilon, \epsilon' \in \mathcal{E}_{N_2}.$

The use of the procedure of sec. C.1 gives the eigensystem associated to \mathbf{A} :

$$\Lambda = \begin{pmatrix} u & 0 & 0 & 0 & 0 \\ 0 & \delta_{\epsilon\epsilon'} u & 0 & 0 & 0 \\ 0 & 0 & u - c & 0 & 0 \\ 0 & 0 & 0 & u & 0 \\ 0 & 0 & 0 & 0 & u + c \end{pmatrix}, \quad (\text{C.40})$$

$$\mathbf{R} = \begin{pmatrix} 1 & 0 & y_N & 0 & y_N \\ 0 & \delta_{\epsilon\epsilon'} & \tilde{y}_\epsilon & 0 & \tilde{y}_\epsilon \\ u & u & u - c & 0 & u + c \\ v & v & v & \rho & v \\ \Theta_N & \tilde{\Theta}_{\epsilon'} & H - cu & 0 & H + cu \end{pmatrix}, \quad (\text{C.41})$$

$$\mathbf{L} = \begin{pmatrix} 1 - \frac{y_N \Phi_N}{2c^2} & -\frac{y_N \Phi_{\epsilon'}}{2c^2} & \frac{y_N \bar{\gamma}u}{2c^2} & \frac{y_N \bar{\gamma}v}{2c^2} & -\frac{y_N \bar{\gamma}}{2c^2} \\ -\frac{\tilde{y}_\epsilon \Phi_N}{2c^2} & \delta_{\epsilon\epsilon'} - \frac{\tilde{y}_\epsilon \Phi_{\epsilon'}}{2c^2} & \frac{\tilde{y}_\epsilon \bar{\gamma}u}{2c^2} & \frac{\tilde{y}_\epsilon \bar{\gamma}v}{2c^2} & -\frac{\tilde{y}_\epsilon \bar{\gamma}}{2c^2} \\ \frac{\Phi_N + cu}{2c^2} & \frac{\tilde{\Phi}_{\epsilon'} + cu}{2c^2} & -\frac{c + \bar{\gamma}u}{2c^2} & -\frac{c + \bar{\gamma}v}{2c^2} & \frac{\bar{\gamma}}{2c^2} \\ -\frac{v}{\rho} & -\frac{v}{\rho} & 0 & \frac{1}{\rho} & 0 \\ \frac{\Phi_N - cu}{2c^2} & \frac{\tilde{\Phi}_{\epsilon'} - cu}{2c^2} & \frac{c - \bar{\gamma}u}{2c^2} & 0 & \frac{\bar{\gamma}}{2c^2} \end{pmatrix}, \quad (\text{C.42})$$

$\epsilon, \epsilon' \in \mathcal{E}_{N_2},$

where, again, the expressions for quantities Φ_N and $\tilde{\Phi}_\epsilon$, Θ_N and $\tilde{\Theta}_\epsilon$ are obtained based on eqs. (C.4)-(C.5) and (C.15)-(C.16), respectively, where the kinetic energy per unit mass must be replaced with $e^{\text{kin}} = u^2/2$.

Appendix D

Positive-Negative Split Jacobians

In order to facilitate the evaluation of the positive-negative split Jacobians ($\mathbf{A}^\pm = \mathbf{R}\Lambda^\pm\mathbf{L}$), the eigenvalues (C.22) are denoted as:

$$\lambda_1 = u, \quad \lambda_2 = u - c, \quad \lambda_3 = u + c. \quad (\text{D.1})$$

Based on eq. (D.1), the positive-negative split eigenvalues can be defined:

$$\lambda_1^\pm = \frac{\lambda_1 \pm |\lambda_1|}{2}, \quad \lambda_2^\pm = \frac{\lambda_2 \pm |\lambda_2|}{2}, \quad \lambda_3^\pm = \frac{\lambda_3 \pm |\lambda_3|}{2}, \quad (\text{D.2})$$

and the following quantities are further introduced:

$$\lambda_a^\pm = \lambda_1^\pm - \frac{\lambda_2^\pm + \lambda_3^\pm}{2}, \quad \lambda_b^\pm = \frac{\lambda_3^\pm + \lambda_2^\pm}{2}, \quad \lambda_c^\pm = \frac{\lambda_3^\pm - \lambda_2^\pm}{2}. \quad (\text{D.3})$$

D.1 One-Dimensional Flows

Based on the definitions given in eqs. (D.1)-(D.2), the positive-negative split of the eigenvalue matrix for one-dimensional flows is:

$$\Lambda^\pm = \begin{pmatrix} \lambda_1^\pm & 0 & 0 & 0 \\ 0 & \delta_{\epsilon\epsilon'}\lambda_1^\pm & 0 & 0 \\ 0 & 0 & \lambda_2^\pm & 0 \\ 0 & 0 & 0 & \lambda_3^\pm \end{pmatrix}, \quad \epsilon, \epsilon' \in \mathcal{E}_{N_2}. \quad (\text{D.4})$$

By evaluating the product $\mathbf{R}\Lambda^\pm\mathbf{L}$ (where \mathbf{R} and \mathbf{L} are given by eqs. (C.34)-(C.35)) one obtains the positive-negative split Jacobians \mathbf{A}^\pm (see eq. (D.5)).

D.2 Stagnation-Line Flows

By applying the procedure used for one-dimensional flows to the stagnation-line eigensystem (C.39)-(C.42), the positive-negative split Jacobians \mathbf{A}^\pm for stagnation-line flows are obtained (see eq. (D.6)).

One-dimensional flows

$$\mathbf{A}^\pm = \left(\begin{array}{l} \lambda_1^\pm - \frac{y_N}{c} \left(\frac{\lambda_a^\pm \Phi_N}{c} + \lambda_c^\pm u \right) \\ - \frac{y_N}{c} \left(\frac{\lambda_a^\pm \tilde{\Phi}_{\epsilon'} e'}{c} + \lambda_c^\pm u \right) \\ - \frac{\tilde{y}_e}{c} \left(\frac{\lambda_a^\pm \Phi_N}{c} + \lambda_c^\pm u \right) \\ \lambda_a^\pm u \left(\frac{\Phi_N}{c^2} - 1 \right) + \lambda_c^\pm \left(\frac{\Phi_N - u^2}{c} \right) \\ u \lambda_1^\pm + \lambda_a^\pm \left(\frac{H \Phi_N}{c^2} - u^2 \right) + \lambda_c^\pm \frac{u}{c} (\Phi_N - H) \end{array} \right) \left(\begin{array}{l} \frac{y_N}{c} \left(\frac{\lambda_a^\pm \tilde{\gamma} u}{c} + \lambda_c^\pm \right) \\ \frac{\tilde{y}_e}{c} \left(\frac{\lambda_a^\pm \tilde{\gamma} u}{c} + \lambda_c^\pm \right) \\ \lambda_b^\pm + \frac{u}{c} \left(\frac{\lambda_a^\pm \tilde{\gamma} u}{c} - \lambda_c^\pm \gamma \right) \\ \lambda_a^\pm u \left(\frac{H \tilde{\gamma}}{c^2} - 1 \right) + \lambda_c^\pm \frac{(H - \tilde{\gamma} u^2)}{c} \\ u \lambda_1^\pm + \lambda_a^\pm \left(\frac{H \Phi_N}{c^2} - u^2 \right) + \lambda_c^\pm \frac{u}{c} (\tilde{\Phi}_{\epsilon'} - H) \end{array} \right), \quad (D.5)$$

$\epsilon, \epsilon' \in \mathcal{E}_{N_2}$.

Stagnation-line flows

$$\mathbf{A}^\pm = \left(\begin{array}{l} \lambda_1^\pm - \frac{y_N}{c} \left(\frac{\lambda_a^\pm \Phi_N}{c} + \lambda_c^\pm u \right) \\ - \frac{y_N}{c} \left(\frac{\lambda_a^\pm \tilde{\Phi}_{\epsilon'} e'}{c} + \lambda_c^\pm u \right) \\ - \frac{\tilde{y}_e}{c} \left(\frac{\lambda_a^\pm \Phi_N}{c} + \lambda_c^\pm u \right) \\ \lambda_a^\pm u \left(\frac{\Phi_N}{c^2} - 1 \right) + \lambda_c^\pm \left(\frac{\Phi_N - u^2}{c} \right) \\ \lambda_a^\pm \frac{\Phi_N v}{c^2} - \lambda_c^\pm \frac{wv}{c} \\ u \lambda_1^\pm + \lambda_a^\pm \left(\frac{H \Phi_N}{c^2} - u^2 \right) + \lambda_c^\pm \frac{u}{c} (\Phi_N - H) \end{array} \right) \left(\begin{array}{l} \frac{y_N}{c} \left(\frac{\lambda_a^\pm \tilde{\gamma} u}{c} + \lambda_c^\pm \right) \\ \frac{\tilde{y}_e}{c} \left(\frac{\lambda_a^\pm \tilde{\gamma} u}{c} + \lambda_c^\pm \right) \\ \lambda_b^\pm + \frac{u}{c} \left(\frac{\lambda_a^\pm \tilde{\gamma} u}{c} - \lambda_c^\pm \gamma \right) \\ \lambda_a^\pm \frac{\tilde{\gamma} av}{c^2} + \lambda_c^\pm \frac{v}{c} \\ \lambda_a^\pm u \left(\frac{H \tilde{\gamma}}{c^2} - 1 \right) + \lambda_c^\pm \frac{(H - \tilde{\gamma} u^2)}{c} \\ \lambda_1^\pm + \frac{\tilde{\gamma}}{c} \left(\frac{\lambda_a^\pm H}{c} + \lambda_c^\pm u \right) \end{array} \right), \quad (D.6)$$

$\epsilon, \epsilon' \in \mathcal{E}_{N_2}$.

Appendix E

Source Term Jacobians

E.1 Kinetic Process Source Term

E.1.1 Two-Dimensional Flows

For the two-dimensional equations (5.26), the Jacobian of the kinetic process source term (5.32) can be formally written as:

$$\frac{\partial \mathbf{S}^k}{\partial \mathbf{U}} = \begin{pmatrix} \frac{\partial \omega_N}{\partial \rho_N} & \frac{\partial \omega_N}{\partial \tilde{\rho}_{\epsilon'}} & \frac{\partial \omega_N}{\partial \rho u} & \frac{\partial \omega_N}{\partial \rho v} & \frac{\partial \omega_N}{\partial \rho E} \\ \frac{\partial \tilde{\omega}_\epsilon}{\partial \rho_N} & \frac{\partial \tilde{\omega}_\epsilon}{\partial \tilde{\rho}_{\epsilon'}} & \frac{\partial \tilde{\omega}_\epsilon}{\partial \rho u} & \frac{\partial \tilde{\omega}_\epsilon}{\partial \rho v} & \frac{\partial \tilde{\omega}_\epsilon}{\partial \rho E} \\ 0 & 0 & 0 & 0 & 0 \\ 0 & 0 & 0 & 0 & 0 \\ 0 & 0 & 0 & 0 & 0 \end{pmatrix}, \quad \epsilon, \epsilon' \in \mathcal{E}_{N_2}. \quad (\text{E.1})$$

As shown in eqs. (3.100)-(3.102), the mass production terms ω_N and $\tilde{\omega}_\epsilon$ are naturally expressed in terms of primitive variables:

$$\mathbf{P} = [\rho_N \quad \tilde{\rho}_\epsilon \quad u \quad v \quad T]^T, \quad \epsilon \in \mathcal{E}_{N_2}. \quad (\text{E.2})$$

To facilitate the evaluation of the Jacobian $\partial \mathbf{S}^k / \partial \mathbf{U}$, the chain rule for matrix Jacobians is exploited:

$$\frac{\partial \mathbf{S}^k}{\partial \mathbf{U}} = \frac{\partial \mathbf{S}^k}{\partial \mathbf{P}} \frac{\partial \mathbf{P}}{\partial \mathbf{U}}. \quad (\text{E.3})$$

The transformation matrix $\partial \mathbf{P} / \partial \mathbf{U}$ is:

$$\frac{\partial \mathbf{P}}{\partial \mathbf{U}} = \begin{pmatrix} 1 & 0 & 0 & 0 & 0 \\ 0 & \delta_{\epsilon\epsilon'} & 0 & 0 & 0 \\ -\frac{u}{\rho} & -\frac{u}{\rho} & \frac{1}{\rho} & 0 & 0 \\ -\frac{v}{\rho} & -\frac{v}{\rho} & 0 & \frac{1}{\rho} & 0 \\ \Upsilon_N & \tilde{\Upsilon}_{\epsilon'} & -\frac{u}{C_v} & -\frac{v}{C_v} & \frac{1}{C_v} \end{pmatrix}, \quad \epsilon, \epsilon' \in \mathcal{E}_{N_2}, \quad (\text{E.4})$$

where quantities Υ_N and $\tilde{\Upsilon}_\epsilon$ are defined as:

$$\Upsilon_N = \frac{e^{\text{kin}} - e_N}{C_v}, \quad \tilde{\Upsilon}_\epsilon = \frac{e^{\text{kin}} - \tilde{e}_\epsilon}{C_v}, \quad \epsilon \in \mathcal{E}_{N_2}. \quad (\text{E.5})$$

Substituting eq. (E.4) in eq. (E.3), it is possible to express the kinetic process source term Jacobian $\partial \mathbf{S}^k / \partial \mathbf{U}$ as:

$$\begin{aligned} \frac{\partial \mathbf{S}^k}{\partial \mathbf{U}} = & \begin{pmatrix} \frac{\partial \omega_N}{\partial \rho_N} + \frac{\partial \omega_N}{\partial T} \Upsilon_N & \frac{\partial \omega_N}{\partial \tilde{\rho}_{\epsilon'}} + \frac{\partial \omega_N}{\partial T} \tilde{\Upsilon}_{\epsilon'} & -\frac{\partial \omega_N}{\partial T} \frac{u}{C_v} & -\frac{\partial \omega_N}{\partial T} \frac{v}{C_v} & \frac{\partial \omega_N}{\partial T} \frac{1}{C_v} \\ \frac{\partial \tilde{\omega}_\epsilon}{\partial \rho_N} + \frac{\partial \tilde{\omega}_\epsilon}{\partial T} \Upsilon_N & \frac{\partial \tilde{\omega}_\epsilon}{\partial \tilde{\rho}_{\epsilon'}} + \frac{\partial \tilde{\omega}_\epsilon}{\partial T} \tilde{\Upsilon}_{\epsilon'} & -\frac{\partial \tilde{\omega}_\epsilon}{\partial T} \frac{u}{C_v} & -\frac{\partial \tilde{\omega}_\epsilon}{\partial T} \frac{v}{C_v} & \frac{\partial \tilde{\omega}_\epsilon}{\partial T} \frac{1}{C_v} \\ 0 & 0 & 0 & 0 & 0 \\ 0 & 0 & 0 & 0 & 0 \\ 0 & 0 & 0 & 0 & 0 \end{pmatrix}, \\ & \epsilon, \epsilon' \in \mathcal{E}_{N_2}. \end{aligned} \quad (\text{E.6})$$

In obtaining eq. (E.6), the fact that the mass production terms ω_N and $\tilde{\omega}_\epsilon$ do not depend on the velocity components u and v has been used. The derivatives of the mass production terms ω_N and $\tilde{\omega}_\epsilon$ with respect to the species densities and temperature can be obtained by means of a term-by-term differentiation of eqs. (3.100)-(3.102). Notice that the derivatives with respect to the species densities in eq. (E.6) are formally different from those appearing in eq. (E.1). This is due to the use of two different sets of variables (conservative and primitive) for the Jacobian evaluation. To give an example, the derivative $\partial \omega_N / \partial \rho_N$ in eqs. (E.1) and (E.6) should be interpreted as:

$$\frac{\partial \omega_N}{\partial \rho_N} = \begin{cases} \left. \frac{\partial \omega_N}{\partial \rho_N} \right|_{\tilde{\rho}_\epsilon, \rho u, \rho v, \rho E = \text{const.}} & \text{in eq. (E.1),} \\ \left. \frac{\partial \omega_N}{\partial \rho_N} \right|_{\tilde{\rho}_\epsilon, u, v, T = \text{const.}} & \text{in eq. (E.6),} \end{cases} \quad (\text{E.7})$$

$$\epsilon \in \mathcal{E}_{N_2}.$$

Similar considerations apply to the other derivatives.

E.1.2 One-Dimensional Flows

For the one-dimensional equations (5.6), the Jacobian of the kinetic process source term (5.11) can be obtained based on eq. (E.6) by neglecting the rows

and the columns relative to the y -direction momentum:

$$\frac{\partial \mathbf{S}^k}{\partial \mathbf{U}} = \begin{pmatrix} \frac{\partial \omega_N}{\partial \rho_N} + \frac{\partial \omega_N}{\partial T} \Upsilon_N & \frac{\partial \omega_N}{\partial \tilde{\rho}_{\epsilon'}} + \frac{\partial \omega_N}{\partial T} \tilde{\Upsilon}_{\epsilon'} & -\frac{\partial \omega_N}{\partial T} \frac{u}{C_v} & \frac{\partial \omega_N}{\partial T} \frac{1}{C_v} \\ \frac{\partial \tilde{\omega}_{\epsilon}}{\partial \rho_N} + \frac{\partial \tilde{\omega}_{\epsilon}}{\partial T} \Upsilon_N & \frac{\partial \tilde{\omega}_{\epsilon}}{\partial \tilde{\rho}_{\epsilon'}} + \frac{\partial \tilde{\omega}_{\epsilon}}{\partial T} \tilde{\Upsilon}_{\epsilon'} & -\frac{\partial \tilde{\omega}_{\epsilon}}{\partial T} \frac{u}{C_v} & \frac{\partial \tilde{\omega}_{\epsilon}}{\partial T} \frac{1}{C_v} \\ 0 & 0 & 0 & 0 \\ 0 & 0 & 0 & 0 \\ 0 & 0 & 0 & 0 \end{pmatrix}, \quad \epsilon, \epsilon' \in \mathcal{E}_{N_2}. \quad (\text{E.8})$$

Quantities $\tilde{\Upsilon}_N$ and Υ_{ϵ} are computed based on eq. (E.5), where the kinetic energy must be replaced with $e^{\text{kin}} = u^2/2$.

E.1.3 Stagnation-Line Flows

For the stagnation-line equations (5.6), the Jacobian of the kinetic process source term (5.21) cannot be deduced from the two-dimensional case. As it was for the eigensystem (see sec. C.3), this is again due to the fact that only the velocity component u contributes to the kinetic energy. When this is taken into account, the transformation matrix $\partial \mathbf{P} / \partial \mathbf{U}$ in eq. (E.4) modifies according to:

$$\frac{\partial \mathbf{P}}{\partial \mathbf{U}} = \begin{pmatrix} 1 & 0 & 0 & 0 & 0 \\ 0 & \delta_{\epsilon\epsilon'} & 0 & 0 & 0 \\ -\frac{u}{\rho} & -\frac{u}{\rho} & \frac{1}{\rho} & 0 & 0 \\ -\frac{v}{\rho} & -\frac{v}{\rho} & 0 & \frac{1}{\rho} & 0 \\ \Upsilon_N & \tilde{\Upsilon}_{\epsilon'} & -\frac{u}{C_v} & 0 & \frac{1}{C_v} \end{pmatrix}, \quad \epsilon, \epsilon' \in \mathcal{E}_{N_2}. \quad (\text{E.9})$$

The application of the chain rule (E.3) leads to:

$$\frac{\partial \mathbf{S}^k}{\partial \mathbf{U}} = \begin{pmatrix} \frac{\partial \omega_N}{\partial \rho_N} + \frac{\partial \omega_N}{\partial T} \Upsilon_N & \frac{\partial \omega_N}{\partial \tilde{\rho}_{\epsilon'}} + \frac{\partial \omega_N}{\partial T} \tilde{\Upsilon}_{\epsilon'} & -\frac{\partial \omega_N}{\partial T} \frac{u}{C_v} & 0 & \frac{\partial \omega_N}{\partial T} \frac{1}{C_v} \\ \frac{\partial \tilde{\omega}_{\epsilon}}{\partial \rho_N} + \frac{\partial \tilde{\omega}_{\epsilon}}{\partial T} \Upsilon_N & \frac{\partial \tilde{\omega}_{\epsilon}}{\partial \tilde{\rho}_{\epsilon'}} + \frac{\partial \tilde{\omega}_{\epsilon}}{\partial T} \tilde{\Upsilon}_{\epsilon'} & -\frac{\partial \tilde{\omega}_{\epsilon}}{\partial T} \frac{u}{C_v} & 0 & \frac{\partial \tilde{\omega}_{\epsilon}}{\partial T} \frac{1}{C_v} \\ 0 & 0 & 0 & 0 & 0 \\ 0 & 0 & 0 & 0 & 0 \\ 0 & 0 & 0 & 0 & 0 \end{pmatrix}, \quad \epsilon, \epsilon' \in \mathcal{E}_{N_2}. \quad (\text{E.10})$$

Quantities $\tilde{\Upsilon}_N$ and Υ_{ϵ} are always computed based on eq. (E.5), where the kinetic energy must be replaced with $e^{\text{kin}} = u^2/2$.

E.2 Convective Source Term

E.2.1 Two-Dimensional Flows

For the two-dimensional equations (5.26), the Jacobian of the convective source term (5.31) is:

$$\frac{\partial \mathbf{S}^c}{\partial \mathbf{U}} = \begin{pmatrix} 0 & \tilde{0}_{\epsilon'} & 0 & 0 & 0 \\ \tilde{0}_\epsilon & \tilde{0}_{\epsilon\epsilon'} & 0 & 0 & 0 \\ 0 & 0 & 0 & 0 & 0 \\ \Phi_N & \tilde{\Phi}_\epsilon & -\bar{\gamma}u & -\bar{\gamma}v & -\bar{\gamma} \\ 0 & 0 & 0 & 0 & 0 \end{pmatrix}, \quad \epsilon, \epsilon' \in \mathcal{E}_{N_2}. \quad (\text{E.11})$$

E.2.2 One-Dimensional Flows

For the one-dimensional equations (5.6), the Jacobian of the convective source term (5.10) is:

$$\frac{\partial \mathbf{S}^c}{\partial \mathbf{U}} = -\frac{\partial \ln A}{\partial x} \begin{pmatrix} (1-y_N)u & -y_N u & y_N & 0 \\ -\tilde{y}_\epsilon u & (\delta_{\epsilon\epsilon'} - \tilde{y}_\epsilon)u & \tilde{y}_\epsilon & 0 \\ -u^2 & -u^2 & 2u & 0 \\ (\Phi_N - H)u & (\tilde{\Phi}_{\epsilon'} - H)u & H - \bar{\gamma}u^2 & \gamma u \end{pmatrix}, \quad (\text{E.12})$$

$$\epsilon, \epsilon' \in \mathcal{E}_{N_2}.$$

E.2.3 Stagnation-Line Flows

For the stagnation-line equations (5.14), the Jacobian of the convective source term (5.19) is:

$$\frac{\partial \mathbf{S}^c}{\partial \mathbf{U}} = -\frac{1}{r} \times$$

$$\begin{pmatrix} 2(1-y_N)\bar{u}\bar{v} & -2y_N\bar{u}\bar{v} & 2y_N & 2y_N & 0 \\ -2\tilde{y}_\epsilon\bar{u}\bar{v} & 2(\delta_{\epsilon\epsilon'} - \tilde{y}_\epsilon)\bar{u}\bar{v} & 2\tilde{y}_\epsilon & 2\tilde{y}_\epsilon & 0 \\ -2u\bar{u}\bar{v} & -2u\bar{u}\bar{v} & 2(\bar{u}\bar{v} + u) & 2u & 0 \\ -3v\bar{u}\bar{v} - 2\Phi_N & -3v\bar{u}\bar{v} - 2\tilde{\Phi}_{\epsilon'} & 3v + 2\bar{\gamma}u & 3(\bar{u}\bar{v} + v) & -2\bar{\gamma} \\ 2(\Phi_N - H)\bar{u}\bar{v} & 2(\tilde{\Phi}_{\epsilon'} - H)\bar{u}\bar{v} & 2(H - \bar{\gamma}u)\bar{u}\bar{v} & 2H & 2\gamma\bar{u}\bar{v} \end{pmatrix},$$

$$\epsilon, \epsilon' \in \mathcal{E}_{N_2}, \quad (\text{E.13})$$

where the contracted notation $\bar{u}\bar{v} = u + v$ has been introduced.

Appendix F

Diffusive Jacobians for Stagnation-Line Flows

When solving the stagnation-line equations (5.14) by means of the fully implicit method, the linearization of the diffusive flux (5.17) and source term (5.20) is performed by using the model proposed by Ramshaw and Chang (1996) for the diffusion velocities. According to this model, the diffusion velocities are computed based on self-consistent effective diffusion coefficients as:

$$u_N^d = D_{NN}^{\text{sc}} \frac{\partial X_N}{\partial r} + \sum_{\epsilon \in \mathcal{E}_{N_2}} \tilde{D}_{N\epsilon}^{\text{sc}} \frac{\partial \tilde{X}_\epsilon}{\partial r}, \quad (\text{F.1})$$

$$\tilde{u}_\epsilon^d = \tilde{D}_{\epsilon N}^{\text{sc}} \frac{\partial X_N}{\partial r} + \sum_{\epsilon' \in \mathcal{E}_{N_2}} \tilde{D}_{\epsilon\epsilon'}^{\text{sc}} \frac{\partial \tilde{X}_{\epsilon'}}{\partial r}, \quad \epsilon \in \mathcal{E}_{N_2}. \quad (\text{F.2})$$

The self-consistent (sc) effective diffusion coefficients are defined as:

$$D_{NN}^{\text{sc}} = (1 - y_N) \frac{ < D_N > }{X_N}, \quad (\text{F.3})$$

$$\tilde{D}_{N\epsilon}^{\text{sc}} = -\tilde{y}_\epsilon \frac{ < \tilde{D}_\epsilon > }{\tilde{X}_\epsilon}, \quad \epsilon \in \mathcal{E}_{N_2}, \quad (\text{F.4})$$

$$\tilde{D}_{\epsilon N}^{\text{sc}} = -y_N \frac{ < D_N > }{X_N}, \quad \epsilon \in \mathcal{E}_{N_2}, \quad (\text{F.5})$$

$$\tilde{D}_{\epsilon\epsilon'}^{\text{sc}} = \delta_{\epsilon\epsilon'} \frac{ < \tilde{D}_\epsilon > }{X_\epsilon} - \tilde{y}_{\epsilon'} \frac{ < \tilde{D}_{\epsilon'} > }{\tilde{X}_\epsilon}, \quad \epsilon, \epsilon' \in \mathcal{E}_{N_2}, \quad (\text{F.6})$$

where the average diffusion coefficients are given by the following expressions:

$$< D_N > = \frac{1 - y_N}{X_{N_2}/\mathcal{D}_{NN_2}}, \quad (\text{F.7})$$

$$< \tilde{D}_\epsilon > = \frac{1 - \tilde{y}_\epsilon}{(X_{N_2} - \tilde{X}_\epsilon)/\mathcal{D}_{N_2 N_2} + X_N/\mathcal{D}_{NN_2}}, \quad \epsilon \in \mathcal{E}_{N_2}. \quad (\text{F.8})$$

Since the solution update is performed on conservative variables, the mole fraction gradients in eqs. (F.1)-(F.2) must be expressed in terms of the partial densities. After some algebra, the mass diffusion fluxes read:

$$\rho_N u_N^d = -a_{NN}^d \frac{\partial \rho_N}{\partial r} - \sum_{\epsilon \in \mathcal{E}_{N_2}} \tilde{a}_{N\epsilon}^d \frac{\partial \tilde{\rho}_\epsilon}{\partial r}, \quad (\text{F.9})$$

$$\tilde{\rho}_\epsilon \tilde{u}_\epsilon^d = -\tilde{a}_{\epsilon N}^d \frac{\partial \rho_N}{\partial r} - \sum_{\epsilon' \in \mathcal{E}_{N_2}} \tilde{a}_{\epsilon\epsilon'}^d \frac{\partial \tilde{\rho}_{\epsilon'}}{\partial r}, \quad \epsilon \in \mathcal{E}_{N_2}, \quad (\text{F.10})$$

where:

$$a_{NN}^d = X_N \left[(1 - X_N) D_{NN}^{sc} - \sum_{\epsilon \in \mathcal{E}_{N_2}} \tilde{D}_{N\epsilon}^{sc} \tilde{X}_\epsilon \right], \quad (\text{F.11})$$

$$\tilde{a}_{N\epsilon}^d = y_N \frac{X_{N_2}}{y_{N_2}} \left[\sum_{\epsilon' \in \mathcal{E}_{N_2}} \left(\delta_{\epsilon\epsilon'} - \tilde{X}_{\epsilon'} \right) \tilde{D}_{N\epsilon'}^{sc} - X_N \tilde{D}_{NN}^{sc} \right], \quad \epsilon \in \mathcal{E}_{N_2}, \quad (\text{F.12})$$

$$\tilde{a}_{\epsilon N}^d = \tilde{y}_\epsilon \frac{X_N}{y_N} \left[(1 - X_N) \tilde{D}_{\epsilon N}^{sc} - \sum_{\epsilon' \in \mathcal{E}_{N_2}} \tilde{D}_{\epsilon\epsilon'}^{sc} \tilde{X}_{\epsilon'} \right], \quad \epsilon \in \mathcal{E}_{N_2}, \quad (\text{F.13})$$

$$\tilde{a}_{\epsilon\epsilon'}^d = \tilde{y}_\epsilon \frac{X_{N_2}}{y_{N_2}} \left[\sum_{\epsilon'' \in \mathcal{E}_{N_2}} \tilde{D}_{\epsilon\epsilon''}^{sc} \left(\delta_{\epsilon'\epsilon''} - \tilde{X}_{\epsilon''} \right) - X_N \tilde{D}_{\epsilon N}^{sc} \right], \quad \epsilon, \epsilon' \in \mathcal{E}_{N_2}. \quad (\text{F.14})$$

Based on the results of app. E, the velocity and temperature gradients can be expressed in terms of those conservative of variables:

$$\frac{\partial u}{\partial r} = -\frac{u}{\rho} \frac{\partial \rho_N}{\partial r} - \frac{u}{\rho} \sum_{\epsilon \in \mathcal{E}_{N_2}} \frac{\partial \tilde{\rho}_\epsilon}{\partial r} + \frac{1}{\rho} \frac{\partial \rho u}{\partial r}, \quad (\text{F.15})$$

$$\frac{\partial v}{\partial r} = -\frac{v}{\rho} \frac{\partial \rho_N}{\partial r} - \frac{v}{\rho} \sum_{\epsilon \in \mathcal{E}_{N_2}} \frac{\partial \tilde{\rho}_\epsilon}{\partial r} + \frac{1}{\rho} \frac{\partial \rho v}{\partial r}, \quad (\text{F.16})$$

$$\frac{\partial T}{\partial r} = \Upsilon_N \frac{\partial \rho_N}{\partial r} + \sum_{\epsilon \in \mathcal{E}_{N_2}} \tilde{\Upsilon}_\epsilon \frac{\partial \tilde{\rho}_\epsilon}{\partial r} - \frac{u}{C_v} \frac{\partial \rho u}{\partial r} + \frac{1}{C_v} \frac{\partial \rho E}{\partial r}. \quad (\text{F.17})$$

The substitution of eqs. (F.9)-(F.17) in eqs. (5.17) and (5.20), allows to write the diffusive flux and source term as in eqs. (5.46)-(5.47):

$$\mathbf{F}^d = \mathbf{A}^d \left(\frac{\partial \mathbf{U}}{\partial r} \right) + \mathbf{B}^d, \quad (\text{F.18})$$

$$\mathbf{S}^d = \mathbf{A}_s^d \left(\frac{\partial \mathbf{U}}{\partial r} \right) + \mathbf{B}_s^d. \quad (\text{F.19})$$

The expressions for the matrices \mathbf{A}^d and \mathbf{A}_s^d , and the vectors \mathbf{B}^d and \mathbf{B}_s^d are given in secs. F.1-F.2.

F.1 Diffusive Flux

After some algebra, the matrix \mathbf{A}^d and vector \mathbf{B}^d are found to be:

$$\mathbf{A}^d = \begin{pmatrix} a_{NN}^d & \tilde{a}_{\epsilon N}^d & 0 & 0 & 0 \\ \tilde{a}_{\epsilon N}^d & \tilde{a}_{\epsilon \epsilon'}^d & 0 & 0 & 0 \\ -\frac{4}{3}\frac{\eta}{\rho}u & -\frac{4}{3}\frac{\eta}{\rho}u & \frac{4}{3}\frac{\eta}{\rho} & 0 & 0 \\ -\frac{\eta}{\rho}v & -\frac{\eta}{\rho}v & 0 & \frac{\eta}{\rho} & 0 \\ b_N^d - \frac{4}{3}\frac{\eta}{\rho}u^2 & \tilde{b}_{\epsilon'}^d - \frac{4}{3}\frac{\eta}{\rho}u^2 & b^d & 0 & \frac{\lambda}{C_v} \end{pmatrix}, \quad (\text{F.20})$$

$\epsilon, \epsilon' \in \mathcal{E}_{N_2}.$

$$\mathbf{B}^d = -\frac{\eta}{r} \begin{bmatrix} 0 & \tilde{0}_\epsilon & \frac{4}{3}\bar{uv} & \bar{uv} & \frac{4}{3}u\bar{uv} \end{bmatrix}^T, \quad (\text{F.21})$$

$\epsilon \in \mathcal{E}_{N_2},$

where, as in app. E, $\bar{uv} = u + v$. Quantities b_N^d , $\tilde{b}_{\epsilon'}^d$ and b^d are defined as:

$$b_N^d = \lambda \Upsilon_N + a_{NN}^d h_N + \sum_{\epsilon \in \mathcal{E}_{N_2}} \tilde{a}_{\epsilon N}^d \tilde{h}_\epsilon, \quad (\text{F.22})$$

$$\tilde{b}_{\epsilon'}^d = \lambda \tilde{\Upsilon}_\epsilon + \tilde{a}_{N\epsilon}^d h_N + \sum_{\epsilon' \in \mathcal{E}_{N_2}} \tilde{a}_{\epsilon'\epsilon}^d \tilde{h}_{\epsilon'}, \quad \epsilon \in \mathcal{E}_{N_2}, \quad (\text{F.23})$$

$$b^d = \left(\frac{4}{3}\frac{\eta}{\rho} - \frac{\lambda}{C_v} \right) u. \quad (\text{F.24})$$

The Jacobian of the vector \mathbf{B}^d is:

$$\frac{\partial \mathbf{B}^d}{\partial \mathbf{U}} = \frac{1}{r\rho} \begin{pmatrix} 0 & \tilde{0}_{\epsilon'} & 0 & 0 & 0 \\ \tilde{0}_\epsilon & \tilde{0}_{\epsilon\epsilon'} & 0 & 0 & 0 \\ \frac{4}{3}\bar{uv} & \frac{4}{3}\bar{uv} & -\frac{4}{3} & -\frac{4}{3} & 0 \\ \bar{uv} & \bar{uv} & -1 & -1 & 0 \\ \frac{8}{3}u\bar{uv} & \frac{8}{3}u\bar{uv} & -\frac{4}{3}(u + \bar{uv}) & -\frac{4}{3}u & 0 \end{pmatrix}, \quad \epsilon, \epsilon' \in \mathcal{E}_{N_2}. \quad (\text{F.25})$$

The eigenvalues of the matrix determined by considering only the rows and columns corresponding to the momentum and global energy equations in the matrix \mathbf{A}^d are:

$$\lambda_1 = \frac{4}{3}\frac{\eta}{\rho}, \quad \lambda_2 = \frac{\eta}{\rho}, \quad \lambda_3 = \frac{\lambda}{C_v}. \quad (\text{F.26})$$

Quantity $\max[(4/3)(\eta/\rho), \lambda/C_v]$ can be used for estimating the spectral radius of the matrix \mathbf{A}^d (Blazek 2006) and it is used in eq. (5.42) for the evaluation of the local time-step in viscous flow calculations.

F.2 Diffusive Source Term

After some algebra, the matrix \mathbf{A}_s^d and vector \mathbf{B}_s^d are found to be:

$$\mathbf{A}_s^d = \frac{1}{r} \begin{pmatrix} 2a_{NN}^d & 2\tilde{a}_{N\epsilon'}^d & 0 & 0 & 0 \\ 2\tilde{a}_{\epsilon N}^d & 2\tilde{a}_{\epsilon\epsilon'}^d & 0 & 0 & 0 \\ -2\frac{\eta}{\rho}(\bar{uv} + u) & -2\frac{\eta}{\rho}(\bar{uv} + u) & 4\frac{\eta}{\rho} & 2\frac{\eta}{\rho} & 0 \\ -\frac{1}{3}\frac{\eta}{\rho}(\bar{uv} + 7v) & -\frac{1}{3}\frac{\eta}{\rho}(\bar{uv} + 7v) & \frac{2}{3}\frac{\eta}{\rho} & \frac{3}{3}\frac{\eta}{\rho} & 0 \\ 2c_N^d & 2\tilde{c}_{\epsilon'}^d & c^d & 0 & 2\frac{\lambda}{C_v} \end{pmatrix}, \quad (\text{F.27})$$

$\epsilon, \epsilon' \in \mathcal{E}_{N_2}.$

$$\mathbf{B}_s^d = \frac{\eta}{r^2} \begin{bmatrix} 0 & \tilde{0}_\epsilon & -6\bar{uv} & -\frac{11}{3}\bar{uv} & -\frac{2}{3}\bar{uv}^* \end{bmatrix}^T, \quad (\text{F.28})$$

$\epsilon \in \mathcal{E}_{N_2},$

where $\bar{uv}^* = 7u^2 + 5uv - 2v^2$. Quantities c_N^d , \tilde{c}_ϵ^d and c^d are defined as:

$$c_N^d = b_N^d - \frac{1}{3}\frac{\eta}{\rho}u(\bar{uv} + 3u) \quad (\text{F.29})$$

$$\tilde{c}_\epsilon^d = \tilde{b}_\epsilon^d - \frac{1}{3}\frac{\eta}{\rho}u(\bar{uv} + 3u), \quad \epsilon \in \mathcal{E}_{N_2}, \quad (\text{F.30})$$

$$c^d = \frac{4}{3}\frac{\eta}{\rho}(2u - v) - \frac{\lambda}{C_v}u. \quad (\text{F.31})$$

The Jacobian of the vector \mathbf{B}_s^d is:

$$\frac{\partial \mathbf{B}_s^d}{\partial \mathbf{U}} = \frac{1}{r^2} \frac{\eta}{\rho} \begin{pmatrix} 0 & \tilde{0}_{\epsilon'} & 0 & 0 & 0 \\ \tilde{0}_\epsilon & \tilde{0}_{\epsilon\epsilon'} & 0 & 0 & 0 \\ 6\bar{uv} & 6\bar{uv} & -6 & -6 & 0 \\ \frac{11}{3}\bar{uv} & \frac{11}{3}\bar{uv} & -\frac{11}{3} & -\frac{11}{3} & 0 \\ \frac{4}{3}\bar{uv}^* & \frac{4}{3}\bar{uv}^* & \frac{2}{3}(15u - 5v) & \frac{2}{3}(4v - 5u) & 0 \end{pmatrix}, \quad (\text{F.32})$$

$\epsilon, \epsilon' \in \mathcal{E}_{N_2}.$

Appendix G

Fourier Transform of the Partial Collision Operators

G.1 Partial Elastic Collision Operator

According to the weak form (6.5), the Fourier transform of the partial elastic collision operator for the collision $s_i + p_j = s_i + p_j$ is:

$$\hat{Q}_{s_ip_j}(\zeta) = \frac{1}{(2\pi)^{3/2}} \iint_{\mathcal{S}^2 \times \mathbb{R}^3 \times \mathbb{R}^3} [\exp(-\imath \mathbf{c}'_{s_i} \cdot \zeta) - \exp(-\imath \mathbf{c}_{s_i} \cdot \zeta)] f_{s_i} f_{p_j} \sigma_{s_ip_j} \times g d\omega' d\mathbf{c}_{p_j} d\mathbf{c}_{s_i}, \quad s, p \in \mathcal{S}, \quad i \in \mathcal{I}_s, \quad j \in \mathcal{I}_p. \quad (\text{G.1})$$

The post-collisional velocity \mathbf{c}'_{s_i} can be expressed as:

$$\mathbf{c}'_{s_i} = \mathbf{c}_{s_i} + \frac{\mu_{sp}}{m_s} (\mathbf{g}' - \mathbf{g}), \quad s, p \in \mathcal{S}, \quad i \in \mathcal{I}_s. \quad (\text{G.2})$$

The use of eq. (G.2) allows to write the difference between the exponentials in eq. (G.1) as follows:

$$\exp(-\imath \mathbf{c}'_{s_i} \cdot \zeta) - \exp(-\imath \mathbf{c}_{s_i} \cdot \zeta) = \exp(-\imath \mathbf{c}_{s_i} \cdot \zeta) \left\{ \exp \left[-\imath \frac{\mu_{sp}}{m_s} (\mathbf{g}' - \mathbf{g}) \cdot \zeta \right] - 1 \right\}. \quad (\text{G.3})$$

The substitution of eq. (G.3) and the use of the relation $d\mathbf{c}_{p_j} d\mathbf{c}_{s_i} = d\mathbf{g} d\mathbf{c}_{s_i}$ ¹ in eq. (G.1) gives:

$$\begin{aligned} \hat{Q}_{s_ip_j}(\zeta) &= \iint_{\mathcal{S}^2 \times \mathbb{R}^3} \frac{1}{(2\pi)^{3/2}} \left[\int_{\mathbb{R}^3} f_{s_i}(\mathbf{c}_{s_i}) f_{p_j}(\mathbf{c}_{s_i} - \mathbf{g}) \exp(-\imath \mathbf{c}_{s_i} \cdot \zeta) d\mathbf{c}_{s_i} \right] \times \\ &\quad \left\{ \exp \left[-\imath \frac{\mu_{sp}}{m_s} (\mathbf{g}' - \mathbf{g}) \cdot \zeta \right] - 1 \right\} \sigma_{s_ip_j} g d\omega' d\mathbf{g}, \end{aligned} \quad (\text{G.4})$$

¹A direct calculation shows that the Jacobian of the transformation $(\mathbf{c}_{s_i}, \mathbf{c}_{p_j}) \rightarrow (\mathbf{c}_{s_i}, \mathbf{g})$ is unit (*i.e.* $|\partial(\mathbf{c}_{s_i}, \mathbf{c}_{p_j})/\partial(\mathbf{c}_{s_i}, \mathbf{g})| = 1$).

The inner integral in eq. (G.4) represents the Fourier transform of the function product $f_{s_i}(\mathbf{c}_{s_i}) f_{p_j}(\mathbf{c}_{s_i} - \mathbf{g})$. In view of the convolution theorem and the translation property of the Fourier transform, the Fourier transform of the function product $f_{s_i}(\mathbf{c}_{s_i}) f_{p_j}(\mathbf{c}_{s_i} - \mathbf{g})$ can be written as:

$$\begin{aligned} & \frac{1}{(2\pi)^{3/2}} \int_{\mathbb{R}^3} f_{s_i}(\mathbf{c}_{s_i}) f_{p_j}(\mathbf{c}_{s_i} - \mathbf{g}) \exp(-i\mathbf{c}_{s_i} \cdot \boldsymbol{\zeta}) d\mathbf{c}_{s_i} = \\ & \frac{1}{(2\pi)^{3/2}} \int_{\mathbb{R}^3} \hat{f}_{s_i}(\boldsymbol{\zeta} - \boldsymbol{\xi}) \hat{f}_{p_j}(\boldsymbol{\xi}) \exp(-i\mathbf{g} \cdot \boldsymbol{\xi}) d\boldsymbol{\xi}, \end{aligned} \quad (G.5)$$

$s, p \in \mathcal{S}, \quad i \in \mathcal{I}_s, \quad j \in \mathcal{I}_p.$

The substitution of eq. (G.5) in eq. (G.4) gives the thesis of Proposition 6.2.1 stated in eq. (6.7):

$$\begin{aligned} \hat{Q}_{s_ip_j}(\boldsymbol{\zeta}) &= \int_{\mathbb{R}^3} \hat{f}_{s_i}(\boldsymbol{\zeta} - \boldsymbol{\xi}) \hat{f}_{p_j}(\boldsymbol{\xi}) \hat{W}_{s_ip_j}(\boldsymbol{\zeta}, \boldsymbol{\xi}) d\boldsymbol{\xi}, \end{aligned} \quad (G.6)$$

$s, p \in \mathcal{S}, \quad i \in \mathcal{I}_s, \quad j \in \mathcal{I}_p,$

where the elastic convolution weight for the collision $s_i + p_j = s_i + p_j$ is:

$$\begin{aligned} \hat{W}_{s_ip_j}(\boldsymbol{\zeta}, \boldsymbol{\xi}) &= \frac{1}{(2\pi)^{3/2}} \iint_{\mathcal{S}^2 \times \mathbb{R}^3} g \sigma_{s_ip_j} \left\{ \exp \left[-i \frac{\mu_{sp}}{m_s} (\mathbf{g}' - \mathbf{g}) \cdot \boldsymbol{\zeta} \right] - 1 \right\} \times \\ & \exp(-i\mathbf{g} \cdot \boldsymbol{\xi}) d\boldsymbol{\omega}' d\mathbf{g}, \quad s, p \in \mathcal{S}, \quad i \in \mathcal{I}_s, \quad j \in \mathcal{I}_p. \end{aligned} \quad (G.7)$$

G.2 Partial Inelastic Collision Operator

The computation of the Fourier transform of the partial inelastic collision operator proceeds in a manner similar to the elastic case.

According to the weak form (6.6), the Fourier transform of the partial inelastic collision operator for the collision $s_i + p_j = s_k + p_l$ is:

$$\begin{aligned} \hat{Q}_{s_ip_j}^{s_k p_l}(\boldsymbol{\zeta}) &= \frac{1}{(2\pi)^{3/2}} \iiint_{\mathcal{S}^2 \times \mathbb{R}^3 \times \mathbb{R}^3} \exp(-i\mathbf{c}_{s_i} \cdot \boldsymbol{\zeta}) f'_{s_k} f'_{p_l} \sigma_{s_k p_l}^{s_ip_j} g' d\boldsymbol{\omega} d\mathbf{c}'_{s_k} d\mathbf{c}'_{p_l} - \\ & \frac{1}{(2\pi)^{3/2}} \iiint_{\mathcal{S}^2 \times \mathbb{R}^3 \times \mathbb{R}^3} \exp(-i\mathbf{c}_{s_i} \cdot \boldsymbol{\zeta}) f_{s_i} f_{p_j} \sigma_{s_ip_j}^{s_k p_l} g d\boldsymbol{\omega}' d\mathbf{c}_{s_i} d\mathbf{c}_{p_j}, \end{aligned} \quad (G.8)$$

$(p_j, s_k, p_l) \in \mathcal{C}_{s_i}^{\text{in}}, \quad s \in \mathcal{S}, \quad i \in \mathcal{I}_s.$

The velocity \mathbf{c}_{s_i} in the exponential contained in the gain part of the Fourier transform can be expressed as:

$$\mathbf{c}_{s_i} = \mathbf{c}'_{s_k} + \frac{\mu_{sp}}{m_s} (\mathbf{g} - \mathbf{g}'), \quad s, p \in \mathcal{S}, \quad i, k \in \mathcal{I}_s. \quad (G.9)$$

The substitution of eq. (G.9) and the use of the relations $d\mathbf{c}_{p_j}d\mathbf{c}_{s_i} = d\mathbf{g}d\mathbf{c}_{s_i}$ and $d\mathbf{c}'_{p_l}d\mathbf{c}'_{s_k} = d\mathbf{g}'d\mathbf{c}'_{s_k}$ ² in eq. (G.8) gives:

$$\begin{aligned}\hat{Q}_{s_ip_j}^{s_kpl}(\zeta) &= \iint_{\mathcal{S}^2 \times \mathbb{R}^3} \frac{1}{(2\pi)^{3/2}} \left[\int_{\mathbb{R}^3} f_{s_k}(\mathbf{c}'_{s_k}) f_{p_l}(\mathbf{c}'_{s_k} - \mathbf{g}') \exp(-i\mathbf{c}'_{s_k} \cdot \zeta) d\mathbf{c}'_{s_k} \right] \times \\ &\quad \exp \left[-i \frac{\mu_{sp}}{m_s} (\mathbf{g} - \mathbf{g}') \cdot \zeta \right] \sigma_{s_kpl}^{s_ip_j} g' d\omega' d\mathbf{g}' - \\ &\quad \iint_{\mathcal{S}^2 \times \mathbb{R}^3} \frac{1}{(2\pi)^{3/2}} \left[\int_{\mathbb{R}^3} f_{s_i}(\mathbf{c}_{s_i}) f_{p_j}(\mathbf{c}_{s_i} - \mathbf{g}) \exp(-i\mathbf{c}_{s_i} \cdot \zeta) d\mathbf{c}_{s_i} \right] \times \\ &\quad \sigma_{s_ip_j}^{s_kpl} g d\omega' d\mathbf{g},\end{aligned}\tag{G.10}$$

$(p_j, s_k, p_l) \in \mathcal{C}_{s_i}^{\text{in}}, \quad s \in \mathcal{S}, \quad i \in \mathcal{I}_s.$

As done for the elastic case, the use of the convolution theorem and the translation property of the Fourier transform allows to write the Fourier transform of the function product $f_{s_k}(\mathbf{c}'_{s_k}) f_{p_l}(\mathbf{c}'_{s_k} - \mathbf{g}')$ in eq. (G.10) as:

$$\begin{aligned}\frac{1}{(2\pi)^{3/2}} \int_{\mathbb{R}^3} f_{s_k}(\mathbf{c}'_{s_k}) f_{p_l}(\mathbf{c}'_{s_k} - \mathbf{g}') \exp(-i\mathbf{c}'_{s_k} \cdot \zeta) d\mathbf{c}'_{s_k} &= \\ \frac{1}{(2\pi)^{3/2}} \int_{\mathbb{R}^3} \hat{f}_{s_k}(\zeta - \xi) \hat{f}_{p_l}(\xi) \exp(-i\mathbf{g}' \cdot \xi) d\xi,\end{aligned}\tag{G.11}$$

$s, p \in \mathcal{S}, \quad k \in \mathcal{I}_s, \quad l \in \mathcal{I}_p.$

The substitution of eqs. (G.5) and (G.11) in eq. (G.10) gives the thesis of Proposition 6.2.1 stated in eq. (6.8):

$$\begin{aligned}\hat{Q}_{s_ip_j}^{s_kpl}(\zeta) &= \int_{\mathbb{R}^3} \hat{f}_{s_k}(\zeta - \xi) \hat{f}_{p_l}(\xi) \hat{G}_{s_ip_j}^{s_kpl}(\zeta, \xi) d\xi - \\ &\quad \int_{\mathbb{R}^3} \hat{f}_{s_i}(\zeta - \xi) \hat{f}_{p_j}(\xi) \hat{L}_{s_ip_j}^{s_kpl}(\xi) d\xi,\end{aligned}\tag{G.12}$$

$(p_j, s_k, p_l) \in \mathcal{C}_{s_i}^{\text{in}}, s \in \mathcal{S}, \quad i \in \mathcal{I}_s,$

where the inelastic gain and loss convolution weights for the collision $s_i + p_j = s_k + p_l$ are:

$$\begin{aligned}\hat{G}_{s_ip_j}^{s_kpl}(\zeta, \xi) &= \frac{1}{(2\pi)^{3/2}} \iint_{\mathcal{S}^2 \times \mathbb{R}^3} g' \sigma_{s_kpl}^{s_ip_j} \exp \left[-i \frac{\mu_{sp}}{m_s} (\mathbf{g} - \mathbf{g}') \cdot \zeta \right] \times \\ &\quad \exp(-i\mathbf{g}' \cdot \xi) d\omega' d\mathbf{g}',\end{aligned}\tag{G.13}$$

$$\hat{L}_{s_ip_j}^{s_kpl}(\xi) = \frac{1}{(2\pi)^{3/2}} \iint_{\mathcal{S}^2 \times \mathbb{R}^3} g \sigma_{s_ip_j}^{s_kpl} \exp(-i\mathbf{g} \cdot \xi) d\omega' d\mathbf{g},\tag{G.14}$$

$(p_j, s_k, p_l) \in \mathcal{C}_{s_i}^{\text{in}}, \quad s \in \mathcal{S}, \quad i \in \mathcal{I}_s.$

²A direct calculation shows that the Jacobian of the transformation $(\mathbf{c}'_{s_k}, \mathbf{c}'_{p_l}) \rightarrow (\mathbf{c}'_{s_k}, \mathbf{g}')$ is unit (*i.e.* $|\partial(\mathbf{c}'_{s_k}, \mathbf{c}'_{p_l})/\partial(\mathbf{c}'_{s_k}, \mathbf{g}')| = 1$).

Appendix H

Isotropic Convolution Weights

H.1 Elastic Collisions

The elastic convolution weight for the collision $s_i + p_j = s_i + p_j$ is:

$$\hat{W}_{s_ip_j}(\zeta, \xi) = \frac{1}{(2\pi)^{3/2}} \iint_{\mathcal{S}^2 \times \mathbb{R}^3} g \sigma_{s_ip_j} \left\{ \exp \left[-i \frac{\mu_{sp}}{m_s} (\mathbf{g}' - \mathbf{g}) \cdot \zeta \right] - 1 \right\} \times \exp(-i \mathbf{g} \cdot \xi) d\omega' d\mathbf{g}, \quad s, p \in \mathcal{S}, \quad i \in \mathcal{I}_s, \quad j \in \mathcal{I}_p. \quad (\text{H.1})$$

In the case of isotropic interactions, the differential cross-section can be taken out of the integral over ω' and eq. (H.1) can be rearranged as:

$$\begin{aligned} \hat{W}_{s_ip_j}(\zeta, \xi) &= \frac{1}{(2\pi)^{3/2}} \int_{\mathbb{R}^3} g \sigma_{s_ip_j} \exp(-i \mathbf{g} \cdot \xi) \times \\ &\quad \left[\exp \left(i \frac{\mu_{sp}}{m_s} \mathbf{g} \cdot \zeta \right) \int_{\mathcal{S}^2} \exp \left(-i \frac{\mu_{sp}}{m_s} g \omega' \cdot \zeta \right) d\omega' - \int_{\mathcal{S}^2} d\omega' \right] d\mathbf{g}, \\ &\quad s, p \in \mathcal{S}, \quad i \in \mathcal{I}_s, \quad j \in \mathcal{I}_p. \end{aligned} \quad (\text{H.2})$$

The integral $\int_{\mathcal{S}^2} d\omega'$ can be readily evaluated and gives 4π . The remaining integral over ω' can be computed by introducing a spherical coordinate system $(\theta_{\omega'}, \phi_{\omega'})$ for the vector ω' with the pole aligned along the direction of the vector ζ . In this way one has:

$$\begin{aligned} \int_{\mathcal{S}^2} \exp \left(-i \frac{\mu_{sp}}{m_s} g \omega' \cdot \zeta \right) d\omega' &= \int_0^{2\pi} \int_0^\pi \exp \left(-i \frac{\mu_{sp}}{m_s} g \zeta \cos \theta_{\omega'} \right) \sin \theta_{\omega'} d\theta_{\omega'} d\phi_{\omega'} \\ &= \int_0^{2\pi} d\phi_{\omega'} \int_0^\pi \exp \left(-i \frac{\mu_{sp}}{m_s} g \zeta \cos \theta_{\omega'} \right) \sin \theta_{\omega'} d\theta_{\omega'} \\ &= 4\pi j_0 \left(\frac{\mu_{sp}}{m_s} g \zeta \right), \quad s, p \in \mathcal{S}, \end{aligned} \quad (\text{H.3})$$

where the zeroth-order spherical Bessel function of first kind $j_0(x)$ is (Abramovitz and Stegun 1972):

$$j_0(x) = \frac{1}{2} \int_0^\pi \exp(-\imath x \cos \theta) \sin \theta d\theta = \frac{\sin x}{x}, \quad x \in \Re. \quad (\text{H.4})$$

The substitution of eq. (H.3) in eq. (H.2) gives:

$$\begin{aligned} \hat{W}_{s_ip_j}(\zeta, \xi) &= \sqrt{\frac{2}{\pi}} \int_{\Re^3} g \sigma_{s_ip_j} j_0 \left(\frac{\mu_{sp}}{m_s} g \zeta \right) \exp \left[-\imath \mathbf{g} \cdot \left(\xi - \zeta \frac{\mu_{sp}}{m_s} \right) \right] d\mathbf{g} - \\ &\quad \sqrt{\frac{2}{\pi}} \int_{\Re^3} g \sigma_{s_ip_j} \exp(-\imath \mathbf{g} \cdot \xi) d\mathbf{g}, \\ s, p \in \mathcal{S}, \quad i \in \mathcal{I}_s, \quad j \in \mathcal{I}_p. \end{aligned} \quad (\text{H.5})$$

Since the differential cross-section only depends on g , the first and second integrals over \mathbf{g} can be computed by adopting a spherical coordinate system (θ_g, ϕ_g) for the vector \mathbf{g} with the pole aligned along the direction of the vectors $\xi - \zeta \mu_{sp}/m_s$ and ξ , respectively. In this situation the velocity differential $d\mathbf{g}$ becomes $g^2 \sin \theta_g d\theta_g d\phi_g dg$. The substitution of the previous relation in eq. (H.5) gives (after a manipulation similar to that of eq. (H.3)):

$$\begin{aligned} \int_{\Re^3} g \sigma_{s_ip_j} j_0 \left(\frac{\mu_{sp}}{m_s} g \zeta \right) \exp \left[-\imath \mathbf{g} \cdot \left(\xi - \zeta \frac{\mu_{sp}}{m_s} \right) \right] d\mathbf{g} = \\ 4\pi \int_0^\infty \sigma_{s_ip_j} j_0 \left(\frac{\mu_{sp}}{m_s} g \zeta \right) j_0 \left(g \left| \xi - \zeta \frac{\mu_{sp}}{m_s} \right| \right) g^3 dg, \end{aligned} \quad (\text{H.6})$$

$$\int_{\Re^3} g \sigma_{s_ip_j} \exp(-\imath \mathbf{g} \cdot \xi) d\mathbf{g} = 4\pi \int_0^\infty \sigma_{s_ip_j} j_0(g \xi) g^3 dg, \quad (\text{H.7})$$

$s, p \in \mathcal{S}, \quad i \in \mathcal{I}_s, \quad j \in \mathcal{I}_p.$

The substitution of eqs. (H.6)-(H.7) in eq. (H.5) gives the thesis of Proposition 6.2.2 stated in eq. (6.12):

$$\begin{aligned} \hat{W}_{s_ip_j}(\zeta, \xi) &= 4\sqrt{2\pi} \int_0^{+\infty} \sigma_{s_ip_j} \left[j_0 \left(\frac{\mu_{sp}}{m_s} g \zeta \right) j_0 \left(g \left| \xi - \zeta \frac{\mu_{sp}}{m_s} \right| \right) - j_0(g \xi) \right] \times \\ &\quad g^3 dg, \quad s, p \in \mathcal{S}, \quad i \in \mathcal{I}_s, \quad j \in \mathcal{I}_p. \end{aligned} \quad (\text{H.8})$$

H.2 Inelastic Collisions

The inelastic gain and loss convolution weights for the collision $s_i + p_j = s_k + p_l$ are:

$$\hat{G}_{s_i p_j}^{s_k p_l}(\zeta, \xi) = \frac{1}{(2\pi)^{3/2}} \iint_{\mathcal{S}^2 \times \mathbb{R}^3} g' \sigma_{s_i p_j}^{s_k p_l} \exp \left[-i \frac{\mu_{sp}}{m_s} (\mathbf{g} - \mathbf{g}') \cdot \zeta \right] \times \exp(-i \mathbf{g}' \cdot \xi) d\omega d\mathbf{g}', \quad (\text{H.9})$$

$$\hat{L}_{s_i p_j}^{s_k p_l}(\xi) = \frac{1}{(2\pi)^{3/2}} \iint_{\mathcal{S}^2 \times \mathbb{R}^3} g \sigma_{s_i p_j}^{s_k p_l} \exp(-i \mathbf{g} \cdot \xi) d\omega' d\mathbf{g}, \quad (\text{H.10})$$

$$(p_j, s_k, p_l) \in \mathcal{C}_{s_i}^{\text{in}}, \quad s \in \mathcal{S}, \quad i \in \mathcal{I}_s.$$

In analogy with the case of an elastic collision, when the interaction is isotropic it is possible to rearrange eqs. (H.9)-(H.10) as:

$$\hat{G}_{s_i p_j}^{s_k p_l}(\zeta, \xi) = \frac{1}{(2\pi)^{3/2}} \int_{\mathbb{R}^3} g' \sigma_{s_i p_j}^{s_k p_l} \exp \left[-i \mathbf{g}' \cdot \left(\xi - \frac{\mu_{sp}}{m_s} \zeta \right) \right] \times \left[\int_{\mathcal{S}^2} \exp \left(-i \frac{\mu_{sp}}{m_s} g \boldsymbol{\omega} \cdot \zeta \right) d\boldsymbol{\omega} \right] d\mathbf{g}', \quad (\text{H.11})$$

$$\hat{L}_{s_i p_j}^{s_k p_l}(\xi) = \frac{1}{(2\pi)^{3/2}} \int_{\mathbb{R}^3} g \sigma_{s_i p_j}^{s_k p_l} \exp(-i \mathbf{g} \cdot \xi) \left[\int_{\mathcal{S}^2} d\boldsymbol{\omega}' \right] d\mathbf{g}, \quad (\text{H.12})$$

$$(p_j, s_k, p_l) \in \mathcal{C}_{s_i}^{\text{in}}, \quad s \in \mathcal{S}, \quad i \in \mathcal{I}_s.$$

The integral $\int_{\mathcal{S}^2} d\boldsymbol{\omega}'$ is equal to 4π while that over $\boldsymbol{\omega}$ in eq. (H.11) can be evaluated by adopting a spherical coordinate system $(\theta_\omega, \phi_\omega)$ for the vector $\boldsymbol{\omega}$ with the pole aligned along the direction of the vector ζ . The application of this procedure leads to:

$$\int_{\mathcal{S}^2} \exp \left(-i \frac{\mu_{sp}}{m_s} g \boldsymbol{\omega} \cdot \zeta \right) d\boldsymbol{\omega} = 4\pi j_0 \left(\frac{\mu_{sp}}{m_s} g \zeta \right), \quad s, p \in \mathcal{S}. \quad (\text{H.13})$$

The pre-collisional relative velocity magnitude g can be related to its post-collisional value g' through the energy balance for the collision:

$$\frac{1}{2} \mu_{sp} g^2 = \frac{1}{2} \mu_{sp} g'^2 + \Delta E_{s_i p_j}^{s_k p_l}, \quad s \in \mathcal{S}, \quad i \in \mathcal{I}_s, \quad (p_j, s_k, p_l) \in \mathcal{C}_{s_i}^{\text{in}}. \quad (\text{H.14})$$

Solving eq. (H.14) for g' and substituting the result obtained in eq. (H.13) one has:

$$\int_{\mathcal{S}^2} \exp \left(-i \frac{\mu_{sp}}{m_s} g \boldsymbol{\omega} \cdot \zeta \right) d\boldsymbol{\omega} = 4\pi j_0 \left(\frac{\mu_{sp}}{m_s} \sqrt{g'^2 + 2 \frac{\Delta E_{s_i p_j}^{s_k p_l}}{\mu_{sp}}} \zeta \right), \quad (\text{H.15})$$

$$(p_j, s_k, p_l) \in \mathcal{C}_{s_i}^{\text{in}}, \quad s \in \mathcal{S}, \quad i \in \mathcal{I}_s.$$

The substitution of eq. (H.15) in eq. (H.11) and the use of the equality $\int_{\mathcal{S}^2} d\omega' = 4\pi$ in eq. (H.12) allows to write:

$$\hat{G}_{s_i p_j}^{s_k p_l}(\zeta, \xi) = \sqrt{\frac{2}{\pi}} \int_{\mathfrak{R}^3} g' \sigma_{s_k p_l}^{s_i p_j} j_0 \left(\frac{\mu_{sp}}{m_s} \sqrt{g'^2 + 2 \frac{\Delta E_{s_i p_j}^{s_k p_l}}{\mu_{sp}}} \zeta \right) \times \\ \exp \left[-i \mathbf{g}' \cdot \left(\xi - \frac{\mu_{sp}}{m_s} \zeta \right) \right] d\mathbf{g}', \quad (\text{H.16})$$

$$\hat{L}_{s_i p_j}^{s_k p_l}(\xi) = \sqrt{\frac{2}{\pi}} \int_{\mathfrak{R}^3} g \sigma_{s_i p_j}^{s_k p_l} \exp(-i \mathbf{g} \cdot \xi) d\mathbf{g}, \quad (\text{H.17})$$

$$(p_j, s_k, p_l) \in \mathcal{C}_{s_i}^{\text{in}}, \quad s \in \mathcal{S}, \quad i \in \mathcal{I}_s.$$

The integrals over \mathbf{g} and \mathbf{g}' can be computed, as in the elastic case (see eqs. (H.6)-(H.7)), by using again spherical coordinates. The application of this procedure to eqs. (H.16)-(H.17) allows to obtain the thesis of Proposition 6.2.2 stated in eqs. (6.13)-(6.14):

$$\hat{G}_{s_i p_j}^{s_k p_l}(\zeta, \xi) = 4\sqrt{2\pi} \int_{\mathcal{G}_{s_i p_j}^{s_k p_l}} \sigma_{s_k p_l}^{s_i p_j} j_0 \left(\frac{\mu_{sp}}{m_s} \sqrt{g'^2 + 2 \frac{\Delta E_{s_i p_j}^{s_k p_l}}{\mu_{sp}}} \zeta \right) \times \\ j_0 \left(g' \left| \xi - \zeta \frac{\mu_{sp}}{m_s} \right| \right) g'^3 dg', \quad (\text{H.18})$$

$$\hat{L}_{s_i p_j}^{s_k p_l}(\xi) = 4\sqrt{2\pi} \int_{\mathcal{G}_{s_i p_j}^{s_k p_l}} \sigma_{s_i p_j}^{s_k p_l} j_0(g\xi) g^3 dg, \quad (\text{H.19})$$

$$(p_j, s_k, p_l) \in \mathcal{C}_{s_i}^{\text{in}}, \quad s \in \mathcal{S}, \quad i \in \mathcal{I}_s.$$

The lower limits on the relative velocity $\mathcal{G}_{s_i p_j}^{s_k p_l}$ and $\mathcal{G}_{s_k p_l}^{s_i p_j}$ account for the existence, in the most general situation, of a threshold value below which the inelastic collision $s_i + p_j = s_k + p_l$ and its inverse $s_k + p_l = s_i + p_j$ do not occur, respectively. These threshold values can be obtained from the energy balance for the collision (H.14) and are:

$$\mathcal{G}_{s_k p_l}^{s_i p_j} = \begin{cases} \sqrt{-\frac{2 \Delta E_{s_i p_j}^{s_k p_l}}{\mu_{sp}}} & \text{if } \Delta E_{s_i p_j}^{s_k p_l} < 0, \\ 0 & \text{if } \Delta E_{s_i p_j}^{s_k p_l} \geq 0, \end{cases} \quad (\text{H.20})$$

$$\mathcal{G}_{s_i p_j}^{s_k p_l} = \begin{cases} \sqrt{\frac{2 \Delta E_{s_i p_j}^{s_k p_l}}{\mu_{sp}}} & \text{if } \Delta E_{s_i p_j}^{s_k p_l} > 0, \\ 0 & \text{if } \Delta E_{s_i p_j}^{s_k p_l} \leq 0, \end{cases} \quad (\text{H.21})$$

$$(p_j, s_k, p_l) \in \mathcal{C}_{s_i}^{\text{in}}, \quad s \in \mathcal{S}, \quad i \in \mathcal{I}_s.$$

Appendix I

Discrete Fourier Transforms and Weighted Convolutions

I.1 Fourier and inverse Fourier Transform

Let $f = f(\mathbf{c})$ be a function of the velocity \mathbf{c} and let $\hat{f} = \hat{f}(\boldsymbol{\zeta})$ be its Fourier transform. According to the definitions introduced in sec. 6.2, the Fourier transform of the function f and the inverse Fourier transform of the function \hat{f} are:

$$\hat{f}(\boldsymbol{\zeta}) = \frac{1}{(2\pi)^{3/2}} \int_{\mathbb{R}^3} \exp(-\imath \boldsymbol{\zeta} \cdot \mathbf{c}) f(\mathbf{c}) d\mathbf{c}, \quad \boldsymbol{\zeta} \in \mathbb{R}^3, \quad (\text{I.1})$$

$$f(\mathbf{c}) = \frac{1}{(2\pi)^{3/2}} \int_{\mathbb{R}^3} \exp(\imath \boldsymbol{\zeta} \cdot \mathbf{c}) \hat{f}(\boldsymbol{\zeta}) d\boldsymbol{\zeta}, \quad \mathbf{c} \in \mathbb{R}^3. \quad (\text{I.2})$$

The integrals in eqs. (I.1)-(I.2) must be replaced with discrete sums because of the discretization of the velocity space introduced in sec. 6.3.1. The substitution of eqs. (6.21) and (6.24) for \mathbf{c}_h and $\boldsymbol{\zeta}_\eta$, respectively, in eqs. (I.1)-(I.2) and the replacement of the continuous integrals with discrete sums, leads to:

$$\hat{f}(\boldsymbol{\zeta}_\eta) = \frac{\Delta c^3}{(2\pi)^{3/2}} \sum_{\mathbf{h} \in \mathcal{H}^3} w_h \exp(-\imath \boldsymbol{\zeta}_\eta \cdot \mathbf{c}_h) f(\mathbf{c}_h), \quad \boldsymbol{\zeta}_\eta \in \mathcal{V}_\zeta, \quad (\text{I.3})$$

$$f(\mathbf{c}_h) = \frac{\Delta \zeta^3}{(2\pi)^{3/2}} \sum_{\boldsymbol{\eta} \in \mathcal{H}^3} w_\eta \exp(\imath \boldsymbol{\zeta}_\eta \cdot \mathbf{c}_h) \hat{f}(\boldsymbol{\zeta}_\eta), \quad \mathbf{c}_h \in \mathcal{V}_c. \quad (\text{I.4})$$

The expansion of the dot product $\boldsymbol{\zeta}_\eta \cdot \mathbf{c}_h$ gives:

$$\begin{aligned} \boldsymbol{\zeta}_\eta \cdot \mathbf{c}_h &= (-L_c + h_x \Delta c)(-L_\zeta + \eta_x \Delta \zeta) + (-L_c + h_x \Delta c)(-L_\zeta + \eta_y \Delta \zeta) + \\ &\quad (-L_c + h_z \Delta c)(-L_\zeta + \eta_z \Delta \zeta), \quad \mathbf{h}, \boldsymbol{\eta} \in \mathcal{H}^3. \end{aligned} \quad (\text{I.5})$$

After some re-arrangement and the use of the relation (6.26) ($\Delta c \Delta \zeta = 2\pi/N_c$), eq. (I.5) can be rewritten as:

$$\begin{aligned} \zeta_\eta \cdot \mathbf{c}_h &= 3L_c L_\zeta - L_c \Delta \zeta (\eta_x + \eta_y + \eta_z) - L_\zeta \Delta c (h_x + h_y + h_z) + \frac{2\pi}{N_c} \mathbf{h} \cdot \boldsymbol{\eta}, \\ \mathbf{h}, \boldsymbol{\eta} &\in \mathcal{H}^3. \end{aligned} \quad (\text{I.6})$$

The substitution of eq. (I.6) in eqs. (I.3)-(I.4) gives:

$$\hat{f}(\zeta_\eta) = \frac{\Delta c^3 \exp[-i\delta(\boldsymbol{\eta})]}{(2\pi)^{3/2}} \sum_{\mathbf{h} \in \mathcal{H}^3} f^*(\mathbf{c}_h) \exp\left(-i \frac{2\pi}{N_c} \mathbf{h} \cdot \boldsymbol{\eta}\right), \quad \zeta_\eta \in \mathcal{V}_\zeta, \quad (\text{I.7})$$

$$f(\mathbf{c}_h) = \frac{\Delta \zeta^3 \exp[i\gamma(\mathbf{h})]}{(2\pi)^{3/2}} \sum_{\boldsymbol{\eta} \in \mathcal{H}^3} \hat{f}^*(\zeta_\eta) \exp\left(i \frac{2\pi}{N_c} \mathbf{h} \cdot \boldsymbol{\eta}\right), \quad \mathbf{c}_h \in \mathcal{V}_c. \quad (\text{I.8})$$

Quantities $\delta(\boldsymbol{\eta})$ and $\gamma(\mathbf{h})$ in the exponentials in front of the sums are:

$$\delta(\boldsymbol{\eta}) = L_c [3L_\zeta - \Delta \zeta (\eta_x + \eta_y + \eta_z)], \quad \boldsymbol{\eta} \in \mathcal{H}^3, \quad (\text{I.9})$$

$$\gamma(\mathbf{h}) = L_\zeta [3L_c - \Delta c (h_x + h_y + h_z)], \quad \mathbf{h} \in \mathcal{H}^3, \quad (\text{I.10})$$

while the functions $f^*(\mathbf{c}_h)$ and $\hat{f}^*(\zeta_\eta)$ have the following expressions:

$$f^*(\mathbf{c}_h) = w_h f(\mathbf{c}_h) \exp[i L_\zeta \Delta c (h_x + h_y + h_z)], \quad \mathbf{c}_h \in \mathcal{V}_c, \quad (\text{I.11})$$

$$\hat{f}^*(\zeta_\eta) = w_\eta \hat{f}(\zeta_\eta) \exp[-i L_c \Delta \zeta (\eta_x + \eta_y + \eta_z)], \quad \zeta_\eta \in \mathcal{V}_\zeta. \quad (\text{I.12})$$

The sums in eqs. (I.7)-(I.8) correspond, respectively, to the FFT and inverse FFT of the functions f^* and \hat{f}^* (with no scaling):

$$\text{FFT}(f^*)(\boldsymbol{\eta}) = \sum_{\mathbf{h} \in \mathcal{H}^3} f^*(\mathbf{c}_h) \exp\left(-i \frac{2\pi}{N_c} \mathbf{h} \cdot \boldsymbol{\eta}\right), \quad \boldsymbol{\eta} \in \mathcal{H}^3, \quad (\text{I.13})$$

$$\text{FFT}^{-1}(\hat{f}^*)(\mathbf{h}) = \sum_{\boldsymbol{\eta} \in \mathcal{H}^3} \hat{f}^*(\zeta_\eta) \exp\left(i \frac{2\pi}{N_c} \mathbf{h} \cdot \boldsymbol{\eta}\right), \quad \mathbf{h} \in \mathcal{H}^3. \quad (\text{I.14})$$

In view of eqs. (I.13)-(I.14), the discrete approximation of the Fourier transform of the function f and the inverse Fourier transform of the function \hat{f} become:

$$\hat{f}(\zeta_\eta) = \frac{\Delta c^3 \exp[-i\delta(\boldsymbol{\eta})]}{(2\pi)^{3/2}} \text{FFT}(f^*)(\boldsymbol{\eta}), \quad \zeta_\eta \in \mathcal{V}_\zeta, \quad \boldsymbol{\eta} \in \mathcal{H}^3, \quad (\text{I.15})$$

$$f(\mathbf{c}_h) = \frac{\Delta \zeta^3 \exp[i\gamma(\mathbf{h})]}{(2\pi)^{3/2}} \text{FFT}^{-1}(\hat{f}^*)(\mathbf{h}), \quad \mathbf{c}_h \in \mathcal{V}_c, \quad \mathbf{h} \in \mathcal{H}^3. \quad (\text{I.16})$$

Based on eqs. (I.15)-(I.16), the following algorithms are proposed for a fast evaluation of the Fourier and the inverse Fourier transform.

Algorithm I.1.1 *Evaluation of the Fourier transform of $f = f(\mathbf{c})$*

```

for all  $\mathbf{h}, \boldsymbol{\eta} \in \mathcal{H}^3$  do
    compute  $\delta(\boldsymbol{\eta})$  through eq. (I.9);
    compute  $f^*(\mathbf{c}_h)$  through eq. (I.11);
end for
Compute the FFT of  $f^*$ ;
for all  $\boldsymbol{\eta} \in \mathcal{H}^3$  do
    Compute  $\hat{f}(\boldsymbol{\zeta}_\eta)$  through eq. (I.15);
end for

```

Algorithm I.1.2 *Evaluation of the inverse Fourier transform of $\hat{f} = \hat{f}(\boldsymbol{\zeta})$*

```

for all  $\mathbf{h}, \boldsymbol{\eta} \in \mathcal{H}^3$  do
    compute  $\gamma(\mathbf{c}_h)$  through eq. (I.10);
    compute  $\hat{f}^*(\boldsymbol{\zeta}_\eta)$  through eq. (I.12);
end for
Compute the  $\text{FFT}^{-1}$  of  $\hat{f}^*$ ;
for all  $\mathbf{h} \in \mathcal{H}^3$  do
    Compute  $f(\mathbf{c}_h)$  through eq. (I.16);
end for

```

I.2 Weighted Convolution

The continuous integrals defining the weighted convolutions in eqs. (6.7)-(6.8) are approximated as follows. Let $\boldsymbol{\kappa} = (\kappa_x, \kappa_y, \kappa_z)$ and $\mathbf{w}_\kappa = (w_{\kappa_x}, w_{\kappa_y}, w_{\kappa_z})$ be, respectively, the vector of indices and the vector of integration weights associated to the discrete Fourier velocity node $\boldsymbol{\xi}_\kappa$. In view of this, the Fourier transform of the partial collision operators for the elastic collision $s_i + p_j = s_i + p_j$ and the inelastic collision $s_i + p_j = s_k + p_l$ become:

$$\hat{Q}_{s_i p_j}(\boldsymbol{\zeta}_\eta) = \frac{\Delta\zeta^3}{(2\pi)^{3/2}} \sum_{\boldsymbol{\kappa} \in \mathcal{H}_\eta^3} w_\kappa \hat{f}_{s_i}(\boldsymbol{\zeta}_\eta - \boldsymbol{\xi}_\kappa) \hat{f}_{p_j}(\boldsymbol{\xi}_\kappa) \hat{W}_{s_i p_j}(\boldsymbol{\zeta}_\eta, \boldsymbol{\xi}_\kappa), \quad (\text{I.17})$$

$$s, p \in \mathcal{S}, \quad i \in \mathcal{I}_s, \quad j \in \mathcal{I}_p, \quad \boldsymbol{\zeta}_\eta \in \mathcal{V}_\zeta, \quad \boldsymbol{\eta} \in \mathcal{H}^3,$$

$$\begin{aligned} \hat{Q}_{s_i p_j}^{s_k p_l}(\boldsymbol{\zeta}_\eta) &= \frac{\Delta\zeta^3}{(2\pi)^{3/2}} \sum_{\boldsymbol{\kappa} \in \mathcal{H}_\eta^3} w_\kappa \hat{f}_{s_k}(\boldsymbol{\zeta}_\eta - \boldsymbol{\xi}_\kappa) \hat{f}_{p_l}(\boldsymbol{\xi}_\kappa) \hat{G}_{s_i p_j}^{s_k p_l}(\boldsymbol{\zeta}_\eta, \boldsymbol{\xi}_\kappa) - \\ &\quad \frac{\Delta\zeta^3}{(2\pi)^{3/2}} \sum_{\boldsymbol{\kappa} \in \mathcal{H}_\eta^3} w_\kappa \hat{f}_{s_i}(\boldsymbol{\zeta}_\eta - \boldsymbol{\xi}_\kappa) \hat{f}_{p_j}(\boldsymbol{\xi}_\kappa) \hat{L}_{s_i p_j}^{s_k p_l}(\boldsymbol{\xi}_\kappa), \end{aligned} \quad (\text{I.18})$$

$$(p_j, s_k, p_l) \in \mathcal{C}_{s_i}^{\text{in}}, \quad s \in \mathcal{S}, \quad i \in \mathcal{I}_s, \quad \boldsymbol{\zeta}_\eta \in \mathcal{V}_\zeta, \quad \boldsymbol{\eta} \in \mathcal{H}^3,$$

where the global integration weight of the discrete Fourier velocity node ξ_κ is $w_\kappa = w_{\kappa_x} w_{\kappa_y} w_{\kappa_z}$. The set \mathcal{H}_η^3 is defined as:

$$\mathcal{H}_\eta^3 = \{(\kappa_x^-, \kappa_x^+) \times (\kappa_y^-, \kappa_y^+) \times (\kappa_z^-, \kappa_z^+)\} \subset \mathcal{H}^3, \quad \eta \in \mathcal{H}^3, \quad (I.19)$$

where the upper (+) and lower (-) limits of the indices κ_x , κ_y and κ_z are computed based on the following relations:

$$\kappa_\alpha^- = \begin{cases} 0 & \text{if } \eta_\alpha < N_c/2, \\ \eta_\alpha - N_c/2 + 1 & \text{if } \eta_\alpha \geq N_c/2, \end{cases} \quad (I.20)$$

$$\kappa_\alpha^+ = \begin{cases} \eta_\alpha + N_c/2 - 1 & \text{if } \eta_\alpha < N_c/2, \\ N_c & \text{if } \eta_\alpha \geq N_c/2, \end{cases} \quad (I.21)$$

$$\alpha \in \{x, y, z\}.$$

The introduction of the above limits is equivalent to set to zero the functions \hat{f}_{s_k} and \hat{f}_{s_i} (in eqs. (I.17)-(I.18)) when their argument $(\zeta_\eta - \xi_\kappa)$ goes beyond the limits of the discretized Fourier velocity space.

Appendix J

Solution of the Constrained Optimization Problems

J.1 Elastic Collisions

The Lagrangian associated to the constrained optimization problem \mathcal{P}_{el} of Proposition 6.3.1 is:

$$\mathcal{L}_{\text{el}} = \sum_{\substack{s \in \mathcal{S} \\ i \in \mathcal{I}_s}} \sum_{\substack{p \in \mathcal{S} \\ j \in \mathcal{I}_p}} \left| \tilde{\mathbf{Q}}_{s_ip_j} - \mathbf{Q}_{s_ip_j} \right|^2 + (\boldsymbol{\Lambda}^{\text{el}})^T \sum_{\substack{s \in \mathcal{S} \\ i \in \mathcal{I}_s}} \sum_{\substack{p \in \mathcal{S} \\ j \in \mathcal{I}_p}} \boldsymbol{\Psi}_{s_i}^{\text{el}} \mathbf{Q}_{s_ip_j}, \quad (\text{J.1})$$

where the vector of Lagrange multipliers $\boldsymbol{\Lambda}^{\text{el}}$ has $\mathcal{N}_s + 4$ components. The solution of the problem \mathcal{P}_{el} is given by stationary points of the Lagrangian \mathcal{L}_{el} . These are found by imposing:

$$\frac{\partial \mathcal{L}_{\text{el}}}{\partial \mathbf{Q}_{s_ip_j}} = \mathbf{0}_{\mathcal{N}_s+4}, \quad s, p \in \mathcal{S}, \quad i \in \mathcal{I}_s, \quad j \in \mathcal{I}_p, \quad (\text{J.2})$$

$$\frac{\partial \mathcal{L}_{\text{el}}}{\partial \boldsymbol{\Lambda}^{\text{el}}} = \mathbf{0}_{\mathcal{N}_s+4}. \quad (\text{J.3})$$

The application of eqs. (J.2)-(J.3) gives:

$$\mathbf{Q}_{s_ip_j} = \tilde{\mathbf{Q}}_{s_ip_j} - (\boldsymbol{\Psi}_{s_i}^{\text{el}})^T \boldsymbol{\Lambda}^{\text{el}}, \quad s, p \in \mathcal{S}, \quad i \in \mathcal{I}_s, \quad j \in \mathcal{I}_p, \quad (\text{J.4})$$

$$\mathbf{0}_{\mathcal{N}_s+4} = \sum_{\substack{p \in \mathcal{S} \\ j \in \mathcal{I}_p}} \boldsymbol{\Psi}_{s_i}^{\text{el}} \mathbf{Q}_{s_ip_j}. \quad (\text{J.5})$$

The left multiplication of eq. (J.4) by the matrix $\boldsymbol{\Psi}_{s_i}^{\text{el}}$ and the sum of the result obtained over all the elastic collisions gives:

$$\sum_{\substack{s \in \mathcal{S} \\ i \in \mathcal{I}_s}} \sum_{\substack{p \in \mathcal{S} \\ j \in \mathcal{I}_p}} \boldsymbol{\Psi}_{s_i}^{\text{el}} \mathbf{Q}_{s_ip_j} = \sum_{\substack{s \in \mathcal{S} \\ i \in \mathcal{I}_s}} \sum_{\substack{p \in \mathcal{S} \\ j \in \mathcal{I}_p}} \boldsymbol{\Psi}_{s_i}^{\text{el}} \tilde{\mathbf{Q}}_{s_ip_j} - \mathcal{N}_s \sum_{i \in \mathcal{I}_s} \boldsymbol{\Psi}_{s_i}^{\text{el}} (\boldsymbol{\Psi}_{s_i}^{\text{el}})^T \boldsymbol{\Lambda}^{\text{el}}. \quad (\text{J.6})$$

The left-hand-side of eq. (J.6) is zero in view of the imposed constraint (J.5). Hence, eq. (J.6) can be solved for the Lagrange multiplier vector to give:

$$\boldsymbol{\Lambda}^{\text{el}} = (\tilde{\boldsymbol{\Psi}}^{\text{el}})^{-1} \tilde{\mathbf{Q}}^{\text{el}}, \quad (\text{J.7})$$

where the matrix $\tilde{\boldsymbol{\Psi}}^{\text{el}}$ and the vector $\tilde{\mathbf{Q}}^{\text{el}}$ are defined as:

$$\tilde{\boldsymbol{\Psi}}^{\text{el}} = \mathcal{N}_s \sum_{\substack{s \in \mathcal{S} \\ i \in \mathcal{I}_s}} \boldsymbol{\Psi}_{s_i}^{\text{el}} (\boldsymbol{\Psi}_{s_i}^{\text{el}})^T, \quad (\text{J.8})$$

$$\tilde{\mathbf{Q}}^{\text{el}} = \sum_{\substack{s \in \mathcal{S} \\ i \in \mathcal{I}_s}} \sum_{\substack{p \in \mathcal{S} \\ j \in \mathcal{I}_p}} \boldsymbol{\Psi}_{s_i}^{\text{el}} \tilde{\mathbf{Q}}_{s_i p_j}. \quad (\text{J.9})$$

The substitution of eq. (J.7) in eq. (J.4) gives the thesis of Proposition 6.3.1 stated in eq. (6.43):

$$\mathbf{Q}_{s_i p_j} = \tilde{\mathbf{Q}}_{s_i p_j} - (\boldsymbol{\Psi}_{s_i}^{\text{el}})^T (\tilde{\boldsymbol{\Psi}}^{\text{el}})^{-1} \tilde{\mathbf{Q}}^{\text{el}}, \quad s, p \in \mathcal{S}, \quad i \in \mathcal{I}_s, \quad j \in \mathcal{I}_p. \quad (\text{J.10})$$

J.2 Inelastic Collisions

The Lagrangian associated to the constrained optimization problem \mathcal{P}_{in} of Proposition 6.3.2 is:

$$\mathcal{L}_{\text{el}} = \sum_{\substack{s \in \mathcal{S} \\ i \in \mathcal{I}_s}} \sum_{\substack{(p_j, s_k, p_l) \\ \in \mathcal{C}_{s_i}^{\text{in}}}} \left| \tilde{\mathbf{Q}}_{s_i p_j}^{s_k p_l} - \mathbf{Q}_{s_i p_j}^{s_k p_l} \right|^2 + (\boldsymbol{\Lambda}^{\text{in}})^T \sum_{\substack{s \in \mathcal{S} \\ i \in \mathcal{I}_s}} \sum_{\substack{(p_j, s_k, p_l) \\ \in \mathcal{C}_{s_i}^{\text{in}}}} \boldsymbol{\Psi}_{s_i}^{\text{in}} \mathbf{Q}_{s_i p_j}^{s_k p_l}, \quad (\text{J.11})$$

where the vector of Lagrange multipliers $\boldsymbol{\Lambda}^{\text{in}}$ has $\mathcal{N}_c + 4$ components. The solution of the problem \mathcal{P}_{in} is given by stationary points of the Lagrangian \mathcal{L}_{in} . These are found by imposing:

$$\frac{\partial \mathcal{L}_{\text{in}}}{\partial \mathbf{Q}_{s_i p_j}^{s_k p_l}} = \mathbf{0}_{\mathcal{N}_c + 4}, \quad (p_j, s_k, p_l) \in \mathcal{C}_{s_i}^{\text{in}}, \quad s \in \mathcal{S}, \quad i \in \mathcal{I}_s, \quad (\text{J.12})$$

$$\frac{\partial \mathcal{L}_{\text{in}}}{\partial \boldsymbol{\Lambda}^{\text{in}}} = \mathbf{0}_{\mathcal{N}_c + 4}. \quad (\text{J.13})$$

The application of eqs. (J.12)-(J.13) gives:

$$\mathbf{Q}_{s_i p_j}^{s_k p_l} = \tilde{\mathbf{Q}}_{s_i p_j}^{s_k p_l} - (\boldsymbol{\Psi}_{s_i}^{\text{in}})^T \boldsymbol{\Lambda}^{\text{in}}, \quad (p_j, s_k, p_l) \in \mathcal{C}_{s_i}^{\text{in}}, \quad s \in \mathcal{S}, \quad i \in \mathcal{I}_s, \quad (\text{J.14})$$

$$\mathbf{0}_{\mathcal{N}_c + 4} = \sum_{\substack{s \in \mathcal{S} \\ i \in \mathcal{I}_s}} \sum_{\substack{(p_j, s_k, p_l) \\ \in \mathcal{C}_{s_i}^{\text{in}}}} \boldsymbol{\Psi}_{s_i}^{\text{in}} \mathbf{Q}_{s_i p_j}^{s_k p_l}. \quad (\text{J.15})$$

The left multiplication of eq. (J.14) by the matrix $\Psi_{s_i}^{\text{in}}$ and the sum of the result obtained over all the inelastic collisions gives:

$$\begin{aligned} \sum_{\substack{s \in \mathcal{S} \\ i \in \mathcal{I}_s}} \sum_{\substack{(p_j, s_k, p_l) \\ \in \mathcal{C}_{s_i}^{\text{in}}}} \Psi_{s_i}^{\text{in}} \mathbf{Q}_{s_i p_j}^{s_k p_l} &= \sum_{\substack{s \in \mathcal{S} \\ i \in \mathcal{I}_s}} \sum_{\substack{(p_j, s_k, p_l) \\ \in \mathcal{C}_{s_i}^{\text{in}}}} \Psi_{s_i}^{\text{in}} \tilde{\mathbf{Q}}_{s_i p_j}^{s_k p_l} - \\ &\quad \sum_{\substack{s \in \mathcal{S} \\ i \in \mathcal{I}_s}} \Psi_{s_i}^{\text{in}} (\Psi_{s_i}^{\text{in}})^T \#(\mathcal{C}_{s_i}^{\text{in}}) \Lambda^{\text{in}}. \end{aligned} \quad (\text{J.16})$$

The left-hand-side of eq. (J.16) is zero in view of the imposed constraint (J.15). In view of this, eq. (J.16) can be solved for the Lagrange multiplier vector to give:

$$\Lambda^{\text{in}} = (\tilde{\Psi}^{\text{in}})^{-1} \tilde{\mathbf{Q}}^{\text{in}}, \quad (\text{J.17})$$

where the matrix $\tilde{\Psi}^{\text{in}}$ and the vector $\tilde{\mathbf{Q}}^{\text{in}}$ are defined as:

$$\tilde{\Psi}^{\text{in}} = \sum_{\substack{s \in \mathcal{S} \\ i \in \mathcal{I}_s}} \mathcal{N}_{s_i}^{\text{in}} \Psi_{s_i}^{\text{in}} (\Psi_{s_i}^{\text{in}})^T, \quad (\text{J.18})$$

$$\tilde{\mathbf{Q}}^{\text{in}} = \sum_{\substack{s \in \mathcal{S} \\ i \in \mathcal{I}_s}} \sum_{\substack{(p_j, s_k, p_l) \\ \in \mathcal{C}_{s_i}^{\text{in}}}} \Psi_{s_i}^{\text{in}} \tilde{\mathbf{Q}}_{s_i p_j}^{s_k p_l}. \quad (\text{J.19})$$

Quantity $\mathcal{N}_{s_i}^{\text{in}}$ is equal to $\#(\mathcal{C}_{s_i}^{\text{in}})$. The substitution of eq. (J.17) in eq. (J.14) gives the thesis of Proposition 6.3.2 stated in eq. (6.48):

$$\begin{aligned} \mathbf{Q}_{s_i p_j}^{s_k p_l} &= \tilde{\mathbf{Q}}_{s_i p_j}^{s_k p_l} - (\Psi_{s_i}^{\text{in}})^T (\tilde{\Psi}^{\text{in}})^{-1} \tilde{\mathbf{Q}}^{\text{in}}, \\ (p_j, s_k, p_l) &\in \mathcal{C}_{s_i}^{\text{in}}, \quad s \in \mathcal{S}, \quad i \in \mathcal{I}_s. \end{aligned} \quad (\text{J.20})$$

Appendix K

Discrete Macroscopic Moments

The macroscopic moments introduced in secs. 1.3-1.4 are approximated as follows:

- Partial densities:

$$\rho_{s_i} = m_s \Delta c^3 \sum_{\mathbf{h} \in \mathcal{H}^3} w_h f_{s_i}(\mathbf{c}_h), \quad s \in \mathcal{S}, \quad i \in \mathcal{I}_s, \quad (\text{K.1})$$

- Hydrodynamic velocity:

$$\mathbf{v} = \frac{\Delta c^3}{\rho} \sum_{\substack{s \in \mathcal{S} \\ i \in \mathcal{I}_s}} \sum_{\mathbf{h} \in \mathcal{H}^3} w_h m_s \mathbf{c}_h f_{s_i}(\mathbf{c}_h), \quad (\text{K.2})$$

- Diffusion velocities:

$$\mathbf{v}_{s_i}^d = \frac{\Delta c^3}{\rho_{s_i}} \sum_{\mathbf{h} \in \mathcal{H}^3} w_h m_s (\mathbf{c}_h - \mathbf{v}) f_{s_i}(\mathbf{c}_h), \quad s \in \mathcal{S}, \quad i \in \mathcal{I}_s, \quad (\text{K.3})$$

- Translational temperature components:

$$T_{s_i \alpha} = \frac{m_s \Delta c^3}{n_{s_i} k_b} \sum_{\mathbf{h} \in \mathcal{H}^3} w_h [v_\alpha - c_{h \alpha}]^2 f_{s_i}(\mathbf{c}_h), \quad (\text{K.4})$$

$$s \in \mathcal{S}, \quad i \in \mathcal{I}_s, \quad \alpha \in \{x, y, z\},$$

- Viscous stress tensor:

$$\underline{\tau} = -\Delta c^3 \sum_{\substack{s \in \mathcal{S} \\ i \in \mathcal{I}_s}} \sum_{\mathbf{h} \in \mathcal{H}^3} w_h m_s (\mathbf{c}_h - \mathbf{v}) \otimes (\mathbf{c}_h - \mathbf{v}) f_{s_i}(\mathbf{c}_h) + p \underline{\mathbf{I}}, \quad (\text{K.5})$$

- Heat flux vector:

$$\mathbf{q} = \Delta c^3 \sum_{\substack{s \in \mathcal{S} \\ i \in \mathcal{I}_s}} \sum_{\mathbf{h} \in \mathcal{H}^3} w_h (\mathbf{c}_h - \mathbf{v}) \left(\frac{1}{2} m_s |\mathbf{c}_h - \mathbf{v}|^2 + E_{s_i} \right) f_{s_i}(\mathbf{c}_h). \quad (\text{K.6})$$

References

- (2012). FFTW-Fastest Fourier Transform in the West. <http://www.fftw.org>. (p. 161)
- (2013). GSL-GNU Scientific Library. <http://www.gnu.org/software/gsl/>. (p. 161)
- Abramovitz, M. and I. A. Stegun (1972). *Handbook of Mathematical Functions with Formulas, Graphs, and Mathematical Tables*. Dover Publications. (p. 151, 224)
- Adamovich, I. V., S. O. Macheret, J. W. Rich, and C. E. Treanor (1995a). Vibrational relaxation and dissociation behind shock waves. Part 1: kinetic rate models. *AIAA J.* 33(6), 1064–1069. (p. 9)
- Adamovich, I. V., S. O. Macheret, J. W. Rich, and C. E. Treanor (1995b). Vibrational relaxation and dissociation behind shock waves. Part 2: master equation modeling. *AIAA J.* 33(6), 1070–1075. (p. 9)
- Adamovich, I. V., S. O. Macheret, J. W. Rich, and C. E. Treanor (1998). Vibrational energy transfer rates using a forced harmonic oscillator model. *J. Thermophys. Heat Transfer* 12(1), 57–65. (p. 9)
- Alexeeev, B. V., A. Chilakhaoui, and I. T. Grushin (1994). Application of the generalized chapman-enskog method to the transport coefficient calculation in a reacting gas mixture. *Phys. Rev. E* 49(4), 2809–2825. (p. 22)
- Aliat, A., A., Chikhaoui, and E. V. Kustova (2003). Nonequilibrium kinetics of a radiative CO flow behind a shock wave. *Phys. Rev. E* 68(5), 056306. (p. 9)
- Alonso, R., I. M. Gamba, and S. H. Tharkabhushanam (2013). Accuracy and consistency of Lagrangian based conservative spectral method for space-homogeneous Boltzmann equation. submitted. (p. 13)
- Alsmeyer, H. (1976). Density profiles in argon and nitrogen shock waves measured by the absorption of an electron beam. *J. Fluid Mech.* 74(3), 497–513. (p. 168)
- Anderson, J. B., J. D. Foch, M. J. Shaw, R. C. Stern, and B. J. Wu (1986). Statistical theory of electronic energy relaxation. In *Proc. of the 15th Int. Symposium on Rarefied Gas Dynamics*. AIP. (p. 178)
- Anderson, J. D. (1989). *Hypersonic and High Temperature Gasdynamics*. New York, NY: McGraw-Hill. (p. 1, 6, 26, 181)
- Annaloro, J. and A. Bultel (2013). Elaboration of collisional-radiative mod-

- els for flows related to planetary entries into the Earth and Mars atmospheres. *Plasma Sources Sci. Technol.* 22(2), 025008. (p. 50)
- Appleton, J. P. and K. N. C. Bray (1964). The conservation equations for a non-equilibrium plasma. *J. Fluid Mech.* 20(4), 659–672. (p. 6)
- Aristov, V. V. (2001). *Direct Methods for Solving the Boltzmann Equation and Study of Nonequilibrium Flows*, Volume 60 of *Fluid Mechanics and Its Applications*. Springer. (p. 12)
- Armenise, I., M. Capitelli, R. Celiberto, G. Colonna, C. Gorse, and A. Lagana (1994). Effects of N + N₂ collisions on the nonequilibrium vibrational distributions of nitrogen under re-entry conditions. *Chem. Phys. Lett.* 227(1), 157–163. (p. 9, 128, 136)
- Babu, V. and V. V. Subramaniam (1995). Numerical solutions to nozzle flows with vibrational nonequilibrium. *J. Thermophys. Heat Transfer* 9(2), 227–232. (p. 9)
- Bhatnagar, P. L., E. P. Gross, and M. Krook (1954). A model for collision processes in gases. I. Small amplitude processes in charged and neutral one-component systems. *Phys. Rev.* 94(3), 511–525. (p. 11)
- Bird, G. A. (1967). The velocity distribution function within a shock wave. *J. Fluid Mech.* 30(3), 479–487. (p. 10)
- Bird, G. A. (1970). Aspects of the structure of strong shock waves. *Phys. Fluids* 13(5), 1172–1177. (p. 10)
- Bird, G. A. (1994). *Molecular Gas Dynamics and the Direct Simulation of Gas Flows*. Clarendon. (p. 2, 3, 5, 10, 161, 162, 163, 164, 170, 171, 175)
- Blazek, J. (2006). *Computational Fluid Dynamics: Principles and Applications*. Elsevier Science. (p. 105, 110, 217)
- Bobylev, A. V. (1975). The method of the fourier transform in the theory of the boltzmann equation for maxwell molecules. *Dokl. Akad. Nauk SSSR* 225(6), 1041–1044. in Russian. (p. 12)
- Bobylev, A. V. (1988). The theory of the nonlinear spatially uniform Boltzmann equation for Maxwell molecules. *Math. Phys. Rev.* 7, 111–233. Soviet Sci. Rev. Sect. C Math. Phys.Rev. (p. 12, 149)
- Bobylev, A. V. and S. Rjasanow (1997). Difference scheme for the Boltzmann equation based on the Fast Fourier Transform. *Eur. J. Mech. B - Fluids* 16, 293–306. (p. 13)
- Bobylev, A. V. and S. Ryasanow (1999). Fast deterministic method of solving the Boltzmann equation for hard spheres. *Eur. J. Mech. B - Fluids* 18(5), 869–887. (p. 12, 13)
- Bourdon, A., M. Panesi, A. Brandis, T. E. Magin, G. Chaban, W. Huo, R. Jaffe, and D. W. Schwenke (2008). Simulation of flows in shock-tube facilities by means of a detailed chemical mechanism for nitrogen excitation and dissociation. In *Proc. of the Summer Program*, Stanford University, Stanford, CA. Center for Turbulent Research. (p. 49, 63)
- Boyd, I. D. (1990). Rotational-translational energy transfer in rarefied

- nonequilibrium flows. *Phys. Fluids A* 2(3), 447–452. (p. 10)
- Boyd, I. D. (1991). Analysis of the vibrational-translational energy transfer using the direct simulation Monte Carlo method. *Phys. Fluids A* 3(7), 1785–1791. (p. 10)
- Boyd, I. D. (1992). Analysis of vibration-dissociation-recombination processes behind strong shock waves of nitrogen. *Phys. Fluids A* 4(1), 178–185. (p. 10)
- Boyd, I. D. (2008). Direct simulation Monte Carlo for atmospheric Entry. In *Non-Equilibrium Gas Dynamics - From Physical Models to Hypersonic Flights*, Lecture Series. von Karman Institute for Fluid Dynamics. (p. 10)
- Broadwell, J. E. (1964). Shock structure in a simple discrete velocity gas. *Phys. Fluids* 7(8), 1243–1247. (p. 12)
- Bruno, D., M. Capitelli, F. Esposito, S. Longo, and P. Minelli (2002). Direct simulation of non-equilibrium kinetics under shock conditions in nitrogen. *Chem. Phys. Lett.* 360(3), 31–37. (p. 10)
- Bruno, D., F. Esposito, and V. Giovangigli (2013). Relaxation of rotational-vibrational energy and volume viscosity in H-H₂ mixtures. *J. Chem. Phys.* 138(8), 084302. (p. 35)
- Bruno, D. and Giovangigli (2012). Relaxation of internal temperature and volume viscosity. *Phys. Fluids* 23(9), 093104. (p. 35)
- Bultel, A., B. G. Chéron, A. Bourdon, O. Motapon, and I. F. Schneider (2006). Collisional-radiative model in air for earth re-entry problems. *Phys. Plasmas* 13(4), 043502. (p. 8)
- Cambier, J.-L. and S. Moreau (1993). Simulation of a molecular plasma in collisional-radiative nonequilibrium. AIAA Paper 1993–3196. 24th Plasma dynamics and Laser Conference, Orlando, FL. (p. 9)
- Candler, G. V. and R. W. MacCormack (1991). Computation of weakly ionized hypersonic flows in thermochemical nonequilibrium. *J. Thermophys. Heat Transfer* 5(3), 266–273. (p. 6, 7, 8, 93, 104, 107, 202)
- Candler, G. V., J. Olejniczak, and B. Harrold (1997). Detailed simulation of nitrogen dissociation in stagnation regions. *Phys. Fluids* 9(7), 2108. (p. 9)
- Capitelli, M. (1986). *Nonequilibrium Vibrational Kinetics*, Volume 39 of *Topics in Current Physics*. Berlin: Springer. (p. 9)
- Capitelli, M., C. M. Ferreira, B. F. Gordiets, and A. I. Osipov (2000). *Plasma Kinetics in Atmospheric Gases*. Springer. (p. 6, 7, 8, 9, 30, 63, 136)
- Center, R. E. (1967). Measurement of shock-wave structure in helium-argon mixtures. *Phys. Fluids* 10(8), 1777–1784. (p. 175)
- Cercignani, C. (2000). *Rarefied Gasdynamics. From Basic Concepts to Actual Calculations*, Volume 21 of *Cambridge Texts in Applied Mathematics*. Cambridge, UK: Cambridge University Press. (p. 11, 12)
- Cercignani, C. and G. Tironi (1967). Non-linear heat transfer between two parallel plates according to a model with correct prandtl number. In *Proc. of the 5th Int. Symposium on Rarefied Gas Dynamics*, New York. Aca-

- demic Press. (p. 11)
- Chaban, G., R. L. Jaffe, D. W. Schwenke, and W. Huo (2008). Dissociation cross-sections and rate coefficients for nitrogen from accurate theoretical calculations. AIAA Paper 2008-1209. 46th AIAA Aerospace Sciences Meeting and Exhibit, Reno, NV. (p. 9, 49, 50)
- Chapman, B., G. Jost, and R. van der Pas (2008). *Using OpenMP*. MIT press. (p. 161)
- Chapman, S. and T. G. Cowling (1970). *The Mathematical Theory of Non Uniform Gases*. Cambridge, UK: Cambridge University Press. (p. 34)
- Chen, R., R. K. Agarwal, and F. G. Tcheremissine (2007). Computation of hypersonic flow of a diatomic gas in rotational nonequilibrium past a blunt body using the generalized Boltzmann equation. AIAA Paper 2007-4550. 39th AIAA Thermophysics Conference, Miami, FL. (p. 12)
- Chernyi, G. . G., S. A. Losev, S. O. Macheret, and B. V. Potapkin (2002a). *Physical and Chemical Processes in Gas Dynamics: Cross Sections and Rate Constants for Physical and Chemical Processes - Volume I*, Volume 196 of *Progresses in Astronautics and Aeronautics*. American Institute of Aeronautics and Astronautics. (p. 7, 9)
- Chernyi, G. . G., S. A. Losev, S. O. Macheret, and B. V. Potapkin (2002b). *Physical and Chemical Processes in Gas Dynamics: Physical and Chemical Kinetics and Thermodynamics of Gases and Plasmas - Volume II*, Volume 197 of *Progresses in Astronautics and Aeronautics*. American Institute of Aeronautics and Astronautics. (p. 7, 8)
- Clarke, P. B., P. L. Varghese, and D. B. Goldstein (2012). A novel discrete velocity method for solving the Boltzmann equation including internal energy and variable grids in velocity space. In *Proc. of the 28th Int. Symposium on Rarefied Gas Dynamics*. AIP. (p. 12)
- Cockburn, B., G. E. Karniadakis, and C.-W. Shu (2011). *Discontinuous Galerkin Methods: Theory, Computation and Applications*, Volume 11 of *Lectures Notes in Computational Science and Engineering*. Berlin: Springer. (p. 11)
- Colonna, G., I. Armenise, D. Bruno, and M. Capitelli (2006). Reduction of state-to-state kinetic to macroscopic models in hypersonic flows. *J. Thermophys. Heat Transfer* 20(3), 477–486. (p. 136)
- Colonna, G. and M. Capitelli (2001). Self-consistent model of chemical, vibrational, electron kinetics in nozzle expansion. *J. Thermophys. Heat Transfer* 15(3), 308–316. (p. 9)
- Colonna, G., M. Tuttafesta, M. Capitelli, and D. Giordano (1999). Non-Arrhenius NO formation rate in one-dimensional nozzle airflow. *Journal of Thermophysics and Heat Transfer* 13(3), 372–375. (p. 9)
- Degond, P. and B. Lucquin-Desreux (1996). The asymptotics of collision operators for two species of particles of disparate masses. *Math. Models Methods Appl. Sci.* 6(3), 405–436. (p. 34)
- Dellacherie, S. (2003). On the Wang Chang-Uhlenbeck equation. *Discrete*

- Cont. Dyn. B* 3(3), 229–253. (p. 20, 148)
- Einfeldt, B., C. D. Munz, P. L. Roe, and B. Sjogreen (1991). On godunov-type methods near low densities. *J. Comput. Phys.* 92(2), 273–295. (p. 109)
- Ern, A. and V. Giovangigli (1998). The kinetic chemical equilibrium regime. *Physica A* 260(1-2), 49–72. (p. 33)
- Esposito, F., I. Armenise, and M. Capitelli (2006). N – N₂ state-to-state vibrational relaxation and dissociation rate coefficients based on quasi-classical calculations. *Chem. Phys.* 331(1), 1–8. (p. 9, 63, 64, 136)
- Esposito, F. and M. Capitelli (1999). Quasi-classical molecular dynamic calculations of vibrationally and rotationally state selected dissociation cross sections: N + N₂(v, j) → 3N. *Chem. Phys. Lett.* 302(1), 49–54. (p. 9, 63, 64, 136)
- Esposito, F. and M. Capitelli (2000). Quasi-classical dynamics and vibrational kinetics of N + N₂(v) system. *Chem. Phys.* 257(2), 193–202. (p. 9)
- Esposito, F., C. Gorse, and M. Capitelli (1999). Quasi-classical dynamics calculations and state-selected rate coefficients for H + H₂(v, j) → 3H processes: application to the global dissociation rate under thermal equilibrium conditions. *Chem. Phys. Lett.* 303(5). (p. 9)
- Ferziger, J. H. and H. G. Kaper (1972). *Mathematical Theory of Transport Processes in Gases*. North-Holland Pub. Co. (p. 2, 3, 4, 19, 20, 25, 31, 34, 39, 40, 41, 44, 169)
- Filbet, F. and G. Russo (2003). High order numerical methods for the space non-homogeneous Boltzmann equation. *J. Comput. Phys.* 186(2), 457–480. (p. 12, 13, 155)
- Frigo, M. and S. G. Johnson (2005). The design and implementation of FFTW3. *Proc. of the IEEE* 93(2), 216–231. (p. 161)
- Gamba, I. M. and S. H. Tharkabhushanam (2009). Spectral-Lagrangian methods for collisional models of non-equilibrium statistical states. *J. Comput. Phys.* 228(6), 2012–2036. (p. 12, 13, 147, 149, 153, 157, 158, 161, 171, 178)
- Gamba, I. M. and S. H. Tharkabhushanam (2010). Shock and boundary structure formation by spectral-Lagrangian methods for the inhomogeneous Boltzmann transport equation. *J. Comput. Math.* 28(4), 430–460. (p. 12, 13, 153, 157, 158, 161, 171, 178)
- Gear, C. W. (1971). *Numerical Initial-Value Problems in Ordinary Differential Equations*. Englewood Cliffs, NJ: Prentice-Hall. (p. 80, 105)
- Gessman, R. J., C. O. Laux, and C. Kruger (1997). Experimental study of kinetic mechanisms of recombining atmospheric pressure air plasmas. AIAA Paper 1997-2364. 28th AIAA Plasma-dynamics and Lasers Conference, Atlanta, GA. (p. 9)
- Giordano, D. (2002). Hypersonic-flow governing equations with electromagnetic fields. AIAA Paper 2002-2165. 33rd Plasmadynamics and Lasers Conference, Maui, HW. (p. 4, 31)

- Giovangigli, V. (1999). *Multicomponent Flow Modeling*. Berlin: Birkhäuser. (p. 3, 4, 19, 22, 23, 24, 25, 31, 33, 34, 37, 41, 44)
- Gnoffo, P. A. (1999). Planetary-entry gas dynamics. *Annu. Rev. Fluid Mech.* 31, 459–494. (p. 1, 2, 3, 4, 6, 126)
- Gnoffo, P. A., R. N. Gupta, and J. L. Shinn (1989). Conservation equations and physical models for hypersonic air flows in thermal and chemical nonequilibrium. NASA Technical Paper 2867. (p. 6, 7, 8, 93, 104, 205)
- Grad, H. (1949). On the kinetic theory of rarefied gases. *Commun. Pure Appl. Math.* 2(4), 331–407. (p. 13)
- Graile, B., T. E. Magin, and M. Massot (2008). Modeling of reactive plasmas for atmospheric entry flows based on kinetic theory. In *Proc. of the Summer Program*, Stanford University, Stanford, CA. Center for Turbulent Research. (p. 35)
- Graile, B., T. E. Magin, and M. Massot (2009). Kinetic theory of plasmas: translational energy. *Math. Models Methods Appl. Sci.* 19(4), 527–599. (p. 34)
- Gupta, R. N., K. Lee, R. A. Thompson, and J. M. Yos (1991). Calculations and curve fits of thermodynamic and transport properties for equilibrium air to 30000K. NASA Report 1260. (p. 74)
- Gupta, R. N. and K. P. Lee (1995). Thermo-chemical nonequilibrium analysis of viscous shock-layers. AIAA Paper 1995–2083. 30th AIAA Thermophysics Conference, San Diego, CA. (p. 101)
- Guy, A., A. Bourdon, and M.-Y. Perrin (2013). Consistent multi-internal-temperatures models for nonequilibrium nozzle flows. *Chem. Phys.* 420(11), 15–24. (p. 63, 193)
- Haack, J. R. and I. M. Gamba (2012a). Conservative deterministic spectral Boltzmann-Poisson solver near the Landau limit. In *Proc. of the 28th Int. Symposium on Rarefied Gas Dynamics*. AIP. (p. 12, 13)
- Haack, J. R. and I. M. Gamba (2012b). High-performance computing for conservative spectral Boltzmann solvers. In *Proc. of the 28th Int. Symposium on Rarefied Gas Dynamics*. AIP. (p. 12)
- Hammerling, P., J. D. Teare, and B. Kivel (1959). Theory of radiation from luminous shock waves in nitrogen. *Phys. Fluids* 2(4), 422–426. (p. 7)
- Hansen, F. (1991). Dissociation of diatomic gases. *J. Chem. Phys.* 95(10), 7226–7233. (p. 7)
- Hash, D. B. and H. A. Hassan (1993). Direct simulation with vibration-dissociation coupling. *J. Thermophys. Heat Transfer* 7(4), 680–686. (p. 10)
- Hirsch, C. (1990). *Numerical Computation of Internal and External Flows*. New York, NY: John Wiley & Sons. (p. 6, 11, 100, 101, 103, 104, 105, 107, 109, 110, 154, 155, 204)
- Hirschfelder, J. O., C. F. Curtiss, and R. B. Bird (1964). *Molecular Theory of Gases and Liquids*. John Wiley & Sons. (p. 168, 169)
- Holway, L. H. (1966). New statistical models for kinetic theory: methods of

- construction. *Phys. Fluids* 9(9), 1658–1668. (p. 11)
- Hugoniot, H. (1887). Memoir on the propagation of movements in bodies, especially perfect gases (first part). *J. de l'Ecole Polytechnique* 57, 3–97. in French. (p. 80, 181)
- Hugoniot, H. (1889). Memoir on the propagation of movements in bodies, especially perfect gases (second part). *J. de l'Ecole Polytechnique* 58, 1–125. in French. (p. 80, 181)
- Ivanov, M. K., A. Kashakovskiy, S. Gimelshein, G. Markelov, A. Alexeenko, Y. Bondar, G. Zhukova, S. Nikiforov, and P. Vashenkov (2006). SMILE system for 2D/3D DSMC computations. In *Proc. of the 25th Int. Symposium on Rarefied Gas Dynamics*. AIP. (p. 10)
- Ivanov, M. S. and S. F. Gimelshein (1998). Computational Hypersonic Rarefied Flows. *Annu. Rev. Fluid Mech.* 30, 469–505. (p. 10)
- Jaffe, R. L. (1986). Rate constants for chemical reactions in high-temperature nonequilibrium air. In *Progresses in Aerospace Sciences*, Volume 103, pp. 123–151. American Institute of Aeronautics and Astronautics. (p. 7)
- Jaffe, R. L. (1987). The calculation of high-temperature equilibrium and nonequilibrium specific heat data for N₂, O₂ and NO. AIAA Paper 1987–1633. 22nd AIAA Thermophysics Conference, Honolulu, Hawaii. (p. 50)
- Jaffe, R. L., D. W. Schwenke, and G. Chaban (2009). Theoretical analysis of N₂ collisional dissociation and rotation-vibration energy transfer. AIAA Paper 2009–1569. 47th AIAA Aerospace Sciences Meeting and Exhibit, Orlando, FL. (p. 9, 49, 50)
- Jaffe, R. L., D. W. Schwenke, G. Chaban, and W. Huo (2008). Vibrational and rotational excitation and relaxation of nitrogen from accurate theoretical calculations. AIAA Paper 2008–1208. 46th AIAA Aerospace Sciences Meeting and Exhibit, Reno, NV. (p. 9, 49, 50, 54)
- Jameson, A. and S. Yoon (1987). Lower-upper implicit schemes with multiple grids for the Euler equations. *AIAA J.* 25(7), 929–935. (p. 105, 106)
- Josyula, E., C. Suchyta, W. Bailey, and P. Vedula (2011). Kinetic view of the influence of internal energy states on shock structure. AIAA Paper 2011–3135. 11th AIAA/ASME Joint Thermophysics and Heat Transfer Conference, Honolulu, HW. (p. 12, 181)
- Kapper, M. G. (2009). *A High-Order Transport Scheme for Collisional-Radiative and Nonequilibrium Plasma*. Ph. D. thesis, The Ohio State University, Columbus, OH. (p. 108, 109, 110)
- Kapper, M. G. and J.-L. Cambier (2011a). Ionizing shocks in argon. Part I: collisional-radiative model and steady-state structure. *J. Appl. Phys.* 109(11), 113308. (p. 9, 108)
- Kapper, M. G. and J.-L. Cambier (2011b). Ionizing shocks in argon. Part II: transient and multi-dimensional effects. *J. Appl. Phys.* 109(11), 113309. (p. 9, 108)
- Kapper, M. G., G. Martins, M. Torrilhon, and T. E. Magin (2011). Numerical schemes for nonequilibrium multicomponent plasmas based on the

- regularized Grad equations. In *Proc. of the 4th European Conference for Aerospace Sciences - EUCASS*. EPD Sciences. (p. 13, 14)
- Kerner, E. H. (1958). Note on the forced and damped oscillator in quantum mechanics. *Can. J. Phys.* 36(3), 371–377. (p. 9)
- Kim, J. G., O. J. Kwon, and C. Park (2009). Master equation study and nonequilibrium chemical reactions for H+H₂ and He+H₂. *J. Thermophys. Heat Transfer* 23(3), 443–453. (p. 9)
- Klomfass, A. and S. Müller (1997). Calculation of stagnation streamline quantities in hypersonic blunt body flows. *Shock Waves* 7(1), 13–23. (p. 101, 102)
- Knab, O., H.-H. Frühauf, and S. Jonas (1992). Multiple temperature descriptions of reaction rate constants with regard to consistent chemistry-vibration coupling. AIAA Paper 1992–2947. 27th AIAA Thermophysics Conference, Nashville, TN. (p. 7, 8)
- Kolobov, V. I., R. R. Arsanbekov, V. V. Aristov, A. A. Frolova, and S. A. Zabelok (2007). Unified solver for rarefied and continuum flows with adaptive mesh and algorithm refinement. *J. Comput. Phys.* 223(2), 589–608. (p. 11, 12)
- Kosuge, S., K. Aoki, and S. Takata (2001). Shock-wave structure for a binary gas mixture: finite-difference analysis of the Boltzmann equation for hard-sphere molecules. *Eur. J. Mech. B - Fluids* 20(1), 87–126. (p. 12)
- Koura, K. (1992). Statistical inelastic cross-section model for the Monte-Carlo simulation of molecules with discrete internal energy. *Phys. Fluids A* 4(8), 1782–1788. (p. 10)
- Koura, K. (1994). A set of model cross-sections for Monte-Carlo simulation of rarefied real gases: atom-diatom collisions. *Phys. Fluids* 6(10), 3473–3486. (p. 10)
- Kustova, E. V. and E. A. Nagnibeda (1998). Transport properties of a reacting gas mixture with strong vibrational and chemical nonequilibrium. *Chem. Phys.* 233(1), 57–75. (p. 34, 35, 36)
- Kuščer, I. (1991). Dissociation and recombination in a nonhomogeneous Gas. *Physica A* 176(3), 542–556. (p. 22)
- Landau, L. and E. Teller (1936). Theory of sound dispersion. *Phys. Z Sowjetunion* 10(1), 34–43. in German. (p. 6, 93)
- Landrum, D. B. and G. V. Candler (1992). Developemt of a new model for vibration-dissociation coupling in nitrogen. AIAA Paper 1992–2853. 27th AIAA Thermophysics Conference, Nashville, TN. (p. 7)
- Lani, A. (2009). *An Object Oriented and High-Performance Platform for Areothermodynamics Simulations*. Ph. D. thesis, Université Libre de Bruxelles, Bruxelles, Belgium. (p. 8, 93)
- Laux, C. O. (2006). Radiation and nonequilibrium collisional radiative models. In *Physico-Chemical Models for High Enthalpy and Plasma Flows*, Lecture Series. von Karman Institute for Fluid Dynamics. (p. 8, 9)
- Le Roy, R. J., Y. Huang, and C. Jary (2006). An accurate analytic poten-

- tial function for ground-state N₂ from a direct-potential-fit analysis of spectroscopic data. *J. Chem. Phys.* 125(16), 164310. (p. 50)
- Leveque, R. J. (2002). *Finite Volume Methods for Hyperbolic Problems*, Volume 31 of *Cambridge Texts in Applied Mathematics*. Cambridge, UK: Cambridge University Press. (p. 13)
- Leveque, R. J. (2008). *Numerical Methods for Conservation Laws*, Volume 31 of *Lectures in Mathematics. ETH Zürich*. Berlin: Birkhäuser. (p. 11, 204)
- Levermore, C. D. and W. J. Morokoff (1998). The gaussian moment closure for gas dynamics. *SIAM J. Appl. Math.* 59(1), 72–96. (p. 13)
- Liou, M.-S. and B. van Leer (1988). Choice of implicit and explicit operators for the upwind differencing method. AIAA Paper 1988-624. 26th AIAA Aerospace Sciences Meeting, Reno, NV. (p. 105)
- Losev, S. A. (1996). Two temperature chemical kinetics in gas dynamics. AIAA Paper 1996-2026. 27th AIAA Fluid Dynamics Conference, Orlando, FL. (p. 7)
- Ludwig, G. and M. Heil (1960). Boundary layer theory with dissociation and ionization. In *Advances in Applied Mechanics*, Volume VI, pp. 39–118. Academic Press, New York. (p. 22)
- Macheret, S. O., A. A. Fridman, I. V. Adamovich, J. W. Rich, and C. E. Treanor (1994). Mechanism of nonequilibrium dissociation of diatomic molecules. AIAA Paper 1994-1984. 6th AIAA/ASME Joint Thermophysics and Heat Transfer Conference, Colorado Springs, CO. (p. 7)
- Macheret, S. O. and J. W. Rich (1993). Theory of nonequilibrium dissociation rates behind strong shock waves. AIAA Paper 1993-2860. 28th AIAA Thermophysics Conference, Orlando, FL. (p. 7)
- Magin, T. E., A. Bourdon, R. Jaffe, and D. W. Schwenke (2009). Internal energy excitation and dissociation of molecular nitrogen in a compressing flow. AIAA Paper 2009-3837. 41st AIAA Thermophysics Conference, San Antonio, TX. (p. 49, 63, 80)
- Magin, T. E., A. Bourdon, R. Jaffe, and D. W. Schwenke (2010). Rovibrational internal energy excitation and dissociation of molecular nitrogen in hypersonic flows. AIAA Paper 2010-4336. 10th AIAA/ASME Joint Thermophysics and Heat Transfer Conference, Chicago, IL. (p. 65, 66)
- Magin, T. E. and G. Degrez (2004). Transport properties of partially ionized and unmagnetized plasmas. *Phys. Rev. E* 70(4), 046412. (p. 43, 45, 74)
- Magin, T. E., M. Massot, and B. Graille (2012). Hydrodynamic model for molecular gases in thermal non-equilibrium. In *Proc. of the 28th Int. Symposium on Rarefied Gas Dynamics*. AIP. (p. 35)
- Magin, T. E., M. Panesi, A. Bourdon, R. L. Jaffe, and D. W. Schwenke (2012). Coarse-grain model for internal energy excitation and dissociation of molecular nitrogen. *Chem. Phys.* 398(4), 90–95. (p. 49, 65, 66)
- Marrone, P. V. and C. E. Treanor (1963). Chemical relaxation with preferential dissociation from excited vibrational levels. *Phys. Fluids* 6(9), 1215–1221. (p. 7)

- Martins, G., M. G. Kapper, M. Torrilhon, and T. E. Magin (2011). Hypersonic simulations based on the regularized Grad equations for multicomponent plasmas. AIAA Paper 2011-3305. 6th AIAA Theoretical Fluid Mechanics Conference, Honolulu, HW. (p. 13)
- Mason, E. A. and L. Monchick (1962). Heat conductivity of polyatomic and polar gases. *J. Chem. Phys.* 36(6), 1622–1639. (p. 34)
- Mieussens, L. (2000). Discrete velocity models and numerical schemes for the Boltzmann-BGK equation in plane and axisymmetric geometries. *J. Comput. Phys.* 162(2), 429–466. (p. 11, 154, 155)
- Mieussens, L. and H. Struchtrup (2004). Numerical comparison of Bhatnagar-Gross-Krook models with proper Prandtl number. *Phys. Fluids* 16(8), 2797–2813. (p. 11, 154)
- Mihalas, D. and B. W. Mihalas (1999). *Fundations of Radiation Hydrodynamics*. Dover Books on Physics. Mineola, NY: Dover Publications. (p. 4)
- Millikan, R. C. and D. R. White (1963). Systematics of vibrational relaxation. *J. Chem Phys.* 39(12), 3209–3214. (p. 6)
- Mitchner, M. and C. H. Kruger (1973). *Partially Ionized Gases*. John Wiley & Sons. (p. 20, 21)
- Monchick, L., K. S. Yun, and E. A. Mason (1963). Formal kinetic theory of transport phenomena in polyatomic gases. *J. Chem. Phys.* 39(3), 645–669. (p. 34)
- Morris, A. B., P. L. Varghese, and D. B. Goldstein (2011). Monte Carlo solution of the boltzmann equation via a discrete velocity model. *J. Comput. Phys.* 230(4), 1265–1280. (p. 12)
- Munafò, A., J. R. Haack, I. M. Gamba, and T. E. Magin (2014). A spectral-Lagrangian Boltzmann solver for a multi-energy level gas. *J. Comput. Phys.* 264, 152–176. (p. 147, 149, 157)
- Munafò, A., M. G. Kapper, J.-L. Cambier, and T. E. Magin (2012). Investigation of nonequilibrium effects in axisymmetric nozzle and blunt body nitrogen flows by means of a reduced rovibrational collisional model. AIAA Paper 2012-0647. 50h AIAA Aerospace Sciences Meeting including the New Horizons Forum and Aerospace Exposition, Nashville, TN. (p. 135)
- Munafò, A., A. Lani, A. Bultel, and M. Panesi (2013). Modeling of non-equilibrium phenomena in expanding flows by means of a collisional-radiative model. *Phys. Plasmas* 20(7), 073501. (p. 122)
- Munafò, A., M. Panesi, R. L. Jaffe, A. Bourdon, and T. Magin (2011). Mechanism reduction for rovibrational energy excitation and dissociation of molecular nitrogen in hypersonic flows. AIAA Paper 2011-3623. 11th AIAA/ASME Joint Thermophysics and Heat Transfer Conference, Honolulu, HW. (p. 49, 65, 69)
- Munafò, A., M. Panesi, R. L. Jaffe, G. Colonna, A. Bourdon, and T. E. Magin (2012). QCT-based vibrational collisional models applied to nonequilibrium nozzle flows. *Eur. Phys. Jour. D* 66, 188. (p. 49, 63, 136)
- Munafò, A., M. Panesi, R. L. Jaffe, A. Lani, and T. E. Magin (2010). Vi-

- brational state to state kinetics in expanding and compressing nitrogen flows. AIAA Paper 2010-4335. 10th AIAA/ASME Joint Thermophysics and Heat Transfer Conference, Chicago, IL. (p. 49, 63, 80)
- Munafò, A., M. Panesi, and T. E. Magin (2014). Boltzmann rovibrational collisional coarse-grained model for internal energy excitation and dissociation in hypersonic flows. *Phys. Rev. E* 89(2), 023001. (p. 49, 65, 69)
- Munafò, A., E. Torres, J. R. Haack, I. M. Gamba, and T. E. Magin (2013). Investigation of nonequilibrium effects across normal shock waves by means of a spectral-lagrangian Boltzmann solver. AIAA Paper 2013-0305. 51st AIAA Aerospace Sciences Meeting Including the New Horizons Forum and Aerospace Exposition, Dallas, TX. (p. 169)
- Nagnibeda, E. and E. Kustova (2009). *Non-Equilibrium Reacting Gas Flows*. Berlin: Springer. (p. 4, 19, 20, 30, 31, 34, 41)
- Ohwada, T. (1993). Structure of normal shock waves: Direct numerical analysis of the Boltzmann equation for hard-sphere molecules. *Phys. Fluids A* 5(1), 217–234. (p. 12)
- Ohwada, T., Y. Sone, and K. Aoki (1989). Numerical analysis of the Poiseuille and thermal transpiration flows between two parallel plates on the basis of the Boltzmann equation for hard-sphere molecules. *Phys. Fluids A* 1(12), 2042–2049. (p. 12)
- Oran, E. S. and J. P. Boris (2000). *Numerical Simulation of Reactive Flow*. Cambridge, UK: Cambridge University Press. (p. 11)
- Panesi, M., R. L. Jaffe, and D. W. Schwenke (2013). Energy transfer study of $\text{N}_2(^1\Sigma_g^+)$ + $\text{N}_2(^1\Sigma_g^+)$ and $\text{N}_2(^1\Sigma_g^+)$ + $\text{N}(^4\text{S}_u)$ interactions by using rovibrational state-to-state model. AIAA Paper 2013-3147. 44th AIAA Thermophysics Conference, San Diego, CA. (p. 49, 135, 193)
- Panesi, M., R. L. Jaffe, D. W. Schwenke, and T. E. Magin (2013). Rovibrational internal energy transfer and dissociation of $\text{N}(^4\text{S}_u)$ + $\text{N}_2(^1\Sigma_g^+)$ system in hypersonic flows. *J. Chem. Phys* 138(4), 044312. (p. 8, 49, 53, 55, 59, 82, 84, 85, 92, 93, 96)
- Panesi, M. and A. Lani (2013). Collisional radiative coarse-grain model for ionization in air. *Phys. Fluids* 25(5), 057101. (p. 9)
- Panesi, M., T. E. Magin, A. Bourdon, A. Bultel, and O. Chazot (2009). Fire II flight experiment analysis by means of a collisional-radiative model. *J. Thermophys. Heat Transfer* 23(2), 236–248. (p. 9)
- Panesi, M., T. E. Magin, A. Bourdon, A. Bultel, and O. Chazot (2011). Electronic excitation of atoms and molecules for the FIRE II flight experiment. *J. Thermophys. Heat Transfer* 25(3), 361–374. (p. 9, 50, 122)
- Panesi, M., T. E. Magin, A. Munafò, A. Bourdon, R. Jaffe, and D. W. Schwenke (2010). Rovibrational internal energy excitation and dissociation of nitrogen in hypersonic flows. In *Proc. of the Summer Program*, Stanford University, Stanford, CA. Center for Turbulent Research. (p. 49, 65, 66)

- Pareschi, L. and B. Perthame (1996). A Fourier spectral method for homogeneous Boltzmann equations. *Trans. Theo. Stat. Phys.* 25, 369–382. (p. 12)
- Pareschi, L. and G. Russo (2000). Numerical solution of the Boltzmann equation I: spectrally accurate approximation of the collision operator. *SIAM J. Numer. Anal.* 37(4), 1217–1245. (p. 12, 13)
- Pareschi, L. and G. Russo (2011). Efficient asymptotic preserving deterministic methods for the Boltzmann equation. In *Models and Computational Methods for Rarefied Flows*, Lecture Series. von Karman Institute for Fluid Dynamics. (p. 12)
- Park, C. (1988). Two-temperature interpretation of dissociation rate data for N₂ and O₂. AIAA Paper 1988–458. 26th AIAA Aerospace Sciences Meeting, Reno, NV. (p. 7)
- Park, C. (1989). Assessment of two-temperature kinetic model for ionizing air. *J. Thermophys. Heat Transfer* 3(3), 233–244. (p. 6)
- Park, C. (1990). *Nonequilibrium Hypersonic Aerothermodynamics*. New York, NY: Wiley. (p. 1, 5, 6, 7, 8, 54, 58, 60, 82, 92, 140)
- Park, C. (1993). Review of chemical-kinetic problems of future NASA missions, I: Earth entries. *J. Thermophys. Heat Transfer* 7(3), 385–398. (p. 6, 7, 93, 128)
- Park, C. (2010). The Limits of Two-Temperature Model. AIAA Paper 2010–911. 48th AIAA Aerospace Sciences Meeting including the New Horizons Forum and Aerospace Exposition, Orlando, FL. (p. 8)
- Park, C., J. T. Howe, R. L. Jaffe, and G. V. Candler (1994). Review of chemical-kinetic problems of future NASA missions, II: Mars entries. *J. Thermophys. Heat Transfer* 8(1), 9–23. (p. 6, 7)
- Parker, J. G. (1959). Rotational and vibrational relaxation in diatomic gases. *Phys. Fluids* 2(4), 449–462. (p. 7, 82)
- Pascal, S. and R. Brun (1993). Transport properties of nonequilibrium gas mixtures. *Phys. Rev. E* 47(5), 3251–3267. (p. 34)
- Pauling, L. and E. B. Wilson Jr. (1985). *Introduction to Quantum Mechanics with Applications to Chemistry*. Dover Books on Physics. Mineola, NY: Dover Publications. (p. 51, 52)
- Petit, J.-P. and J.-S. Darrozes (1975). New formulation of the equations of motion of an ionized gas in collision dominated regime. *JMec.* 14(4), 745–759. in French. (p. 34)
- Phelps, A. V., C. H. Greene, and J. P. Burke (2000). Collision cross sections for argon atoms with argon atoms for energies from 0.01 eV to 10 keV. *J. Phys. B* 33(16), 2965–2981. (p. 169)
- Pierrot, L., L. Yu, R. J. Gessman, C. O. Laux, and C. Kruger (1999). Collisional-radiative modeling of nonequilibrium nitrogen plasmas. AIAA Paper 1999–3478. 30th Plasmadynamics and Lasers Conference, Norfolk, VA. (p. 9)
- Plectcher, R. P., J. C. Tannehill, and D. Anderson (2011). *Computational*

- Fluid Mechanics and Heat Transfer.* Computational and Physical Processes in Mechanics and Thermal Sciences. Taylor & Francis. (p. 105)
- Prabhu, R. K. (1994). An implementation of a chemical and thermal nonequilibrium flow solver on unstructured meshes and application to blunt bodies. NASA Contract Report 194867. (p. 104, 109)
- Quirk, J. J. (1994). A contribution to the great Riemann solver debate. *Int. J. Numer. Meth. Fluids* 18(6), 555–574. (p. 109)
- Radhakrishnan, K. and A. C. Hindmarsh (1993). Description and use of LSODE, the Livermore solver for ordinary differential equations. NASA Report 1327. (p. 80)
- Ramshaw, J. D. and C. H. Chang (1996). Friction-weighted self-consistent effective binary diffusion approximation. *J. Non-Equilib. Thermodyn.* 21(3), 223–232. (p. 106, 215)
- Rankine, W. J. M. (1870). On the thermodynamic theory of waves of finite longitudinal disturbances. *Phil. Trans. Royal Soc.* 160, 277–288. (p. 80, 181)
- Robben, F. and L. Talbot (1966a). Experimental study of the rotational distribution function of nitrogen in a shock wave. *Phys. Fluids* 9(4), 653–662. (p. 7)
- Robben, F. and L. Talbot (1966b). Measurements of rotational temperatures in a low density wind tunnel. *Phys. Fluids* 9(4), 644–652. (p. 7)
- Roe, P. L. (1981). Approximate Riemann solvers, parameter vectors and difference schemes. *J. Comput. Phys.* 43(2), 357–372. (p. 103, 108)
- Schwartz, R. N., Z. I. Slawsky, and K. F. Herzfeld (1952). Calculation of vibrational relaxation times in gases. *J. Chem. Phys.* 20(10), 1591–1599. (p. 7)
- Schwenke, D. W. (1988). Calculations of rate constants for three-body recombination of H₂ in the presence of H₂. *J. Chem. Phys.* 89(4), 2076–2091. (p. 50)
- Schwenke, D. W. (2008). Dissociation cross-sections and rates for nitrogen. In *Non-Equilibrium Gas Dynamics - From Physical Models to Hypersonic Flights*, Lecture Series. von Karman Institute for Fluid Dynamics. (p. 9, 49, 50, 54)
- Seagal, B. M. and J. H. Ferziger (1970). Shock-wave structure using nonlinear model Boltzmann equations. *Phys. Fluids* 15(7), 1233–1247. (p. 11)
- Shakhov, E. M. (1968). Generalization of the Krook kinetic relaxation equation. *Fluid Dyn.* 3(5), 95–96. (p. 11)
- Sharma, S. P., W. M. Huo, and C. Park (1992). Rate parameters for coupled vibration-dissociation in a heneralized SSH appoximation. *J. Thermophys. Heat Transfer* 6(1), 9–21. (p. 7)
- Sharma, S. P., M. R. Ruffin, W. D. Gillespie, and S. A. Meyer (1993). Vibrational relaxation measurements in an expanding flow using spontaneous Raman scattering. *J. Thermophys. Heat Transfer* 7(4), 697–703. (p. 136, 139, 144)

- Struchtrup, H. (2005). *Macroscopic Transport Equations for Rarefied Gas Flows*. Berlin: Springer. (p. 3, 13)
- Struchtrup, H. and M. Torrilhon (2003). Regularization of Grad's 13-moment equations: derivation and analysis. *Phys. Fluids* 15(9), 2668–2680. (p. 13, 14)
- Suresh, A. and H. T. Huynh (1997). Accurate monotonicity-preserving schemes with Runge-Kutta time stepping. *J. Comput. Phys.* 136(1), 83–99. (p. 109)
- Svehla, R. A. (1995). Transport coefficients for the nasa Lewis chemical equilibrium program. NASA Technical Memorandum 4647. (p. 162)
- Tan, Z. and P. L. Varghese (1994). The $\Delta\text{-}\epsilon$ method for the Boltzmann equation. *J. Comput. Phys.* 110(2), 327–340. (p. 12)
- Tcheremissine, F. G. (1998). Conservative evaluation of Boltzmann collision integral in discrete ordinates approximation. *Computers Math. Appl.* 35(1). (p. 12)
- Tcheremissine, F. G. (2001). Solution of the Boltzmann equation in stiff regime. In *Hyperbolic Problems: Theory, Numerics, Applications*, Volume 141 of *ISNM International Series of Numerical Mathematics*, pp. 883–887. Birkhäuser. (p. 12)
- Tcheremissine, F. G. (2006). Solution to the Boltzmann kinetic equation for high-speed flows. *Comput. Math. Math. Phys.* 46(2), 315–329. (p. 12)
- Thivet, F. (1992). *Modeling of Hypersonic Flows in Thermal and Chemical Nonequilibrium*. Ph. D. thesis, Ecole Centrale Paris, Châtenay-Malabry, France. in French. (p. 80, 101)
- Torres, E. and T. E. Magin (2012). Statistical simulation of internal energy exchange in shock waves using explicit transition probabilities. In *Proc. of the 28th Int. Symposium on Rarefied Gas Dynamics*. AIP. (p. 161, 182)
- Torrilhon, M. and H. Struchtrup (2004). Regularized 13-moment equations: shock structure calculations and comparison to Burnett models. *J. Fluid Mech.* 513, 171–198. (p. 13)
- Treanor, C. E. (1965). Vibrational energy transfer in high energy collisions. *J. Chem Phys.* 43(2), 532–538. (p. 9)
- Treanor, C. E., I. V. Adamovich, M. J. Williams, and J. W. Rich (1996). Kinetics of nitric oxide formation behind shock waves. *J. Thermophys. Heat Transfer* 10(2), 193–199. (p. 9)
- Treanor, C. E. and P. V. Marrone (1962). Effect of the dissociation on the rate of vibrational relaxation. *Phys. Fluids* 5(9), 1022–1026. (p. 7)
- van Albada, G. D., B. van Leer, and W. W. Roberts (1982). A comparative study of computational methods in cosmic gasdynamics. *Astron. Astrophys.* 108(1), 76–84. (p. 105)
- van Leer, B. (1979). Towards the ultimate conservative difference scheme. *J. Comput. Phys.* 32(1), 101–136. (p. 104, 155)
- Vincenti, W. J. and C. H. Kruger (1965). *Introduction to Physical Gasdynamics*.

- namics. New York, NY: Wiley. (p. 4, 26)
- Wang-Chang, C. S. and G. E. Uhlenbeck (1951). Transport phenomena in polyatomic gases. University of Michigan Engineering Research Report CM-651. (p. 34, 35)
- Zang, J. Y. and J. C. Huang (1995). Rarefied flow computation using non-linear model boltzmann equations. *J. Comput. Phys.* 120(2), 323–339. (p. 11)
- Zel'dovich, Y. B. and Y. P. Raizer (2002). *Physics of Shock Waves and High-Temperature Hydrodynamic Phenomena*. Dover Books on Physics. Mineola, NY: Dover Publications. (p. 4)

